IMPROVED DEWATERABILITY OF IRON OXIDE DISPERSIONS

A thesis submitted for admission to the degree of

DOCTOR OF PHILOSOPHY

Applied Science (Minerals and Materials)

Melanie Jane M^{c}Guire

BSc (Hons)

Ian Wark Research Institute

ARC Special Research Centre for Particle and Material Interfaces

University of South Australia, Mawson Lakes, South Australia, 5095.

September 2008

To Mum and Dad,

without whom I would not have made it to or through this journey,

on so many almost indescribable levels.

TABLE OF CONTENTS

TABLE OF CONTENTS ..... **v**
LIST OF FIGURES ..... **xi**
LIST OF TABLES ..... **xix**
JOURNAL PUBLICATIONS ..... **xxi**
NOMENCLATURE ..... **xxiii**
ABSTRACT ..... **xxv**
AUTHOR'S STATEMENT ..... **xxvii**
ACKNOWLEDGEMENTS ..... **xxix**

CHAPTER 1 INTRODUCTION **1**
1.1 Aims and objectives 2
1.2 Chapter outline 3

CHAPTER 2 LITERATURE REVIEW **7**
2.1 Introduction 7
2.2 Importance of efficient dewatering methods 7
2.3 Fundamentals of dewatering 8
2.3.1 Primary dewatering 8
2.3.2 Secondary dewatering 10
2.3.3 Dewaterability of iron oxide 10
2.4 Interfacial chemistry 11
2.4.1 Zeta potential 13
2.4.1.1 Measurement of zeta potential 15
2.4.2 Effect of simple and hydrolysable metal salts on interfacial chemistry 16
2.4.3 The effect of polymer adsorption on interfacial chemistry 17
2.5 Particle interaction forces 19
2.5.1 Electrical double layer forces 19
2.5.2 van der Waals forces 20
2.5.3 The DLVO theory of colloidal stability 21
2.6 Non DLVO interaction forces 22
2.6.1 Structural or hydration forces 22
2.6.2 Hydrophobic forces 23
2.6.3 Steric forces 23

2.6.4 Bridging and depletion forces 24
2.7 Rheology and particle interactions 24
2.7.1 Dispersion rheology and its relationship to zeta potential 25
2.7.2 The impact of pulp rheology on the dewaterability of mineral dispersions 26
2.8 Flocculation and dewatering 30
2.8.1 Flocculation mechanisms 30
2.8.1.1 Bridging flocculation 31
2.8.1.2 Charge neutralisation 31
2.8.1.3 Electrostatic patch mechanism 32
2.8.1.4 Polymer complex formation 33
2.8.1.5 Depletion Flocculation 34
2.8.2 Dewatering through flocculation 34
2.9 Polymer adsorption 35
2.9.1 Kinetics of polymer adsorption 35
2.9.2 Adsorbed polymer conformation 37
2.9.3 Adsorption isotherms 38
2.9.3.1 Langmuir and Freundlich adsorption models 40
2.9.4 Factors influencing adsorption 40
2.9.5 Adsorption mechanisms 41
2.10 Chapter summary 42

CHAPTER 3 EXPERIMENTAL METHODOLOGY 45
3.1 Introduction 45
3.2 Materials 45
3.2.1 Mineral samples 45
3.2.2 Polymeric flocculants 46
3.2.3 General methods 47
3.2.3.1 Reagents 47
3.2.3.2 Glassware preparation 47
3.2.3.3 Solution preparation 48
3.2.3.4 pH control and measurement 49
3.3 Characterisation methods 49
3.3.1 Scanning Electron Microscopy (SEM) 49
3.3.2 Energy Dispersive Spectroscopy (EDAX) 50
3.3.3 X-Ray Diffraction (XRD) 50
3.3.4 Particle size distribution 51

3.4 Surface chemistry 52
3.4.1 Zeta potential measurements 52
3.4.2 Acoustosizer calibration 53
3.4.3 Estimation of adsorbed polymer layer thickness 53
3.5 Adsorption studies 54
3.5.1 Polymer adsorption experiments 54
3.5.2 Fourier Transform Infrared Diffuse Reflectance Spectroscopy 58
3.6 Rheology 58
3.7 Atomic Force Microscopy studies 61
3.7.1 Colloidal Probe Mounting 61
3.7.2 Calibration of cantilevers 62
3.7.3 Sample preparation 64
3.7.4 Force measurements 65
3.8 Dewatering studies 66
3.9 Error analysis 66

CHAPTER 4 SPECTROSCOPIC INVESTIGATION OF THE ADSORPTION MECHANISMS FOR POLYACRYLAMIDE POLYMERS ONTO IRON OXIDE PARTICLES 69
4.1 SUMMARY 69
4.2 Introduction 70
4.3 Results and Discussion 71
4.3.1 Adsorption Isotherms and Surface Chemistry 71
4.3.2 Infrared Spectroscopy 78
4.4 Conclusion 86

CHAPTER 5 THE EFFECT OF POLYMER STRUCTURE TYPE, PH AND SHEAR ON THE INTERFACIAL CHEMISTRY, RHEOLOGY AND DEWATERABILITY OF MODEL IRON OXIDE DISPERSIONS 89
5.1 SUMMARY 89
5.2 Introduction 90
5.3 Results and Discussion 91
5.3.1 Polymeric structure and pH: effect on surface chemistry 91
5.3.2 Polymeric structure, pH and shear: effect on dewatering behaviour 93
5.3.3 Shear and flocculant concentration/type: influence on pulp rheology 97
5.4 Conclusion 100

CHAPTER 6 THE EFFECT OF ANIONIC AND CATIONIC POLYACRYLAMIDE FLOCCULANTS, PH AND SHEAR ON THE INTERFACIAL CHEMISTRY, RHEOLOGY AND DEWATERABILITY OF MODEL IRON OXIDE DISPERSIONS.....103

6.1 Introduction.....104

6.2 Results and Discussion.....105

6.2.1 Influence of polymer structure type on interfacial chemistry.....105

6.2.2 Influence of polymer structure type on the adsorption behaviour.....108

6.2.3 Dewatering behaviour.....111

6.2.4 Influence of polymer structure type on pulp rheology.....116

6.2.5 The impact of different polymeric functional groups on the dewatering of iron oxide.....119

6.3 Conclusion.....123

CHAPTER 7 SYNERGISTIC EFFECT OF METAL SALT COAGULANTS AND POLYACRYLAMIDE-ACRYLATE FLOCCULANT ON THE DEWATERABILITY OF HEMATITE DISPERSIONS.....125

7.1 SUMMARY.....125

7.2 Introduction.....126

7.3 Results and Discussion.....127

7.3.1 Surface chemistry.....127

7.3.2 Adsorption isotherms.....132

7.3.3 Dewatering behaviour.....134

7.4 Conclusions.....137

CHAPTER 8 DISCUSSIONS AND APPLIED STUDY.....139

8.1 Discussion.....140

8.1.1 Introduction.....140

8.1.2 The mechanisms of polymer adsorption and their effect on dewatering.....140

8.1.3 Influence of polymer structure type on interfacial chemistry.....141

8.1.4 Influence of polymer structure type on adsorption.....143

8.1.5 Adsorption and dewatering behaviour.....146

8.1.6 Influence of polymer structure type on pulp rheology.....148

8.1.7 Influence of polymer structure type, pH and shear on the consolidation of iron oxide dispersions.....152

8.1.8 The Atomic Force Microscope as a probe into the rheological properties of iron oxide dispersions 153
8.1.9 The influence of metal salt coagulants and PAM A on the dewaterability of hematite dispersions 154
8.2 Case study 155
8.2.1 Introduction 155
8.2.2 Characterisation 155
8.2.2.1 Solution speciation 155
8.2.2.2 Mineralogy 156
8.2.2.3 Particle physical parameters (size, density and shape) 158
8.2.3 Interfacial Chemistry 160
8.2.4 Optimisation procedure 160
8.2.5 Settling behaviour 161
8.2.6 Influence of pH 163
8.3 Summary 165

CHAPTER 9 CONCLUSIONS AND FUTURE RECOMMENDATIONS 167
9.1 Conclusions 167
9.2 Future recommendations 173

CHAPTER 10 REFERENCES 177

APPENDIX: ATOMIC FORCE MICROSCOPY MEASUREMENT OF FORCES BETWEEN TWO IRON OXIDE SURFACES 195
10.1 SUMMARY 195
10.2 Introduction 196
10.3 AFM interparticle force measurements 196
10.3.1 The effect of polymer addition at high pH on interparticle normal forces 196
10.4 AFM lateral force measurements 208
10.5 Comparison between rheological data and lateral force measurements 211
10.6 Conclusion 216

LIST OF FIGURES

Figure 2.1: Schematic Diagram of a Dewatering Process. 9

Figure 2.2: Iron oxide surface groups as a function of pH. 11

Figure 2.3: The variation in zeta potential observed for hematite after various agitation times [54]. 12

Figure 2.4: Schematic representation of the electrical double layer (top), and in variation in electrical potential with distance from the particle surface (bottom) [47]. 14

Figure 2.5: Model for treating the effect of adsorbed polymer on zeta potential [82]. 18

Figure 2.6: Zeta potential of Fe_2O_3 particles vs. pH in the presence of PAA [34]. 18

Figure 2.7: Interaction energy potential between particles as a function of distance, where V_R is electrical double layer repulsion, V_A is van der Waal's attraction, and V_m is the energy barrier created by the sum of the two effects [93]. 22

Figure 2.8: Schematic representation of bridging flocculation, where multiple particles are held together by one polymer molecule. 32

Figure 2.9: Schematic illustration of charge neutralisation flocculation mechanism between oppositely charged mineral particles and polymers. 32

Figure 2.10: Schematic representation of electrostatic patch flocculation mechanism between oppositely charged mineral particles and polymers. 33

Figure 2.11: Schematic representation of depletion flocculation. 34

Figure 2.12: Effect of polymers on colloidal stability [2]. 36

Figure 2.13: Loop-train-tail model describing conformation changes upon polymer adsorption onto a solid surface..... 37

Figure 2.14: Schematic illustration of a possible conformation for the adsorbed PEO and PAM at the kaolinite-solution interface at temperatures: (a) 20-40 ^{o}C, PEO and 20 ^{o}C, PAM and (b) 60 ^{o}C, PEO and >20 ^{o}C PAM, where δ adsorbed layer thickness [32]. 38

Figure 2.15: Types of solid-solution adsorption isotherms [143]..... 39

Figure 2.16: The three main chemisorption modes for the adsorption of polyacrylamide polymer acid groups to the oxide surface; a) monodentate chelation, b) bidentate chelation and c) bidentate bridging. 42

Figure 3.1: The structures of the four polyacrylamides used in this study, where the ratio of x:y is 3:1. 47

Figure 3.2: SEM images of (a) hematite, (b) hematite, (c) fine magnetite, (d) coarse magnetite. Hematite was used in all experiments with the exception that magnetite was used for AFM measurements. 50

Figure 3.3: The particle size distribution of hematite as shown by the Malvern Mastersizer. 51

Figure 3.4: A schematic diagram of the Acoustosizer measurement cell [113]. 53

Figure 3.5: Schematic diagram of the complexation reaction required for the UV-vis measurement of polyacrylamide adsorption. 55

Figure 3.6: Typical calibration curves of polymer concentration vs. absorbance for (a) PAM A, (b) PAM N, (c) PAM S, and (d) PAM C using the starch-triiodide method..... 57

Figure 3.7: Schematic of instrumentation used for the vane technique. 59

Figure 3.8: Generic plot generated by a typical vane measurement showing torque as a function of time from which yield stress can be calculated. 60

Figure 3.9: Schematic of colloidal probe mounting method. 62

Figure 3.10: AFM friction loop; the photodiode response to cantilever twist, V, is plotted against the lateral piezo displacement (nm), taken from Cain *et al*. [161]. 63

Figure 3.11: Schematic representation of the cantilever submerged in solution as per the experimental set up for AFM force measurements. 65

Figure 4.1: Electrokinetic zeta potential of Fe_2O_3 in 10^{-3} KNO_3 at 8 wt% solids as a function of pH. 71

Figure 4.2: Mineral surface groups as a function of pH. 72

Figure 4.3: Adsorption isotherms fitted with Langmuir and Freundlich models for the adsorption of PAM A onto iron oxide at a) pH 6, b) pH 8.5 and c) pH 11. 74

Figure 4.4: Adsorption isotherms fitted with Langmuir and Freundlich models for the adsorption of PAM N onto iron oxide at a) pH 6, b) pH 8.5 and c) pH 11. 75

Figure 4.5: Comparison between the experimental adsorption densities and those predicted by the Langmuir and Freundlich models. 76

Figure 4.6: The infrared spectra of PAM A; a) unadsorbed; b) adsorbed to iron oxide at pH 6; c) adsorbed to iron oxide at pH 8.5; and d) adsorbed to iron oxide at pH 11. 80

Figure 4.7: The infrared spectra of PAM N a) unadsorbed, b) adsorbed to iron oxide at pH 6, c) adsorbed to iron oxide at pH 8.5, and d) adsorbed to iron oxide at pH 11. 84

Figure 4.8: The infrared spectra comparing of PAM N at high pH in comparison with PAM A and PAM N at natural pH. 87

Figure 5.1: Electrokinetic zeta potential of Fe_2O_3 particles in 10^{-3} KNO_3 at 8 wt% solids as a function of PAM A concentration (a) and PAM N concentration (b) 92

Figure 5.2: Settling rate of Fe_2O_3 in 10^{-3} KNO_3 at 8 wt% solids as a function of PAM A concentration (a) and PAM N concentration (b) at pH 6, 8.5 and 11. 94

Figure 5.3: Consolidation of Fe_2O_3 particles in 10^{-3} KNO_3 upon addition of PAM A (a) and PAM N (b), pre and post-shear measurements. 96

Figure 5.4: Yield stress (τ) of Fe_2O_3 in 10^{-3} KNO_3 upon addition of PAM A (a) and PAM N (b), pre and post-shear measurements. 98

Figure 6.1: The zeta potential of iron oxide particles in 10^{-3} M KNO_3 as a function of polymer addition at (a) pH 6, (b) pH 8.5 and (c) pH 11 107

Figure 6.2:Adsorption of PAM onto iron oxide particles in 10^{-3} M KNO_3 at (a) pH 6, (b) pH 8.5 and (c) pH 11. Fits to the Freundlich model are included as solid lines.....110

Figure 6.3: The settling rates of iron oxide dispersions as a function of polymer addition at (a) pH 6, (b) pH 8.5 and (c) pH 11 in 10^{-3} M KNO_3 background electrolyte 113

Figure 6.4: Consolidation of iron oxide dispersions as a function of polymer addition at (a) pH 6 (b) pH 8.5, and (c) pH 11.....116

Figure 6.5: Shear yield stress as a function of PAM concentration on iron oxide particles with 10^{-3} M KNO_3 at (a) pH 6, (b) pH 8.5 and (c) pH 11 119

Figure 6.6: Summary of settling rates showing dewatering with all four polymers at (a) pH 6, (b) pH 8.5 and (c) pH 11 121

Figure 6.7: Summary of consolidation of iron oxide after dewatering with all four polymers at (a) pH 6, (b) pH 8.5 and (c) pH 11.....122

Figure 7.1: Zeta potential as a function of pH for iron oxide particles with 10^{-3} M $MnSO_4$, $MnCl_2$, $Mn(NO_3)_2$ and K_2SO_4. Note that 10^{-3} M KNO_3 is present in all samples, and is hence labelled the control group.....128

Figure 7.2: Calculated hydrolysis diagram (A) and fractional abundance (B) of Mn(II) with the distribution of various species: Mn^{2+} (open triangle), $Mn(OH)^{+}$ (open circle), $Mn(OH)_3^{-}$ and $Mn(OH)_4^{2-}$ taken from [31].....129

Figure 7.3: Zeta potential of iron oxide particles as a function of PAM A addition in the presence of 10^{-3} M $MnSO_4$, $MnCl_2$, $Mn(NO_3)_2$ and K_2SO_4 at (a) pH 6 and (b) pH 11. Note that 10^{-3} M KNO_3 is present in all samples, and is hence labelled the control group. 131

Figure 7.4: Adsorption isotherms for PAM A adsorption onto iron oxide particles in the presence of 10^{-3} M $MnSO_4$, $Mn(NO_3)_2$ and K_2SO_4 at (a) pH 6 and (b) pH 11. Note that 10^{-3} M KNO_3 is present in all samples, and is hence labelled the control group..... 133

Figure 7.5: Settling rates of iron oxide particles as a function of pH in the presence of 10^{-3} M $MnSO_4$, $MnCl_2$, $Mn(NO_3)_2$ and K_2SO_4, both unflocculated and flocculated with 50 g/t PAM A. Note that 10^{-3} M KNO_3 is present in all samples, and is hence labelled the control group. 135

Figure 7.6: Consolidation of iron oxide particles as a function of pH in the presence of 10^{-3} M $MnSO_4$, $MnCl_2$, $Mn(NO_3)_2$ and K_2SO_4, both unflocculated and flocculated with 50 g/t PAM A. Note that 10^{-3} M KNO_3 is present in all samples, and is hence labelled the control group. 137

Figure 8.1: The zeta potential of iron oxide particles in 10^{-3} M KNO_3 as a function of polymer addition at (a) pH 6, (b) pH 8.5 and (c) pH 11. 142

Figure 8.2: Adsorption of PAM onto iron oxide particles in 10^{-3} M KNO_3 at (a) pH 6, (b) pH 8.5 and (c) pH 11. Fits to the Freundlich model are included as solid lines. 144

Figure 8.3: Shear yield stress as a function of PAM A concentration on iron oxide particles with 10^{-3} M KNO_3 at (a) pH 6, (b) pH 8.5 and (c) pH 11. 149

Figure 8.4: The shear yield stress as a function of zeta potential squared, for iron oxide pulps flocculated with 0 – 500 g/t polymer in the presence of 10^{-3} M KNO_3 at (a) pH 6, (b) pH 8.5 and (c) pH 11. 151

Figure 8.5: XRD diffraction pattern of the Northparkes tailings after washing to remove dissolved solids. Mineral identification shown in key 157

Figure 8.6: SEM images of the Northparkes tailings particles showing (A) coarse particles, secondary electron, (B) coarse particles, backscattered electron; (C) fine particle, secondary electron; (D) fine particles backscattered electron. 159

Figure 8.7: Particle size of the Northparkes tailings determined by laser diffraction 159

Figure 8.8: Zeta potential and attenuation particle size of the fine Northparkes tailings particles as a function of pH. 161

Figure 8.9: Settling rates of plant pulp as flocculated with different polymers at pH 7.5. 162

Figure 8.10: The settling rates of the plant samples flocculated with 40 g/t polymer at three pH values 163

Figure 8.11: The consolidation of the plant samples flocculated with 40 g/t polymer at three pH values 164

Figure 8.12: The shear yield stress of the plant samples flocculated with 40 g/t polymer at three pH values 165

Figure 0.1: Force vs Separation for two iron oxide surfaces at pH 11 with and without the presence of polymer at 20 ppm.....197

Figure 0.2: Force vs Separation for two iron oxide surfaces at pH 11 after the addition of (a) 20 ppm PAM A and (b) 20 ppm PAM N. 198

Figure 0.3: Force vs Separation for two iron oxide surfaces at pH 11 with increasing concentration of (a) PAM A and (b) PAM N. 201

Figure 0.4: Log(Force) vs. separation for the approach of two iron oxide surfaces in the presence of 20 ppm PAM A at pH 11, with the fit to the Poisson-Boltzmann equation symbolised as a line. 202

Figure 0.5: The approximate zeta potential of the magnetite probe as calculated via the Poisson-Boltzmann equation using mica values from the literature [199]. 203

Figure 0.6: Schematic representation of polymer addition to iron oxide (SC = surface coverage)..... 204

Figure 0.7: Schematic representation of a force curve and particle position upon approach, where the apparent separation at (A) is twice the effective mobile layer, (B) is the thickness to which the (layer-covered) probe will penetrate the mobile layer under the applied force, and (C) is at infinite force where the surfaces are considered to be in contact. The layer on the particle and the plate can be considered the effective mobile layer. 206

Figure 0.8: Force vs Separation for two iron oxide surfaces at pH 11 with PAM A and PAM N addition with similar % surface coverage..... 208

Figure 0.9: The lateral displacement (the 256 points in each trace are over a total..... 209

Figure 0.10: Lateral force measurements between two iron oxide surfaces after addition of PAM A and PAM N up to 20 ppm at pH 11 in 10^{-3} M KNO_3..... 210

Figure 0.11: Schematic representation of the radius of the area of contact (R), where h is the effective mobile layer, r is the radius of the probe and s is the distance between the solid surfaces at an applied force of 1 nN. (a) where the effective mobile layers are in contact and (b) where the probe has pressed through the effective mobile layer. 213

Figure 0.12: Rheology/Lateral Force comparison for PAM A and PAM N at different surface coverage for (a) Yield Stress and (b) Lateral Force. 215

LIST OF TABLES

Table 2.1: The industrial benefits of optimising dewatering methods. 8

Table 3.1: Properties of the four polyacrylamides used in this study. 46

Table 3.2: Summary of the inorganic reagents used for these investigations. 48

Table 3.3: Estimates of accuracy of measured quantities for experimental techniques. 67

Table 4.1: Freundlich model isotherm parameters summarised for (a) PAM A and (b) PAM N adsorption onto iron oxide. 78

Table 4.2: The major infrared species vibrations summarised for PAM A adsorption onto iron oxide particles. 81

Table 4.3: The major infrared species vibrations summarised for PAM N adsorption onto iron oxide particles. 85

Table 6.1: Freundlich model isotherm parameters summarised for PAM S and PAM C at pH 6 110

Table 7.1: The Freundlich model adsorption affinities for pH 6 and 11 for iron oxide particle dispersions containing 10^{-3} M $MnSO_4$, $Mn(NO_3)_2$, K_2SO_4 and the control group 134

Table 7.2: Salt concentration and ionic strengths of each dispersion condition 136

Table 8.1: Freundlich model isotherm parameters summarised for PAM A, PAM N, PAM S and PAM C, at (a) pH 6, (b) pH 8.5 and (c) pH 11. 146

Table 8.2: Solution speciation by ICP of the Northparkes tailing supernatant following 6 months aging with and without the presence of mineral particles. 155

Table 8.3: Chemical, morphological and mineralogical assessment of coarse and fine particles in the Northparkes tailings via EDAX and SEM images. 157

Table 0.1: Percentage of adsorbent capacity for each polymer and each concentration...199

Table 0.2: Calculated effective surface potential of each polymer system at each concentration. 205

Table 0.3: Estimated effective mobile layer thickness from the interaction force measurements in Error! Reference source not found.....207

Table 0.4: A comparison between the bulk rheology of flocculated iron oxide dispersions and the lateral forces observed in similar systems under similar conditions (SC = surface coverage). 214

JOURNAL PUBLICATIONS

Melanie J. M^{c}Guire, Jonas Addai-Mensah, Kristen E. Bremmell, *The effect of polymer structure type, pH and shear on the interfacial chemistry, rheology and dewaterability of model iron oxide dispersions*. Colloids and Surfaces A: Physicochemical and Engineering Aspects 275 (1-3): 153-160 MAR 1 2006

Melanie J. M^{c}Guire, Jonas Addai-Mensah, Kristen E. Bremmell, *Spectroscopic investigation of the adsorption mechanisms of polyacrylamide polymers onto iron oxide particles*. Journal of Colloid and Interface Science 299 (2): 547-555 JUL 15 2006

Melanie J. M^{c}Guire, Kristen E. Bremmell, Jonas Addai-Mensah, *Synergistic effect of metal salt coagulants and polyacrylamide-acrylate flocculant on the dewaterability of hematite dispersions.* Journal of Colloid and Interface Science, submitted.

Melanie J. M^{c}Guire, Jonas Addai-Mensah, Kristen E. Bremmell, *The impact of polymeric flocculant structure and adsorption behaviour on the interfacial chemistry, rheology and dewatering behaviour of colloidal iron oxide dispersions*. In preparation.

CONFERENCE PAPERS

1. Melanie M^{c}Guire, Kristen Bremmell and Jonas Addai-Mensah. *Improving dewatering of hydrophilic iron oxide dispersions through interfacial chemistry and particle interactions*. 23rd Australian Colloid and Surface Chemistry Student Conference, February 2004.

2. Melanie M^{c}Guire, Kristen Bremmell and Jonas Addai-Mensah. *The dewaterability of iron oxide dispersions and the mechanisms of polymer adsorption*. 24th Australian Colloid and Surface Chemistry Student Conference, Beechworth, February 2006.

3. Melanie M^{c}Guire, Kristen Bremmell and Jonas Addai-Mensah. *Improved dewaterability of iron oxide dispersions: The role of polymeric flocculant type, pH, and shear*. Chemeca, Auckland, September 2006.

4. Melanie M^{c}Guire, Jonas Addai-Mensah and Kristen Bremmell. *The impact of polymeric flocculant structure and adsorption behaviour on the interfacial chemistry and rheology of colloidal iron oxide dispersions*. Chemeca, Auckland, September 2006.

5. Melanie M^{c}Guire, Jonas Addai-Mensah and Kristen Bremmell. *Mechanisms and forces underpinning flocculation of iron oxide particles for enhanced dewatering of mineral tailings*. 12th IACIS International Conference on Surface and Colloid Science, Beijing 2007.

NOMENCLATURE

Symbols

A_H	Hamaker constant (J)
C_{eq}	polymer equilibrium solution concentration (moles/dm^3)
E	energy (J)
F	force (N)
I	ionic strength (moles/dm^3)
k_B	Boltzmann's constant
k_t	torsional spring constant of the cantilever (Nm)
k_z	flexural spring constant of the cantilever (N/m)
M	molarity (moles/dm^3)
N_A	Avogadro's number
T	absolute temperature (K)
x	deflection of the cantilever (m)
κ	reciprocal Debye length (1/m)
Δ	thickness of the Stern plane (m)
δ	adsorbed layer thickness (m)
ϕ	volume fraction
μ_D	dynamic mobility (m^2/Vs)
ω	angular frequency of the applied field (Radian/s)
ρ	density (g/cm^3)
ε	dielectric constant (C^2/m·J)
η	viscosity of the dispersion medium (Pa·s)
z	ionic valency
n_0	is the number concentration of ions in bulk solution
e	electronic charge (C)
τ	yield stress (Pa)
θ	fractional surface coverage (%)
Γ	adsorbed amount (mg/m^2)
Ψ_o	potential at the surface of a particle (V)
Ψ_d	Stern potential (V)
ζ	zeta potential (V)

Abbreviations

AFM	Atomic Force Microscope
BET	Brunauer Emmett Teller
EDAX	energy dispersive spectroscopy
ESA	electrosonic amplitude
ICP	Inductively coupled plasma
iep	isoelectric point
Mwt	average molecular weight of polymer (g/mol)
PAM	polyacrylamide
rpm	revolutions per minute
SEC	size exclusion chromatography
SEM	scanning electron microscope
XRD	X-ray defraction

ABSTRACT

Iron oxide is a crucial hydrophilic mineral in the minerals, metals and materials industries. Colloidal iron oxide dispersions have proven difficult to dewater to high solid-loading during routine hydrometallurgical processes. Despite this, there are a limited number of studies integrating interfacial chemistry, flocculation and dewatering behaviour of iron oxide in the literature.

In this study, fundamental investigations of the principles underpinning hematite pulp dewatering behaviour were examined to determine the effectiveness of four polyacrylamide polymers (homo-polymer, PAM N, anionic carboxylate substituted copolymer, PAM A, anionic sulphonate substituted copolymer, PAM S, and cationic trimethyl amino ethyl substituted copolymer, PAM C) as flocculants and four metal salts ($Mn(NO_3)_2$, $MnSO_4$, $MnCl_2$, and K_2SO_4) as coagulants. Effects of flocculant structure type and concentration, metal salt type and pH on the surface chemistry, pulp rheology and the dewaterability of dispersions were considered. Experiments were conducted at the isoelectric point (iep -pH 8.5), below (pH 6) and above (pH 11) the iep of the hematite to investigate particle charge effect in the presence and absence of the coagulants and/or flocculants.

Investigations into the polymer adsorption mechanisms conducted using infrared spectroscopy found PAM A to chemically adsorb onto hematite particles via bidentate chelation on either side of the iep, and via monodentate chelation at the iep. These bonding mechanisms were found to influence the pulp particle interactions (rheology) and hence dewatering behaviour. Hydrogen bonding also occurred between PAM A and PAM N and the hematite particles. Spectroscopic evidence was also provided, for the first time, of the partial hydrolysis of non-ionic polyacrylamide at high pH.

Flocculation in general was found to be most effective when the polymer was of similar charge to the hematite particles. Settling rates of over 100 m/h were achieved at and below the iep after flocculation with the charged polymers, whilst consolidation was generally unaffected by flocculation at any pH. Bridging mechanisms between polymers of similar charge to the particles was most effective. Electrostatic and charge patch flocculation mechanisms prevailing between oppositely charged polymer and hematite particles provided less-improved dewatering.

Surface chemistry was greatly influenced by the anionic polymers at and below the iep of hematite. Addition of sulphate ions caused pronounced particle surface charge suppression with significant zeta potential reduction below the iep. The sulphate ion also facilitated PAM A adsorption above the iep which led to a significant improvement in settling rate. Dewatering of flocculated pulps was more efficient at and below the iep of hematite, with the negatively charged dispersion at high pH generally comprising a turbid supernatant. Manganese salts in synergy with PAM A significantly enhanced settling rates at and below the iep, however, the effect was subtle when compared to the addition of the sulphate ion. Application of mechanical shear to the pre-sedimented pulps produced outstanding improvement in particle consolidation, with up to 20 wt% increase in solid loading observed.

AUTHOR'S STATEMENT

I declare that this thesis does not incorporate, without acknowledgement, any material previously submitted for a degree or diploma in any university, and that to the best of my knowledge it does not contain material previously published or written by another person except where due reference is made in the text.

Melanie M^{c}Guire

ACKNOWLEDGEMENTS

First of all, I'd like to thank the Academy……. no, just kidding! Never again will I look at another thesis without appreciating the long hours of preparation behind it. I have a new found respect for everyone who has achieved this title.

There are many people that I need to thank for their contribution either to my work or directly to me throughout my candidature. Firstly, I would like to thank my supervisors, Dr Kristen Bremmell and Associate Professor Jonas Addai-Mensah. Kristen, thank you for your support and patience. I really appreciate all of your efforts over the years, and for sticking by me when it looked like it was never going to work out! Jonas, what can I say? You are an amazing and unique human being. Thank you for your advice, direction, and diligence. I really appreciate all of your efforts and I could not have completed this without you both.

Secondly, I would like to thank the people who gave of their time to teach me various experimental techniques. Dr Gillian Kaggwa for adsorption work, Dr Linh Chiem for DRIFT and ATR-FTIR, Ms Le Huynh for the Acoustosizer, Mr Andrew Robinson for the Mastersizer and Vane Rheometer, and Dr Igor Ametov and Dr Yasushi Saiki for the AFM. I'd also like to thank fellow P523A members Dr Angus McFarlane and Mr Heramb Bal for all of their technical advice and general support. A warm thank you goes to Dr David Beattie who helped to confirm my interpretations of my infrared spectra, and again to Le Huynh, Andrew Robinson and Igor Ametov for general assistance with equipment and for sharing their technical knowledge with me so generously.

A very special thank you must go to my "student husband" Dr Yasushi Saiki. Yasushi, all that I can say is that I love you. I cannot thank you enough for all of your help and advice regarding the AFM. For teaching me how to use it, extract and interpret the data, and for encouraging me when all I wanted to do was cry. I can honestly say that if it weren't for you that there would be no AFM chapter in this thesis. Even though the work was not ultimately included, my appreciation for you is regardless!! You are an amazing scientist and an even better friend. Thank you.

I would like to thank all of my other friends and colleagues at The Wark for general support and for creating such a pleasant working environment. I'd like to thank AMIRA for project funding and the ARC for my scholarship. I'd also like to thank Dr Gayle Morris for funding so that I could present my work overseas.

There are other people throughout the past few years who have significantly impacted on my life outside of uni (not that I had much of one for a long time!), and who also must be thanked. Britt Crew, Braedyn and Jaida Ruciack, thank you for all of the joy that you have brought to my life over the past 7 years. Your love and support have helped me through this experience enormously and I dare say that I would have lost all sanity at some points had it not been for our time together. Thank you to my Grandparents for their constant love, support and encouraging emails. And to my Nana who didn't get to see this completed, thank you for always believing in me and for being so proud of us. To my brother Michael, you are my best friend. Thank you for being the person who always "gets me."

I'd also like to thank my husband Dwayne Bridgland. I really appreciate all of the things that you did for me around the house to allow me to concentrate on my thesis. I'd also like to thank you for sitting with me through some of those long nights in the AFM room. Your company definitely made it seem easier.

Last, and most definitely not least, I'd like to thank my parents, John and Debbie McGuire. Thank you for all of your help! I can't even count all of the forms in which that help came. Financially, emotionally, mentally, you really are my strength and I'm the luckiest girl in the world to have parents like you.

CHAPTER 1 Introduction

The dewatering of colloidally stable mineral tailings presents a substantial problem to the mining and minerals processing industry. Although recent advances in technology have improved the efficiency of thickeners, current dewatering methods still only produce thickened mineral waste dispersions of low to moderate solid content of approximately 25 to 60 wt%, corresponding to ~ 12-30 vol% [1]. Consequently, several million tonnes of fairly dilute mineral waste dispersions (most of which is equally voluminous trapped process water) are impounded in dams every year worldwide [1].

Characteristically, the colloidal size particles present in these low solid-loading mineral waste dispersions are too fine to settle under gravity, and instead rely on electrostatic and van der Waals interactions to dictate their aggregation behaviour. Conventional methods for the dewatering of such dispersions include pH control and chemical additive-mediated, gravity assisted sedimentation, involving the use of coagulants (e.g. Ca(II)) and high molecular weight polymeric flocculants. High molecular weight (e.g. $>10^6$ Da) polymers provide attractive bridging interactions between the colloidal particles and assist particle size enlargement necessary to facilitate gravity sedimentation [2-9]. Polymers of differing functionality and molecular architecture are known to take on many different conformations in solution and at the particle-solution (solid-liquid) interface, providing various ways in which they may interact with and bridge the particles [10].

Iron oxide represents typical, hydrophilic mineral oxides that commonly form a major component of both valuable and waste mineral dispersions which must be dewatered routinely during hydrometallurgical mineral processing operations. Due to its hydrophilic nature, colloidally stable iron oxide dispersions have proven to be significantly difficult to dewater to a high solid loading [7, 11-13]. Upon flocculation, primary dewatering results from the free and hindered settling of flocs, which occurs in the upper half of the thickener. The settling behaviour is usually improved through pH control, chemical additive polymeric flocculant selection, and solution speciation [1]. Whilst acceptable settling rates (e.g. 3-10 m/h) are readily achievable via flocculation of mineral particles, the main problem lies within the secondary dewatering step that occurs when the thickened tailings are consolidated within the bottom section of the thickener and/or during impoundment in tailings dams [11].

Low settling rates (e.g. <1 m/h) and underflow pulp solid content of 50-60 wt% (~20-30 vol%) are typically obtained upon coagulation and thickening of colloidal size iron oxide slurries using electrolytes of high ionic strength [12, 14]. The poor clarification rate and modest consolidation achievable for iron oxide dispersions is attributed to the interfacial chemistry and particle interactions which are considered to be the principle controlling factors of the dewatering process (under the usual plant thickener operating conditions). These factors are far from being optimised [12].

The use of very high molecular weight (e.g. $>3 \times 10^6$ Da) flocculants has been successful in the production of large flocs that display high settling rates (e.g. >10 m/h), however, the large flocs settle into a loosely packed network of particles leading to poor sediment bed compaction [1]. The amount of flocculant used and flocculation performance depend not only on the structure and conformation of the polymers in solution, but also on the interfacial chemistry and orthokinetic (shear) conditions which prevail [15].

The use of conventional polyacrylamides in water treatment and minerals processing industries as flocculants [6, 8, 16-18], depressants [19-21] and dispersants [7] is rapidly increasing. Effective use as dewatering aids requires an improved understanding and identification of the adsorption and flocculation mechanisms of such polymers with differing functionality, molecular structure and size. The adsorption mechanisms of polyacrylamides are an important factor underpinning particle interactions and the dewatering process. For better flocculation performance and improved dewatering behaviour, interfacial chemistry conditions conducive to certain adsorption mechanisms are pivotal issues which need to be investigated systematically in order to fully understand the thickening process of iron oxide dispersions.

1.1 AIMS AND OBJECTIVES

The aims of this project are:

1) To quantify and gain a thorough and precise understanding of the adsorption mechanisms of two high molecular weight polymeric flocculants ($7.5\text{-}9 \times 10^6$ Da), anionic

polyacrylamide (PAM A) and non-ionic polyacrylamide (PAM N) onto iron oxide surfaces through characterisation studies using UV-visible and infrared spectroscopies.

2) To investigate the effect of flocculant structure type and pH on the interfacial chemistry and particle interactions of iron oxide dispersions with the key objective of enhancing pulp dewaterability. More specifically, the effect of pH and polyacrylamide structure type (anionic, non-ionic, and cationic) and concentration on particle zeta potential, shear yield stress and dewatering behaviour of iron oxide will be investigated, as will be the influence of shear on sediment consolidation.

3) To investigate the synergistic or antagonistic effect of four metal salts ($Mn(NO_3)_2$, $MnSO_4$, $MnCl_2$, and K_2SO_4) used in conjunction with a high molecular weight, anionic polyacrylamide flocculant on the dewaterability of iron oxide dispersions.

4) To apply the knowledge gained throughout this work to a real plant case study of a given mixed oxide tailings dispersion. This will allow the direct application of this work to a real tailings system.

1.2 CHAPTER OUTLINE

After a brief introduction to the research questions to be answered and the aims of this work in **Chapter 1**, **Chapter 2** gives an in depth description of the work to date on the relevant principles underpinning this project. Fundamental principles of dewatering, interfacial chemistry, particle interaction forces (both DLVO and non-DLVO), rheology, flocculation and mechanisms of polymer adsorption will be discussed.

Chapter 3 is an outline of all of the materials and experimental methods used throughout this body of work to investigate particle interactions and interfacial chemistry and their influence on the dewatering behaviour of iron oxide dispersions.

Chapter 4 describes the adsorption mechanisms and adsorption isotherms of two high molecular weight polymeric flocculants adsorbed onto iron oxide particles characterised by UV-vis and IR spectroscopies. Experiments are conducted at three pH values in order to investigate the adsorption mechanisms underpinning the flocculation process.

Chapter 5 outlines the effect of polymer structure type, pH and shear on the interfacial chemistry, rheology and dewaterability of model iron oxide dispersions. Zeta potential measurements, adsorption experiments, dewatering tests and shear yield stress measurements are investigated in order to determine the effect of an anionic and non ionic polyacrylamide on the dewatering of iron oxide dispersions.

Chapter 6 is an extension to the investigations in Chapter 5, and further investigates the effect of polymer structure type by investigating the influence of a cationic polymer and another anionic polymer in order to distinguish between polymers with the same anionicity but with different functional groups.

Chapter 7 investigates the influence of metal salts as coagulants in conjunction with an anionic polyacrylamide to determine whether the metal salts act synergistically with the polymer to improve dewatering.

Chapter 8 is both a discussion of all of the investigations throughout this body of work, along with the direct application of the theories and principles determined to a real plant tailings sample.

Chapter 9 gives the conclusions and future recommendations.

CHAPTER 2 Literature Review

2.1 INTRODUCTION

Enhancement of the dewatering behaviour of hydrophilic iron oxide pulps is of great importance to both the mineral industry (cost) and the environment (reduced water usage, contamination of environment). Despite extensive research in this area [6, 13, 17, 18, 22-33], there remains a paucity of knowledge regarding the attainment of ultimate mineral pulp dewaterability. It is most desirable to form dense, fast settling flocs that may compact and consolidate under applied moderate shear and compression.

The impact of conventional polyacrylamide based flocculant charge, structure and functional groups on dewaterability of iron oxide dispersions is largely unknown, despite the extensive studies reported in the literature [5, 25, 26, 34-37]. Particle surface chemistry in the presence and absence of polymeric flocculants and its impact on particle interactions (measured in bulk through rheology, and between two surfaces using the Colloid Probe AFM) are of great interest with regards to dewatering also. This chapter consists of a review of the scientific investigations carried out to date in these areas.

2.2 IMPORTANCE OF EFFICIENT DEWATERING METHODS

Improving the dewaterability of mineral tailings has long been of high importance to the mining/mineral processing industry [6, 8, 12, 18, 26, 30, 32, 38]. The cost of tailings disposal is phenomenal financially, in terms of both impoundment space requirements and the millions of tonnes of wasted entrapped process water and valuable species. Water wastage, reagent loss and seepage are of continued environmental concern, as is the space, time and energy required for disposal. Tailings thickening generally occurs through gravity driven, chemically mediated thickeners, which whilst having significantly improved over time are far from efficient.

The sustainability of the mineral processing industry is highly dependent on improved dewatering methods for waste tailings treatment. The major benefits of the optimisation of dewatering methods are outlined in Table 2.1.

Table 2.1: The industrial benefits of optimising dewatering methods.

	Requirement	Economic benefit	Environmental benefit	Social benefit
Increased water recycling	Increased tailings consolidation	Reduced water acquisition costs	Conservation of valuable water and land resources	Increased compliance with water restrictions
Reduced reagent usage/increased reagent recovery	Optimisation of surface chemistry	Reduced acquisition costs	Less contamination through tailings dam seepage	Reduced effect on local environment
Reduced energy usage	Increased tailings consolidation	Reduced pumping costs	Reduced greenhouse emissions	Increased compliance with Kyoto protocol

2.3 FUNDAMENTALS OF DEWATERING

In mineral processing operations, the gangue minerals which are collected as tailings are fed into a thickener. Flocculants are added to the tailings to enhance the dewatering rate, and the clarified supernatant is then pumped as an overflow and recycled upstream for re-use. The tailings thickening process is described schematically in Figure 2.1.

2.3.1 Primary dewatering

Particles found in mineral tailings are generally too fine to settle under gravity, and instead rely upon their electrostatic and van der Waals interactions to dictate their behaviour. The surface chemistry of colloidally stable particles usually works against destabilisation of the dispersion, with the predominant electrostatic repulsion keeping the particles dispersed. Aggregation or flocculation of the particles facilitates the destabilisation and settling of the pulp, and is assisted through pH control, chemical additive selection, and solution speciation [1].

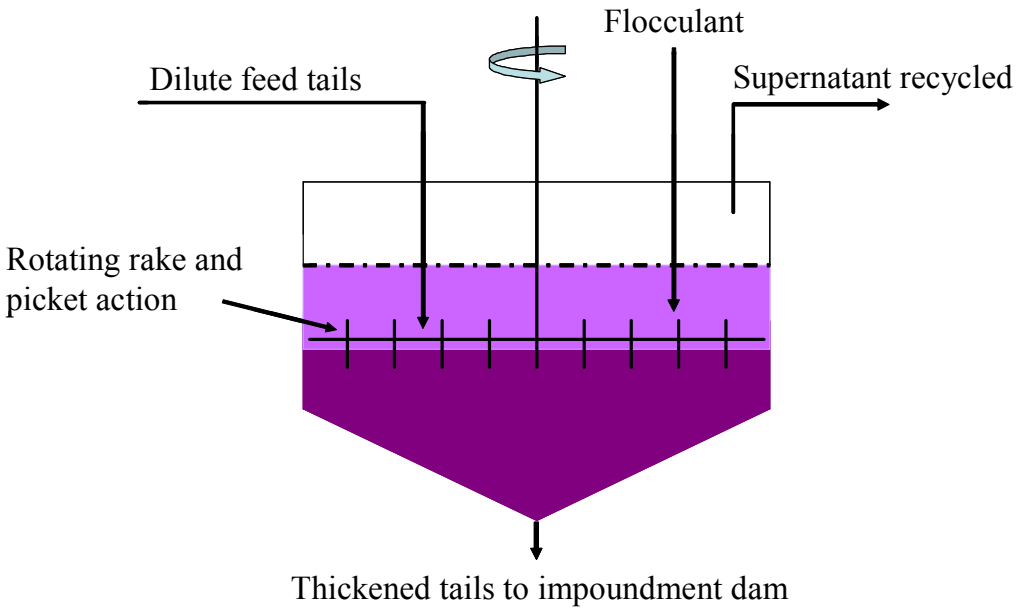


Figure 2.1: Schematic Diagram of a Dewatering Process.

Extensive research has been conducted into the enhancement of the settling rate of the gangue particles through flocculant addition [7, 16, 17, 38-40]. Industrial settling rates between 1-10 m/h are generally considered to be adequate, although rates higher than this would greatly increase processing speeds.

Flocculation of particles causes floc formation, bringing the particles together to form heavier aggregates that lead to faster settling rates. Primary dewatering results from the free and hindered settling of flocs, which occurs in the upper half of the thickener (see Figure 2.1).

Besra *et al*. [25] have found non-ionic polyacrylamide to be a successful flocculant for negatively charged kaolin dispersions, increasing the settling rate from 0.4 cm/s to 1.4 cm/s. In another publication, the same authors observed that flocculation with a cationic polyacrylamide increased the settling rate of kaolin dispersions ten-fold [24]. Anionic polyacrylamide gave optimal flocculation performance at ~ 50 % surface coverage [41], with the unadsorbed flocculant hindering dewatering [42].

2.3.2 Secondary dewatering

Secondary dewatering occurs when thickened tails are compressed by the weight of the particles above within the bottom of the thickener (Figure 2.1) and tailings dam in an attempt to remove trapped water from within the network of flocculated particles [11]. A rake constantly rotates at the bottom of the thickener, which facilitates consolidation. This action is mimicked in bench tests through the application of shear via an impeller, and has been utilised in previous dewatering studies for improving the consolidation of the thickened tails [6, 8, 29].

Surface chemistry is also very important in the secondary dewatering stage [12]. If the particles possess a certain amount of charge, which is detrimental to primary dewatering, this can enhance the consolidation. The particle charge acts as a "lubricating layer," which allows the particles to slide past one another allowing more efficient packing. Franks *et al*. [43] have used this concept to develop a flocculation process using a stimulus sensitive flocculant that can bridge particles during the primary dewatering step and then (after stimulus) change conformation to give a slight repulsion in the secondary dewatering phase to create the lubricating effect for enhanced consolidation. The pulp rheology may also have a significant effect on the secondary dewatering phase [44, 45], and will be discussed further in Section 2.7.

2.3.3 Dewaterability of iron oxide

Iron oxide is a typical mineral commonly found in waste tailings that must be dewatered prior to impoundment. Hydrophilic in nature, it does not easily aggregate and instead forms colloidally stable dispersions that have proven difficult to dewater in the past [7, 11, 13, 46].

High molecular weight flocculants are commonly used in industry, and cause the formation of large, loose flocs that dewater at high rates. However, this often results in a consolidated particle bed containing a large volume of trapped water [1]. The resulting network is one that displays appreciable mechanical strength and low permeability [47]. It is this that makes the secondary dewatering stage challenging. The poor level of flocculation, clarification and modest consolidation currently achievable for iron oxide dispersions is indicative of the interfacial chemistry and particle interactions being the controlling factors

of the dewatering process. Therefore, these factors warrant further investigation and understanding.

Settling rates (primary dewatering zone, Figure 2.1) and consolidation (secondary dewatering zone, Figure 2.1) are parameters which can be measured simply with batch settling tests. It is also possible to measure the rheology of the resulting pulp, which can then be used to estimate the effectiveness of the particular dewatering method for practical use in an industrial thickener. Whilst consolidation and rheology are of utmost importance to this application [48], such data is often unreported. Investigation of iron oxide settling behaviour was reported by Karmakar and Singh [16], involving amylose-grafted polyacrylamide, but did not disclose any consolidation data. Hulston *et al*. [18] have shown that flocculation of iron oxide with PAM A at 25 ^{o}C increased settling rates by ~30 %, and that equilibrium bed heights were increased with temperature. The kinetics of flocculation have been studied extensively with various polymers [3, 13, 49], along with the electrokinetic properties of adsorbed polymer layers by Chibowski and Wiśniewska [34], but again, with no reference to secondary dewatering.

2.4 INTERFACIAL CHEMISTRY

The colloidal stability that underpins the difficulty of dewatering mineral dispersions arises from the surface charge which particles acquire when in contact with an aqueous solution [50]. The surface charge of mineral particles becomes positive under acidic conditions where particles are protonated, and negative under basic conditions where deprotonation occurs. Each mineral has a specific pH point at which the surface becomes neutral and this is known as the isoelectric point (iep) [50]. Figure 2.2 is a schematic representation of the surface groups of iron oxide as a function of pH [36, 51].

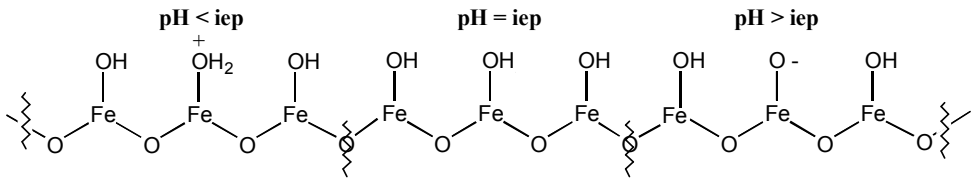


Figure 2.2: Iron oxide surface groups as a function of pH.

In the present work, hematite ($\alpha - Fe_2O_3$), which is one of the most commonly occurring iron oxide phases that is also present in mineral waste tailings and concentrates, is of interest. In an aqueous environment, the surface of the iron oxide particles may be hydrolysed to oxyhydroxide (FeOOH), and hydroxide ($Fe(OH)_3$), depending upon prevailing solution conditions [52, 53]. Single, double and triple coordination of Fe-OH groups at the particle surface may occur at various crystallographic faces. This may lead to different charging behaviour and reactivities at the various faces [52]. It has been established by several interfacial studies of iron oxide that isoelectric point (iep) values in the range of 5-9 are commonly observed [37, 51-59], and the importance of characterising samples prior to use is important for this reason [54]. Cromières *et al*. [54] have also shown the importance of consistent shaking times (or mixing times in this study). Figure 2.3 shows time-dependent electrokinetic behaviour variabilities for the same sample [54].

****This drawing has been removed. Please see referenced source for drawing.****

Figure 2.3: The variation in zeta potential observed for hematite after various agitation times [54].

2.4.1 Zeta potential

Zeta potential is a measure of the magnitude of the electrical double layer potential of the particles that induces repulsion between the particles in solution [50]. Figure 2.4 illustrates the variation in electrical potential distribution as a function of the distance from the particle surface. The potential at the surface of the particle, Ψ_o (V), decays linearly to the Stern plane where it is equal to the Stern potential, Ψ_d (V). At the plane of shear, the potential is called the zeta potential, ζ (V), a measurable parameter. As the distance from the surface increases, the concentration of counter-ions decays to the bulk concentration and correspondingly, Ψ_d, decays to zero. κ (1/m) is the reciprocal Debye length and Δ (m) is the thickness of the Stern plane. These parameters will be discussed further in Section 2.5.1.

When the zeta potential is of a high magnitude, the electrostatic repulsion between the particles is strong and will allow the formation of a stable dispersion. When the zeta potential is low, repulsion is at a minimum which allows the particles to come closer together. Particles undergo primary minimum aggregation due to van der Waals attractive forces upon close approach over a separation distance < 5 nm. The dispersion then becomes unstable and dewaters more readily [50]. Strong interparticle attraction, however, is detrimental to the pulp consolidation as the particles quickly form large, open flocs which trap water within their network resulting in a poorly compacted bed of particles.

The adsorbed layer thickness (δ) of a non ionic polymer onto a mineral surface can be estimated from the change in zeta potential upon polymer adsorption using the following expression [50]:

$$\tanh\left(\frac{z_2 e\zeta_2}{4kT}\right) = \tanh\left(\frac{z_1 e\zeta_1}{4kT}\right) e^{-\kappa(\Delta-\delta)}$$

Equation 2.1

where z_2 and z_1 are the valences of potential determining ions, e is the electron charge, ζ_2 and ζ_1 are the particle zeta potential values in the absence and presence of polymer respectively [V], *k* is Boltzmann's constant, T is the absolute temperature [K], $1/\kappa$ is the debye length [m], and Δ is the stern plane thickness [m] (0.4 nm for 10^{-3} M background electrolyte) [60].

****This drawing has been removed. Please see referenced source for drawing.****

Figure 2.4: Schematic representation of the electrical double layer (top), and in variation in electrical potential with distance from the particle surface (bottom) [47].

2.4.1.1 Measurement of zeta potential

Zeta potential may be determined experimentally using techniques such as electrophoresis and electroacoustics. The electrophoretic technique can only be used for dilute dispersions (< 0.02 wt %) as it requires the passage of light through the dispersion without significant attenuation in intensity of the radiation. This technique is therefore unsuitable for mineral processing applications where dispersions are of a much higher solid content. For concentrated dispersions, the electroacoustic technique is commonly used. The Electroacoustosizer is based on the principle that application of an alternating electric field to a dispersion of charged colloidal particles generates a series of sound waves [61]. This phenomenon is called Electrokinetic Sonic Amplitude Effects (ESA). The presence of the ESA requires that there be a density difference between the particles and the fluid, or the two phases would move as one and be indistinguishable to the instrument. ESA effects and their relationship to measuring zeta potential and particle size theory is extensively described in the literature [61-65], and will not be discussed further here. For a colloidal dispersion of a given volume fraction (ϕ, v/v), the ESA may be related to the particle averaged complex dynamic mobility (μ_D), by the following expression [65]:

$$\text{ESA}(\omega) = A(\omega)\ \phi \frac{\Delta\rho}{\rho} \mu_D Z \qquad \textbf{Equation 2.2}$$

where ω is the angular frequency of the applied field, A is the constant dependent upon the electronics of the measuring instrument, and ρ and Δρ are the densities of the suspending medium and the colloidal particles respectively. Z is a field factor that is related to the acoustic impedances of the dispersion and the glass delay rods used in the measuring instrument. The dynamic mobility, μ_D, is related to the size, a, of the particles and also to particle charge (through zeta potential):

$$\mu_D = \frac{2\varepsilon\zeta}{3\pi} G(a,\omega)\left[1 + f\right] \qquad \textbf{Equation 2.3}$$

where ε is the dielectric permittivity ($C^2/m \cdot J$) and η is the viscosity of the dispersion medium (Pa·s), G and f are complex functions which depend on the particle size and the

measuring frequency. Calculation of the zeta potential and particle size is determined from the real magnitude and imaginary (lag phase) of the mobility, respectively [66].

2.4.2 Effect of simple and hydrolysable metal salts on interfacial chemistry

Enhanced dewatering through the addition of hydrolysable metal ions has been widely studied in the literature [12, 31, 67-76]. In most dewatering applications, coagulation with metal ions and anions alone is not sufficient to achieve the desirable dewatering rate, and thus must be used synergistically with another dewatering method such as polymeric flocculation [31]. Iron oxide is known to be present in many phases in mineral tailings, with anhydrous particles generally hydrolysing such that hydroxide groups (–OH) are present on the particle surface. Depending on the surface charge, specific interactions may occur between the surface groups and anionic or cationic species in solution.

Multivalent ions are often present in plant process water and tailings. Hydrolysable metal ions and metal salts have been previously utilised to enhance dewatering of mineral systems [31, 77] and manipulate the surface chemistry [69-71, 78-80]. The coagulants are primarily used to change the surface chemistry of dispersions in order to enhance polymer-particle interactions and improve the dewatering process. As the adsorption of a hydrolysed ion depends critically on the pH of the system [78], pH can also be used to exploit the properties of these ions. Certain metal ions undergo hydrolysis at a given pH via the following scheme [50]:

$$M^{n+} + x\,OH^- \leftrightarrow M(OH)_x^{(n-x)+} \qquad \textbf{Equation 2.4}$$

$$M(OH)_x^{(n-x)+} + OH^- \leftrightarrow M(OH)_{x+1}^{(n-x+1)+} \qquad \textbf{Equation 2.5}$$

$$M(OH)_{x+1}^{(n-x+1)+} + H^+ \leftrightarrow M(OH)_{x-1}^{(n-x+1)+} + H_2O \qquad \textbf{Equation 2.6}$$

One of the advantages of specific adsorption of hydrolysed metal ion complexes is that dramatic reduction in the magnitude of particle zeta potential and even charge reversal can occur, making it an effective means of regulating surface chemistry. Increasing the ionic strength of a colloidally stable system can overcome the repulsive electrostatic barrier between particles by compressing the electrical double layer, assisting in coagulation.

Nyström *et al*. [79] investigated the effects of Na^{+}, Ca^{2+}, Ba^{2+}, and La^{3+} on the zeta potential and yield stress of calcite dispersions and found that the monovalent ions had the weakest effect on the zeta potential and the trivalent ion had the strongest effect. An increase in the concentration of metal ions was found to increase the yield stress of each system, due to the increase in strength of the particle network. Huang and Fuerstenau [69] discovered that the addition of lead and cadmium ions to quartz and talc dispersions could, in the case of quartz, control the stabilisation of the system, whilst Johnson *et al*. [80] found the addition of aluminium ions successful in manipulating the surface chemistry of kaolinite.

It is pertinent to note that whilst solution metal hydroxy complexes may specifically adsorb onto iron oxide particles in aqueous dispersions and markedly impact on the electrokinetic zeta potential, simple ions such as NH_4^{+} have been shown to induce a similar effect on the interfacial chemistry of negatively charged iron oxide particles [12]. Likewise, simple anionic species (e.g. $SO_4^{=}$) may also exert significant impact on the zeta potential of the positively charged oxide particles through specific adsorption, impacting upon colloidal stability [74, 81].

2.4.3 The effect of polymer adsorption on interfacial chemistry

The adsorption of polymers onto mineral surfaces can have a significant impact on the zeta potential of a dispersion [82]. The surface potential is measured at the plane of shear as the zeta potential (refer back to Figure 2.4). An adsorbed polymer layer causes a shift in the plane of shear leading to a smaller zeta potential being measured at the new plane of shear, which is described schematically in Figure 2.5. Polymers can also act to shield the charge of a mineral particle by covering some of the charged functional groups on the mineral surface [50]. Adsorption of charged polymers can, in some cases, even lead to charge reversal. Chibowski and Wiśniewska [34] found that addition of 0.01 ppm low molecular weight polyacrylic acid shielded the charge of iron oxide particles in 10^{-2} M NaCl, whilst addition of 0.1 ppm of the same polymer caused charge reversal at low pH as seen in Figure 2.6.

This drawing has been removed. Please see referenced source for drawing.

Figure 2.5: Model for treating the effect of adsorbed polymer on zeta potential [82].

This drawing has been removed. Please see referenced source for drawing.

Figure 2.6: Zeta potential of Fe_2O_3 particles vs. pH in the presence of PAA [34].

2.5 PARTICLE INTERACTION FORCES

2.5.1 Electrical double layer forces

The double layer model suggests that all charged particles have a double layer of counter-charged ions surrounding the particle. The first layer consists of a tightly packed layer of ions, whilst the second layer is more loosely packed. The concentration of ions in the outer layer decreases with distance from the particle surface until the concentration of ions equals that of the bulk solution. The result is an electric potential that develops around the particle. The overlap of this charged outer layer with that of similarly charged particles prevents the particles from aggregating, which hinders the settling rate (as discussed previously in Section 2.3.1). Previous solutions have been to increase the ionic strength of the solution, thus screening the repulsive barrier, allowing the particles to come close enough to each other such that van der Waals forces can dominate [51, 83]. Whilst this method does increase particle aggregation and settling rates, it forms a solid bed where in the particles form a tight network that doesn't collapse easily, giving poor consolidation [84].

The thickness of double layer is often described by the Debye length (κ^{-1} m), which can be estimated from the following expression:

$$\kappa = \left(\frac{2z^2 n_0 e^2}{\varepsilon_0 \varepsilon k T} \right)^{-1/2} \qquad \textbf{Equation 2.7}$$

where z is the ionic valency, n_0 is the number concentration of ions in bulk solution, e (C) is the electronic charge, ε ($C^2/J \cdot m$) is the dielectric constant of the bulk solution, ε_0 ($A^2 \cdot s^4 / kg \cdot m^3$) is the permittivity of free space and T (K) is the absolute temperature. This equation shows that the thickness of the double layer is dependent upon the temperature, electrolyte concentration and permittivity of the bulk solution.

The electrical double layer force between two surfaces (eg. a substrate and a colloidal probe) can be calculated from continuum theory [85]. It is a modified version of the Poisson-Boltzmann equation and makes one of two boundary condition assumptions. The

first of these is that the surface charge remains constant (F^{cc} – constant charge, N), and the equation is given by [85]:

$$F^{cc} = \frac{2\pi R\kappa}{\varepsilon\varepsilon_0}\left[2\sigma_S\sigma_P e^{-D/\kappa} + (\sigma_S^2 + \sigma_P^2)e^{-2D/\kappa}\right] \qquad \textbf{Equation 2.8}$$

and the second, assuming constant potentials of the substrate, ψ_S (V), and the colloidal probe, ψ_P (V), is given by [85]:

$$F^{cp} = \frac{2\pi R\varepsilon\varepsilon_0}{\kappa}\left[2\psi_S\psi_P e^{-D/\kappa} + (\psi_S^2 + \psi_P^2)e^{-2D/\kappa}\right] \qquad \textbf{Equation 2.9}$$

where F^{cp} – constant potential (N), D is distance (m), R is the radius of curvature (m) of the probe, σ_S and σ_P are the surface charge densities of the substrate and the probe, and κ is the inverse of the Debye length (m).

2.5.2 van der Waals forces

van der Waals interactions exist between all atoms, molecules and surfaces. There are three types of van der Waals forces; Debye, Keesom and London (or dispersion) interactions. Debye interactions arise between a permanent rotating dipole and an induced dipole, whereas Keesom interactions arise between permanently rotating dipoles. London (dispersion) interactions are the result of two induced dipoles. This interaction originates from the high frequency fluctuations in the electron density of a molecule that induces the orientation of the electrons of a neighbouring molecule such that a phase shift between the polarisabilities occurs causing a net attractive force. London forces therefore occur between all molecules, both polar and non-polar molecules.

The van der Waals interaction between two approaching bodies as a function of separation distance can be predicted via two methods; the continuum (macroscopic) approached developed by Lifshitz [86, 87], and the microscopic approach developed by Hamaker [88]. These two approaches have been discussed extensively in the above literature and colloidal theory text books [86, 89, 90], and will not be discussed further here.

The Hamaker approach for determining the interaction of two identical spherical particles of radius R (m) separated by a distance H (m), provided R >> H, the van der Waals force, F_{VDW} (N), is given by the following expression [91]:

$$F_{VDW} = -\frac{RA_H}{12H^2}$$ **Equation 2.10**

where A_H is a materials property termed the Hamaker constant (J).

A number of methods currently exist for calculating A_H. Of these, the approach of Lifshitz [87] provides the most accurate result by defining A_H in terms of several characteristic bulk physical properties, namely the dielectric constants and refractive indices of the dispersed and continuous phases. For the most simple case in which two bodies 1 and 2 are interacting across a third medium 3 and the electronic absorption frequencies of the three media are identical, A is given by [91]:

$$A_H = \frac{3kT}{4}\left(\frac{\varepsilon_1 - \varepsilon_3}{\varepsilon_1 + \varepsilon_3}\right)\left(\frac{\varepsilon_2 - \varepsilon_3}{\varepsilon_2 + \varepsilon_3}\right) + \frac{3h\nu_e}{8\sqrt{2}} \frac{\left(n_1^2 - n_3^2\right)\left(n_2^2 - n_3^2\right)}{\sqrt{n_1^2 + n_3^2}\sqrt{n_2^2 + n_3^2}\left[\sqrt{n_1^2 + n_3^2} + \sqrt{n_2^2 + n_3^2}\right]}$$

Equation 2.11

where ε_1, ε_2, ε_3 are dielectric constants of the three media, n_1, n_2,n_3 are the refractive indices of the three media, v_e is the adsorption frequency in the ultraviolet region, k is Boltzman's constant, h is Planck's constant and T is the absolute temperature.

2.5.3 The DLVO theory of colloidal stability

DLVO theory is named after the people who developed it; Derjaguin, Landau, Verwey and Overbeek [47]. Also known as the double layer theory, it describes colloidal stability in terms of electrical double layer and van der Waals interaction forces between particles as a function of separation distance [92]. Thus the following equation is given by (and expressed schematically in Figure 2.7):

$V_T = V_A + V_R$ **Equation 2.12**

****This drawing has been removed. Please see referenced source for drawing.****

Figure 2.7: Interaction energy potential between particles as a function of distance, where V_R is electrical double layer repulsion, V_A is van der Waal's attraction, and V_m is the energy barrier created by the sum of the two effects [93].

Whilst the DLVO theory of colloidal stability predicts the behaviour of many colloidal systems successfully [77, 84, 94, 95], the complexity of flocculated systems requires the description of additional forces to adequately describe their behaviour [12, 31, 96, 97]. This is described below in Section 2.6.

2.6 NON DLVO INTERACTION FORCES

In general, DLVO theory is generally sufficient for many colloidal systems, however, it fails to encompass anything other than the total potential energy between two particles, given by Equation 2.7, which only includes van der Waals and electrical double layer forces. A number of non-DLVO type forces are described below [98].

2.6.1 Structural or hydration forces

Hydration forces are an observed repulsive force between two particles interacting across an aqueous medium that have been brought within a close proximity of each other (< 10 nm) [84]. This short-range repulsive force has been described to be the result of a strongly

surface-associated layer of water molecules around each particle [99]. The exertion of a small repulsive force results when another structured water layer approaches, forcing the molecules to adopt an entropically unfavourable conformation.

2.6.2 Hydrophobic forces

Hydrophobic interactions occur when hydrophobic particles (e.g. copper sulphide, talc, etc.) are dispersed in an aqueous solution. The hydrophobic particles (which are hydrophobic due to a lack of hydrogen bonded surface species e.g. -OH) aggregate in water (due to the unfavourable surface-hydrophilic solvent -OH interaction) to minimise the total surface area of the particles that are in contact with the water [84]. Whilst these forces are of vast importance to the mineral industry, they have little effect on this body of work as both the mineral dispersions and polymers are hydrophilic.

2.6.3 Steric forces

Steric forces exist between particles that have a very high coverage of adsorbed layers of organic or inorganic polymer [84]. For flocculated dispersions, additional repulsive electrical double layer forces are observed due to the charge carried by the polyelectrolyte molecules themselves; this is referred to as electrosteric repulsion. For particles with an adsorbed polyelectrolyte layer, the strength and range of electrosteric repulsion can be controlled by varying the pH and ionic strength of the dispersion in order to optimize the polymers interfacial conformation [34, 84, 100-102].

Low molecular weight polymers are often adsorbed to colloidal particles to induce steric stabilisation, preventing coagulation of the dispersion [7, 103, 104]. Steric interactions are typically shorter range than the electrostatic interactions, but may be greater in magnitude in the presence of high molecular weight polymers. The conformation of the adsorbed polymer layer also affects this type of interaction [105]. Solberg and Wågberg observed cationic polyacrylamide to be effective for flocculation of their model silica dispersion, but found that it caused steric stabilisation of a cellulose fiber system [106].

2.6.4 Bridging and depletion forces

Bridging forces arise whereby a high molecular weight polymer (usually > 1×10^6 Da) attaches to more than one particle and brings them close together. This is discussed further in Section 2.9.1.1. Depletion forces arise whereby unadsorbed polymer molecules are present in solution and particles aggregate through the exclusion of these polymers from their interstitial area. This is also discussed further in Section 2.9.1.5.

An Atomic Force Microscopy study by Bremmell and Scales [100] found polyelectrolyte to adsorb to a hematite/silica system in a flat, uncoiled conformation, which they suggested would be useful for bridging flocculation.

2.7 RHEOLOGY AND PARTICLE INTERACTIONS

Rheology is the study of deformation and flow behaviour of matter under applied stress. In recent years, rheological measurements have been used as an indicator of the total inter-particle force under a variety of dispersion conditions. Rheology is very important to dewatering applications. If the thickened pulp (at the bottom of a thickener) has a high yield stress, it may be un-pumpable, making it difficult to transport to impoundment dams. In addition, a rigid pulp structure (as indicated by a high yield stress) is often detrimental to consolidation as it traps large volumes of water within the particle network. Pulps with lower yield stresses are easier to transport, and often are more compact due to easier floc breakage allowing tighter packing of particles.

Shear yield stress is the measure of the force required to break the structural network of particles that gives rigidity to the dispersion before flow can occur [47], and will be used as the primary measure for evaluating the pulp rheology throughout this work. Shear yield stress can be measured using the vane technique (see Chapter 3), which gives us insights into the particle interactions within the dispersion [107, 108]. This technique has been used extensively in the literature as an indirect technique to examine the relative inter particle interactions in colloidal dispersions under various surface chemistry conditions [12, 17, 22, 77, 98, 109-111].

2.7.1 Dispersion rheology and its relationship to zeta potential

An understanding of the link between colloidal particle interactions and zeta potential enables the manipulation of the physicochemical parameters in order to optimise the dewatering process. Various models have been developed in order to link pulp rheology with interfacial chemistry. The elastic floc model [112] was developed to predict the behaviour of flocculated dispersions. The yield stress is designated as the energy required for stretching and breaking the bonds between coagulated particles, before flow can occur. The interaction potential between particle pairs is given by the following expression:

$$C_{FP} = \frac{1}{20 r \eta_s D c_{FP}} \left\{ \frac{A_H}{12 d_1^{\,2}} + B(d_1)\xi^2 \right\} \qquad \textbf{Equation 2.13}$$

where C_{FP} is the maximum tensile stress (N) to which flocs can be subjected before flow occurs, D_{CFP} is the shear rate (1/s), d_1 is the separation distance (m), r is the particle radius (m), η_s is the dispersion viscosity (Pa·s), A_H is Hamaker constant (J), B is a fitting parameter which is negative in value and dependent on the elasticity of the interparticle bonds and ζ is particle zeta potential (V). When DLVO forces dominate the particle interactions, the magnitude of the yield stress is proportional to the square of the zeta potential such that;

$$\tau_y = \tau_{y\max}\left(1 - K\zeta^2\right) \qquad \textbf{Equation 2.14}$$

where τ_y (Pa) and $\tau_{y\ max}$ (Pa) are the shear yield stress and maximum yield stress respectively, and K is a fitting parameter. Whilst this model has been used extensively, it is inappropriate for pulp rheology (due to it focusing on only two particles) when the particles are aggregated into a three dimensional network [113]. A more recent model has been developed by Kapur *et al*., [114] and Scales *et al*., [111], and is given by the following expression:

$$\tau = K'\left[\frac{A}{12\pi h^2} + \frac{\varepsilon\varepsilon_0\zeta^2 e^{-\kappa h}}{\kappa}\right] \qquad \textbf{Equation 2.15}$$

where K' is a structure parameter, h is the interparticle distance (m), ε and ε_0 are the dielectric constants of the medium and free space, respectively, ζ is the particle zeta potential (V), κ is the inverse of the Debye length (m). This model directly relates zeta potential and yield stress to one another, providing a tool with which to investigate the existence of DLVO and non-DLVO forces. The above elastic floc model has been used previously in the literature to highlight the presence of non-DLVO forces [12, 31, 96, 97, 115].

2.7.2 The impact of pulp rheology on the dewaterability of mineral dispersions

A number of colloidal particle interactions relating to dewatering have been characterised using rheology. Addai-Mensah and Ralston [12] reported that for iron oxide pulps, shear yield stress was large when zeta potential was low, and small when zeta potential was high, consistent with DLVO expectations. A high yield stress and a low zeta potential was found to be more efficient for increased settling rates as electrostatic repulsion was at a minimum, allowing aggregation of particles. There was no noticeable impact on the consolidation of the dispersion.

Abu-Orf and Ömeci [116] found that the network strength of sludge (measured by torque rheometry) correlated well with optimal flocculant dosage. The strength of the particle network increased with polymer addition, but a noticeable dip was observed when the optimal flocculant dosage was reached. After the optimum dosage, the strength of the particle network continued to increase, and hence the strength of the flocs. Abu-Orf and Dentel [117] also found that whilst this was useful for dewatering, that the strength of the flocs was dependent on the mixing time and that further along the dewatering process the flocs would break and cause poor dewaterability.

Mpofu *et al*. [6] reported flocculated pulp yield stress to be dependent on polymer structure type. Using Equation 2.15, kaolinite dispersions flocculated with polyacrylamide and polyethylene oxide polymers where shown to display non-DLVO behaviour. McFarlane *et al*. [29] found that increasing the agitation speed used to shear dewatered clay dispersions severely reduced the shear yield stress and increased the consolidation. Non-ionic polyacrylamide flocs were stronger than anionic polyacrylamide flocculated pulps. This was rationalised in terms of polymer bridging forces which were expected to be stronger

for the non-ionic polyacrylamide than the anionic polyacrylamide in flocculating negatively charged kaolinite particles.

2.8 MEASUREMENT OF INTERPARTICLE FORCES BY COLLOIDAL PROBE ATOMIC FORCE MICROSCOPY

The Atomic Force Microscope (AFM) was originally developed in 1986 by Binnig *et al*. [118] based on the technology used in the Scanning Tunnelling Microscope (STM). The STM was designed to image the surface of conducting and semi-conducting materials by laterally measuring the tunnelling current between a sharp tip and the conducting surface. The AFM on the other hand, was developed to directly measure the force between the tip and the sample rather than measuring current, negating the need for a conducting material. This allows direct measurement of forces between any two samples.

2.8.1 Fundamental principles

The main components of the AFM are shown in a schematic in Figure 2.8. A colloid probe is mounted at the tip of a cantilever which approaches the sample surface such that the forces can be measured between the two. The cantilever deflects the laser beam as a direct result of forces acting between the tip and surface, and hence the direct force can be measured. These laser deflections directed to the flipside of the cantilever are monitored optically and are redirected to a position-sensitive, photo-diode detector where the laser signal is intercepted and any deflection in the cantilever calculated. This deflection can be converted into interaction forces, F (N), by Hooke's law:

$$F = -k_z x \qquad \textbf{Equation 2.16}$$

where k_z is the flexural spring constant of the cantilever and x is the deflection of the cantilever. Careful calibration of the cantilever in each experiment is therefore essential.

Traditionally, a spherical particle (radius *a*, m) is used as the colloidal probe in order to compare with theories according to the Derjaguin approximation measuring the force between two surfaces given by [119]:

$$F(\Delta X^0 + D_0) = \frac{2\pi}{(1/a + 1/R_0)} E(D_0) \qquad \textbf{Equation 2.17}$$

where E is energy (J), D_0 is the separation at the centre of two bodies (m), X^0 is a constant set by the choice of origin for the separation ΔX. The sample surface can be of any shape. Force measurements can be taken in air and liquid, which makes the AFM a very versatile analytical tool.

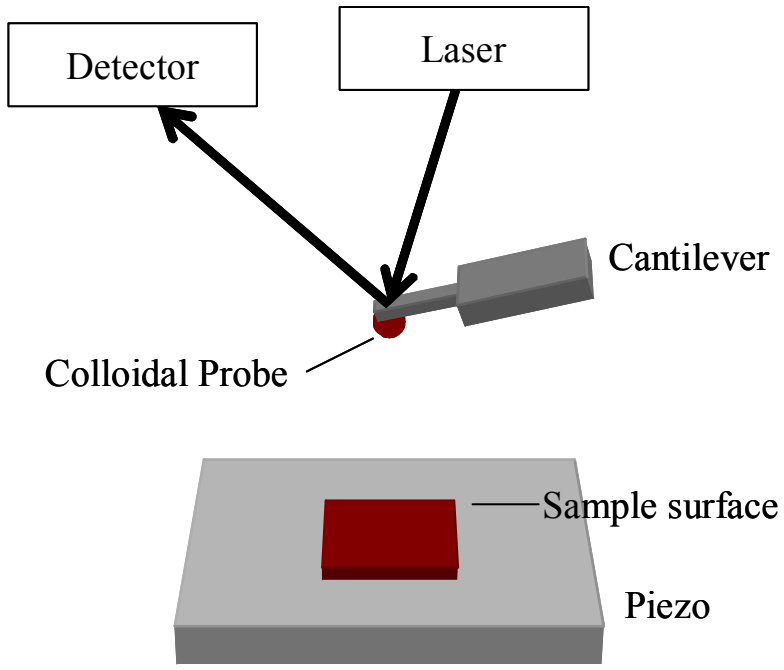


Figure 2.8: Basic schematic diagram of the colloid probe AFM.

2.8.2 Atomic Force Microscopy on mineral surfaces

AFM has proved an effective tool in the measurement of various forces between mineral surfaces. Toikka *et al*. [59] measured the adhesion of iron oxide to silica as a function of pH and ionic strength, and found that adhesion only occurred between the iep's of the two

oxides and therefore that electrostatic interactions were the main impacting factor on adhesion. Pochard *et al.* [120], however, found this relationship to be less straightforward and suggest that the state of the dispersion (measured in this case between model hematite and TiO_2 systems) depends on the surface density of condensed monovalent counter-ions rather than on the surface charge.

Larson and Pugh [75] used the AFM to measure the adsorption of copper (II) onto silicon nitride by monitoring the change in resonant frequency of the cantilever, showing how truly diverse the experiments on this instrument can be. Lateral forces can be measured in addition to direct or normal forces, as has been seen in several studies. Lateral Force Microscopy (LFM) has been used by Such *et al.* [121] to measure the frictional properties of oxide nanostructures patterned on Si surfaces, and Yuan and Lenhoff [122] measured the surface mobility of colloidal latex particles adsorbed on mica. Fieler *et al.* [123] successfully measured the friction forces between a silica sphere and a titanium dioxide wafer in solution, and found that force measurements in liquid allowed the surface separation, adhesion and applied force to be controlled independently, as opposed to conducting the same experiments in air.

2.8.3 Atomic Force Microscopy on mineral surfaces with adsorbed polymer layers

AFM has been widely used to image adsorbed polymers on mineral surfaces [20, 124-127] and measure interaction forces involving mineral surfaces and polymers [4, 5, 100, 128, 129]. Biggs [4] was able to measure both bridging and steric forces between zirconia surfaces. Biggs and Healy [128] have demonstrated the use of the AFM to monitor the changes in polymer conformation at the solid/water interface. Zirconia (ZrO_2) was the surface used in the experiment, and it was discovered that polyacrylic acid, whilst in a tight coil on the surface at low pH, gradually uncoiled and formed straight strands (with one or two points of contact with the surface) with increasing pH. Bremmell and Scales [100] measured adhesive forces between adsorbed anionic polyelectrolyte layers in high ionic strength solutions and discovered that the polyelectrolytes adsorbed in a flat conformation, and that upon separation, an adhesive force resulted between the silica probe and the iron oxide surface due to an “uncoiling” of the polymer, and this adhesion was dependent on the functional groups of the polymer.

2.8.4 Atomic Force Microscopy and rheology

Whilst AFM is used to measure the forces between only two approaching bodies, it is useful in comparison to the measurement of the bulk rheology, which takes into account the three dimensional network of particles. Much work has been conducted into the rheology of droplet emulsions using AFM [130-134].

Whilst AFM techniques have been used to enhance knowledge of rheology of bio-systems, little correlations have been drawn in the literature between such methods and the rheology of mineral dispersions. Piétrement and Troyon [135], however, successfully ascertained the shear strength of coated silicon substrates using a combination of modulated lateral force microscopy and magnetic force modulation microscopy using a home made AFM instrument with an additional lateral scanner. Pederson and Bergström [136] measured the forces between zirconia surfaces in polyacrylic acid and compared them to rheological observations in a similar fashion to that which is planned in this study. They were able to use the AFM data obtained to investigate a previous suggestion (by Green and Bergström [137]), which was based on electroacoustic and rheological data, that polyacrylic acid adsorbed in a flat conformation to their zirconia surface. AFM results suggested this was not the case. In this case, AFM measurements were able to provide useful information which, when combined with electroacoustic and rheological data, gave a more accurate view of the adsorbed polymer conformation than electroacoustic and rheological data could alone.

2.9 FLOCCULATION AND DEWATERING

Dickinson *et al*. [2] have stated that when a high molecular weight polymer (2×10^6 Da) is added to a stable dispersion of particles at a low polymer concentration (below saturation coverage of the particles), the primary effect is bridging flocculation. For high polymer concentrations that are enough to completely cover the surface of the particles, the polymer layers induce repulsion between particles and steric stabilisation occurs.

2.9.1 Flocculation mechanisms

There are many mechanisms by which flocculation can occur, as displayed schematically and described below.

2.9.1.1 Bridging flocculation

Bridging flocculation occurs when high molecular weight polymers hydrogen bond to more than one particle effectively "bridging" them together (see Figure 2.9) [90]. This method of flocculation is predominant in mineral processing. Bridging polymers are generally larger than 1×10^6 Da [6, 8, 13, 17, 18, 25, 26, 29-33, 38, 110, 138-144]. Non-ionic polymers, and indeed, most other polyelectrolytes can flocculate charged and uncharged particles [142, 145, 146]. Effective bridging flocculation requires that the adsorbed polymer extends far enough from the particle surface to attach to other particles and that there is sufficient free surface available for adsorption of these extended chains [143].

2.9.1.2 Charge neutralisation

Charge neutralization is a major mechanism for polyelectrolytes where the suspended particles have a charge opposite to that of ionic polymers functional groups (Figure 2.10). In many dewatering applications, effective flocculants are those having a charge opposite to that of particles. The advantage of using the oppositely charged polymers is that they reduce the repulsion and cause the particles to come close enough to one another in order to allow flocculation to occur [11]. This reduction in repulsion, however, may be detrimental to consolidation of mineral dispersions as discussed previously in Section 2.3.2. Polymers with a lower molecular weight than that required for bridging flocculation ($< 1 \times 10^6$ Da) are effective in this mechanism.

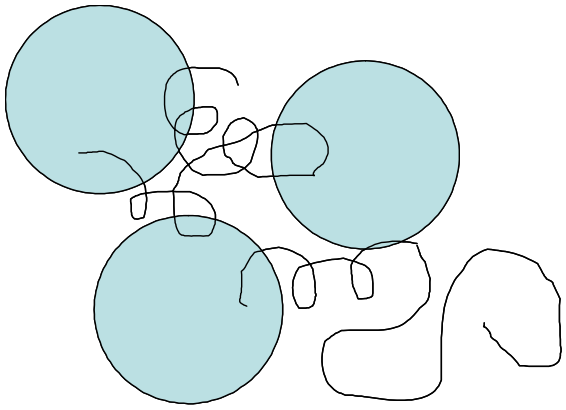


Figure 2.9: Schematic representation of bridging flocculation, where multiple particles are held together by one polymer molecule.

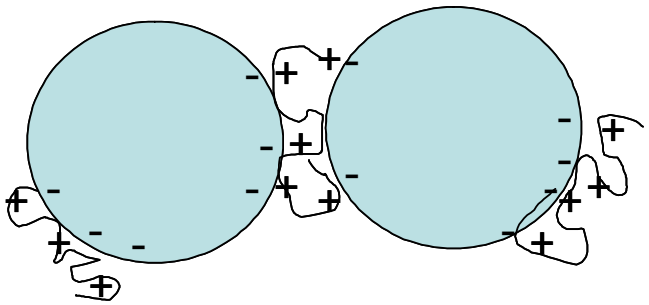


Figure 2.10: Schematic illustration of charge neutralisation flocculation mechanism between oppositely charged mineral particles and polymers.

2.9.1.3 Electrostatic patch mechanism

This occurs when particles have a fairy low density of immobile particle surface charges and the adsorbing polymer has a high charge density. If a charged polymer adsorbs, areas of excess charge develop opposite to that of the polymer adsorbing, and that charged patch can then be electrostatically attracted to the polymer attached to a nearby particle. Particles having this type of charge neutralization may interact in such a way that positive and negative patches come in to contact giving quite strong attachment [140], as described schematically in Figure 2.11.

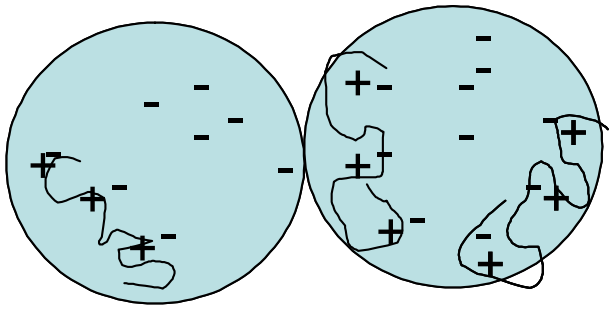


Figure 2.11: Schematic representation of electrostatic patch flocculation mechanism between oppositely charged mineral particles and polymers.

2.9.1.4 Polymer complex formation

Synergistic effects of high molecular weight polymers with added polymer and/or charged particles (such as metal salt coagulants) in colloidal dispersions are supportive to the flocculation process [147, 148]. In mineral tailings dewatering where polymeric flocculants are used, there are many species which may interact with the added polymer (such as metal ions), either naturally present or advertantly added to enhance dewatering. In cases such as this, polymer complex formation may occur [11, 50]. Mpofu *et al*. [31] were successful in using manganese and calcium ions at their hydrolysis pH with kaolinite dispersions in synergy with high molecular weight polyacrylamide to increase the settling rates and the consolidation. Addition of metal ions changes the surface chemistry of negatively charged mineral surfaces, allowing enhancement of dewatering through exploring the synergistic effects of such ions with high molecular weight polymers.

Bremmell and Addai-Mensah [77] were able to manipulate the surface chemistry of talc using magnesium ions to achieve higher settling rates of flocculated talc dispersions. The addition of these ions was, however, detrimental to the final solids content of the dewatered pulp. This was due to the reduction in the electrical double layer leading to a decrease in interparticle repulsion that allows quicker aggregation, but poorer consolidation as a result of particle networking.

2.9.1.5 Depletion Flocculation

Depletion flocculation is an entropic effect and it depends on particle and polymer volume fractions. It occurs when free non-adsorbing polymer molecules present in the dispersion are excluded from the space between two approaching particles due to their large size (Figure 2.12). The resulting osmotic pressure forces the particles to flocculate [50].

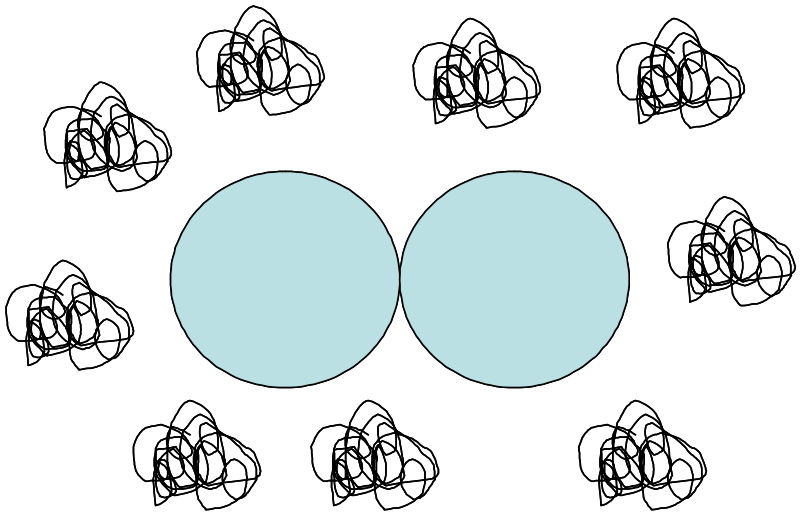


Figure 2.12: Schematic representation of depletion flocculation.

2.9.2 Dewatering through flocculation

A number of the above mentioned flocculation methods have been found to effectively flocculate particles and assist in dewatering. In general, bridging flocculation is most commonly used. It is useful for achieving high settling rates as compared with other flocculation mechanisms, but can have little effect on improving the consolidation of mineral pulps. Petzold *et al*. [149] determined that dual flocculation by the addition of a cationic polyacrylamide followed by an anionic polyacrylamide was most successful for dewatering clay dispersions, in terms of both settling rate and consolidation. A combination of charge patch and bridging flocculation was believed to be the underpinning mechanism of flocculation. Yu *et al*. [150] discovered that for a low molecular weight cationic flocculant, charge neutralisation was the main flocculation mechanism for dewatering of kaolin dispersions, whilst for high molecular weight cationic polyacrylamide, bridging flocculation was predominant. Yan *et al*. [40] observed the same

to be true with polyacrylic acid flocculation of alumina particles. McCarron *et al*. [151] found that flocculation of kaolin dispersions with high molecular weight cationic polyacrylamide at low concentrations had bridging flocculation as the predominant mechanism, but that at higher concentrations, charge neutralisation was predominant.

2.10 POLYMER ADSORPTION

The investigation of polymer adsorption at mineral interfaces is often used to understand how adsorbed polymers influence the interfacial properties of mineral particles [152-154]. Parameters of interest in polymer adsorption studies include adsorption kinetics, adsorption isotherms, adsorbed polymer conformation and adsorption mechanisms, which will all be discussed in this section.

2.10.1 Kinetics of polymer adsorption

Flocculation kinetics are described by three characteristic time scales as described schematically in Figure 2.13 [2];

t_a: polymer adsorption
t_r: adsorbed polymer rearrangement
t_c: particle collision

Whilst t_r (h) is dependent on the surface chemistry of the polymer, t_a (h) and t_c (h) can be approximated using equations of second-order reaction kinetics [2], by the following expressions [141]:

$$t_a = -[\ln(1-f)] / k_{12}N_0 \qquad \textbf{Equation 2.18}$$

$$t_c = 1 / k_{11}N_0 \qquad \textbf{Equation 2.19}$$

where N_0 is the (initial) particle concentration, and f is the fraction of polymer required to form stable flocs. k_{12} and k_{11} are rate constants determined by the Smoluchowski expression for perikinetic coagulation;

$$k_{ij} = (2kT /3n) (a_i + a_j)^2 / a_i a_j \qquad \textbf{Equation 2.20}$$

where k is Boltzmann's constant, T is the temperature (K), η is the viscosity of the medium, a_i and a_j are the radii (m) of the colliding entities [2].

****This drawing has been removed. Please see referenced source for drawing.****

Figure 2.13: Effect of polymers on colloidal stability [2].

McFarlane *et al*. [155] investigated the influence of flocculant adsorption kinetics on the dewaterability of clay dispersions. They found that slow adsorption of polyacrylamides lead to an increase in floc size and strength giving a fast dewatering rate, whilst fast adsorption kinetics lead to an inefficient distribution of polymer per particle and lead to a poor dewatering rate.

2.10.2 Adsorbed polymer conformation

The adsorption of polymers onto surfaces has been widely studied [2, 4, 36, 100, 136, 141, 156, 157]. The adsorption of polymers at the interface involves changes in the conformation of the chains. The most common model describing these conformational changes is the loop-train-tail model developed by Jenckel and Rumbach [158]. A train describes the conformation in which the polymer segment is in contact with the surface; a loop refers to the conformation in which the segments are bound by trains at either end; and tails are polymer segments bound by trains at one end [159]. Such conformations can be observed in Figure 2.14:

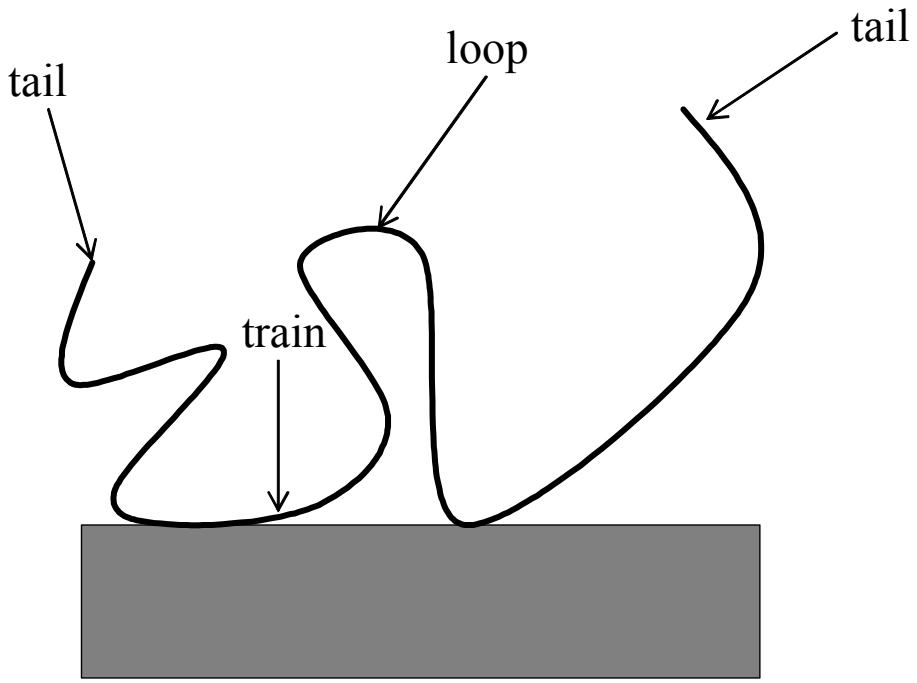


Figure 2.14: Loop-train-tail model describing conformation changes upon polymer adsorption onto a solid surface.

The conformation of the adsorbed polymer can be modified by changing many variables, including pH, temperature and ionic strength (see Figure 2.15) [160]. If the polymer is anionically charged, its conformation at the surface can be changed by adsorbing the polymer at different pH values. The polymer will become more expanded as the adsorption pH becomes higher than its pKa. If the polymer is cationically charged, the reverse is true

as the adsorption pH becomes lower than its pKb. Liufu *et al*. found that this to be true with a cationic polymer flocculating silica nano-particles [161].

****This drawing has been removed. Please see referenced source for drawing.****

(b) δ lower, highly collapsed conformation with less loops and tails. More trains, poor bridging.

Figure 2.15: Schematic illustration of a possible conformation for the adsorbed PEO and PAM at the kaolinite-solution interface at temperatures: (a) 20-40 ^{o}C, PEO and 20 ^{o}C, PAM and (b) 60 ^{o}C, PEO and >20 ^{o}C PAM, where δ adsorbed layer thickness [32].

Mpofu *et al*. [32] reported that there was a collapse in polymer structure as clay mineral dispersion temperature was increased from 40 ^{o}C to 60 ^{o}C, and suggested that this could be due to a decrease in solvency. This collapse in polymer structure hinders the flocculation process as there are less polymer loops and tails extending into the solution to enhance bridging flocculation.

2.10.3 Adsorption isotherms

Adsorption experiments and isotherms derived from them are commonly used to gain insight into the mechanisms of polymer adsorption and flocculation of mineral particles. This forms a basis of knowledge which can be utilised to gain understanding of the aggregation process, and allow determination of the best conditions for polymer adsorption and hence flocculation. Four types of adsorption isotherms have been previously classified [162]; S-shaped (S), Langmuir (L), high affinity (H) and constant partition (C), as shown in Figure 2.16. For all isotherms except for (L) and (C), adsorption may increase beyond monolayer adsorption, such that multilayers are formed.

****This drawing has been removed. Please see referenced source for drawing.****

Figure 2.16: Types of solid-solution adsorption isotherms [162].

The slope of the adsorption isotherm provides an indication of the ease of polymer adsorption. The S isotherm is uncommon for polymer adsorption, as with the C isotherm. The L isotherm indicates that as the concentration of polymer increases, there are less adsorption sites available and hence it becomes increasingly difficult for the polymer to adsorb onto the surface. This isotherm arises when none of the energy terms from the adsorbed species, solvent or solute are dependent on concentration. The H isotherm represents solutes with a high affinity to the solid substrate even at low concentrations, and is generally thought to represent monolayer adsorption. This type of isotherm is commonly associated with polymer adsorption as the solute molecules are adsorbed as a relatively large unit [163]. H type isotherms have been observed for the adsorption of polyacrylamides [6, 8, 21, 164], polyethylene oxide [6, 8, 17, 31, 32] and polysaccharides [20, 165, 166] onto mineral particles' surfaces.

2.10.3.1 Langmuir and Freundlich adsorption models

The adsorption isotherms can be fitted to the Langmuir and Freundlich models for polymer adsorption at the solid-liquid interface [78], the former which can be expressed as [167]:

$$\theta = \frac{\Gamma_{ads}}{\Gamma^{m}_{ads}} = \frac{KC_{eq}}{55.5 + KC_{eq}} = \frac{bC_{eq}}{1 + bC_{eq}}$$ **Equation 2.21**

where θ is the fractional surface coverage, Γ_{ads} is the amount of polymer adsorbed (mg/m^2), Γ^{m}_{ads} is the adsorption plateau (mg/m^2), C_{eq} is the polymer equilibrium solution concentration (moles/dm^3), K is the adsorption equilibrium constant (dm^3/moles) and b is the Langmuir affinity constant (=K/55.5, where 55.5 is the molar concentration of water). Equation 2.22 may be rearranged as below to enable the plotting of a linear graph as C_{eq}/Γ_{ads} vs. C_{eq}, which allows the adsorption plateau and the Langmuir affinity constant to be determined.

$$\frac{C_{eq}}{\Gamma_{ads}} = \frac{1}{\Gamma^{m}_{ads} b} + \frac{C_{eq}}{\Gamma^{m}_{ads}}$$ **Equation 2.22**

The Freundlich model is given by the following equation [168]:

$$\boldsymbol{\Gamma_{ads} = k_F C_{eq}^{1/n_F}}$$ **Equation 2.23**

where Γ_{ads} is the amount of polymer adsorbed (mg/m^2), and k_F and n_F are constants described as the adsorbent capacity and the adsorption affinity constant (reciprocated), respectively [20, 47, 78, 169]. A logarithmic plot of Equation 2.24 as Equation 2.25 allows a straight line to be fitted to the data yielding estimates of k_F and $1/n_F$ from the intercept and slopes, respectively:

$$\log \Gamma_{ads} = \log k_F + (1/n_F) \log C_{eq}$$ **Equation 2.24**

2.10.4 Factors influencing adsorption

There are many factors influencing the adsorption behaviour of polymers. These include molecular weight, charge density, functionality and dosage, mineral particle zeta potential, particle size/surface area and solid concentration, presence of simple and hydrolysable metal ions, pH, temperature, and the degree of shear/compression [47, 89, 90].

The nature of the solid surface adsorption site is an important factor governing polymer adsorption. Properties such as surface charge, potential, degree of solvation and the degree of surface impurities affect polymer adsorption [89]. The polymer charge determines the mode of interaction between the polymer and the solid surface. For charged polymers, the adsorption is primarily driven by electrostatic interactions. In the case of uncharged polymers, electrostatic interactions are less dominant as hydrogen bonding and solvation effects predominate. pH and ionic strength of the solvent primarily govern the solid surface characteristics [12, 54], which in turn dictate adsorption behaviour.

Co-polymers (e.g. Nonylphenol-polypropylene oxide-polyethylene oxide copolymers and homopolymer ethylene oxide and polypropylene oxide-polyethylene oxide ABA copolymers) have been investigated with relation to dewatering [159, 170], as have polyacrylamides [6, 8, 31, 156]. The polyacrylamides are relatively successful as a dewatering aid, and are traditionally used in industry as they are relatively inexpensive. Polyacrylamides will be used throughout this study.

2.10.5 Adsorption mechanisms

Previous work investigating polymer adsorption mechanisms has included the use of both diffuse reflectance infrared Fourier transform (DRIFT) [35, 171, 172] and attenuated total reflectance Fourier transform infrared (ATR-FTIR) [36, 37] methodologies to spectroscopically determine the mechanisms of polyacrylate/acrylic acid polymer adsorption onto hematite and aluminium oxide. Whilst electrostatic interactions play a dominant role in the adsorption process of a charged polymer, this can not be determined spectroscopically. Infrared spectroscopy can, however, determine the existence of hydrogen and chemical bonding. There are three main mechanisms reported for polyacrylate polymer adsorption to an iron oxide surface; monodentate chelation, bidentate chelation and bidentate bridging (Figure 2.17) [35, 36].

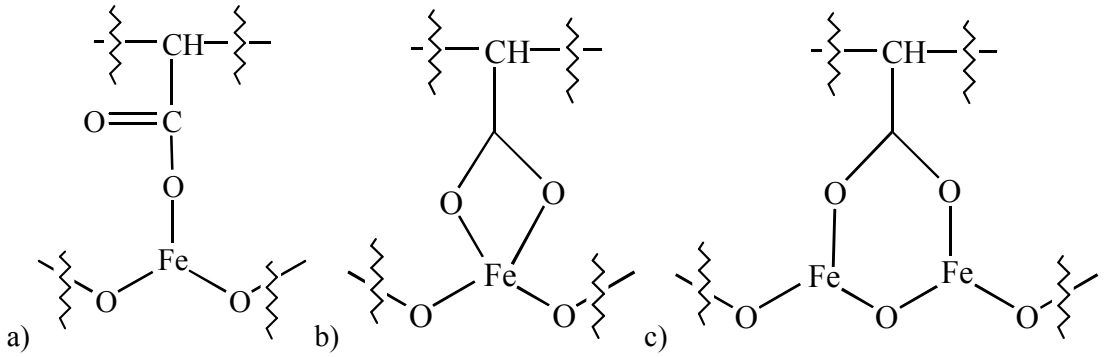


Figure 2.17: The three main chemisorption modes for the adsorption of polyacrylamide polymer acid groups to the oxide surface; a) monodentate chelation, b) bidentate chelation and c) bidentate bridging.

Jones *et al*. [35] reported that at pH 7, monodentate adsorption of polyacrylate groups onto hematite surfaces was a major adsorption mechanism, along with hydrogen bonding occurring transversely between the carboxylate group of the polymer and hematite surface hydroxyl groups, and sideways within the polymer itself. At pH 11-14 however, an asymmetric bidentate bridging structure formed. Kirwan *et al*. [36] found that at low pH (pH 2), bidentate chelation was predominant for polyacrylic acid adsorption onto hematite, and that this was independent of the polymer chain length. Studies of the adsorption of non-ionic polyacrylamide onto various minerals (predominantly via DRIFT) [6, 51, 103], have shown the main bonding mechanism to be hydrogen bonding.

2.11 CHAPTER SUMMARY

Despite extensive research into the flocculation of mineral dispersions with high molecular weight flocculants, the specific effects of the flocculation of colloidal iron oxide dispersions with conventional polyacrylamides of different structures/functionality are yet to be investigated in depth. This body of work aims to fill the void in knowledge for the influence of polymer structure type, pH and shear on the interfacial chemistry, rheology and dewaterability of model iron oxide dispersions. Polymer adsorption mechanisms and their impact on dewatering and the influence of adsorbed metal salts have not yet been fully quantified and are not yet understood. Inaugural AFM studies into the rheological

behaviour of these systems will create a body of knowledge that will enhance the optimisation of the influencing parameters to improve the overall dewaterability of these dispersions.

CHAPTER 3 Experimental methodology

3.1 INTRODUCTION

Two iron oxide samples and four, high molecular weight polyacrylamide polymers were utilised in this study. Colloidal size (<5 μm) hematite was used for all of the adsorption, surface chemistry, rheology and dewatering studies, whilst larger (15-300 μm), spherical particles of magnetite were used for Atomic Force Microscopy (AFM) work. Four polyacrylamide polymers were used in this study. The particles and polymers were characterised with various techniques including Scanning Electron Microscopy (SEM), Energy Dispersive Spectroscopy (EDAX), X-Ray Diffraction (XRD), Size Exclusion chromatography (SEC) and laser diffraction with the Malvern Mastersizer. All characterisation methods and general procedures and equipment used for this study are described below.

3.2 MATERIALS

3.2.1 Mineral samples

Colloidal size iron oxide (<5 μm, 99+% pure hematite, Aldrich) was used as purchased for preparing the mineral dispersions. The particle density is 5.12 g/cm^3 and the BET surface area is 4.84 m^2/g. Particle mean size was discovered to be ~1.6 μm.

For AFM force measurements, spherical iron oxide particles (magnetite, < 300 μm, SphereOX, Chesapeake Specialty Products, Baltimore) were used as colloidal probes (Figure 3.2). A polished hematite sample was used as the substrate.

3.2.2 Polymeric flocculants

Four polyacrylamides were used in this study; non ionic homo-polymer, PAM N, anionic carboxylate substituted copolymer, PAM A, anionic sulphonate substituted copolymer, PAM S, and cationic trimethyl amino ethyl substituted copolymer, PAM C (CIBA, Australia). Their properties are summarised in Table 3.1, and their structures are shown in Figure 3.1. Measured molecular weights were found to be significantly lower than manufacturer's specifications.

Table 3.1: Properties of the four polyacrylamides used in this study.

Name	Nominal [a] molecular weight	SEC data [b]		pKa [c]	Charge density [a]
		$\underline{M_n}$	$\underline{M_w}$		
PAM A	7.5×10^6 Da	3.58×10^5 Da	2.52×10^6 Da	4.5	25 mol%
PAM N	9.0×10^6 Da	2.52×10^5 Da	1.82×10^6 Da	-	-
PAM S	7.5×10^6 Da	4.48×10^5 Da	2.49×10^6 Da	1.5	25 mol%
PAM C	5.0×10^6 Da	-	-	9.5	25 mol%

a. Manufacturers specifications

b. [148]

c. based on pKa of specific functional groups

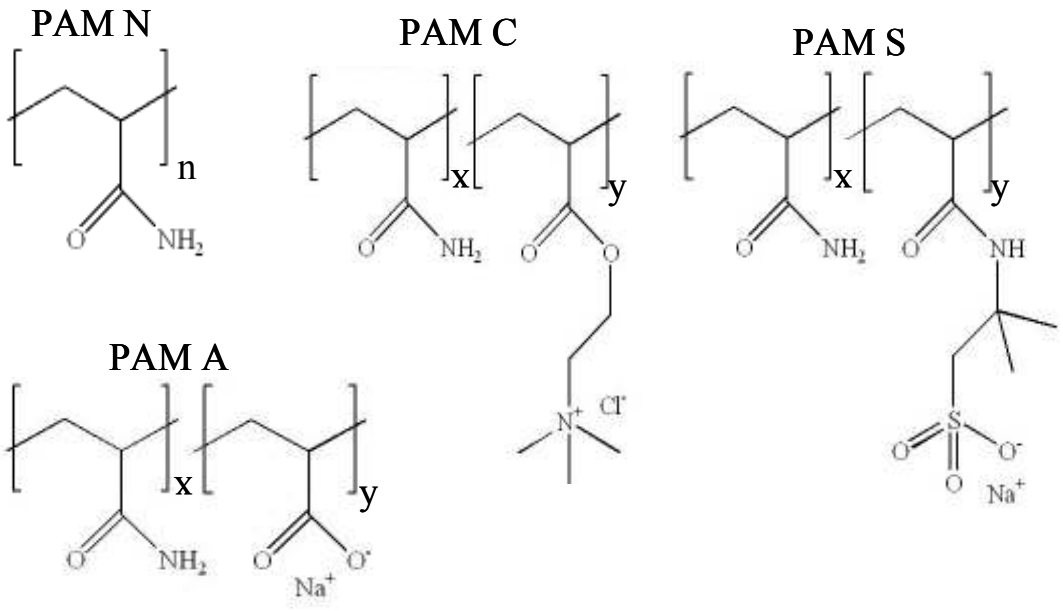


Figure 3.1: The structures of the four polyacrylamides used in this study, where the ratio of x:y is 3:1.

3.2.3 General methods

3.2.3.1 Reagents

The reagents used in this study were purchased from commercial companies and are summarised in Table 3.2.

3.2.3.2 Glassware preparation

All glassware was treated prior to use as follows. They were washed thoroughly with detergent and tap water and rinsed with deionised water. Glassware was then rinsed with acetone and placed in an oven > 70 ^{o}C for at least 30 min prior to storage in a dry cupboard.

Table 3.2: Summary of the inorganic reagents used for these investigations.

Reagent	Purity (minimum %)	Supplier
HNO_3	99	BDH Australia
KOH	85	Chem-Supply
KNO_3	99	Chem-Supply
$Mn(NO_3)_2$	98	Chem-Supply
$MnCl_2$	98	AnalaR
$MnSO_4$	99	Ajax
KBr	Spectroscopic grade	MERCK
K_2SO_4	99	M&B
$CaCl_2$	99	Ajax
Starch	99.6	Ajax
CdI_2	99	AnalaR
CH_2COONa	99.9	BDH Australia
NaF	99	Ajax
Acetone	99.5	Univar
Bromine	99.5	Chem-Supply

3.2.3.3 Solution preparation

All solutions were made with 10^{-3} M KNO_3 background electrolyte in high purity Milli-Q water (surface tension = 72.8 mN/m at 20 ^{o}C and specific conductivity <0.5 μS/cm at pH 5.6) produced by an Elga UHS system. Mineral dispersions were prepared at 8 wt% except where polymeric flocculant was to be added for dewatering tests for which the total volume was reduced by the amount of polymer solution to be added in order to maintain an 8 wt% iron oxide dispersion. Dispersions were stirred via an overhead stirrer at ~ 400 rpm for at least 20 min to ensure homogeneity. Polymer stock solutions were prepared at 1.0 g/dm^3. Complete dissolution of polymer and solution homogeneity was achieved by stirring at ~ 100 rpm for approximately 15 h. The solution was used within 3 days to minimise aging effects. Metal salt (e.g. $MnSO_4$) addition was achieved by adding a known

mass of the desired metal salt to a known volume of 10^{-3} M KNO_3 background electrolyte prior to mixing with a known amount of iron oxide particles.

3.2.3.4 pH control and measurement

Dispersion and polymer solution pH was controlled via the addition of HNO_3 and KOH. The final dispersion pH was adjusted after mixing, just prior to experimental use. pH was measured using a B417 bench pH meter (HANNA Instruments), which was calibrated prior to each experiment using buffer solutions at pH 4, 7 and 10 (Chem Supply, Australia).

3.3 CHARACTERISATION METHODS

3.3.1 Scanning Electron Microscopy (SEM)

Scanning electron microscopy was used to visually examine the size and shape of the hematite and magnetite particles. The instrument used was a Camscam CFSE CS44 (Cambridge, UK), which was equipped with a field emission gun operated at an accelerating voltage of 22 kV and an E-SEM model E-3 (Electroscan, Ma., USA) using operating variables 0-30 ^{o}C and 1-20 torr. Samples were mounted onto an aluminium sample holder with double-sided, conductive adhesive tape and coated with a thin layer of carbon to reduce surface charging. Figure 3.2 shows the SEM images for hematite (a, b) and magnetite (c, d). It is clear that whilst the manufacturer quotes <5 μm, the particles are primarily <0.5 μm. The particles do, however, form aggregates as is observed in Figure 3.2b, where the aggregate is over 5 μm in diameter. The samples of magnetite came in "fine" size, where it appears in Figure 3.2c that the particles are between 15 and 100 nm, and "coarse" shown in Figure 3.2d where the particles are up to 300 μm in size.

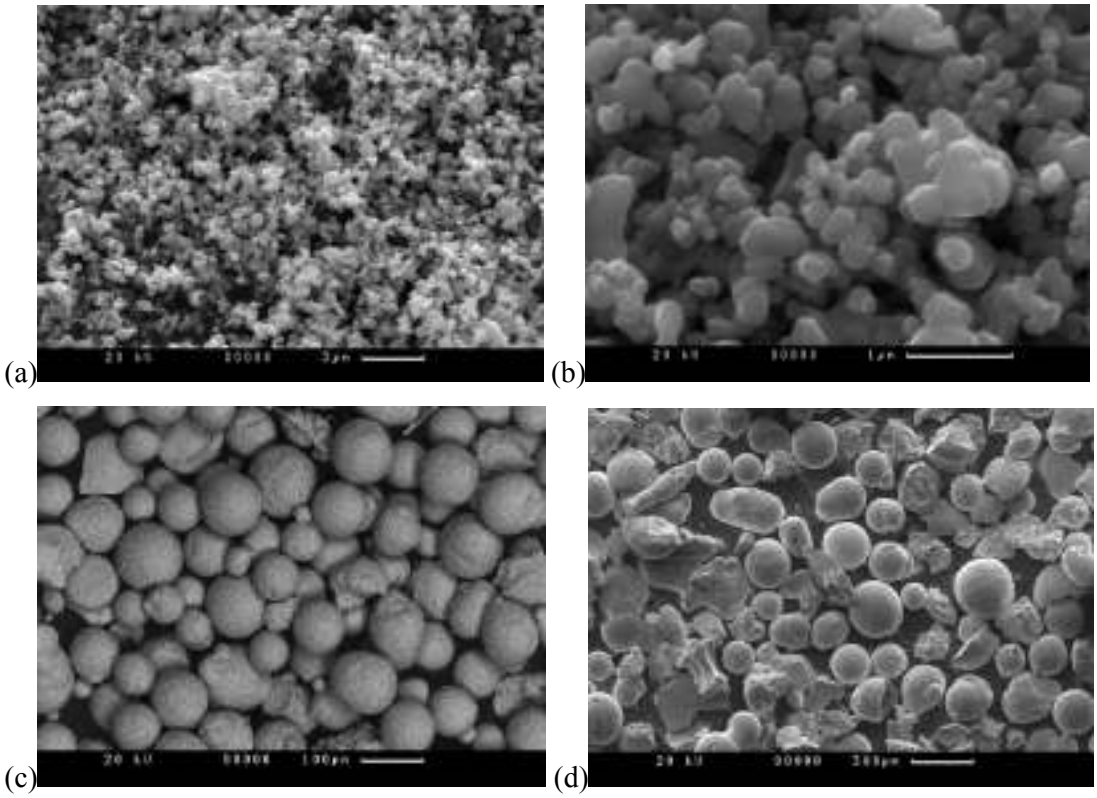


Figure 3.2: SEM images of (a) hematite, (b) hematite, (c) fine magnetite, (d) coarse magnetite. Hematite was used in all experiments with the exception that magnetite was used for AFM measurements.

3.3.2 Energy Dispersive Spectroscopy (EDAX)

EDAX measurements were taken during the SEM analysis to determine the bulk composition of the hematite. During an EDAX measurement, the surfaces of the particles are probed to a depth of 1 μm, and therefore reflect the bulk composition of each particle. The sample was found to contain only the elements Fe and O, and is considered to be pure.

3.3.3 X-Ray Diffraction (XRD)

X-ray diffraction analysis was carried out on both iron oxide samples using an XRD diffractometer (Philips PW1050 X-ray generator with Sietronic data collection). X-ray patterns were obtained from powdered samples using Cu Kα radiation (λ = 1.5406 Å) generated at 40 kV and 10 mA in θ/20 scanning mode at 1^{o} per min. XRD analysis revealed that the hematite was pure, in agreement with the EDAX data.

3.3.4 Particle size distribution

Laser diffraction particle sizing was employed to determine the particle size distribution of the hematite sample. The experiments were carried out on the Malvern 2600C Mastersizer (Malvern Instruments Ltd., Malvern, UK). A laser light (2mW He-Ne laser, $\lambda = 6.328$ nm) incident on the sample is scattered and focused onto a 31-element solid state detector behind the sample. The measurements were carried out in Milli-Q water at room temperature, with sonication used to disaggregate the particles. The measurements were taken every 30 s over 10 min to ensure particle size equilibrium. The mean diameter of the particles was measured to be ~ 1.6 μm (see Figure 3.3), which is an overestimation compared to the images of the particles seen in Figure 3.2, due to aggregation of particles. Particles were also found in smaller quantity to be ~ 0.25 μm (smaller peak on graph), which is seen in Figure 3.2 to be closer to the size of the singular particles.

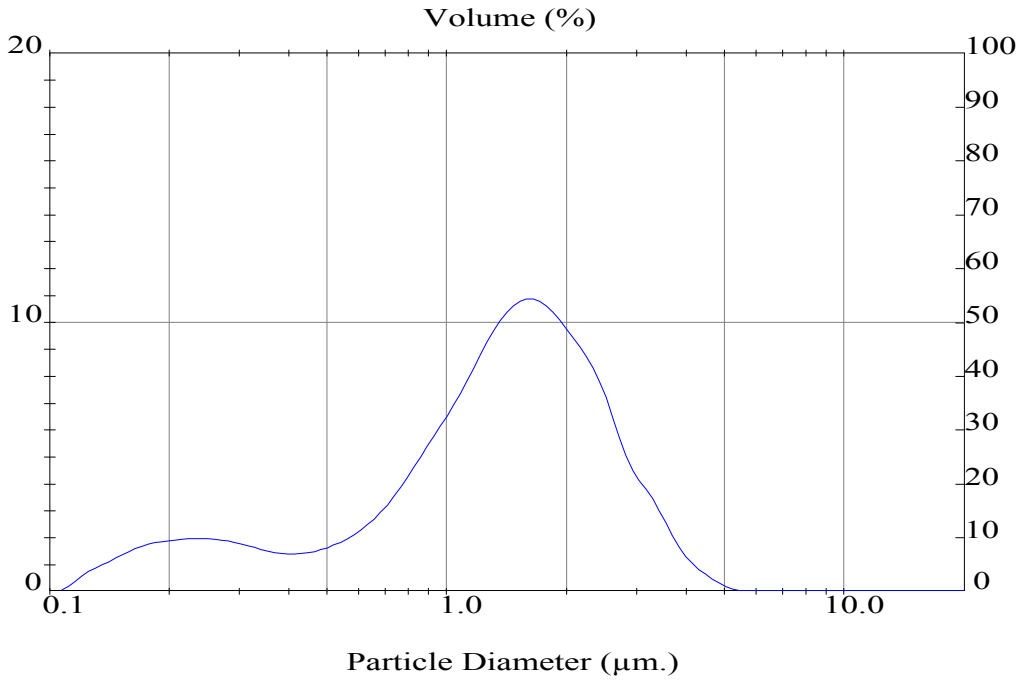


Figure 3.3: The particle size distribution of hematite as shown by the Malvern Mastersizer.

3.4 SURFACE CHEMISTRY

3.4.1 Zeta potential measurements

Particle zeta potential measurements (ζ) were carried out using the Acoustosizer (Colloidal Dynamics Inc., Australia), and determined from dynamic mobility measurements. A schematic of the instrument is shown in Figure 3.4. A sample vessel containing a pH probe, temperature probe and conductivity probe allows direct measurement of these variables. Auto-titration syringes allow automatic titration of reagents in precise quantities which were utilised for pH titration and polymer addition in this case. The vessel contains a heat exchange thermocouple – temperature probe combination which allows precise temperature measurement (± 0.1 ^{o}C) and a variable speed overhead stirrer impeller, which allows continuous sample mixing. In later models than that in the schematic, the sample is continually pumped through a cell (containing two parallel electrode plates which generate pulsed alternating electric fields) by a variable speed peristaltic pump. Sound waves from the oscillation of particles are generated following the application of an AC voltage across the suspension sample which are transmitted through glass rods to a detector and converted to a Fourier Transform signal.

Measurements were made on 8 wt% mineral suspensions made according to Section 3.2.3. The pH sweep was made by adjusting the suspension to pH 2 with HNO_3 followed by the titration addition of KOH whilst the measurements were taken. For the measurement of zeta potential with polymer addition, the suspension was titrated with polymer solution whilst the measurements were taken. Equilibrium times and speeds were 60 seconds at 250 rpm to best mimic dewatering tests. Measurements were taken at 22.5 ^{o}C ± 0.5. Background corrections were performed when measuring the zeta potential of high ionic strength suspensions (greater than 10^{-3} M) by measuring the Electronic Sonic Amplitude (ESA) signal of the electrolyte solution in which the mineral dispersion to be measured was prepared with. The raw electrolyte signal was subtracted from the total ESA signal response by the Acoustosizer.

****This drawing has been removed. Please see referenced source for drawing.****

Figure 3.4: A schematic diagram of the Acoustosizer measurement cell [113].

3.4.2 Acoustosizer calibration

Calibration of the ESA signal was carried out prior to measurements by monitoring the ESA signal for a standard electrolyte. Potassium tungstosilicate ($K_4(SiW_{12}O_{40})$) salt was used as the calibrant (at 20.0 ± 0.1 °C) due to its high chemical stability and the strong electroacoustic signal it provides. The calibration solution was refreshed approximately after every 6 months, unless particulate contamination or optical clarity was visually determined to be poor. Purity of the calibrant was ensured by monitoring the pH and conductivity of the solution as shown on the instrument display panel. Between measurements, the cell and circuit was cleaned with deionised water.

3.4.3 Estimation of adsorbed polymer layer thickness

The zeta potential of iron oxide particles flocculated with PAM N at 8 wt% solid was measured by auto-titrating PAM N (0-500 g/ton solid) to the circulating dispersions (~ 250 rpm). Zeta potential measurements were recorded after each subsequent polymer addition, after which the supernatant was reclaimed in a beaker. The supernatant was then used to perform a background correction and subtracted from the original reading in order to estimate the thickness of the adsorbed non-ionic polymer layer. The model is only suitable

for non-ionic polymers that do not alter either surface charge or ion distribution in the double layer.

The adsorbed layer thickness (δ) of PAM N onto iron oxide was determined using the following expression [50]:

$$\tanh\left(\frac{z_2 e\zeta_2}{4kT}\right) = \tanh\left(\frac{z_1 e\zeta_1}{4kT}\right) e^{-\kappa(\Delta-\delta)}$$

Equation 3.1

where z_2 and z_1 are the valences of potential determining ions, e is the electron charge, ζ_2 and ζ_1 are the particle zeta potential values in the absence and presence of polymer respectively [V], *k* is Boltzmann's constant, T is the absolute temperature [K], $1/\kappa$ is the debye length [m], and Δ is the stern plane thickness [m] (0.4 nm for 10^{-3} M background electrolyte) [60].

3.5 ADSORPTION STUDIES

3.5.1 Polymer adsorption experiments

Adsorption of PAM onto iron oxide particles was conducted using the depletion technique and UV-Visible spectroscopy for polymer detection. An iron oxide suspension of known concentration (8 wt%) was flocculated with a known quantity of polymer to provide a dosage in the range of 0-7500 g polymer/ton solid in a 20 cm^3 scintillation vial. After conditioning overnight (24 h) by a rotary shaker (Ratex Instrument R.S.M.6) to ensure equilibrium, the suspensions were centrifuged (11,000 rpm for 10 min) and an aliquot of the supernatant was removed for complexation using the starch-triiodide method (Figure 3.5) [173].

The method involves oxidation of the amide functional groups with bromine, the excess of which is removed with NaF. The newly formed amide oxidation product then oxidises iodide to iodine, which is measured as a starch triiodide complex at a wavelength of 600 nm. The absorbance was compared with a calibration curve (calibration curves shown in

Figure 3.6), prepared from polymer solutions of known concentration. The amount of polymer left in the supernatant was then subtracted from the initial amount in solution to give the amount of polymer that adsorbed onto the mineral particles. Absorbance was measured using a Cary 5 UV-vis spectrophotometer (Varian Instruments) at a wavelength of 600 nm.

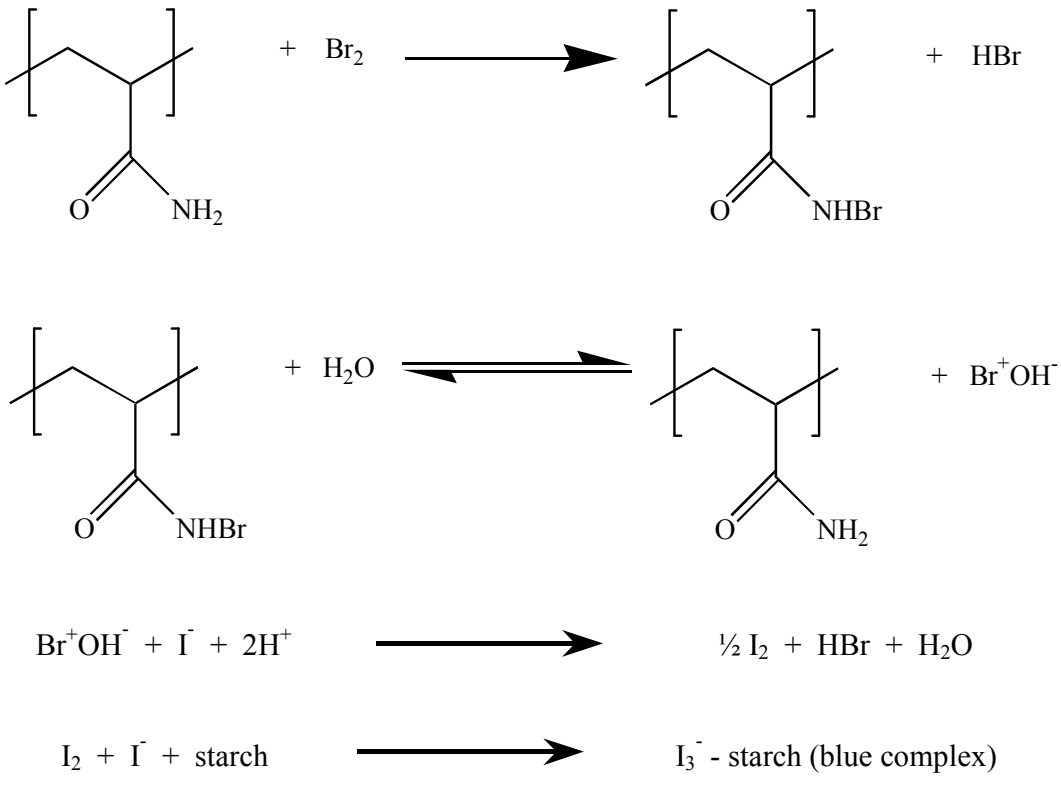


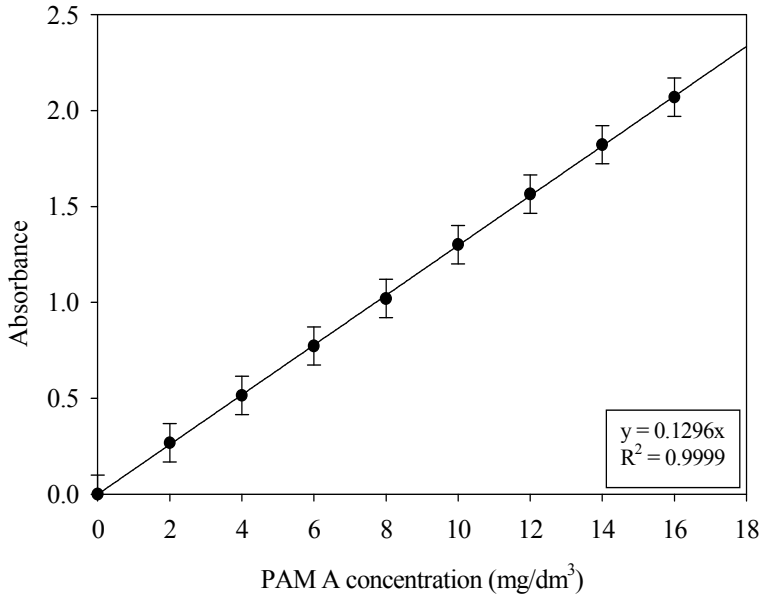
Figure 3.5: Schematic diagram of the complexation reaction required for the UV-vis measurement of polyacrylamide adsorption.

It was assumed that the amount of polymer depleted from solution was adsorbed onto the solid surface. The adsorbed amount (Γ) can then be calculated using the following equation;

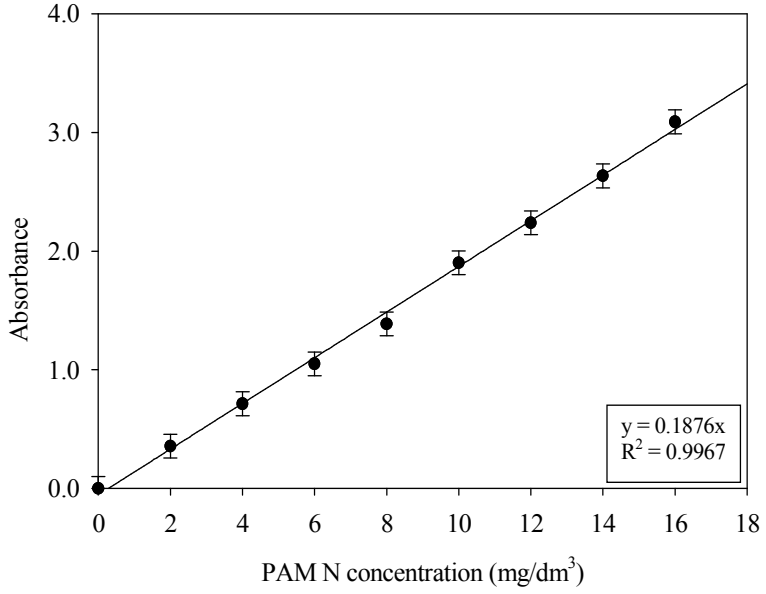
$$\Gamma = \frac{1}{m \times A_s}(c_f - c_i)V$$

Equation 3.2

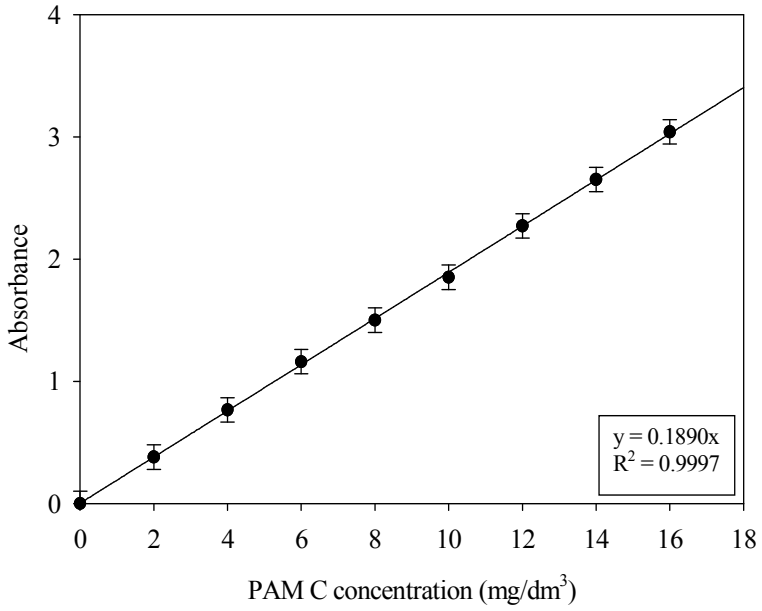
where, m is mass of the solid substrate, A_s is the specific surface area of the solid substrate, c_i and c_f are the polymer concentration before and after adsorption, respectively and V is the volume of the suspension.



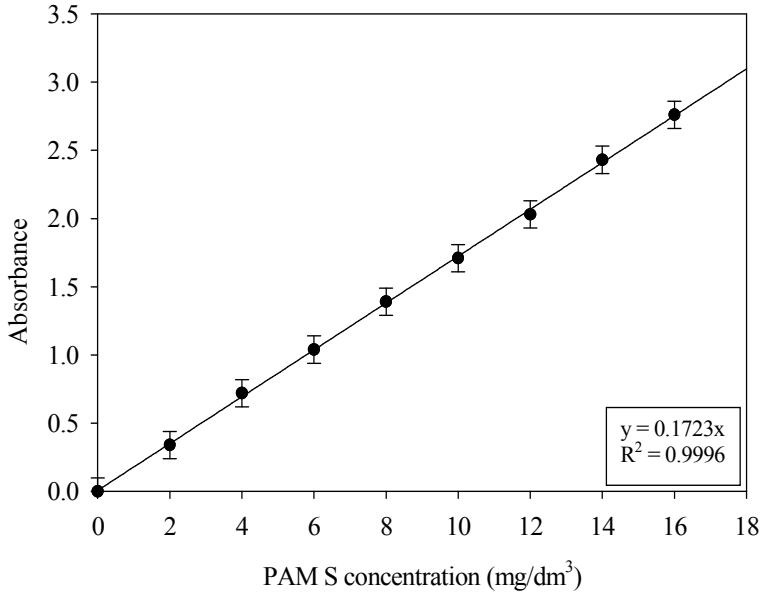
(a)



(b)



(c)



(d)

Figure 3.6: Typical calibration curves of polymer concentration vs. absorbance for (a) PAM A, (b) PAM N, (c) PAM S, and (d) PAM C using the starch-triiodide method.

3.5.2 Fourier Transform Infrared Diffuse Reflectance Spectroscopy

Characterisation of polymer adsorption mechanisms was achieved using Fourier Transform Infrared Diffuse Reflectance Spectroscopy (FTIR-DRIFT). Samples were obtained from the residue remaining from the preparation of the adsorption measurements in Section 3.5.1, and from a polymer concentration of 250 mg/dm^3. The samples were vacuum filtered, and then rinsed twice thoroughly with background electrolyte (as made in Section 3.2.3) to remove any unadsorbed species. These samples were air-dried in a desiccator for a minimum of 24 hrs. Dried, spectroscopic grade, potassium bromide (MERCK) was ground and mixed with the samples to dilute the dried residue to 2 wt% solid.

The spectra were recorded on a Nicolet FT-IR, using a DRIFT accessory (Spectratech) from 1024 scans at a resolution of 4 cm^{-1}, after N_2 purging for 30 min. The spectrum of the iron oxide solid particles with no adsorbed polymer was subtracted from that of the flocculated particles to give the adsorbed polymer spectrum. The unadsorbed polymer spectrum was collected using an ATR accessory (Zn crystal, Spectratech) with the polymer solution at ~4 wt%. This was due to specular reflectance occurring (when attempted with DRIFT) which leads to poor results. Specular reflectance occurs when light strikes on a powder surface and is reflected rather than passing through the particle [164, 174]. The adsorbed polymer spectra were not attempted with the ATR accessory due to difficulty distinguishing between adsorbed polymer and unadsorbed loops and tails given the molecular weight of the polymer. Spectra were multiplied to enable comparison.

3.6 RHEOLOGY

Rheological measurements were carried out on 30-60 wt% solid pulps which had been generated by dewatering tests. Pulps were prepared as in Section 3.8, with the exception that 1000 g of suspension was prepared in order to generate enough pulp suitable for measurement with the vane rheometer. Prior to measurement, the supernatant of the presedimented pulp was removed (via siphoning), and the resulting sediment poured into a 150 cm^3 beaker and left quiescently for a further 24 h. The sediments were handled with great care in order to prevent any noticeable beak down of particle network and pulp structure that may result during transfer to another vessel. Whilst this transfer of the pulp

can result in a decrease in yield stress, the physical properties of the measuring cylinders used in the dewatering tests and the length of the vane rheometer made it impossible to measure the yield stress *in situ*. Every effort was made to transfer the sediment reproducibly.

The shear yield stress (τ_y) was then measured (pre-shear measurement) via the vane technique [107]. The vane is a six blade unit (diameter (d) = 24 mm, height (h) = 17 mm), powered by the Haake VT550, and rotated at a rate of $\gamma = 0.021\ s^{-1}$, where τ_y is independent of shear rate [113]. A schematic is shown in Figure 3.7. The height above the unit (h_t) was always approximately 8 mm, and the distance between the unit and the bottom of the beaker (h_b) was always at least half of h. The distance between the unit and the side of the beaker was always greater than the radius (r) of the unit.

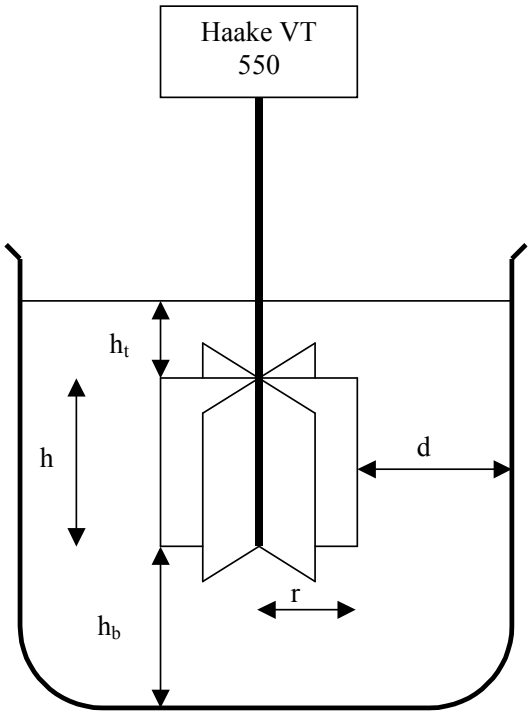


Figure 3.7: Schematic of instrumentation used for the vane technique.

The spring torque response was measured with the use of a torsion head, with the maximum observed torque (T_m) corresponds to the amount of yielding. Assuming that the

suspension yields instantaneously along the cylindrical surface inscribed by the vanes edges, τ_y is calculated with the following equation:

$$T_m = \frac{\pi d^3}{2}\left(\frac{h}{d} + \frac{1}{3}\right)\tau_y \qquad \textbf{Equation 3.3}$$

where d and h are the diameter of the vane and the height (m), respectively, and where T_m is the maximum torque (Nm) and τ_y is the yield stress (Pa). Figure 3.8 represents a generic plot generated by typical vane measurement showing torque as a function of time from which yield stress can be calculated according to Equation 3.3.

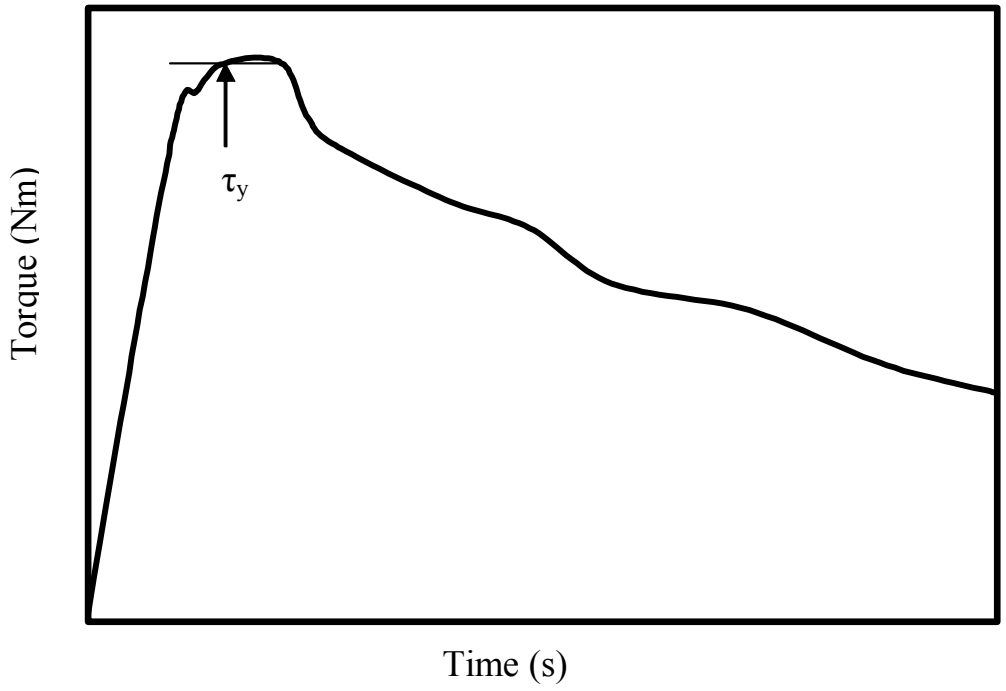


Figure 3.8: Generic plot generated by a typical vane measurement showing torque as a function of time from which yield stress can be calculated.

3.7 ATOMIC FORCE MICROSCOPY STUDIES

All AFM studies were carried out using a MFP-3D Instrument (Asylum Research, USA), utilising Igor Pro 5.04B Software. Iron oxide probe-mounted Silicon nitride rectangular cantilevers (Olympus RC800PSA) were used for both normal and lateral force measurements, due to their appropriateness to lateral force work.

3.7.1 Colloidal Probe Mounting

Cantilevers of dimension 200 μm × 20 μm with a manufacturer's spring constant of and 0.76 N/m was selected for colloidal probe mounting. Magnetite particles (as seen in Figure 3.2c) with a radius ~ 9 μm were chosen to be mounted. Particles were washed twice (via shaking a 20 dm^3 scintillation vial containing both particles and KOH for ~ 1 min) with 1 M KOH, followed by several washes in Milli-Q water until the supernatant was observed to be clear. The particles were then suspended in Milli-Q water and pipetted and dispersed onto a glass microscope slide. Particles of the appropriate size were selected visually under an Olympus BH2 Optical Microscope, and their size measured with the accompanying software.

The spheres were attached to a cantilever according to the method proposed by Ducker *et al*. [175]. A small hotplate was placed on the microscope stage and was used to heat a glass slide containing resin (Shell Epikote 1004), particles and a cantilever. Pre-sharpened tungsten wires were used to manipulate both the particles and the resin, and were themselves manipulated via the use of a three-way translation stage mounted to the side of the microscope stage. This method is described schematically in Figure 3.9. The tungsten wire was dipped into the molten resin and then touched to the cantilever such that a small amount of molten resin was left on the tip. The wire was then exchanged for another clean wire and then used to pick up an appropriate particle through capillary force. The particle was then touched to the molten resin on the cantilever, which remains attached when cooled to room temperature. It is essential to ensure that there is a small amount of resin on the cantilever, as too much can engulf the particle, which would lead to force measurements between a surface and the resin. The cantilever was then left over night (after the glass slide was removed from the hotplate).

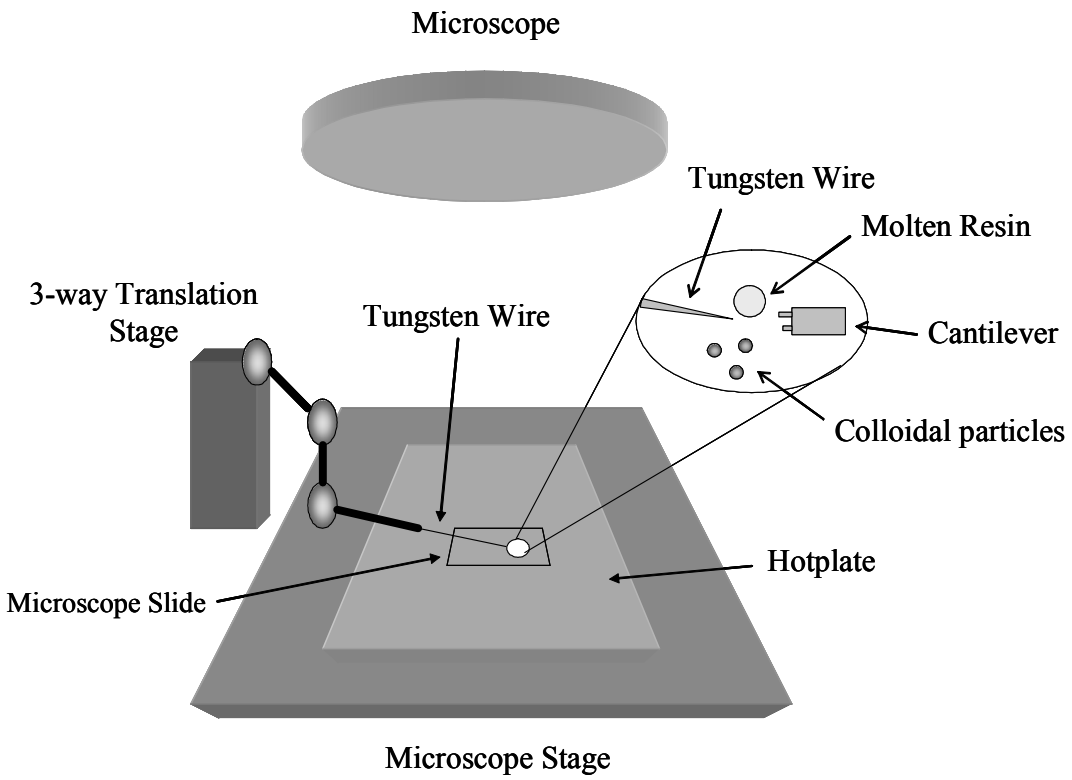


Figure 3.9: Schematic of colloidal probe mounting method.

3.7.2 Calibration of cantilevers

The flexural spring constants, k_Z, were determined via the thermal noise method incorporated into the AFM instrument, which consists of determining the vertical photodiode sensitivity (by measuring the slope of the constant compliance region of a force curve obtained against a hard surface), and measuring the fundamental resonant frequency of the cantilever (by taking a thermal scan and fitting the resonant peaks) [176].

The torsional spring constants, k_ϕ, were determined via a method proposed by Green *et al*. [177], and is given by:

$$k_\phi = 0.1592 \rho b^4 L Q_t \omega_t^2 \Gamma_i^t(\omega_t) \qquad \textbf{Equation 3.4}$$

where ρ is the density of the surrounding liquid (usually air), b the width of the cantilever, L the length of the cantilever, Q the quality factor of the resonance frequency of the

cantilever, ω the fundamental radiant resonant frequency. The subscripted t represents torsional. Γ_i is the imaginary part of the hydrodynamic function, and was determined by an analytical equation described elsewhere by the same authors [178]. F_f, the frictional force, is related to $k_ø$ as follows [123]:

$$F_f = \frac{k_\phi \Delta x_L}{H_P^2} \qquad \textbf{Equation 3.5}$$

where Δx_L is the lateral displacement of the probe, and H_P is the height of the probe (i.e., the diameter). The lateral displacement values were calculated in a similar manner to that of the flexural spring constant, using the lateral sensitivity of the photodiode detector taken from the constant slope region (S) of the lateral voltage hysteresis determined against a hard surface in air. The surfaces initially stick together (See Figure 3.10, points A-B), until the friction force is overcome. The trace occurs from A-C, and the retrace from C-A, with the frictional force again observed between C and D.

****This drawing has been removed. Please see referenced source for drawing.****

Figure 3.10: AFM friction loop; the photodiode response to cantilever twist, V, is plotted against the lateral piezo displacement (nm), taken from Cain *et al.* [179].

When a probe is mounted at a distance (ΔL) from the tip of the cantilever (determined visually under an Olympus BH2 Optical Microscope, with ΔL measured with the accompanying software), the resulting flexural spring constant, k_z, is given by the following expression [177]:

$$\frac{k_z}{k_z probe} = \left(\frac{L - \Delta L}{L}\right)^3$$ **Equation 3.6**

where L is the length of the cantilever. The corrected torsional spring constant after probe mounting is determined by [177]:

$$\frac{k_\phi}{k_\phi probe} = \left(\frac{L - \Delta L}{L}\right)$$ **Equation 3.7**

3.7.3 Sample preparation

Solutions of various pH values were made as per Section 3.2.3.3, as were polymer solutions. A small, polished, hematite plate (~ 13 mm^2), was glued to a glass Petri dish lid (100 mm diameter) with the same resin used in 3.7.1. The hematite wafer was removed and sonicated prior to each measurement, and washed with KOH and Milli-Q water before reattachment to the Petri dish lid which had also been sonicated. This sample-containing dish, along with the probe mounted cantilever were then plasma cleaned and submerged in Milli-Q water for 30 min to ensure re-hydration of the iron oxide surfaces.

After the samples had been loaded onto the instrument and the cantilever had been lowered such that the particle and the plate were within ~ 2 mm of each other, the cantilever holder was removed and the sample solution (Milli-q water containing the standard background electrolyte or polymer) was pipetted onto the hematite wafer. The cantilever holder was then lowered until a meniscus formed between the wafer and the cantilever holder, as shown schematically in Figure 3.11.

Solutions were then left for 30 mins to reach equilibrium before measurements were taken. Measurements were performed in the following order, in one experimental session.

1) Measurement of normal and lateral forces at pH 11 in 10^{-3} M KNO_3
2) Measurement of normal and lateral forces at pH 11 in 2 ppm polymer solution
3) Measurement of normal and lateral forces at pH 11 in 10 ppm polymer solution

4) Measurement of normal and lateral forces at pH 11 in 20 ppm polymer solution
5) Measurement of normal and lateral forces at pH 11 after removal of 20 ppm polymer solution and replacement with 10^{-3} M KNO_3 background electrolyte such that the polymer is still adsorbed on the iron oxide surfaces

This procedure was repeated at least 3 times to ensure reproducibility.

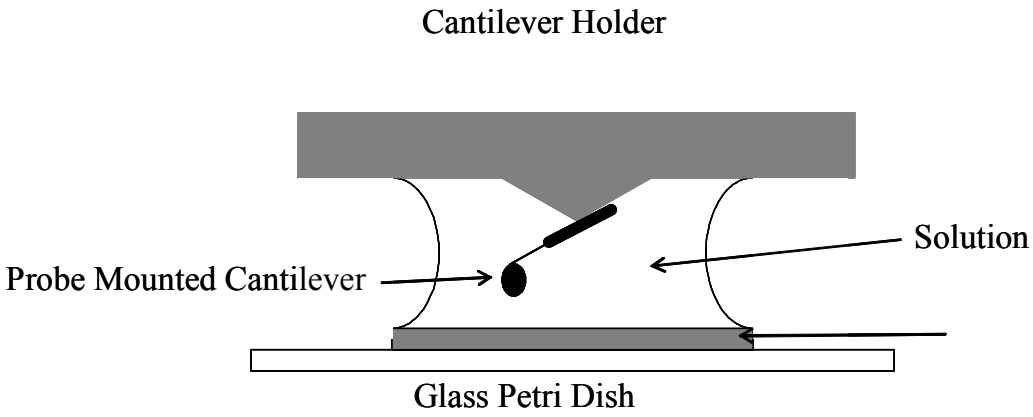


Figure 3.11: Schematic representation of the cantilever submerged in solution as per the experimental set up for AFM force measurements.

3.7.4 Force measurements

Normal force measurements were carried out in contact mode at an approach and retract speed of 1 μm/s. The raw data from the instrument is given in deflection, which was converted to force using Hooke's Law;

$$F = -k_Z x \qquad \textbf{Equation 3.8}$$

where x is the deflection.

Lateral force measurements were carried out in contact mode, by scanning the surface at an angle of 90^o, allowing measurement of the torsional distortion of the cantilever. Applied

load was fixed at 5 nN, a fixable parameter within the software provided. Lateral signals were obtained in open loop mode, for both the trace and retrace. ΔV was calculated as half of the voltage difference between the trace and retrace (Figure 3.10), which was converted first into lateral displacement, and then into frictional force, via Equation 3.5.

3.8 DEWATERING STUDIES

Settling tests were performed as follows. 500 g suspension of 8 wt% solid Fe_2O_3 was prepared with a 10^{-3} M KNO_3 background electrolyte and stirred via an overhead stirrer at 400 rpm for 20 min to ensure homogeneity. Following pH adjustment, the suspension was stirred via an overhead stirrer at 250 rpm for 60 s, with flocculant addition occurring in the first 5 s when required. The suspension was quickly poured into a 500 cm^3 measuring cylinder and inverted twice after which the settling rate was measured over a specific distance (5.6 cm) by timing the movement of the solid-liquid interface (mudline). After 24 h, the consolidated bed volume was measured. In the case of flocculant addition, the original suspension volume was reduced by an amount equal to the flocculant volume in order to keep the final suspension solid content at 8 wt% solid Fe_2O_3.

The shear yield stress was measured at this point as described in Section 3.6. The pulp was then sheared using a tall four bladed impeller, for 10 min at 100 rpm, and left for a further 24 h prior to the post-shear measurement of the shear yield stress as described in Section 3.6. The final pulp solid loading was measured with the Infrared Moisture Determination Balance (AND AD4715).

3.9 ERROR ANALYSIS

Throughout this body of work, most experimental measurements were reproduced at least three times to allow the variation in estimated data to be analysed. The experimental results reported in this study are given at a 95% confidence level [180]. The method used to assess the adequacy of a model fitted data is based on analysis of the residuals, e_i, which is expressed as:

$$e_i = Y - Y' \qquad \textbf{Equation 3.9}$$

where Y is the measured variable and Y' is predicted variable. The residual contains both components of the experimental error and the unknown model or lack of fit error. When the experimental error is known, the significance of the lack of fit error can be tested. In this study, the estimate of pure error was obtained from replicate data (as seen in Table 3.1). A lack of fit test of the model was carried out against the data using the following expression [180]:

$$f = \frac{\sum_{i=1}^{n}\left(S_i^{\,2} - vS_e^{\,2}\right)}{(n-p-v)S_e} \qquad \textbf{Equation 3.10}$$

where n is the number of fitted data points, p is the number of fitted parameters, v is the degree of the lack of fit error, S_i is the lack of fit standard error and S_e is the pure experimental standard error.

Table 3.3: Estimates of accuracy of measured quantities for experimental techniques.

Quantity	**Units**	**Estimated Error**
time	s, min, h	± 2.3×10^{-3} %
pH	-	± 0.2 units
Zeta potential	mV	± 2.5 units
Absorbance	-	± 0.05-3.0 %
Shear yield stress	Pa	± 5-10 %
Settling rate	m/h	± 1.0-5.0 %
Lateral force	N	± 20-25 %

CHAPTER 4 Spectroscopic investigation of the adsorption mechanisms for polyacrylamide polymers onto iron oxide particles*

4.1 SUMMARY

The mechanisms of high molecular weight polyacrylamide non-ionic homopolymer and 25 mole% anionic acrylate substituted copolymer adsorption onto iron oxide particles were investigated via DRIFT and UV-Vis spectroscopies at three pH values (6, 8.5 and 11). Whilst electrostatic interactions play an important role in the charged polymer adsorption, this information is not spectroscopically available. At pH values above and below pH 8.5 (the isoelectric point), bidentate chelation together with hydrogen bonding were the main adsorption mechanisms for the anionic polymer. At the iep, monodentate chelation was observed to be the main mechanism of adsorption along with hydrogen bonding. For the non-ionic polymer in all cases, hydrogen bonding through the carbonyl group was the main mechanism of adsorption observed. The adsorption of both polymers conformed well to the Freundlich model suggesting that the adsorbed polymer amount increases with increasing polymer concentration up to 7500 g/t solid, rather than approaching monolayer coverage. Spectroscopic evidence was found to suggest that hydrolysis of non-ionic polyacrylamide occurs at high pH.

* Published in Journal of Colloid and Interface Science (2006), 299, 547-555.

4.2 INTRODUCTION

The use of polyacrylamides in water treatment and minerals processing industries as flocculants [6, 8, 16-18, 32], depressants [19-21] and dispersants [7] has rapidly increased in recent years. Efficient use requires a thorough understanding and identification of the adsorption mechanisms of such polymers with differing functionality and molecular structures. In flocculation and dewatering applications, the efficacy of a given high molecular weight polymer is dependent upon its chemical structure characteristics (e.g. functional groups), water speciation and the mineral pulp chemistry. Understanding the polymeric flocculant adsorption behaviour and subsequent flocculation will enable the dewatering process to be optimised. The potential bonding mechanisms are dependent on the polymer functional group, molecular weight and charge density. Whilst electrostatic interactions can be determined through knowledge of the zeta potential of the particle and the polymer, hydrogen bonding and chemical bonding can be probed via infrared spectroscopy.

The aim of this work was to gain a thorough and precise understanding of the adsorption mechanisms and behaviour of two high molecular weight polymeric flocculants (7.5-9 $\times$ 10^6 Da), anionic polyacrylamide (PAM A) and non-ionic polyacrylamide (PAM N) onto iron oxide through characterisation studies using UV-vis and infrared spectroscopies. From this basis it will be possible to determine if the bonding mechanisms of PAM A and PAM N impact their performance as flocculants.

The studies were conducted at three pH values; pH 8.5 (the iep of the iron oxide), pH 6 and pH 11, where the charge on the particles are approximately 0 mV, +40 mV and -40 mV, respectively. These pH values are within mineral processing plant tailings thickener operating range.

4.3 RESULTS AND DISCUSSION

4.3.1 Adsorption Isotherms and Surface Chemistry

Figure 4.1 shows the zeta potential of the iron oxide particles (at 8 wt %) used in this study as a function of pH in 10^{-3} KNO_3. The particle zeta potential is high and positive (+115 mV) at low pH and decreases in magnitude as the pH is increased. At high pH, the zeta potential is –70 mV. This data shows the iron oxide sample to have an isoelectric point (iep) of ~8.7, consistent with reported iron oxide iep's in the range of pH 5-9 [54]. At low pH (below the iep), the mineral particle surface is protonated (as seen in Figure 4.2), giving rise to the positive zeta potential. Similarly, at high pH (above the iep), the mineral particle surface is deprotonated. At the iep, the surface is neutral (Figure 4.2). The zeta potential is approximately +40 mV, 0 mV (iep) and –40 mV, at pH values 6, 8.5 and 11, respectively, which are the three operating pH values for this study.

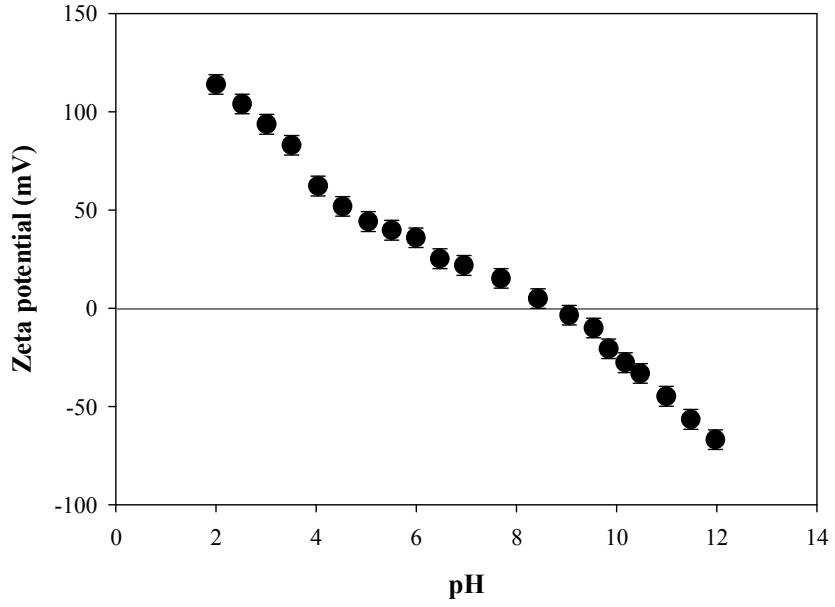


Figure 4.1: Electrokinetic zeta potential of Fe_2O_3 in 10^{-3} KNO_3 at 8 wt% solids as a function of pH.

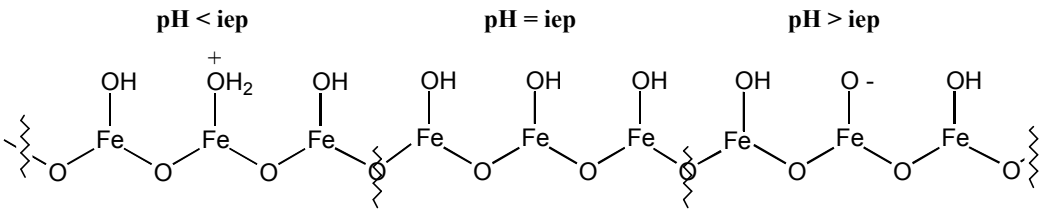


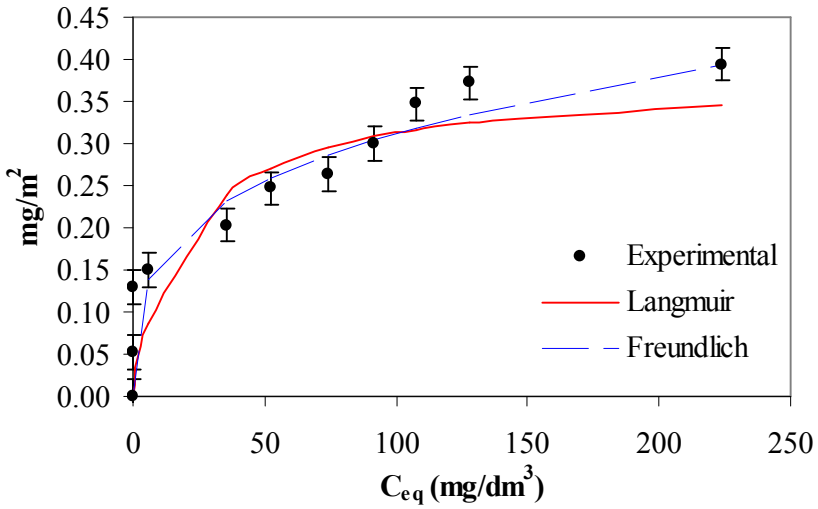
Figure 4.2: Mineral surface groups as a function of pH.

Figure 4.3 shows the adsorption isotherms of PAM A adsorption onto iron oxide particles at three pH values, 6, 8.5 and 11. The adsorption for PAM A at pH 6 (Figure 4.3a) is slightly greater than at the iep (Figure 4.3b), and is also three times greater than the adsorption at pH 11 (Figure 4.3c). Electrostatic interactions between the anionically charged polymer and iron oxide particles partially explain the adsorption trends. Electrostatic attraction will occur at pH 6, which is below the particle iep, and repulsion between the polymer and particle will occur at pH 11, where they both carry a negative charge.

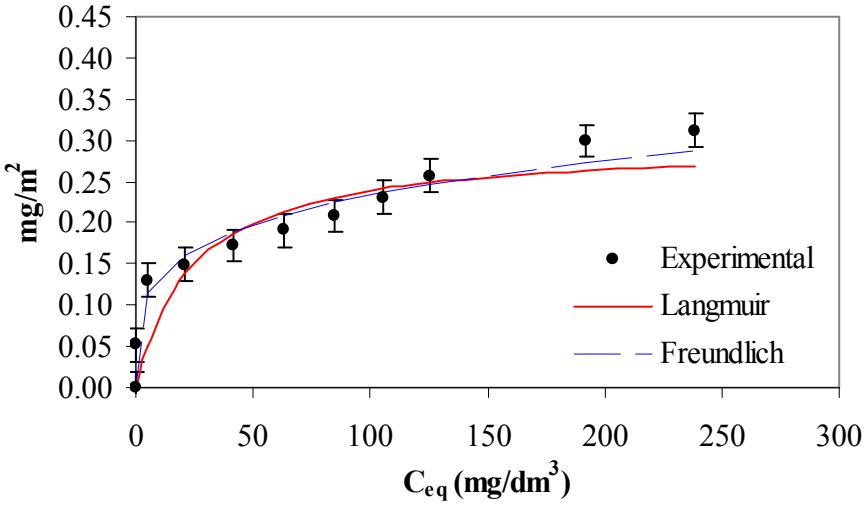
Adsorption isotherms for the non-ionic polymer PAM N (Figure 4.4) indicate that the adsorption values are more than double those observed for PAM A. It appears that due to the absence of electrostatic interactions, PAM N enabled more polymer molecules to adsorb onto the particles' surface, suggesting that it has a more contracted interfacial conformation than PAM A. This follows logic as PAM A would be expected to have a more expanded conformation due to intramolecular repulsion forces caused by the charge on the polymer. Bal [147] measured the viscosity of PAM A and PAM N to be 7.62 and 2.28 Pa·s, respectively, supporting this hypothesis.

The possibility that PAM N may aggregate and contribute to increased adsorption when compared to PAM A may not be completely discounted. Such polymer chain interactions could be facilitated by a high concentration of PAM N molecules in solution and the fact that they are practically uncharged and will therefore not experience any repulsive electrostatic interactions upon approach. On the other hand, however, the tendency for self-avoidance in a good solvent situation will be expected to counteract any significant aggregation propensity. Without measurement of polymer hydrodynamic radius in solution at various pH and polymer concentration it is difficult to tell if aggregates such as dimers are forming.

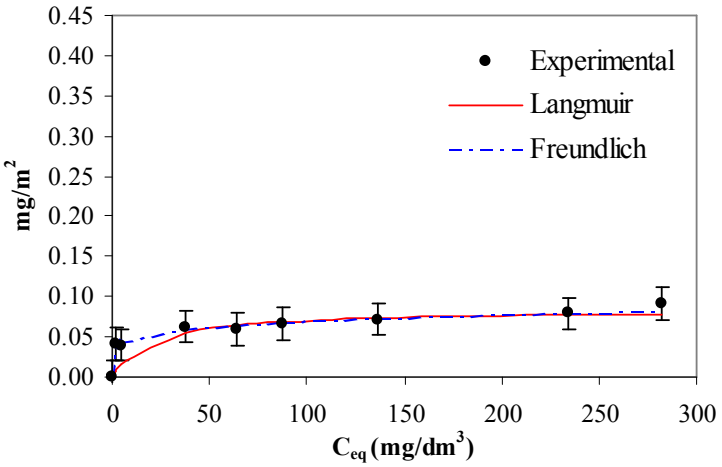
Adsorption is highest for the system at pH 8.5 (iep), where the particles have a neutral charge. It is also apparent that, as in the case of PAM A, the adsorption plateau densities for systems prepared at pH 6 and pH 8.5 are considerably greater than for pH 11. For PAM A, poorer adsorption at high pH can be attributed to electrostatic repulsion between the negatively charged particle surface and the negatively charged polymer carboxylate (COO^-) groups. Kirwan *et al*. [37] reported that at high pH (~13), anionic polyacrylate would not adsorb unless there was an excess of cations present in solution, suggesting that the electrostatic repulsion was too high to allow adsorption. However, it has also been suggested that PAM N hydrolyses at high pH, which would lead to an increased anionicity and hence electrostatic repulsion with the negatively charged surface, hindering adsorption at high pH in the manner of PAM A [181]. Further discussion of the hydrolysis of PAM N will occur later in this chapter.



a)

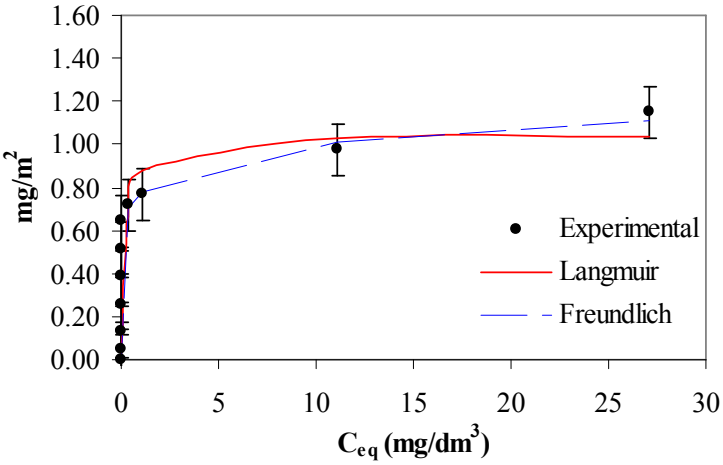


b)

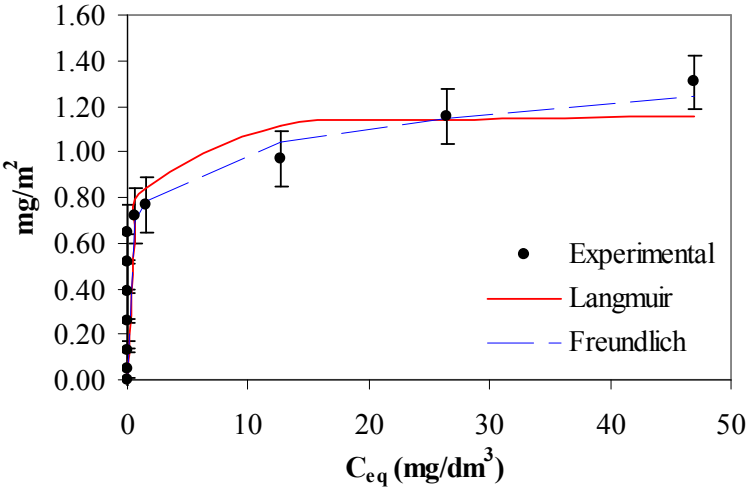


c)

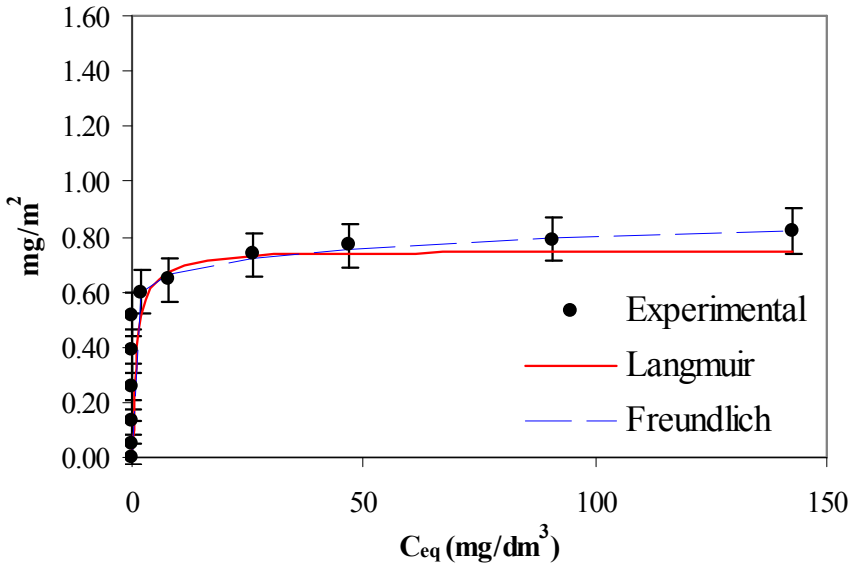
Figure 4.3: Adsorption isotherms fitted with Langmuir and Freundlich models for the adsorption of PAM A onto iron oxide at a) pH 6, b) pH 8.5 and c) pH 11.



a)



b)

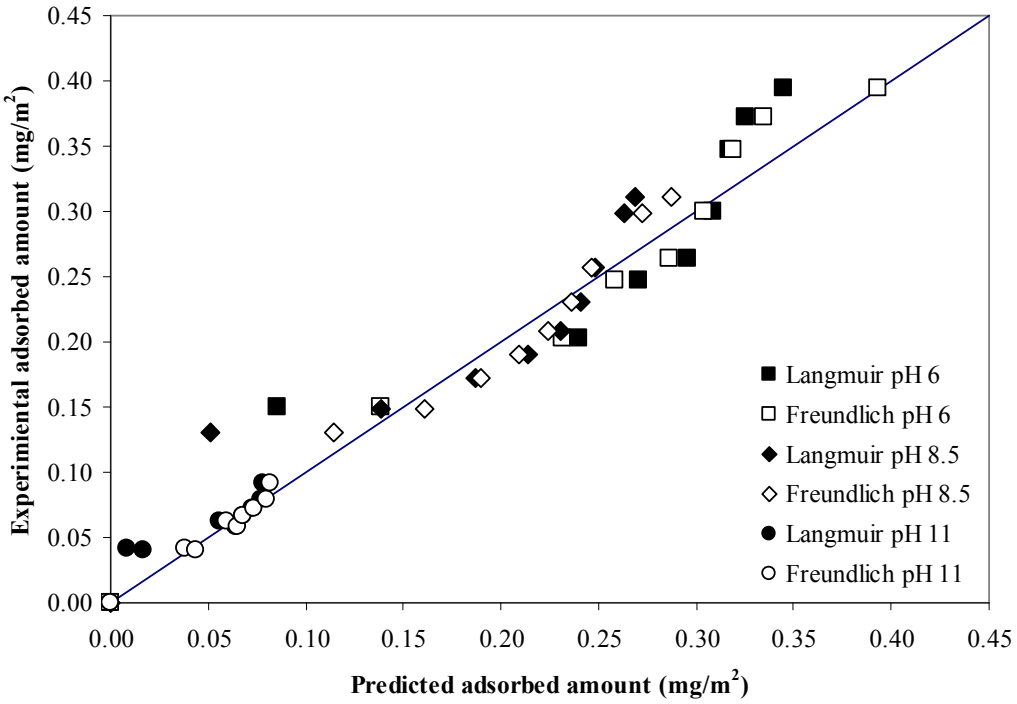


c)

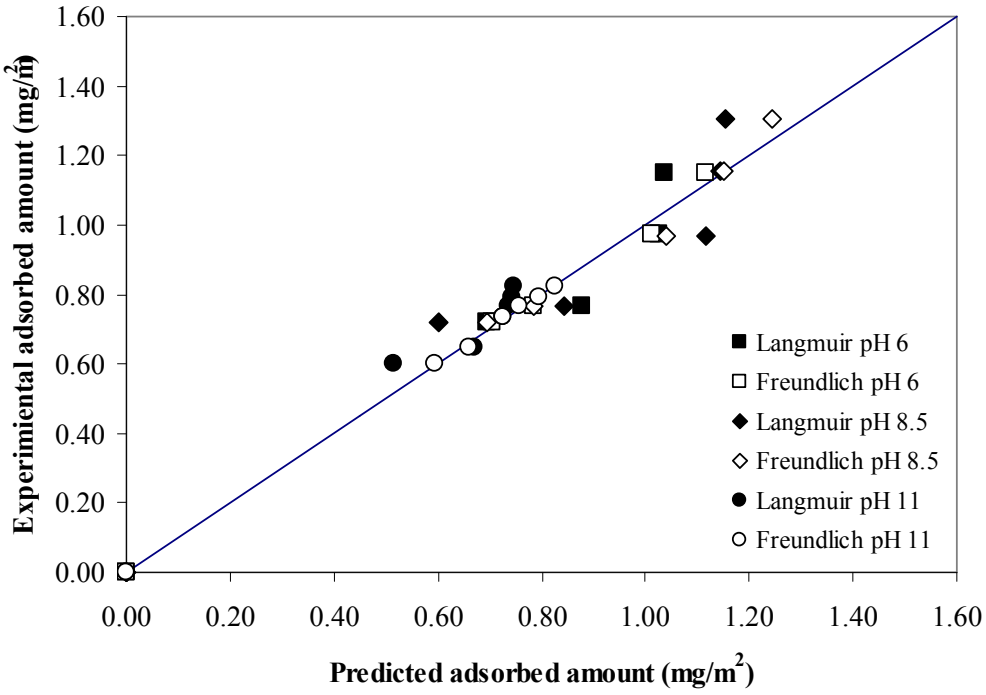
Figure 4.4: Adsorption isotherms fitted with Langmuir and Freundlich models for the adsorption of PAM N onto iron oxide at a) pH 6, b) pH 8.5 and c) pH 11.

To elucidate adsorption mechanisms, the adsorption isotherms were fitted to the Langmuir and Freundlich models for polymer adsorption at the solid-liquid interface [90, 167, 168], which are described in Equations 2.22 and 2.24, respectively.

The adsorption plateau densities for PAM A found via the Langmuir model at pH 6, 8.5 and 11 were 0.38, 0.30 and 0.08 mg/m^2 respectively, whilst for PAM N, the values were 1.04, 1.17 and 0.75 mg/m^2, respectively. The Freundlich model was generally observed to be more accurate in fitting the isotherms, as indicated by Figure 4.5, in which the experimental data are plotted against the values predicted by each model. The better fit of the present high molecular weight polymer adsorption by the Freundlich than Langmuir model was confirmed by minimum variance criterion analysis of the residuals given by the difference between the observed and predicted adsorption densities [180].



a)



b)

Figure 4.5: Comparison between the experimental adsorption densities and those predicted by the Langmuir and Freundlich models.

The Freundlich parameters for both PAM A and PAM N are summarised in . The adsorption affinity constant is the reciprocal of the actual adsorption affinity, that is, the natural attraction between the adsorbate (polymer) and the adsorbent (surface). Therefore, the higher the adsorption affinity constant value, the lower the affinity between the polymer and the surface. The adsorbent capacity constant is the calculated amount of polymer that can be received by the surface.

The adsorption affinity constants correlate well with the adsorption data. PAM N has roughly double the affinity for the iron oxide surface, which is reflected in the adsorbent capacity values and in the adsorbed amounts shown in Figure 4.3 and Figure 4.4, however both polymers have a higher affinity for the surface at pH 11 which is not reflected in either. In the case of PAM A, this may be attributed to electrostatic repulsion hindering the adsorbed amount. Also, due to its more expanded conformation, it is expected that steric hindrance would also play a role. In the case of PAM N, it may be that higher affinity and faster adsorption leads to a flatter conformation on the surface, which could result in more trains forming on the surface [148].

Table 4.1: Freundlich model isotherm parameters summarised for (a) PAM A and (b) PAM N adsorption onto iron oxide.

(a)

pH	Adsorption affinity constant ($1/n_F$)	k_F (dm^3/g_{solid})
6	0.29	0.40
8.5	0.24	0.38
11	0.16	0.16

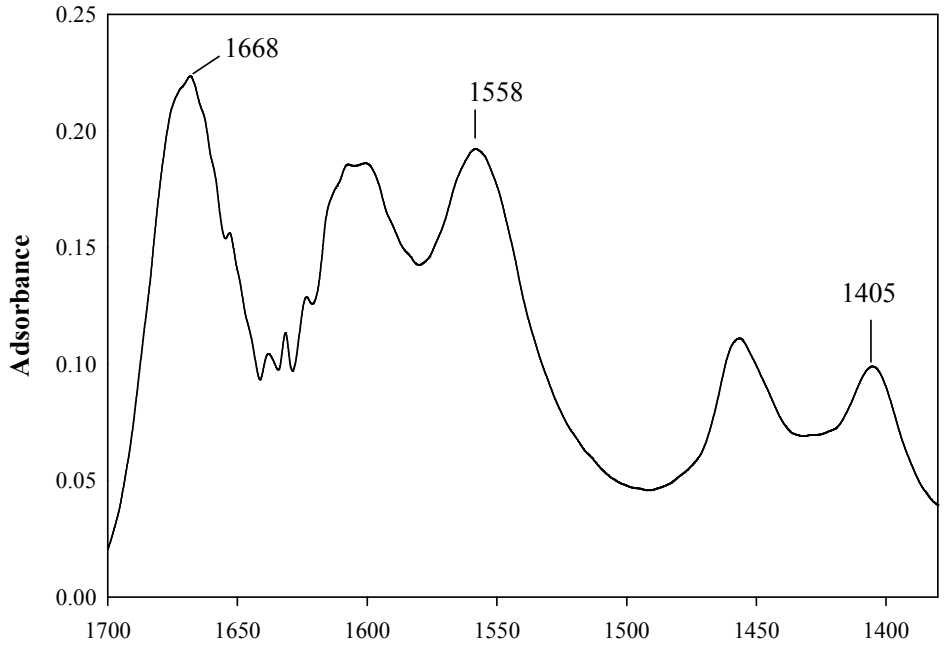
(b)

pH	Adsorption affinity constant ($1/n_F$)	k_F (dm^3/g_{solid})
6	0.11	3.77
8.5	0.14	3.56
11	0.08	2.73

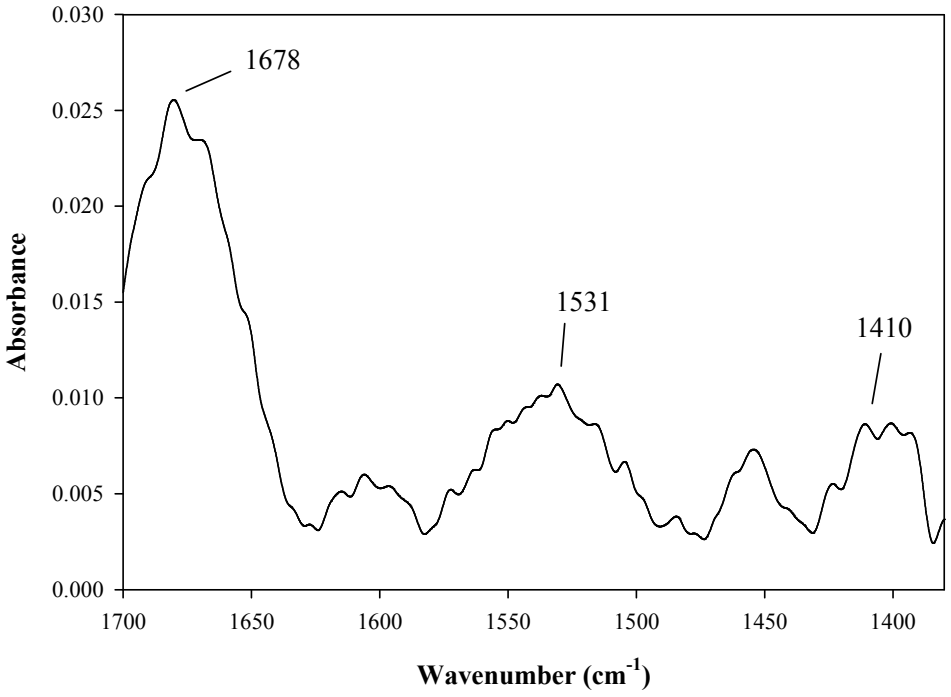
When applying these models, it should be recognised that there are underlying assumptions made that may not be entirely valid in the present systems. The Langmuir isotherm is based on a gas-solid interface which assumes that adsorption to monolayer coverage is reversible and takes place in dynamic equilibrium on a homogenous surface [47, 167, 169], whereas the Freundlich isotherm assumes that Langmuirian adsorption takes place on a heterogeneous surface and that adsorption does not approach monolayer coverage, instead that it increases with the amount of polymer added [168, 169]. As the Freundlich model more closely fits the adsorption isotherms shown in Figure 4.3 and Figure 4.4, it is postulated that the different species present on the iron oxide particle surface (the protonated and deprotonated hydroxyl groups) give rise to a heterogeneous surface that has continued, irreversible, multi-segmented polymer adsorption as the polymer concentration is increased, as seen previously in the literature [20].

4.3.2 Infrared Spectroscopy

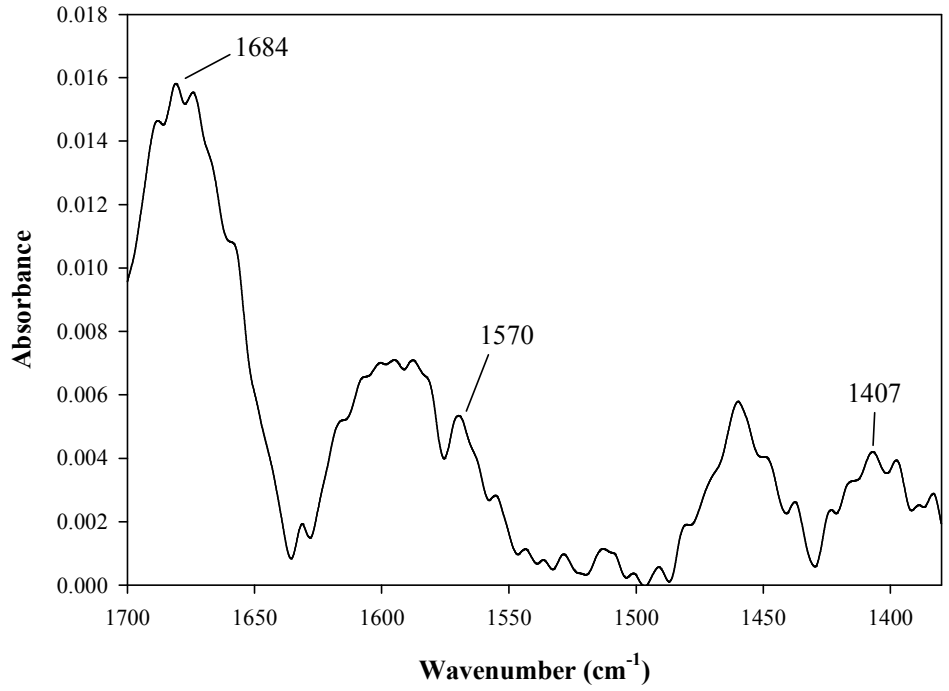
The infrared spectra of PAM A (a) unadsorbed; (b) adsorbed to iron oxide at pH 6; (c) adsorbed to iron oxide at pH 8.5; and (d) adsorbed to iron oxide at pH 11 are depicted in Figure 4.6. As expected, there is a peak resulting from the carbonyl stretching vibration (which is in all cases present due to the primary amide group) ranging from 1668 – 1684 cm^{-1}. The NH_2 bending vibration occurs in all cases between 1600 and 1609 cm^{-1}, with the CH_2 bending occurring predictably between 1452 and 1463 cm^{-1}. All of the relevant peaks are summarised in Table 4.2.


0.25
0.20
0.15
0.10
0.05
0.00
Adsorbance
1668
1558
1405
1700
1650
1600
1550
1500
1450
1400
Wavenumbers (cm-1)

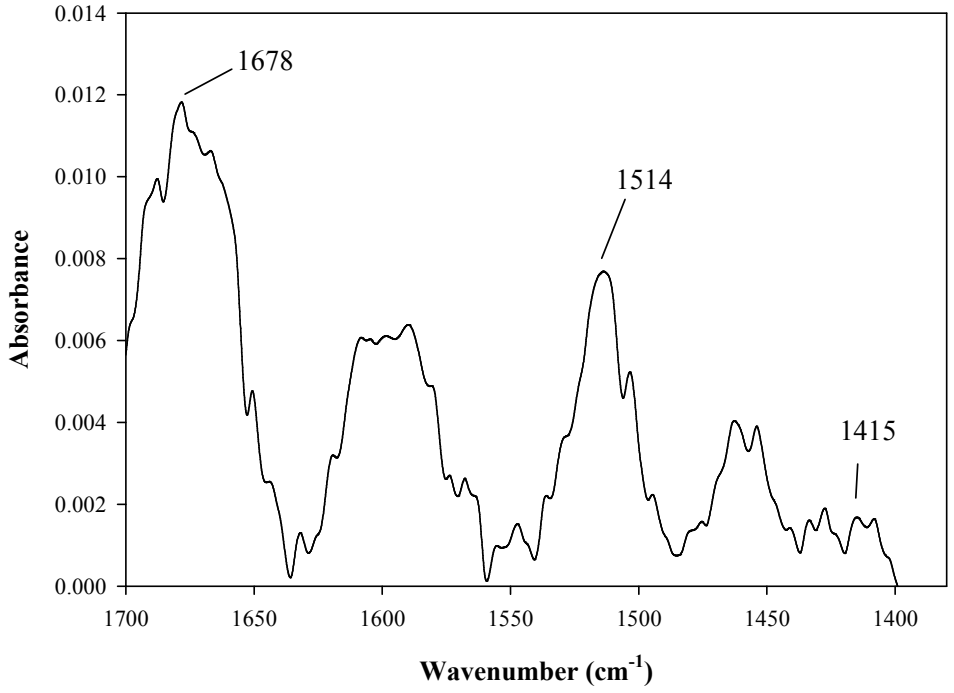
a)


0.030
0.025
0.020
0.015
0.010
0.005
0.000
Absorbance
1678
1531
1410
1700
1650
1600
1550
1500
1450
1400
Wavenumber (cm-1)

b)



c)



d)

Figure 4.6: The infrared spectra of PAM A; a) unadsorbed; b) adsorbed to iron oxide at pH 6; c) adsorbed to iron oxide at pH 8.5; and d) adsorbed to iron oxide at pH 11.

Table 4.2: The major infrared species vibrations summarised for PAM A adsorption onto iron oxide particles.

	C=O	$COO^-_{(asym)}$	$COO^-_{(sym)}$	$\Delta\nu$
PAM A	1668 ±2	1558 ±2	1405 ±2	153 ±4
pH 6	1678 ±2	1531 ±2	1410 ±2	121 ±4
pH 8.5	1684 ±2	1570 ±2	1407 ±2	163 ±4
pH 11	1678 ±2	1514 ±2	1415 ±2	99 ±4

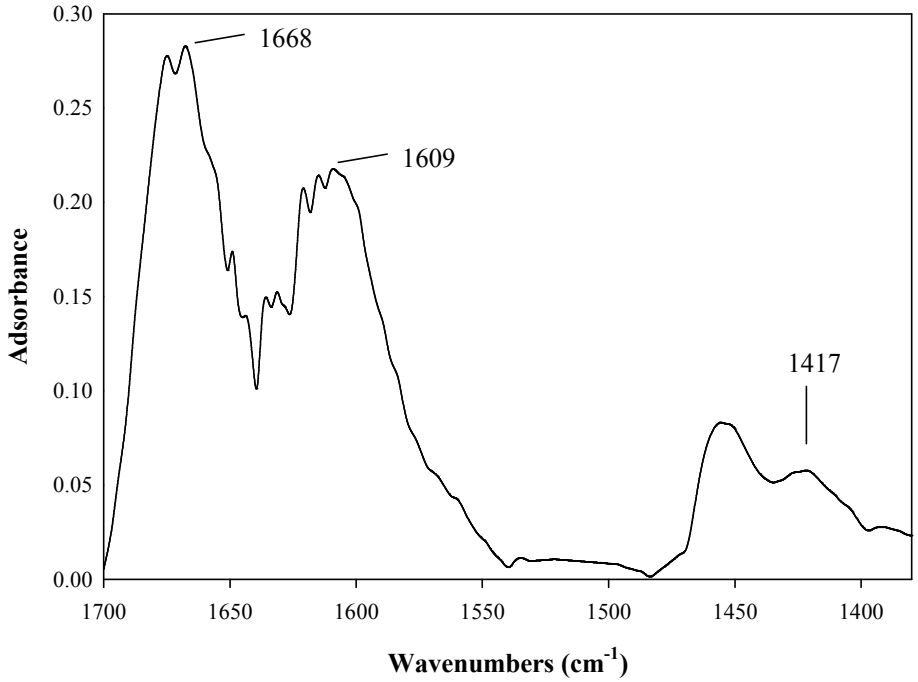
It has been previously noted in the literature that it is possible to discriminate between different bonding mechanisms of a polymer to a metal oxide surface by measuring the distance between the asymmetric and symmetric $-COO^-$ frequencies (Δv) found in the spectra for carboxylate groups [35, 36]. When there is a distinct -C=O vibration at around 1650 cm^{-1}, and Δv of the adsorbed polymer is greater than Δv of the unadsorbed polymer, the monodentate structure is found to occur (Figure 2.17a). When the difference between the two $-COO^-$ stretches is found to be smaller for that of the adsorbed polymer compared to the unadsorbed, and there is a lack of the -C=O stretch, the adsorption mechanism is via bidentate chelation (Figure 2.17b). If there is a lack of the -C=O stretch and the difference between the two $-COO^-$ stretches is found to be similar for both the adsorbed and unadsorbed polymer, then the adsorbed structure is said to be bidentate bridging (Figure 2.17c). In the case of polyacrylamide, it is expected that the carbonyl peak will still be present at around 1650 cm^{-1} due to the amide group, which will make it more difficult to assign a monodentate structure. The vibration due to the carbonyl group of the amide interferes with the detection of a carbonyl peak due to the carboxyl group. The other criterion for monodentate bridging is that $\Delta v_{(ads)}$ is greater than $\Delta v_{(unads)}$.

When PAM A is adsorbed onto the iron oxide particles at pH 8.5, $\Delta v_{(ads)}$ is greater than $\Delta v_{(unads)}$ ($\Delta v_{(ads)}$ is 163 ±4, $\Delta v_{(unads)}$ is 153 ±4), indicating that monodentate chelation is the mechanism of chemisorption. This has been observed in previous work by Jones *et al.* [35] at pH 7 where polyacrylic acid was used instead of PAM A. In the case of PAM A adsorption at pH 6, $\Delta v_{(ads)}$ is smaller than $\Delta v_{(unads)}$, suggesting bidentate chelation to be the mechanism of chemisorption. This is in agreement with work by Kirwan *et al.* [36] that shows polyacrylate adsorption onto hematite at low pH to occur via the same mechanism. For pH 11, $\Delta v_{(ads)}$ is much smaller than $\Delta v_{(unads)}$, suggesting again that bidentate chelation

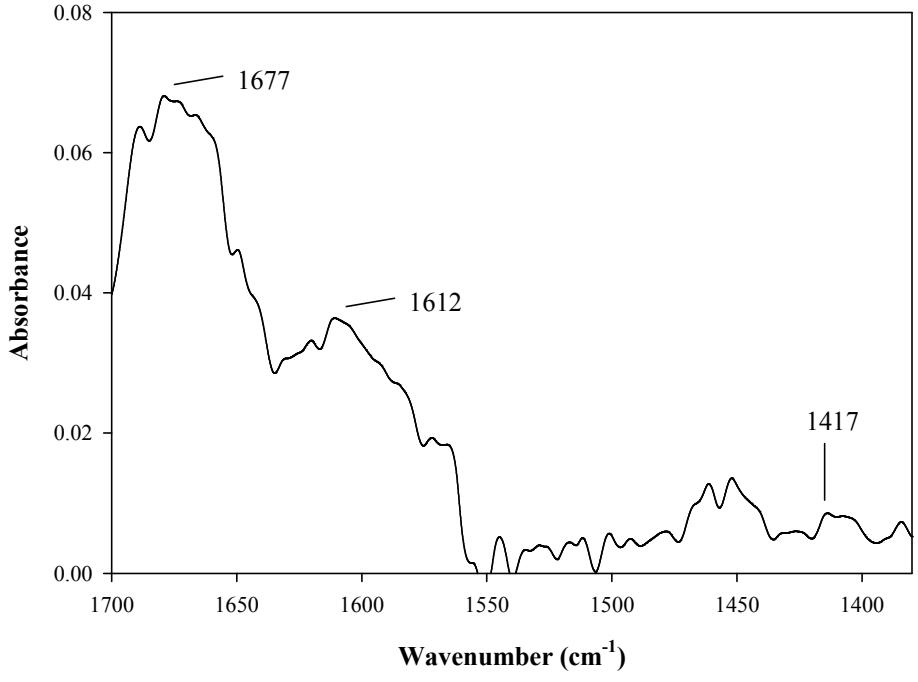
is the main adsorption mechanism via the carboxylate group. Jones *et al*. [35] found an asymmetric bidentate bridging structure at high pH, whereas a bidentate chelating structure was found in this study. The variance in adsorption mechanisms observed for these two studies may originate in the differences between the two polymers (PAM A is a 25% substituted co-polymer and pure polyacrylic acid homopolymer is used in the other study) and the differences in the particle surface (the zeta potential is unknown for the high pH sample in the other study) are responsible.

Also of note is that in all cases the carbonyl peak shifts, indicating its role in hydrogen bonding, as has been shown many times in the literature [15, 35, 51, 101, 103, 104, 182]. The carbonyl peak shifts more at pH 8.5, suggesting that there is more hydrogen bonding occurring at the iep than at the other two pH values, most likely as a result of the protonated and deprotonated sites in the charged systems taking part in the chemical bonding over the weaker hydrogen bonding. It is also evident that the asymmetric COO^- signal is shifted significantly either side of the iep (for pH 6 and 11), showing that it too plays a role in hydrogen bonding [183].

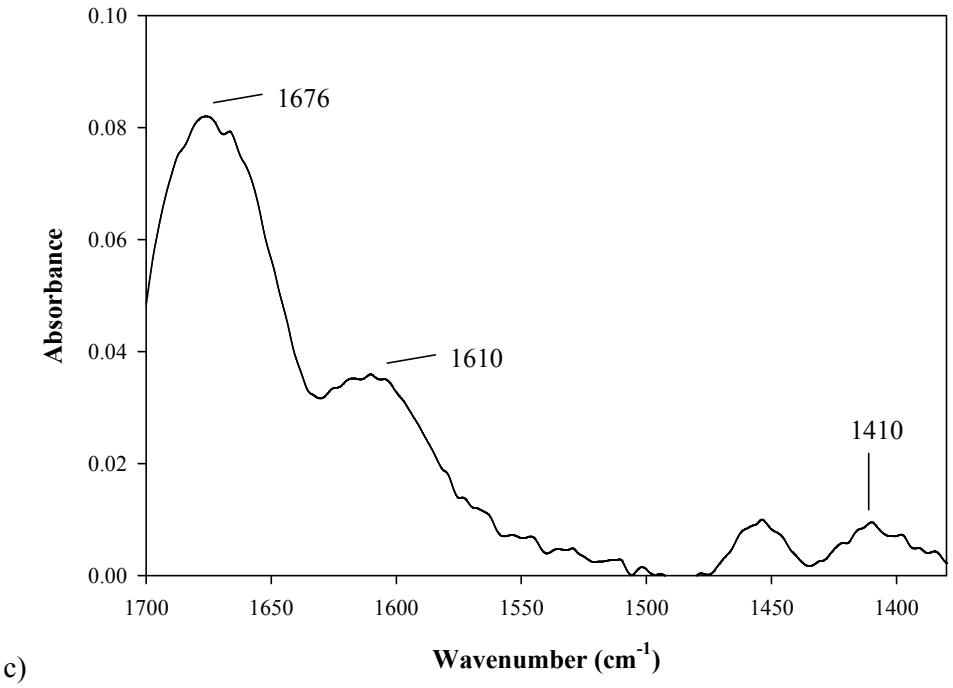
Infrared spectra of PAM N adsorbed onto iron oxide particles at three pH values are illustrated in Figure 4.7. The main peaks and their positions are summarised in Table 4.3. The carbonyl peak of the primary amide group shifts 9, 8 and 12 cm^{-1} for pH values 6, 8.5 and 11, respectively. It is clear, due to the peak shifts that hydrogen bonding is again occurring in conjunction with the carbonyl peak on the primary amide group, and the hydroxyl groups present on the surface of the iron oxide particles. This interaction is consistent, regardless of pH. Similar bonding has been found to occur in the literature for polyacrylamide polymers onto kaolinite and titania pigment particles [6, 103].


0.30
0.25
0.20
0.15
0.10
0.05
0.00
Adsorbance
1668
1609
1417
1700
1650
1600
1550
1500
1450
1400
Wavenumbers (cm-1)

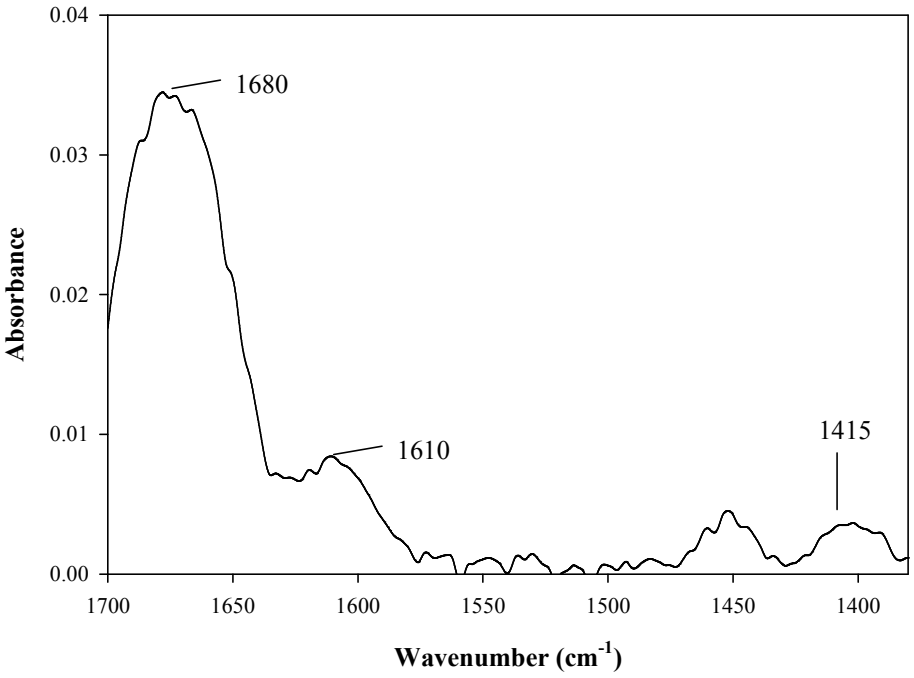
a)


0.08
0.06
0.04
0.02
0.00
Absorbance
1677
1612
1417
1700
1650
1600
1550
1500
1450
1400
Wavenumber (cm-1)

b)



c)



d)

Figure 4.7: The infrared spectra of PAM N a) unadsorbed, b) adsorbed to iron oxide at pH 6, c) adsorbed to iron oxide at pH 8.5, and d) adsorbed to iron oxide at pH 11.

Table 4.3: The major infrared species vibrations summarised for PAM N adsorption onto iron oxide particles.

	C=O	NH_2	CN
PAM N	1668 ±2	1609 ±2	1417 ±2
pH 6	1677 ±2	1612 ±2	1417 ±2
pH 8.5	1676 ±2	1610 ±2	1410 ±2
pH 11	1680 ±2	1610 ±2	1415 ±2

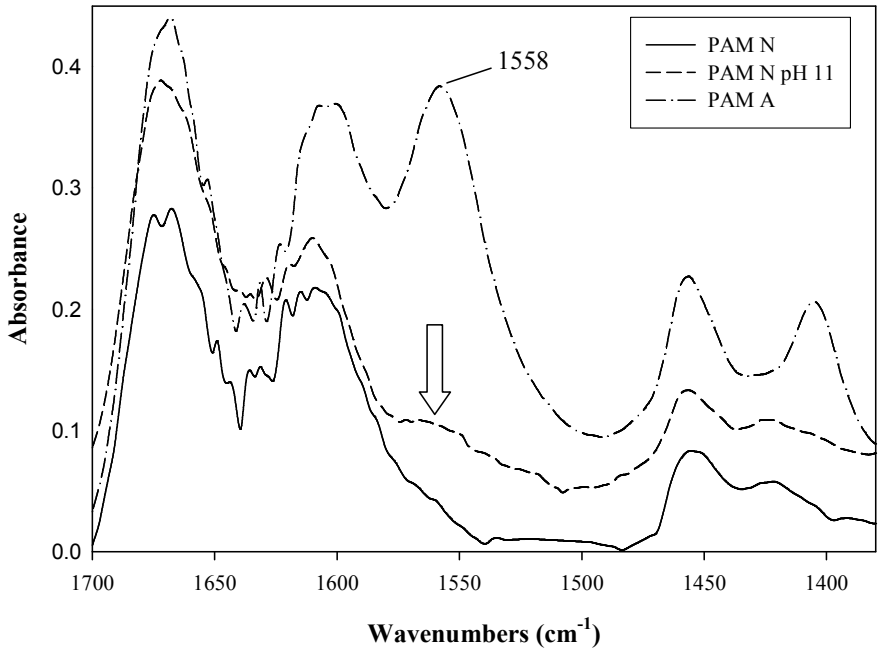


Figure 4.8: The infrared spectra comparing of PAM N at high pH in comparison with PAM A and PAM N at natural pH.

Whilst references to the hydrolysis of PAM occurring at high pH have been made by several authors [51, 181], it has not yet been shown spectroscopically. is a representation of the spectra for PAM A and PAM N at their pristine pH, along with PAM N prepared at pH 11. If the hydrolysis of PAM N has occurred, it is expected that a peak would appear in the region where the asymmetric COO^- stretch appears in the PAM A spectrum, due to the conversion of primary amide groups to carboxylate groups. A shoulder peak is observed at

1558 cm^{-1} (arrowed,) where one is lacking in the PAM N spectrum recorded at the lower, pristine pH, indicating that a small amount of hydrolysis has occurred. This supports the hypothesis that PAM N is capable of behaving in a similar way to PAM A at high pH if significant hydrolysis of the primary amide groups occurs. It is suspected that the amount of hydrolysis is low (~ 5%), making it impossible to detect via DRIFT when the polymer is adsorbed onto the iron oxide particles at pH 11. This concurs with the adsorption isotherms for PAM N, where it would be expected that a non-ionic polymer would adsorb equally at each pH. Instead, for pH 11, there is a lower adsorbed amount (Figure 4.4) suggesting that electrostatic repulsion is occurring between the partially hydrolysed polymer and the negatively charged surface.

4.4 CONCLUSION

Adsorption isotherms and mechanisms for two, high molecular weight polyacrylamides (one anionic and one non-ionic) onto iron oxide particles were investigated at 3 pH values. Adsorption isotherms showed that for both polymers, adsorption was most facilitated at and below the iep. In all cases, the Freundlich model for adsorption gave the best fit, indicating that the adsorption of the polymer increases with an increase in polymer concentration, rather than approaching monolayer coverage. PAM N was found to have a higher adsorbed amount, in general, which is due to the more contracted interfacial conformation expected from the non-ionic polymer. PAM A and PAM N both had lower adsorbed amounts at high pH.

For anionic PAM A, at the two pH values on either side of the particle iep (pH 8.5), the main chemisorption mode was bidentate chelation between the carboxyl group of the polymer and a hydroxyl group on the oxide particle surface. At the iep, the mode of chemisorption was found to be monodentate chelation through the polymers carboxyl group and a hydroxyl group on the mineral surface. Hydrogen bonding through the carbonyl group on the polymer was also found to be present at all pH values, whilst the asymmetric COO^- was only found to hydrogen bond either side of the iep. For PAM N, it was observed that for all pH values, hydrogen bonding through the carbonyl group on the polymer with the mineral surface hydroxyls was again present, and was the only adsorption mechanism that could be determined via these methods. Spectroscopic evidence was also found in support of the hydrolysis of non-ionic PAM at high pH.

CHAPTER 5 The effect of polymer structure type, pH and shear on the interfacial chemistry, rheology and dewaterability of model iron oxide dispersions*

5.1 SUMMARY

The effect of high molecular weight (7.5-9 x 10^6 Da) polyacrylamide flocculant structure type (anionic polyacrylamide, PAM A and non-ionic polyacrylamide, PAM N) on the interfacial chemistry, rheology and dewaterability of a colloidal iron oxide dispersion has been investigated at three pH values where the particles are at the isoelectric point (iep) and either side of the iep. PAM A was found to adsorb with a lower affinity than PAM N at all pH values tested, however, PAM A had a more significant effect on the particle zeta potential and the shear yield stress. Highest settling rates (100 m/h) were achieved with PAM A at pH values at and below the iep, with flocculant dosage below 100 g polymer/t solid. Settling rates with PAM N at similar concentrations, however, were between 5-10 m/h. Pulp pH and the addition of the flocculants (up to 500 g polymer/t solid) had no noticeable effect on the extent of the pulp consolidation. Significantly, shear of pre-sedimented dispersions was found to increase the consolidation by up to 15 wt%. Polymer structure type was found to have a significant effect on the rheology of the dispersion, with PAM A-flocculated dispersions leading to a higher yield stress than dewatering with PAM N.

---

* Published in Colloids and Surfaces A (2006), 275, 153-160.

5.2 INTRODUCTION

Different aspects of the flocculation of mineral dispersions using high molecular weight polymers have been investigated in the literature [9, 10, 13, 18, 23, 27, 34, 138, 139, 157, 172, 182, 184-190]. Chibowski and Wiśniewska [34] found flocculant structure type and pH to have a large impact on interfacial chemistry and particle interactions with the adsorption of polyacrylamide and polyacrylic acid onto hematite. The adsorbed polymer layer was observed to grow thicker with an increase in pH. Radeva and Petkanchin [10] discovered that at low polymer concentrations, polyethylenimine unfolded when the hematite was of opposite charge to the polymer (at pH 6 and 9.8), and that most of the polymer functional groups were in contact with the surface. This would be unfavourable for dewatering as a flat interfacial conformation would be detrimental to bridging flocculation. Ferretti *et al*. [13] found that a large, rigid polysaccharide (schizophyllan) was useful for hematite dewatering, as the small hematite particles adsorbed to the schizophyllan aggregates with high affinity. Addai-Mensah and Ralston [12] and Hulston *et al*. [18] reported settling rates of less than 10 m/h for pulps flocculated with anionic polyacrylamide.

The specific effects of the flocculation of colloidal iron oxide dispersions with conventional, high molecular weight polyacrylamides of different structures/functionality are yet to be investigated sufficiently. A comprehensive understanding of the influence of polymer structure type, pH and shear on the interfacial chemistry, rheology and dewaterability of model iron oxide dispersions is required in order to optimise the dewatering process.

The aim of this work is to investigate the effect of flocculant structure type and pH on the interfacial chemistry and particle interactions of iron oxide dispersions with the key objective of enhancing pulp dewaterability. More specifically, the effect of pH and polyacrylamide structure type (anionic vs. non-ionic) and concentration on particle zeta potential, shear yield stress and dewatering behaviour of iron oxide, and also the influence of shear on the consolidation of iron oxide particles. These investigations were conducted at 20 ^{o}C, and three pH values; the iep (pH 8.5), pH 6 and pH 11 where the zeta potentials of the particles are approximately +40 mV and -40 mV, respectively. These pH values are within mineral processing plant operating parameters.

5.3 RESULTS AND DISCUSSION

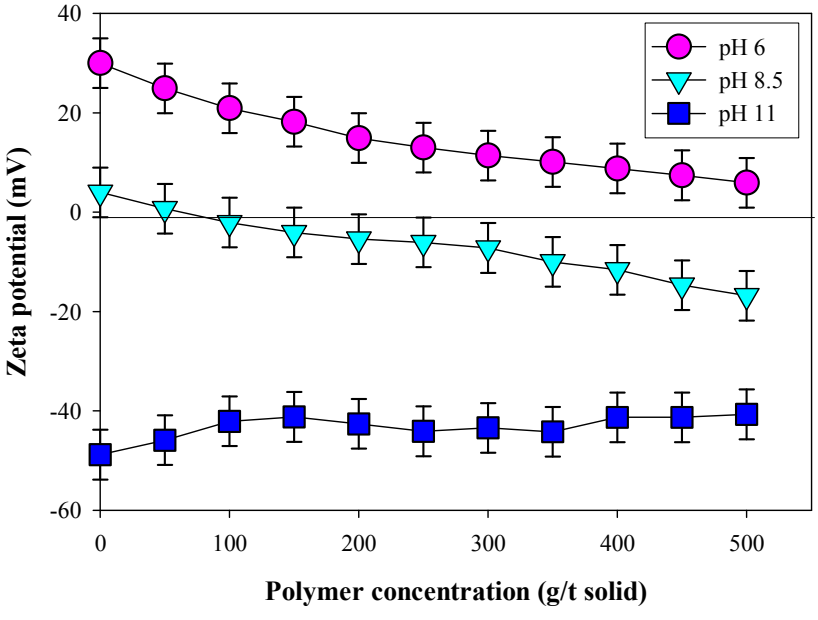
5.3.1 Polymeric structure and pH: effect on surface chemistry

Zeta potential of iron oxide particles following the addition of up to 500 g polymer/t solid of PAM A is shown in Figure 5.1a. At pH 6 and 8.5, there is a monotonic decrease of 20-25 mV upon the addition of polymer. At pH 11, however, there is an overall decrease in magnitude of 10 mV and after the addition of 100 g polymer/t solid, the zeta potential is relatively constant. For PAM N (Figure 5.1b), the zeta potential following the addition of up to 500 g polymer/t solid shows a subtle increase in the zeta potential at pH 6 and 8.5 (approximately 5 mV), and a more noticeable decrease in magnitude at pH 11 (~ 10 mV).

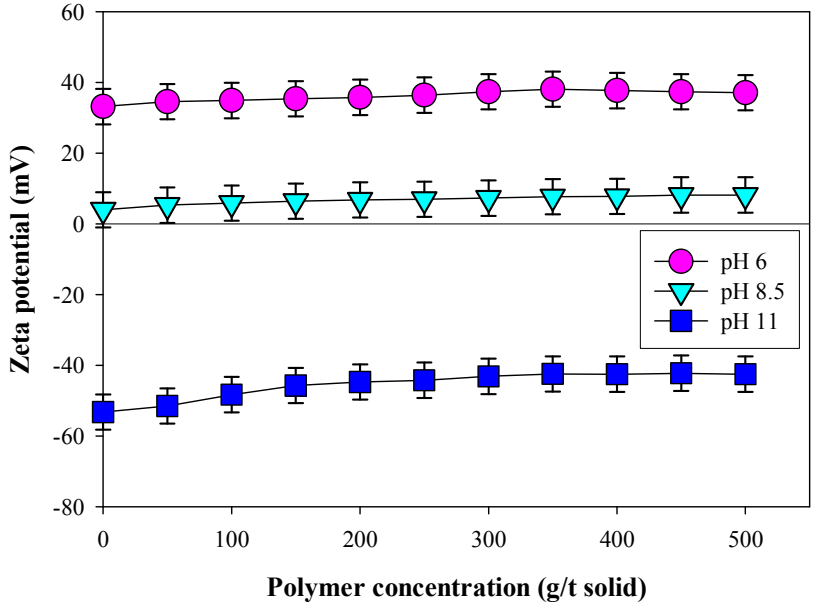
There are a few possibilities for the difference in behaviour caused by pH for anionic PAM A, as previously noted in the literature [40]. The polymer may shield the particles positive or negative charges at pH 6 and pH 11 respectively, by displacing the plane of shear further from the particle surface. Whilst this will result in a decrease in magnitude of the zeta potential, the presence of COO^- groups in the Stern and diffuse layer will cause the zeta potential to become more negative above the iep, and less positive below the iep. In the case of pH 8.5, the particle surface contains an equal number of positively and negatively charged sites. The negatively charged polymer can adsorb at the positive sites causing effective shielding of these groups, and also increasing the overall negative character of the aggregate as the adsorbing polymer is negatively charged.

For PAM N addition of up to 500 g polymer/t solid, it appeared that adsorbed polymer had no significant effect on the particle zeta potential. The adsorption isotherms (Figure 4.4), however, indicate that PAM N adsorbs at a high affinity at all three pH values. The observation that there is little change in the zeta potential suggests that at <500 g polymer/t solid, either the adsorption has not come to equilibrium (only 1 min passes before each measurement), or a patchy, thin layer has formed (due to contracted conformation and that at 500 g polymer/t solid, there is less than 20% of monolayer coverage at all pH values). The latter has been directly observed for adsorption of a non-ionic polyacrylamide onto dehydroxylated silica using AFM [20]. Brooks [82] contends that the zeta potential of particles should increase after the adsorption of a neutral polymer (as long as the shear plane is not shifted too far from the particle surface) due to the change in the ion distribution in the diffuse double layer. As the polymer adsorbs, the ions in the diffuse

layer are rearranged and can be pushed away from the surface slightly to cause an increase in the zeta potential measured at the shear plane. However, where this appears to occur at pH 6 and 8.5, the change in zeta potential is within the experimental error.



(a)



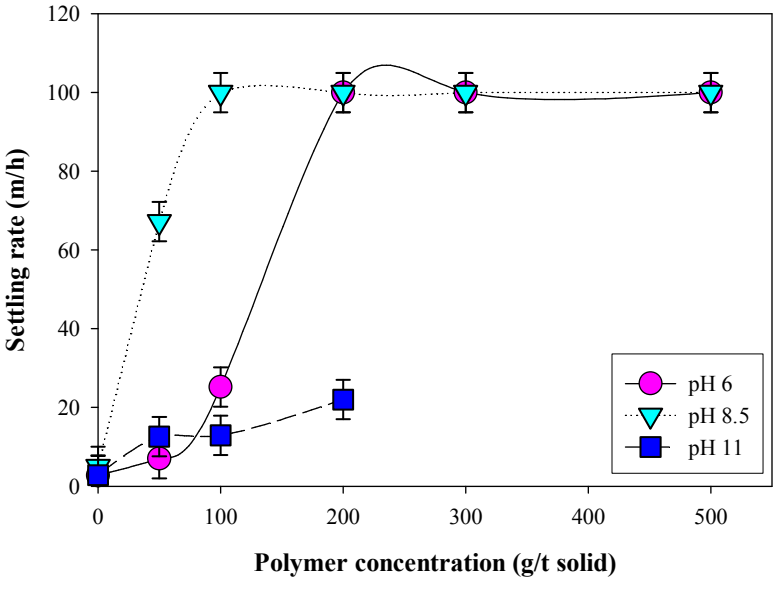
(b)

Figure 5.1: Electrokinetic zeta potential of Fe_2O_3 particles in 10^{-3} KNO_3 at 8 wt% solids as a function of PAM A concentration (a) and PAM N concentration (b) at pH 6, 8.5 and 11.

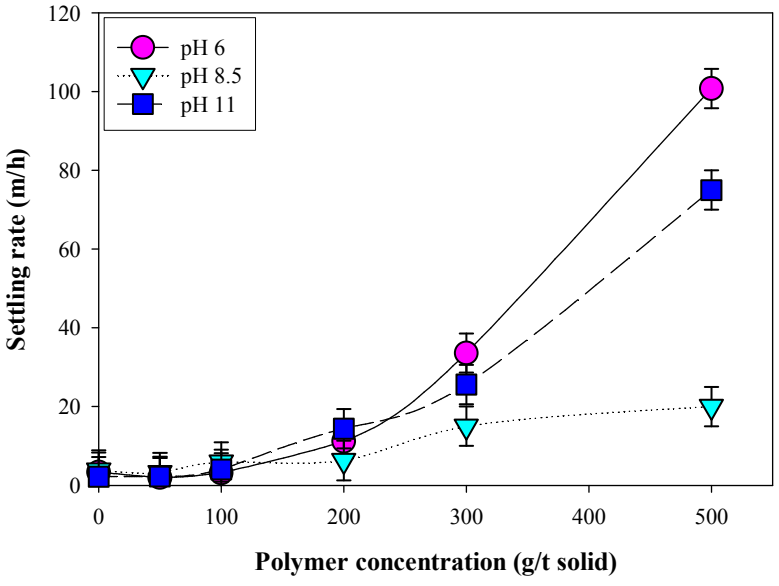
The zeta potential data can be modelled with Equation 2.1 to estimate the adsorbed layer thickness of non-ionic polymers based on the expectation that the zeta potential decreases in magnitude. This was not the case for pH 6 or pH 8.5, however the data at pH 11 was fitted to Equation 2.1, which indicated that the adsorbed layer thickness of PAM N plateaus at approximately 2.3 nm after the addition of 300-500 g polymer/t solid. This value is similar to the layer thickness found by Mpofu *et al*. [6] for PAM N adsorption onto kaolinite. As this equation is not valid for charged polymers, no adsorbed layer thickness estimate could be made for PAM A.

5.3.2 Polymeric structure, pH and shear: effect on dewatering behaviour

Figure 5.2a describes the settling data for flocculation of iron oxide with PAM A. At pH 6 and 8.5, the settling rates are significantly higher than at pH 11. At pH 6, the addition of 100 g PAM A/t solid gives rise to a settling rate of 25.2 m/h, and a fast settling rate of ~100 m/h at the iep (pH 8.5). At pH 11, the settling rate was 12.9 m/h. Whilst conducting the settling tests, it was visually apparent that the dewatering behaviour was different and inferior at pH 11. The supernatant was cloudy, rendering the mudline (solid-liquid interface) indeterminable, and hence there are no values for >200 g polymer/t solid. It is apparent that there is a large difference in dewatering rates between the two lower pH values and pH 11 after flocculation with PAM A. The pH-mediated trends observed here suggest that reduced bridging occurs at pH 11 where less polymer is adsorbed (Figure 4.3). The settling behaviour exhibited by the hematite pulps in the present work compares well with other studies [14, 18]. Addai-Mensah *et al*. [14] observed settling rates as low as ~1 m/h after flocculation with 100 g PAM A/t solid, and Hulston *et al*. [18] reported a settling rate of 7.54 m/h upon addition of ~10 g PAM A/t solid at high pH (>pH 12), along with high background electrolyte concentration (~0.7 M of various sodium-based salts).



(a)



(b)

Figure 5.2: Settling rate of Fe_2O_3 in 10^{-3} KNO_3 at 8 wt% solids as a function of PAM A concentration (a) and PAM N concentration (b) at pH 6, 8.5 and 11.

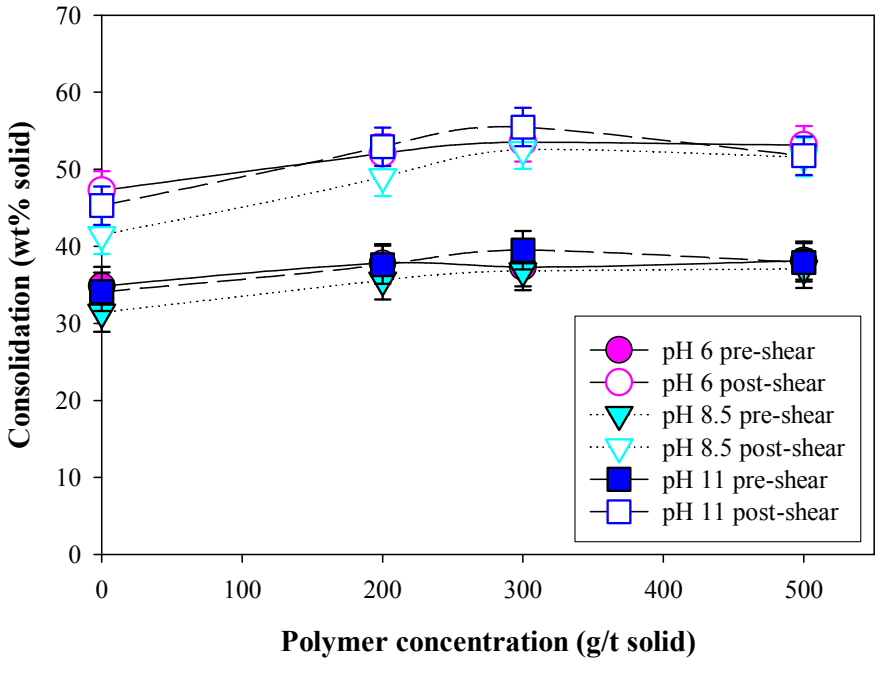
The settling rates achieved via flocculation with PAM N are reduced in comparison with those attained with PAM A (Figure 5.2b). It takes the addition of 500 g polymer/t solid to

achieve a settling rate of 20 m/h at the iep, and 200 g polymer/t solid to achieve the same at pH values 6 and 11.

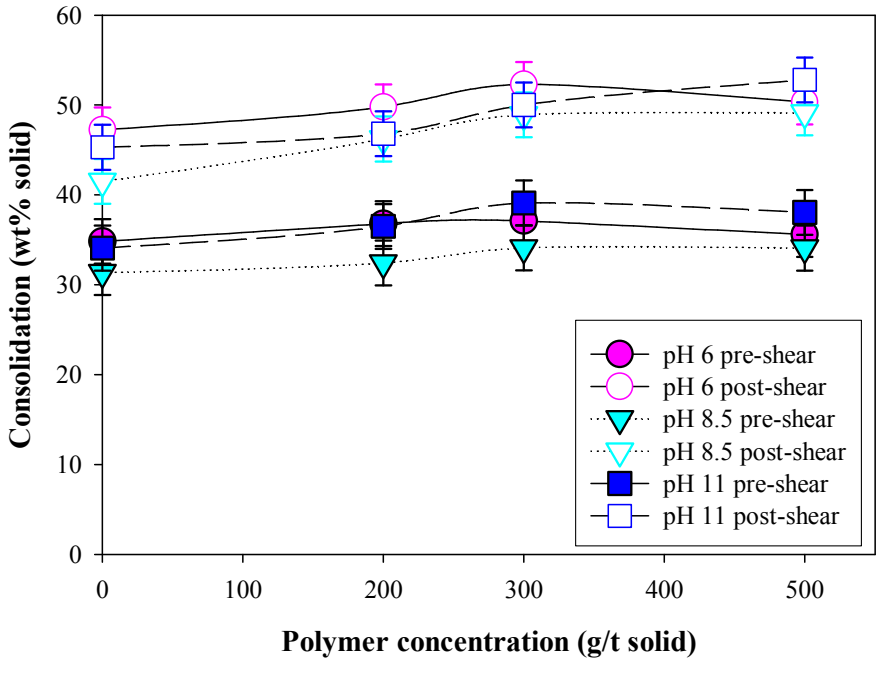
Visually, the flocs formed in the settling tests were much smaller for PAM N than for PAM A, suggesting that there was less extensive interparticle bridging by PAM N. The adsorption isotherms may provide insight into the reason for the poor settling behaviour due to flocculation with PAM N. Figure 4.4 shows that PAM N adsorbs with roughly twice the affinity for the mineral than does PAM A. These observations are consistent with the idea that PAM N has a more contracted conformation in solution than does PAM A [26] as it is uncharged, as confirmed by viscosity data in Chapter 4. Therefore, PAM N comprises of less loops and tails that extend into solution to facilitate extensive particle bridging [34].

Figure 5.3 indicates that there is little difference between the consolidation behaviour of the pulps at the three different pH values for both flocculants at polymer concentrations >200 g polymer/t solid. Below this flocculant concentration, the final sediment solid content was noticeably lower at the iep. This is consistent with DLVO theory; in the absence of any repulsive electrostatic barrier, the fast forming flocs trap water and lead to poor consolidation [92]. The result in this study is consistent with work done by Mpofu *et al*. [17], who found flocculation with 500 g/t PAM A to have little effect on the consolidation of smectite at pH 7.5 and 10.5, as did McFarlane *et al*. [30] using 250 g/t PAM A at pH 7.5.

Shear-mediated consolidation behaviour of sedimented iron oxide dispersions after flocculation with PAM A and N are also displayed in Figure 5.3. Shear action is observed to have a significant effect on pulp consolidation, giving an improvement of ~10 wt% solid, irrespective of pH and flocculant addition/structure type. The results are consistent with the shear stresses provided by agitation breaking down the large, loose flocs into smaller ones, allowing the particles to rearrange into a more compact bed. This has been observed previously in the literature, although to a lesser degree at 5-7 wt% improvement for smectite and kaolinite [29, 30]. It wasn't, however, observed for the same particle/polymer system (smectite/kaolinite with PAM A) elsewhere [6, 32]. In this study it is shown to be independent of polymer type or concentration, and thus appears to be dominated by a mechanical effect on the particle networking. This is highly significant for dewatering improvement, as irrespective of flocculant type, this consolidation improvement occurs. This means that a flocculant that gives superior settling rates can be chosen, and that dramatic improvement in consolidation can be achieved through shear.



(a)



(b)

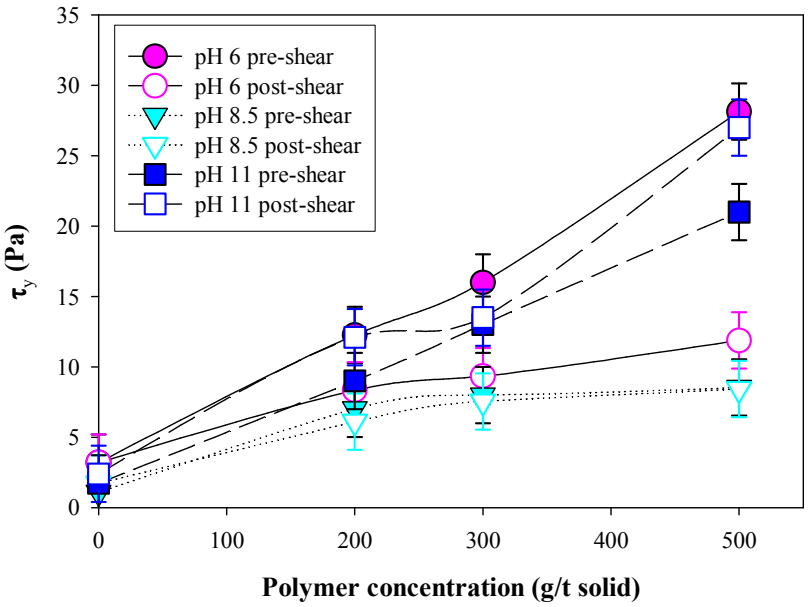
Figure 5.3: Consolidation of Fe_2O_3 particles in 10^{-3} KNO_3 upon addition of PAM A (a) and PAM N (b), pre and post-shear measurements.

5.3.3 Shear and flocculant concentration/type: influence on pulp rheology

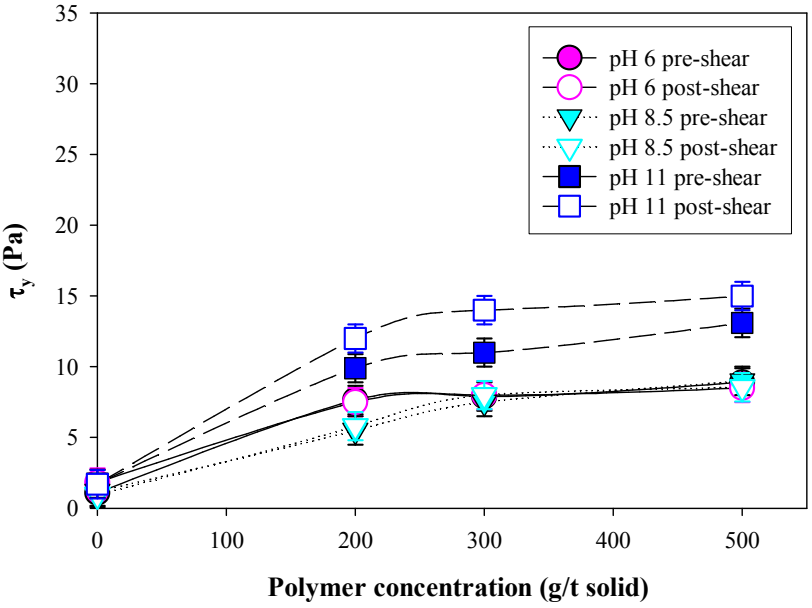
An increase in polymer concentration of up to 500 g polymer/t solid led to a systematic increase in yield stress (Figure 5.4). Flocculation with PAM A (Figure 5.4a) caused a higher yield stress than with PAM N (Figure 5.4b) after the addition of >300 g polymer/t solid. At the iep, the pulp behaves similarly for both polymers; the yield stress increased monotonically from ~1 Pa for 0 g polymer/t solid to ~8 Pa for 500 g polymer/t solid. The major difference between the rheological effects of the two flocculants occurs at pH 6 and 11.

An increase in yield stress correlates with the increase in polymer concentration. As the number of polymer molecules increase and adsorb onto the particles, increased bridging forces develop to form flocs and network between particles. Adsorption density data in Figures 4.3 and 4.4 indicate that at the polymer concentrations used for settling, all of the polymer molecules adsorb onto the iron oxide particles. The trend of yield stress increasing with polymer concentration is in agreement with that of Addai-Mensah *et al*. [14] , but the yield stresses are slightly lower than those of Hulston *et al*. [18]. The variation may be attributed to differences in particle size and ionic strength of the background electrolyte. Iron oxide particles used in the present work are coarser and the ionic strength lower than those used by Hulston *et al*. [18]. A high ionic strength leads to a compression of the electrical double layer which allows van der Waals forces to take effect, leading to stronger floc networks and higher yield stress values.

An AFM study conducted at high pH by Bremmell *et al*., [100] showed that an increase in (high molecular weight) polymer concentration had no significant effect on the repulsive forces between two oxide surfaces upon approach. There was, however, a significant increase in adhesion forces (upon separation of the surfaces) with an increase in polymer concentration, which correlates well with the increase in shear yield stress with an increase in polymer concentration observed in this study. The AFM will be utilised in a similar manner in Chapter 7.



(a)



(b)

Figure 5.4: Yield stress (τ) of Fe_2O_3 in 10^{-3} KNO_3 upon addition of PAM A (a) and PAM N (b), pre and post-shear measurements.

In the case of PAM A-induced flocculation, the particles being positively charged at pH 6 form a stronger network with the negatively charged polymer molecules through both electrostatic attraction and chemical bonding and complexation [35, 36, 51, 101] as seen in

Chapter 4, thus leading to the highest observed yield stress. This was significantly reduced post-shear for pH 6, and increased post-shear for pH 11. A similar increase in yield stress due to shear at pH 11 was also observed for PAM N-flocculated pulp, with little change observed post-shear for flocs at pH 8.5 and 6. Upon agitation, the shear forces break up the particle network and lower the yield stress. For PAM N at pH 6, however, the behaviour of the pulp is different with an insignificant change in behaviour observed post-shear, suggesting that the flocculant structure and its adsorption mechanisms are responsible. The polymer-particle bonding via chemical complexation is not available due to the lack of the negatively charged carboxylate group. Weaker hydrogen bonds are responsible for polymer adsorption at pH 6 (as seen in Chapter 4), reflecting significantly lower yield stress values in comparison with PAM A [101].

At the iep (pH 8.5), polymer structure type and shear have no effect on the yield stress of the particles. In addition, the yield stress at this pH is lower than when the flocculated particles are charged, which demonstrates the system exhibits non-DLVO behaviour [92], illustrating the importance of polymer bridging in flocculated systems. This will be explored further using the elastic floc model [111] in Chapter 9. It is expected that an increase in yield stress after shear would occur due to the increase in volume fraction reported in the consolidation data in Figure 5.3. Similarly, it is expected that a decrease in yield stress would occur due to a rupturing of the floc structure and destruction of polymer bridges. That systems at pH 6 and 8.5 showed either a decrease (pH 6 with PAM A), or no change in yield stress after shear, suggests that significant changes are occurring within the flocs as a result of the application of shear which are associated with floc rupture.

It is pertinent to note that the pulp behaved similarly at pH 11 for both polymers; the yield stresses were high and increase after application of shear. It is expected that the different functionality between the polymers would cause different behaviour as seen at pH 6. One of the main bonding mechanisms between the particle surface and polymer that is expected to occur at pH 11 is hydrogen bonding [51, 139] between the mineral surface and an amide functional group that is common in both polymers. In addition for PAM A, complexation between the carboxylate groups and the metal ion (Fe) has been observed at pH 11-14 [37, 39], which was also established in Chapter 4 for this system. Lee and Somasundaran (1989) also cited that PAM is known to hydrolyse at pH 10 [191], which has been confirmed in Chapter 4. This would modify PAM N with carboxylate functional groups in place of the primary amide groups, providing functionality consistent with that of PAM A. The similar bonding mechanism may account for the comparable behaviour for both

polymers at pH 11 and account for the high yield stress. The higher post-shear yield stress may be attributed to the shearing of particles providing enough energy for the particles to overcome the electrostatic repulsive barrier, allowing more particle – polymer interactions. This facilitates a more compact, stronger network causing a higher yield stress. The adsorption mechanisms from Chapter 4 correlate well with the rheology data reported here.

For PAM A flocculated pulps, the yield stresses are higher for systems at pH 6 and 11 than they are at pH 8.5, suggesting that the bidentate chelation mechanism of adsorption (observed at pH 6 and pH 11) is stronger than the monodentate chelation that occurs at the iep, as would be expected through the extra chemical bond. With regards to the bidentate chelation mechanism observed above and below the iep, the yield stress for pH 11 was lower than at pH 6 pre-shear, which was suggested previously to be due to an electrostatic barrier between the negative particle and the negative polymer needing to be overcome before extensive bonding could occur. The yield stress of pH 11 flocculated pulps post-shear was similar to that of pH 6 pre-shear, suggesting that this is indeed related to the adsorption mechanisms. Once the electrostatic barrier was overcome through the application of shear, the polymer was able to bond more extensively to the particles, giving a similar yield stress to that observed at pH 6 where there is no electrostatic repulsion.

5.4 CONCLUSION

The effect of polymer structure type, interfacial chemistry and particle interactions on the dewaterability of model iron oxide dispersions have been investigated. The polymer structure type was found to influence the surface chemistry of the dispersion in that the addition of anionically charged PAM A had a greater effect on the zeta potential than did the neutral polymer, PAM N. The settling rates were dependent on polymer structure, type and pH. Highest settling rates (100 m/h) were achieved at pH ≤ iep with a minimal dosage of PAM A (as low as 50 g polymer/t solid).

Shear has a pronounced effect on the consolidation of the model dispersion, increasing the dewaterability by up to 15 wt%. This is independent of both pH and polymer addition or type, and is a significant improvement upon currently achievable pulp consolidation. Polymer structure type has an effect on the rheology of the model dispersion, with

flocculation with PAM A causing a similar or higher yield stress than its counterpart, PAM N.

PAM A, in general, is shown to be a more effective flocculant than PAM N. Expanded conformation in solution is essential for bridging flocculation, and it therefore seems pertinent to choose a charged polymer over a non-charged polymer for dewatering applications. PAM A, which has acrylic acid groups which can adsorb to the surface in multiple ways, is also superior for this reason. It is of interest as to whether any charged functional group will be equally efficient, or if it is functional group specific. This will be investigated in Chapter 6.

CHAPTER 6 The effect of anionic and cationic polyacrylamide flocculants, pH and shear on the interfacial chemistry, rheology and dewaterability of model iron oxide dispersions

SUMMARY

In this study, the effect of polymeric flocculant structure type (anionic sulphonate substituted copolymer (PAM S), and cationic trimethyl amino ethyl substituted copolymer (PAM C)), along with shear on the interfacial chemistry, rheology and dewaterabilty of iron oxide dispersions has been investigated as a function of pH. PAM C had a higher adsorption affinity than PAM S at all pH values studied. The adsorption isotherms followed the Freundlich (rather than Langmuir) model for adsorption, consistent with the observation that the amount of polymer adsorbed increased monotonically with increasing polymer concentration up to 7500 g/t solid. Upon flocculation with up to 500 g polymer/t solid, settling rates in the range of 3-100 m/h were observed, along with sediment consolidation in the range 35-40 wt%. Settling rates varied depending on polymeric flocculant type, and were high for flocculation with both polymers. Settling was most effective at and below the iep. Polymer structure type did not have any noticeable impact on the extent of pulp consolidation, except for high polymer dosage (500 g/t) of PAM S at low pH. Moderate shear dramatically improved the consolidation (to 55 wt% solid) of pre-sedimented pulps, especially when the polymer had the same charge as the dispersion.

For the selection of a flocculant, a polymer which will display an opposite charge to that of the particles has been shown to provide an improved flocculation and dewatering performance. This indicates that the predominant flocculation mechanism for these polymers is bridging, facilitated through chemical and hydrogen bonding. Electrostatic or charge patch mechanisms are indicated where the polymers are of opposite charge to the particles.

6.1 INTRODUCTION

Polymeric flocculant structure and adsorption behaviour have long been known to play a role in the dewatering of mineral dispersions [6, 26], as has interfacial chemistry and rheology [12, 34, 44, 45]. It was found in Chapter 5 that anionic PAM A was a superior choice of flocculant when compared to non-ionic PAM N for the dewatering of iron oxide dispersions, which suggests that a charged polymer in general would be preferred due to their expanded conformation in solution being more conducive to bridging flocculation. It is for this reason that two more polyacrylamides (anionic sulphonate substituted copolymer (PAM S), and cationic trimethyl amino ethyl substituted copolymer (PAM C)) were chosen for investigation in this chapter. PAM S was chosen to investigate whether it is the charge alone, or the functional group that is responsible for the superior settling rates achieved by PAM A in Chapter 5, whilst PAM C was chosen to investigate the use of a cationic polymer. All polymers were chosen with as similar nominal molecular weights as available to endeavour to keep molecular weight effects to a minimum (see Table 3.1).

Tekin *et al*. [192] have shown that a cationic PAM (of similar molecular weight to the cationic PAM used in this study) can cause charge reversal when adsorbed onto sepiolite (predominantly consisting of SiO_2 and MgO), shifting the iep from ~6.5 to ~8, and that in general it caused an increase in zeta potential (at pH 4 from ~ + 20 mV to ~ +50 mV), although only slightly at high pH. Besra *et al*. [24, 42] have also found cationic polyacrylamides useful in dewatering applications, and it is for this reason that it will be studied here. McFarlane *et al*. [155] and Bal [186] found sulphonate substituted PAM to be effective at dewatering clays and gibbsite, respectively (in most cases more effective than PAM A due to it adsorbing slowly and adopting a conformation at the interface which is preferential for bridging flocculation [148]), and thus it is also of interest here.

Shear action is important in the compression zone at the bottom of plant thickeners, and its role in enhancing dewaterability of tailings was evaluated here by applying shear to the pre-consolidated pulps resulting from batch sedimentation tests. The application of shear has previously been found to have a positive effect on the dewaterability of clay suspensions, in Chapter 5 and in the literature [6, 29, 110]; thus it will be of interest here to examine the effect of different functional groups.

The aim of this study is to improve the settling behaviour and the consolidation of iron oxide dispersions through flocculation with polyacrylamides at different pH values and utilising the application of shear. High molecular weight polymers (>10^6 Da), which are commonly used for the dewatering of mineral tailings are of interest here [1, 24, 27, 32, 141]. Polyacrylamides are common industry flocculants, and in this study, two high molecular weight polyacrylamides have been used in order to optimise the current dewatering practices.

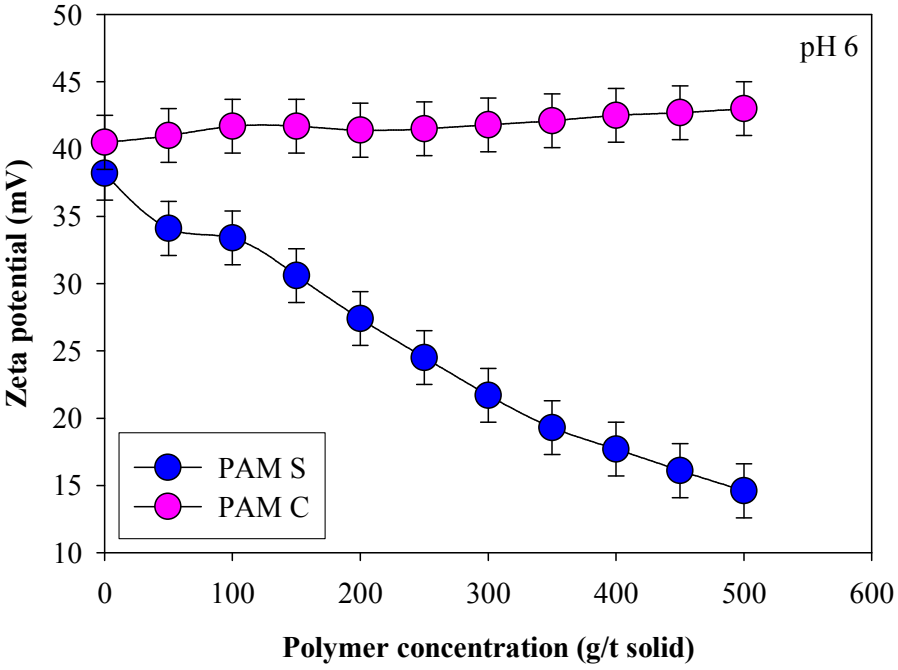
The work was carried out at pH 8.5, where the particles are at the iep, and at pH 6 and 11 where the particles are charged + 40 and – 40 mV, respectively. Investigation of PAM S and PAM C in this chapter will allow the van der Waals and electrostatic interactions to be probed by observing the dewatering behaviour resulting from the interactions between cationic (PAM C), non-ionic (PAM N) and anionic (PAM A and S) polymers with positive (pH 6), neutral (pH 8.5) and negatively (pH 11) charged iron oxide dispersions.

6.2 RESULTS AND DISCUSSION

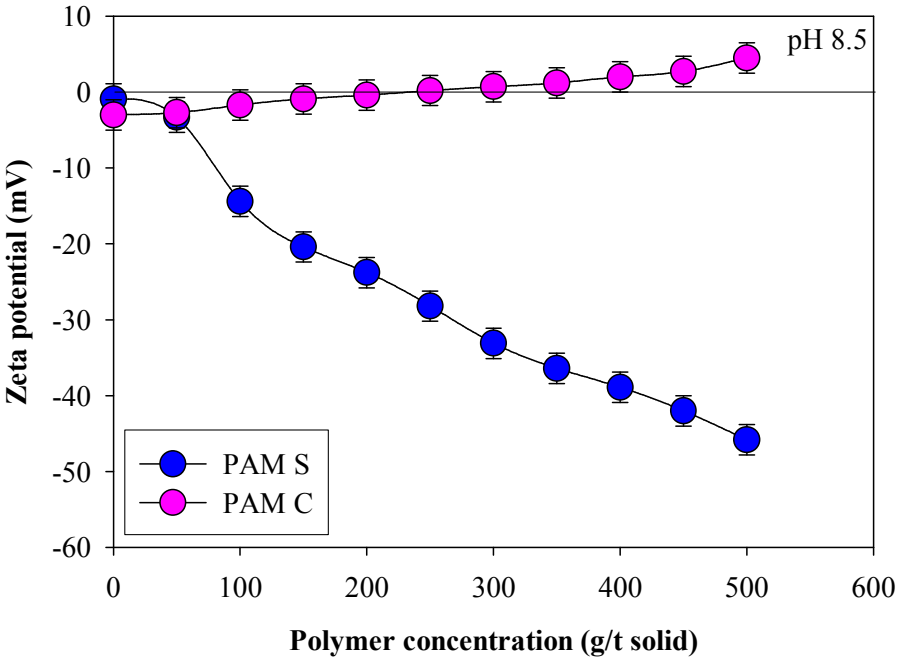
6.2.1 Influence of polymer structure type on interfacial chemistry

Figure 6.1 shows the zeta potential of iron oxide particles as a function of polymer concentration up to 500 grams polymer / ton solid. At pH 6 (Figure 6.1a), for zero polymer addition, the zeta potential was ~ 40 mV. PAM S significantly lowered the zeta potential from ~ 40 mV to ~ 16 mV, whilst PAM C adsorption increased the zeta potential very slightly. Adsorption of polymers is known to shield the charge of particles [50] and as PAM S is anionically charged, its adsorption will also make the zeta potential more negative. A small but noticeable increase in zeta potential after PAM C addition is due to a change in the ion distribution in the diffuse double layer [82]. In comparison to PAM A at high pH (which is similar to PAM C at low pH due to the like-charged polymer-particle systems), the effect seen is slightly different, but similar to effects observed by Tekin *et al*. [192]. In Chapter 5, PAM A was shown to shield the charge of the particles slightly rather than making the zeta potential more negative, which is opposite to what is observed here. Tekin *et al*. [192] observed that PAM C addition significantly increased the zeta potential

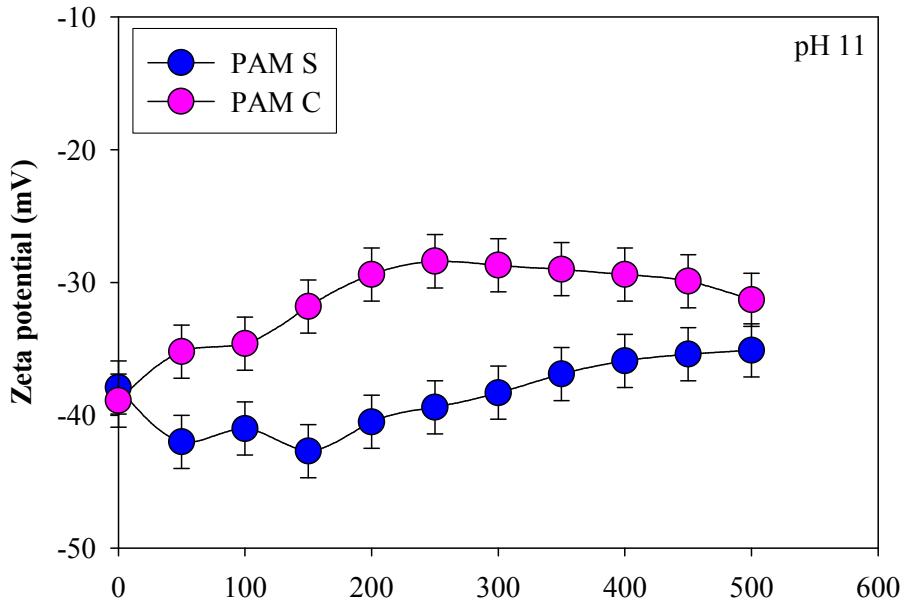
at low pH. Their polymer dosage was much higher than the dosage in this study, and thus the effects could be similar if the polymer dosages were the same.



(a)



(b)



(c)

Figure 6.1: The zeta potential of iron oxide particles in 10^{-3} M KNO_3 as a function of polymer addition at (a) pH 6, (b) pH 8.5 and (c) pH 11

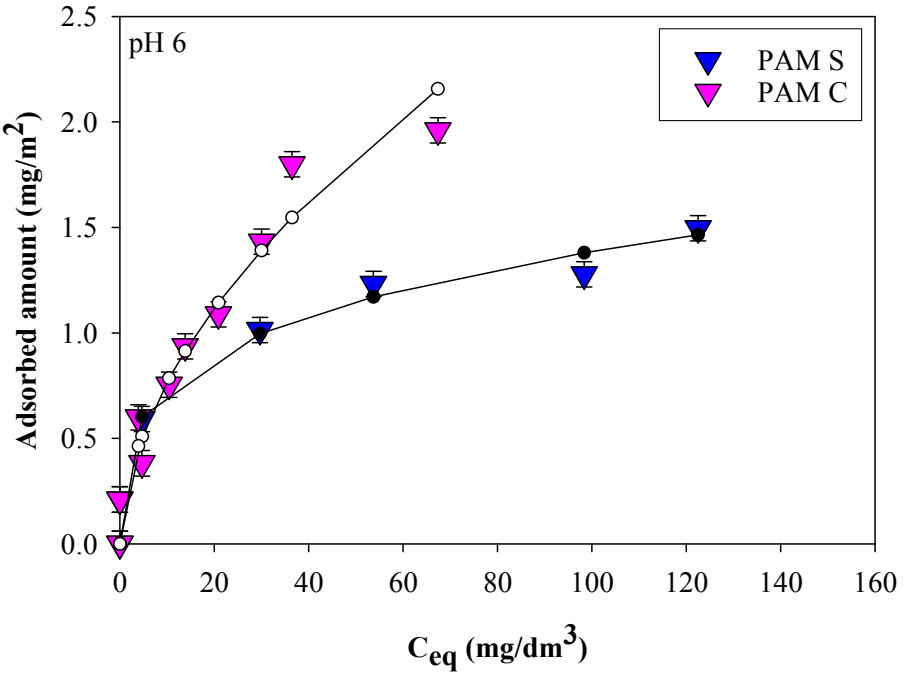
At pH 8.5 in Figure 6.1b, a similar trend is observed in the case of each polymer with one exception. PAM S had a much greater effect, reducing the zeta potential of the particles by ~ 45 mV. It is further from its pKa of 1.5 at this pH, and would be fully dissociated at this point, which could explain the larger effect. It also had a larger effect when compared to that of PAM A in Chapter 5. PAM S has a higher viscosity than PAM A (8.73 PAM S > 7.62 PAM A Pa.s [147]), suggesting a more expanded interfacial conformation.

Figure 6.1c displays the zeta potential at pH 11 where the pristine particles have a charge of ~ -40 mV. PAM C neutralises the charge on the particles, leading to a decrease in the magnitude of the zeta potential, as has been seen previously in the literature [192]. PAM S has more of a negative effect initially, with charge shielding behaviour beginning after 200 g/t polymer addition. The zeta potential appears to be relatively stable between 50-150 g/t. This is similar to that seen for PAM A in Chapter 5, except that PAM A doesn't initially make the dispersion more negative. This is suspected to be due to PAM S having a larger adsorbed amount than PAM A (approx 0.1 mg/m^2 compared to ~ 0.05 mg/m^2 at around 250 g/t). As there is a greater amount of anionic polymer adsorbed on the surface in the case of PAM S, this must initially lead to increased negativity in the zeta potential.

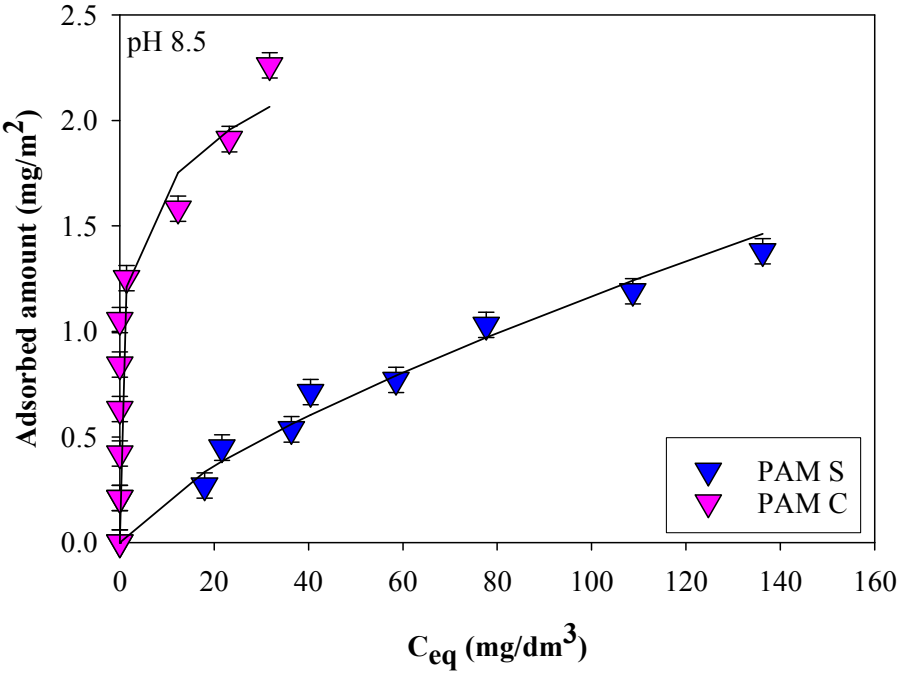
6.2.2 Influence of polymer structure type on the adsorption behaviour

Figure 6.2 depicts the adsorption of both polyacrylamide polymers onto iron oxide at three pH values. The isotherms were fitted to both the Langmuir and Freundlich models described by Equations 2.22 and 2.24, respectively (as seen in Figure 6.2b). The isotherms, similarly to those in Chapter 5, are better described by the Freundlich model of adsorption, indicating that polymer continues to adsorb with increasing polymer concentration up to 7500 g/t solid, with no adsorption plateau being reached [50]. Regardless of pH, it can be seen PAM C has a higher adsorbed amount than PAM S.

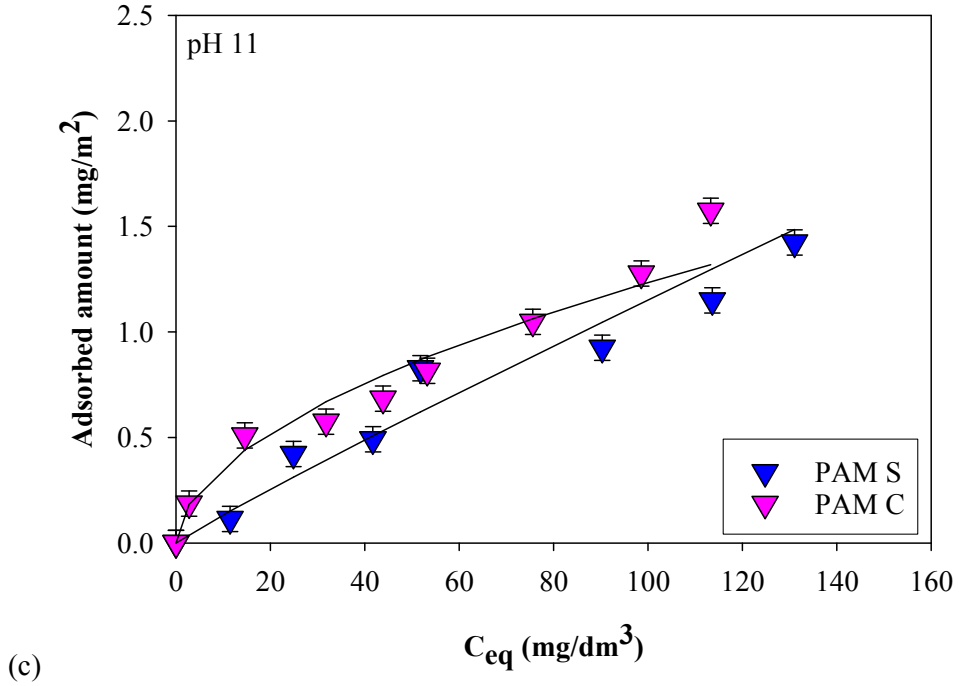
Figure 6.2a shows that PAM C has the highest adsorbed amount at pH 6, despite being a similar (cationic) charge to the particles. Anionic polymer PAM S should be more attracted to the particles due to electrostatic attraction with the positively charged surface. The adsorption affinity constants were calculated using the Freundlich model [47, 90, 168, 169] and are shown in Table 6.1. PAM C has a low adsorption affinity at pH 6, and PAM S has a higher adsorbent capacity than PAM C, indicating that electrostatics do play a role. It has been established previously that higher adsorption is accompanied by faster adsorption kinetics for a polymer which has a smaller conformation at the interface [148]. It was found with clays, that PAM A and PAM S adsorb slowly and have a more expanded conformation. With the adsorption affinities ranked PAM S > PAM C at pH 6, it would appear that PAM C has the largest interfacial conformation. This is expected due to PAM C having a pKb of ~ 9.5, and having a more expanded conformation due to having a similar charge to the particles, and due to intramolecular repulsion. It is, however, unusual that PAM C has a higher adsorbed amount when it seems to have a more expanded interfacial conformation coupled with an electrostatic repulsion from the surface. Viscosity measurements by Bal [147] indicate PAM S to have a more expanded conformation than PAM C, which would explain the lower adsorbed amount. It thus appears that the adsorption affinity of PAM C can not be likened to adsorption kinetics in this case [148].


pH 6
PAM S
PAM C
Adsorbed amount (mg/m2)
Ceq (mg/dm3)
0.0
0.5
1.0
1.5
2.0
2.5
0
20
40
60
80
100
120
140
160

(a)


pH 8.5
PAM S
PAM C
Adsorbed amount (mg/m2)
Ceq (mg/dm3)
0.0
0.5
1.0
1.5
2.0
2.5
0
20
40
60
80
100
120
140
160

(b)



(c)

Figure 6.2:Adsorption of PAM onto iron oxide particles in 10^{-3} M KNO_3 at (a) pH 6, (b) pH 8.5 and (c) pH 11. Fits to the Freundlich model are included as solid lines.

Table 6.1: Freundlich model isotherm parameters summarised for PAM S and PAM C at pH 6

	polymer	$1/n_F$ adsorption affinity constant	k_F (dm^3/g_{solid})
pH 6	**PAM S**	0.27	1.91
	PAM C	0.54	1.06
pH 8.5	**PAM S**	0.73	0.20
	PAM C	0.17	5.48
pH 11	**PAM S**	0.94	0.07
	PAM C	0.53	0.51

Adsorption isotherms for PAM S and PAM C onto iron oxide at pH 8.5, where the particles have no charge, are depicted in Figure 6.2b. PAM C again had the highest adsorbed amount. In this case, PAM C has both a higher adsorption affinity and adsorbent capacity. This suggests that PAM C has a less expanded conformation at pH 8.5 (which

correlates with it being closer to its pKb at this pH, and also that it has the same charge as the particles at pH 6), which allows greater polymer adsorption as each polymer molecule takes up less space on the surface of the particles. This, coupled with the lack of electrostatic repulsion between the polymer and the particles explains the increase in the adsorbed amount of PAM C, when compared to the system at pH 6. Both the pKa values and the viscosity data [147] for PAM S and PAM A indicate that PAM S should have a larger interfacial conformation than PAM A, but the adsorption at this pH is much larger for PAM S than it was for PAM A in Chapter 5. This suggests that the carboxylic acid group present on PAM A is less attracted to the surface than the sulphonate group attached to PAM S.

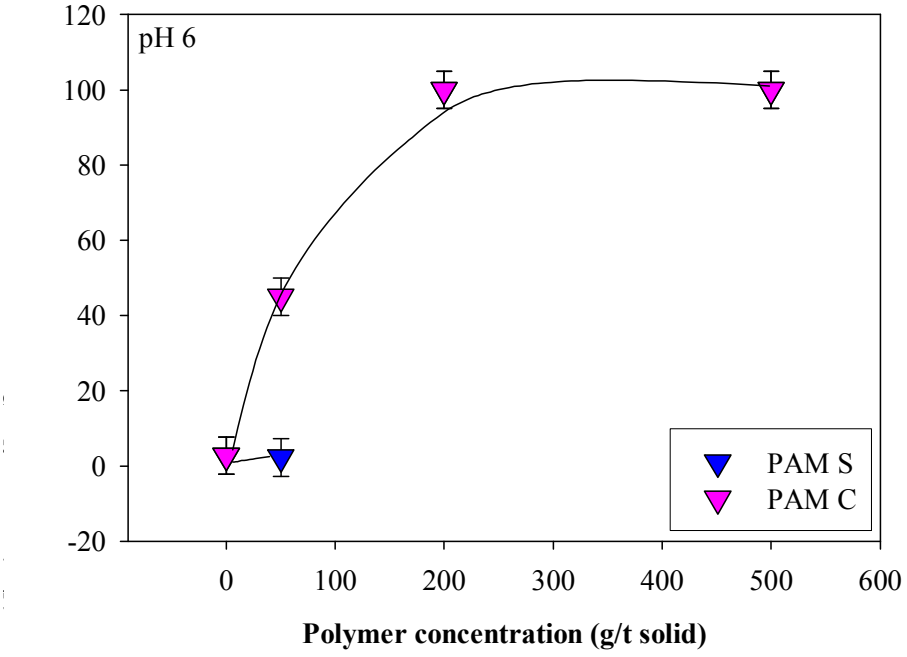
McFarlane [148] reported that for PAM A and PAM S adsorption onto negatively charged smectite particles, PAM S adsorption had a lower adsorbed amount, whilst for kaolinite it was similar for both polymers. Middleton *et al*. [193] observed that the sulphonate group on PAM S had weaker interactions with cations which explained the adsorption difference with smectite, but the fact that they are similar for kaolinite and different for iron oxide suggests a definite preferential adsorption of the sulphonate group to the iron oxide surface over the carboxylate group in PAM A.

In Figure 6.2c, where the particles are at pH 11 and are negatively charged, the adsorption isotherms for PAM S and PAM C are shown. At pH 11, we would expect that the cationic polymer (PAM C) would have a higher adsorption due to no electrostatic repulsion to the surface, which is observed. PAM S also has high adsorption, indicating that electrostatic forces are not the dominant mechanism responsible for adsorption onto the iron oxide surface. At pH 11, the PAM S isotherm is of a different shape to those at pH 6 and 8.5. At pH 11, PAM S is following the L isotherm rather than the H isotherm (see Figure 2.16). This is consistent with an electrostatic repulsion between the polymer and the surface.

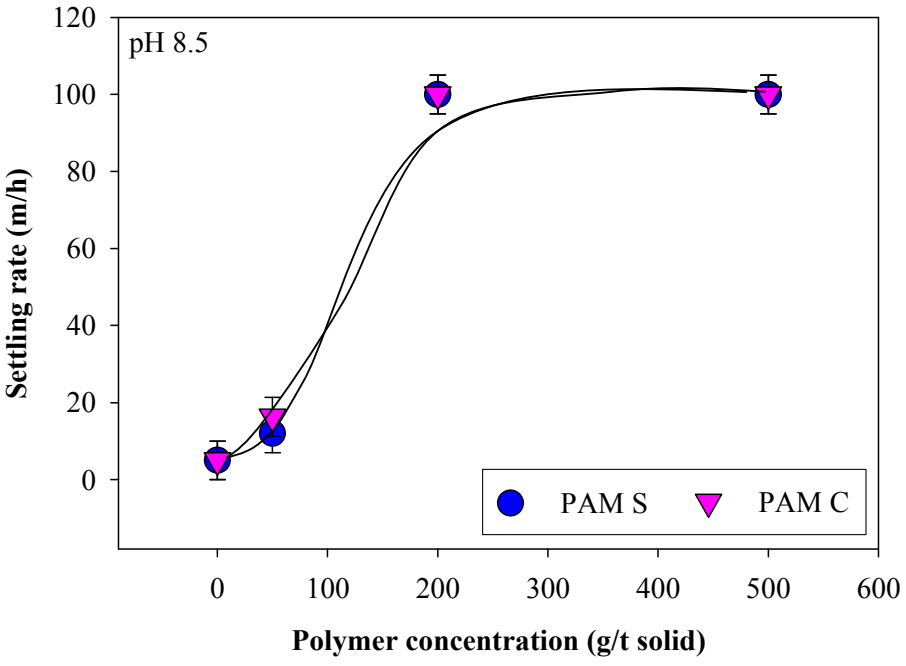
6.2.3 Dewatering behaviour

Settling rates of the iron oxide dispersions flocculated with PAM S and PAM C at the three pH values increase with increasing polymer addition (Figure 6.3). It should be noted that in each case where the settling rate is reported at 100 m/h, that this is the upper limit of detection for the method used. PAM S flocculated dispersions result in poor supernatant

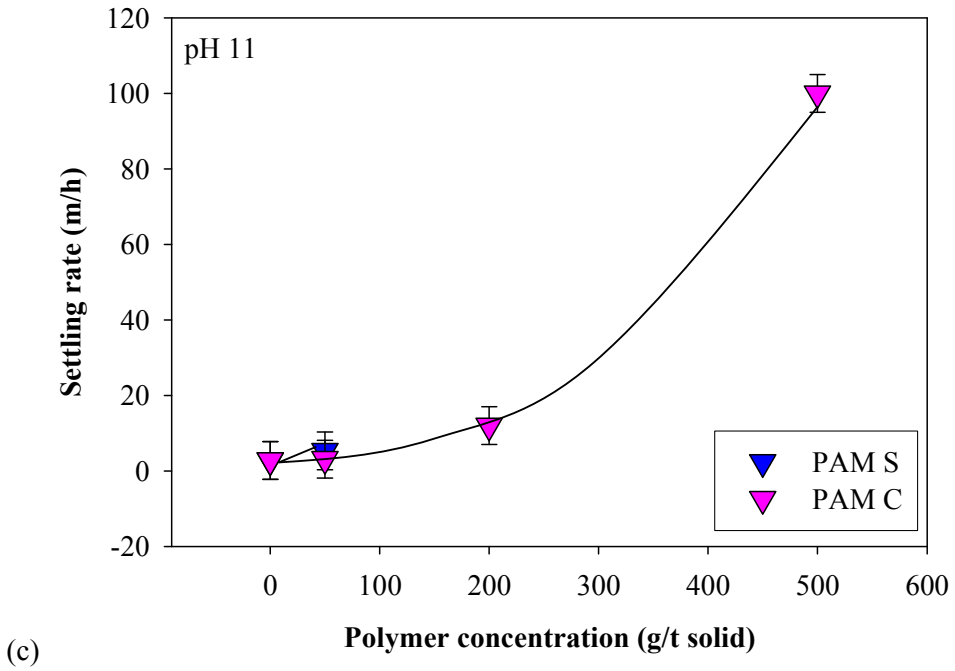
clarity, with the mudline indeterminable either side of the iep, suggesting that the difficulty only occurs when the particles are charged. As the mudline was undeterminable there are only two reported measurements for PAM S. If electrostatic interactions were the driving force for flocculation, it would be expected that the anionic PAM S would flocculate best at pH 6 where their charge is opposite to that of the particles. This is not, however, the case. PAM C is a better flocculant at low dosages, consistent with the same observation for PAM A being a better flocculant at high pH in Chapter 5.



(a)



(b)



(c)

Figure 6.3: The settling rates of iron oxide dispersions as a function of polymer addition at (a) pH 6, (b) pH 8.5 and (c) pH 11 in 10^{-3} M KNO_3 background electrolyte

Figure 6.3b shows the settling rates when the dispersion comprised neutrally charged particles. At pH 8.5, flocculation with PAM S and PAM C resulted in settling rates of 100 m/h upon the addition of 200 g/t. At pH 11, as seen in Figure 6.3c, it takes the addition of 500 g/t to achieve 100 m/h. The supernatant was also turbid, with the mud-line being indeterminable in many cases (hence the missing points on the graph). PAM S was difficult to observe due to turbidity at high pH, but it was observed to have a slightly better effect at 50 g/t.

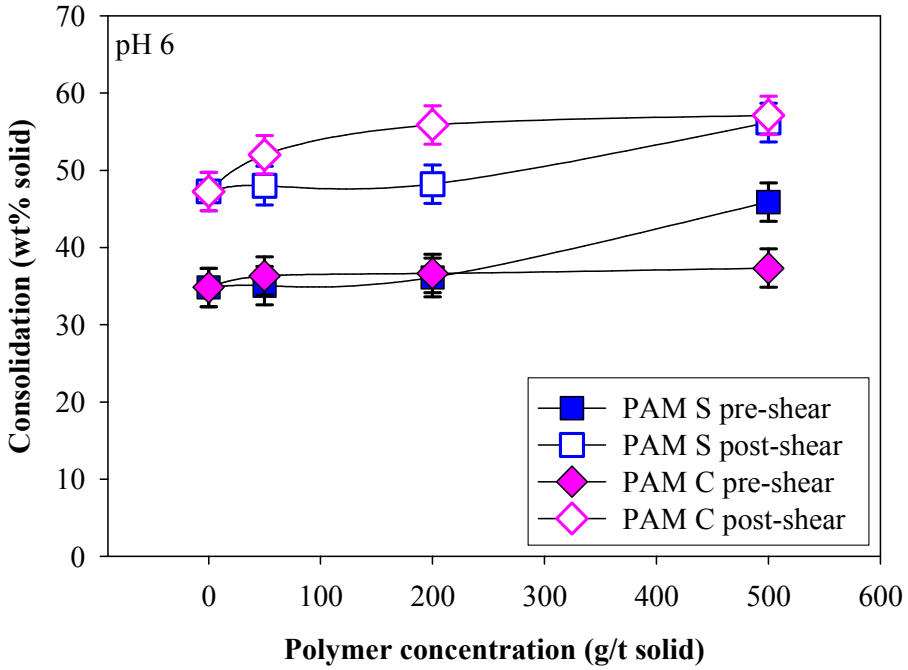
McFarlane [148] found that PAM S was more effective than PAM A for achieving high settling rates for negatively charged smectite and kaolinite dispersions at pH 7.5, which was not observed here. Bal [186] also reported that PAM S was more effective than PAM C at producing high settling rates when gibbsite is positively charged, and that ionic PAM A was more effective than both. In this case, the behaviour of PAM A and PAM S are similar; indicating that the different functional groups do not impact upon flocculation at this pH, and PAM C is most effective. Bal's [186] results correlate directly with the adsorbed amounts for polyacrylamide on to gibbsite, in that a higher adsorbed amount gave higher settling rates. This was loosely observed for the system discussed in this chapter

also, with PAM C flocculation resulting in greatest adsorption and highest settling rate, followed by PAM S and PAM A. The difference in adsorbed amounts for PAM S and PAM A was not, however, reflected in the settling rates.

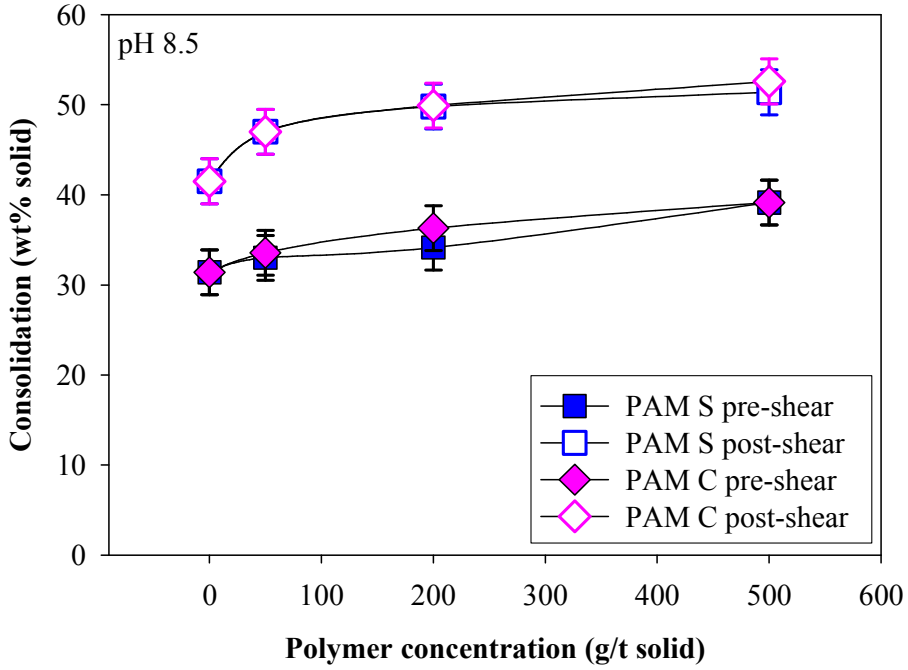
The influence of polymer structure type, pH and shear on the consolidation of iron oxide dispersions is depicted in Figure 6.4. Polymer addition had a small effect on particle consolidation, but in all cases, shear can be seen to have a large effect. There are pH dependent trends observed, as discussed below.

For unsheared and sheared dispersions at pH 6, Figure 6.4a shows that the addition of up to 500 g PAM C/t has no noticeable effect on the consolidation of sedimented pulps. PAM S, however, whilst not having much effect with the addition of up to 200 g/t, had a larger effect at 500 g/t by increasing the consolidation by ~10 wt%. The effect of shear is dramatic. In most cases, it increases the consolidation by 10-15 wt%, with the exception of PAM C, where the application of shear increases the consolidation by 15-20 wt%. This is due to the cationic polymer interactions with the positively charged dispersion. The input of energy into the dispersion by the application of shear allows the particles to pack closer together by overcoming the electrostatic barrier (as observed with PAM A in Chapter 5), allowing increased polymer/particle interactions and van der Waals forces to take effect. Also, due to the particles and the polymer both having a positive charge, this forms a lubricating layer between the particles which allows them to slip past one another more easily to form a more compact, consolidated bed.

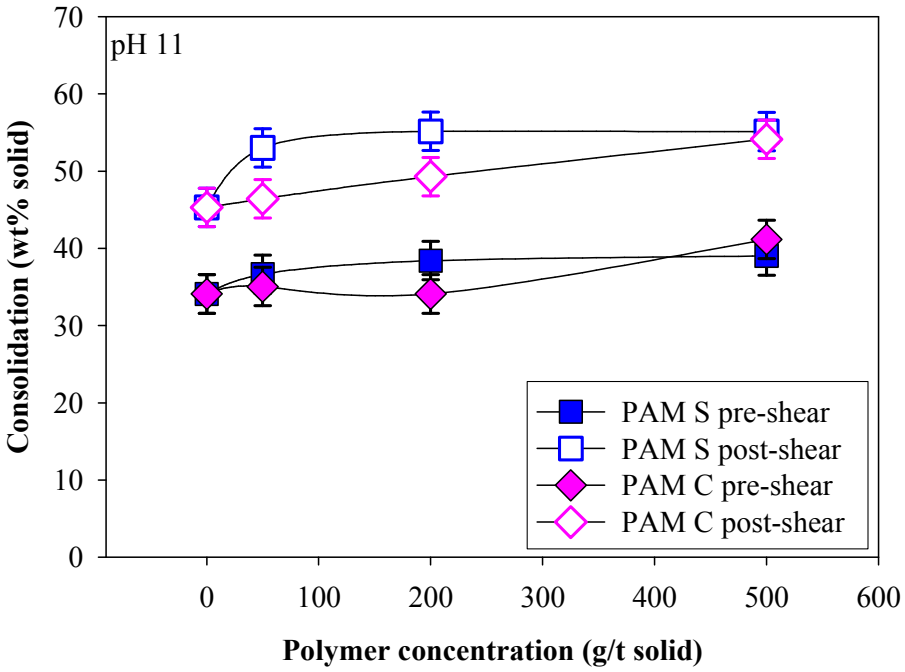
In Figure 6.4b, where the particles in the dispersion are neutrally charged, both polymers have a marked effect on the sediment consolidation by increasing it by to 7 wt%. At this pH, application of shear to the consolidated bed increased the sediments solid content by 10-15 wt%. A similar effect is observed for the pulps at pH 11 (Figure 6.4c), where we see a marked increase in consolidation due to shear but insignificant polymer addition effect. It can be noted, however, that at pH 11, the pulp flocculated with anionic PAM S improved the most after the application of shear, in agreement with the pulp flocculated with cationic PAM C improving the most after shear at low pH, due to overcoming the electrostatic repulsion.


pH 6
Consolidation (wt% solid)
Polymer concentration (g/t solid)
PAM S pre-shear
PAM S post-shear
PAM C pre-shear
PAM C post-shear
0
10
20
30
40
50
60
70
0
100
200
300
400
500
600

(a)


pH 8.5
Consolidation (wt% solid)
Polymer concentration (g/t solid)
PAM S pre-shear
PAM S post-shear
PAM C pre-shear
PAM C post-shear
0
10
20
30
40
50
60
0
100
200
300
400
500
600

(b)



(c)

Figure 6.4: Consolidation of iron oxide dispersions as a function of polymer addition at (a) pH 6 (b) pH 8.5, and (c) pH 11

As mentioned in Chapter 5, an improvement in sediment consolidation following the application of shear has been previously observed in recent studies by McFarlane *et al*., although to a lesser extent (5-7 wt%) for smectite and kaolinite [29, 30], whilst no effect was observed by Mpofu *et al*. [6, 32]. In this study, the effect of shear was shown to be independent of polymer type or concentration in Chapter 5. It does appear that dispersions flocculated by polymers with the same charge have a better response to shear for enhanced consolidation.

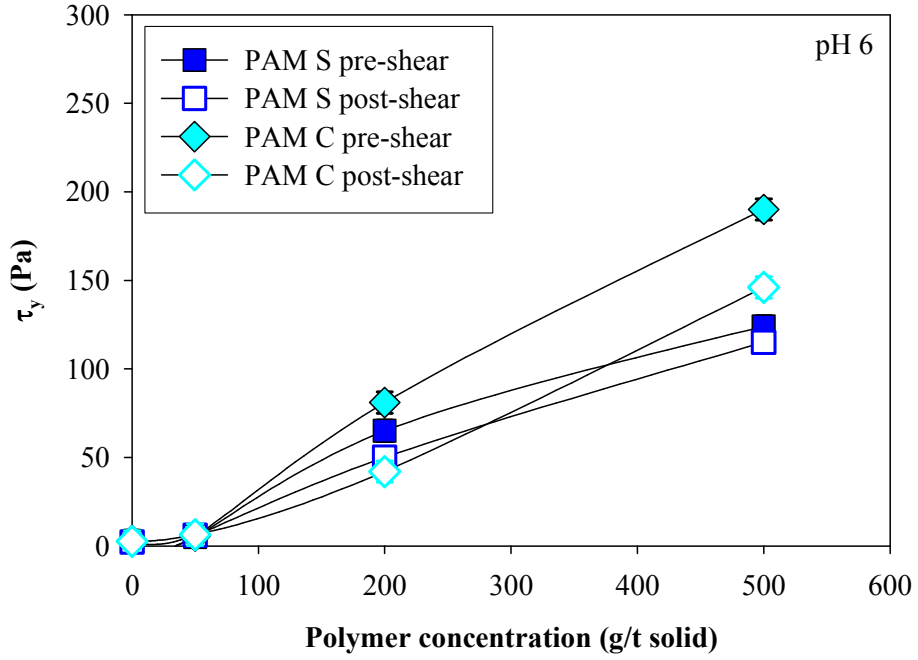
6.2.4 Influence of polymer structure type on pulp rheology

The shear yield stress as a function of polymer concentration is shown in Figure 6.5. In general, there is an increase in yield stress with an increase in polymer addition, which is due to the increased bridging and enhanced polymer particle interactions for a stronger particle network. It is apparent that PAM S and PAM C addition, both pre and post-shear, exert a much higher yield stress on each system than was observed in the previous chapter

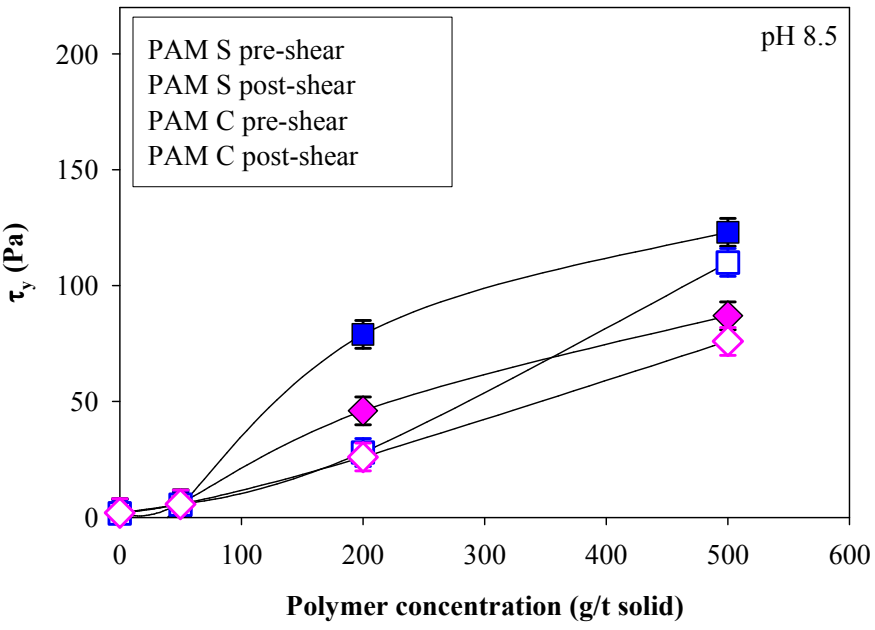
for PAM A and PAM N. PAM S and PAM C addition was also observed by Bal to give higher yield stresses than PAM A flocculated gibbsite pulps at pH 7.5 [147], with values at 200 g/t being 200, 290 and 350 Pa for PAM A, PAM C and PAM S flocculated pulps, respectively. It can also be seen (in), that PAM S and PAM C have a much higher adsorbed amount than PAM A. PAM N can only bond to the iron oxide particles via hydrogen bonds, whereas PAM A can bond electrostatically and chemically. This may also be the case for the other charged polymers, which explains PAM N flocculated dispersions having a low yield stress despite a high adsorbed amount. It has been noted in previous spectroscopic studies along with Chapter 4, that PAM A interacts with the negatively charged particles at high pH via a chemical bond to the iron oxide surface [35, 37], and it appears that this may also be the case for PAM S and PAM C. Spectroscopic studies on the adsorption of such polymers are not available as yet.

In Figure 6.5a, the rheology of pulps flocculated with PAM S, and PAM C at pH 6 is described pre and post-shear. The application of shear decreased the yield stress, due to a break up of the flocs. The same trend is displayed at pH 8.5 as shown in Figure 6.5b.

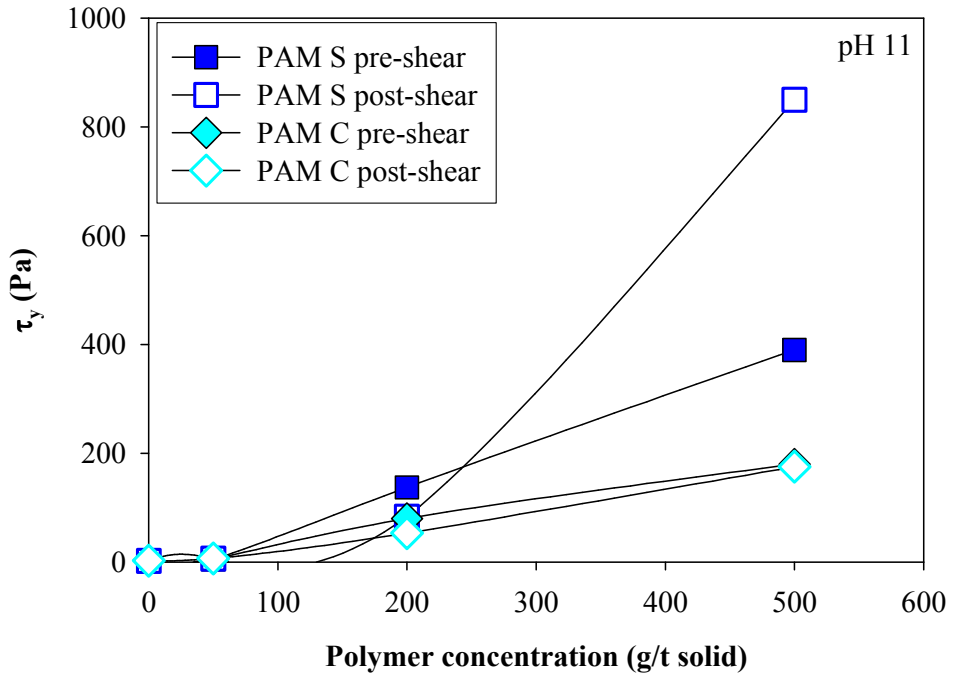
At pH 11 in Figure 6.5c, flocculation of iron oxide dispersions with PAM S, and PAM C increased the yield stress as for pH 6 and 8.5, however a different effect is seen after the application of shear. For both pH 6 and 8.5, the application of shear in all cases lowers the yield stress. Here we see for the PAM S flocculated pulps that shearing increased the yield stress. It has been previously noted that upon the application of shear at high pH, the yield stress of PAM A flocculated iron oxide increased (Chapter 5). This may be attributed to elimination of longer range electrostatic repulsion by the input of greater energy into the dispersion, allowing the polymers to interact more closely and create stronger networks with the particles which facilitate a higher yield stress. This is also observed here with anionic PAM S. PAM C, again, has a lower yield stress after shear.


pH 6
PAM S pre-shear
PAM S post-shear
PAM C pre-shear
PAM C post-shear
τ_y (Pa)
Polymer concentration (g/t solid)
0
50
100
150
200
250
300
0
100
200
300
400
500
600

(a)


pH 8.5
PAM S pre-shear
PAM S post-shear
PAM C pre-shear
PAM C post-shear
τ_y (Pa)
Polymer concentration (g/t solid)
0
50
100
150
200
0
100
200
300
400
500
600

(b)



(c)

Figure 6.5: Shear yield stress as a function of PAM concentration on iron oxide particles with 10^{-3} M KNO_3 at (a) pH 6, (b) pH 8.5 and (c) pH 11

The consolidation of iron oxide is dramatically improved after shear when the polymer and particles are of the same charge, which correlates directly with the yield stress for PAM S flocculated pulps decreasing after shear. This was not seen, however, in the rheological data for PAM C at pH 6. Bal [147] found that in all cases for PAM S and PAM C flocculated gibbsite dispersions that yield stress decreased after shear, and this effect has not been seen elsewhere. It appears to be specific to the anionic polymers at high pH.

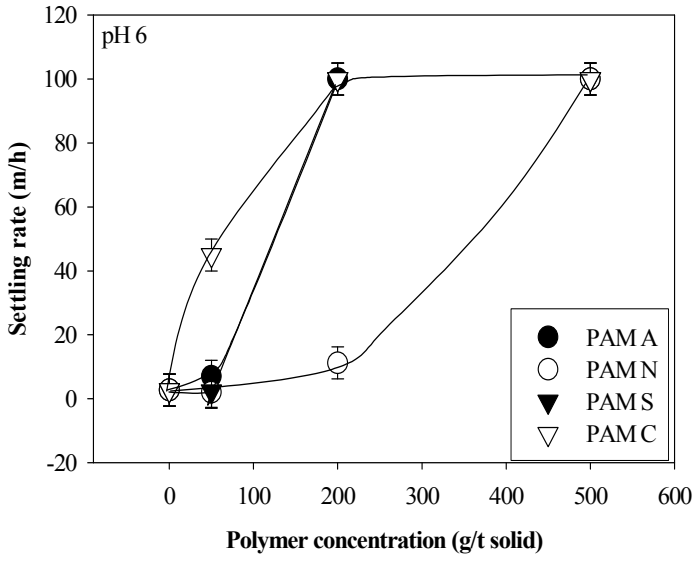
6.2.5 The impact of different polymeric functional groups on the dewatering of iron oxide

When looking at the data from Chapters 5 and 6, there are several trends emerging from the investigation of all four polyacrylamides and their effects on dewatering iron oxide dispersions. The first is primarily the effect of polymer charge. PAM N has the least effect on the settling rate, due to its non-ionic nature (see summary of settling rates in Figure

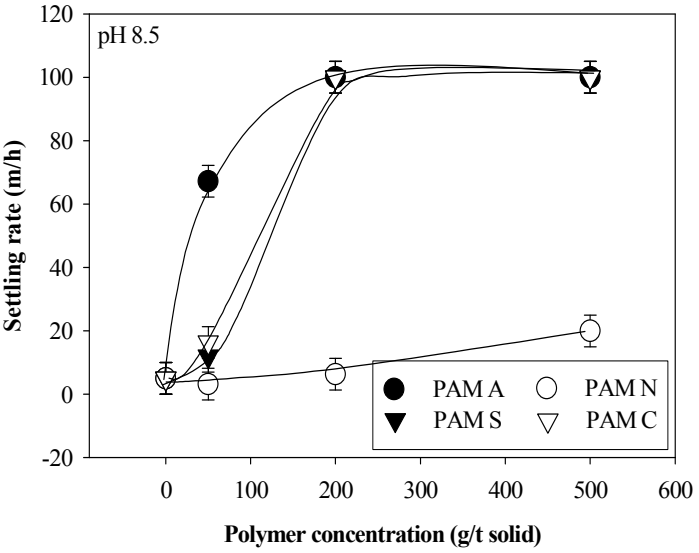
6.6). This is similar to the settling data for PAM C at pH 11, as it is above its pKb and non-ionic at this point. Settling rates appear to be better when the polymer has the same charge as the dispersion, with the data at pH 6 showing the cationic polymer to dewater more effectively, and the limited data showing the anionic polymers as more effective at high pH. As the settling rates are higher when the particles have the same charge as the particles, then the major mechanism of flocculation is bridging by chemical bonding and hydrogen bonding. With regards to the specific functional groups that differentiate anionic PAM A and PAM S, PAM A is a better flocculant at and above the iep of iron oxide. PAM A and S, however, display similar flocculation behaviour when the particles in the dispersion are positively charged. PAM S gives a higher adsorbed amount at each pH, suggesting that it has favourable functional groups for adsorption, but PAM A, whilst having a lower adsorbed amount, induces higher settling rates. As shown by the zeta potential for flocculated particles, the data suggests that the electrical double layer repulsive forces and, hence, energy barrier, will be greater for PAM S based flocs than PAM A based flocs.

With regards to consolidation, it also appears that a polymer of similar charge to the dispersion is optimal (see Figure 6.7). This is due to the flocculated pulps being more sensitive to the application of shear which allows closer packing of particles.

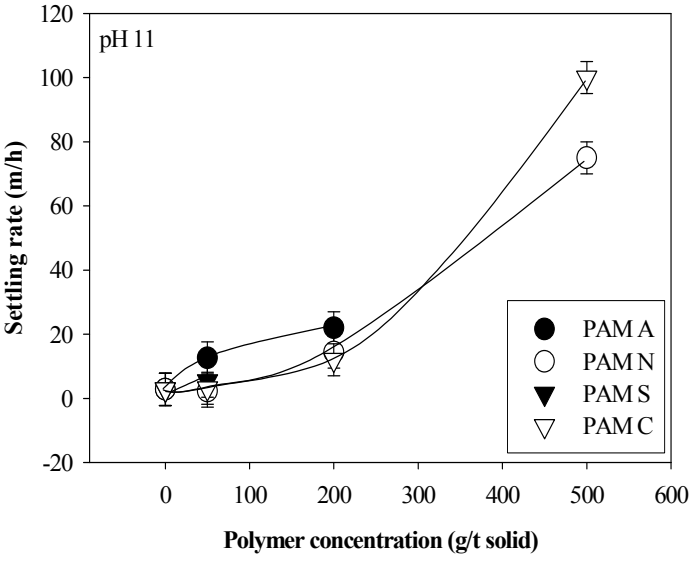
McFarlane [148] found that anionic PAM A and PAM S were more effective on negatively charged smectite and kaolinite dispersions, and that PAM C was not as effective. McFarlane suggested that bridging flocculation was the predominant flocculation method (rather than depletion) and that charge patch was less effective as exhibited through PAM C's poor performance. Many authors, however, have found cationic polymers useful for dewatering clays, although some were in synergy with an anionic polymer [40, 149-151]. Mpofu *et al*. [6, 8, 17, 31, 32] generally found anionic PAM A to be successful in flocculation of clays, but generally found non-ionic PEO to be most successful. It thus appears that there is no specific trend in the literature as to whether polymers of the same charge as the dispersion are more or less successful in flocculation of that system although that appears to be the case here.



(a)

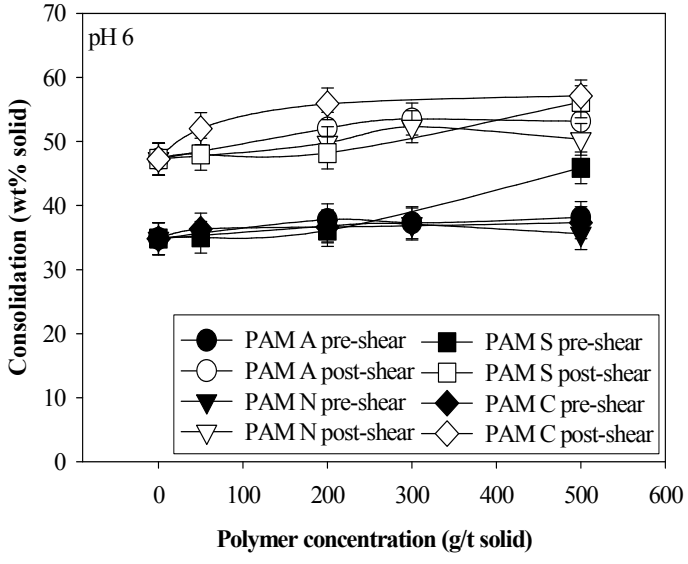


(b)

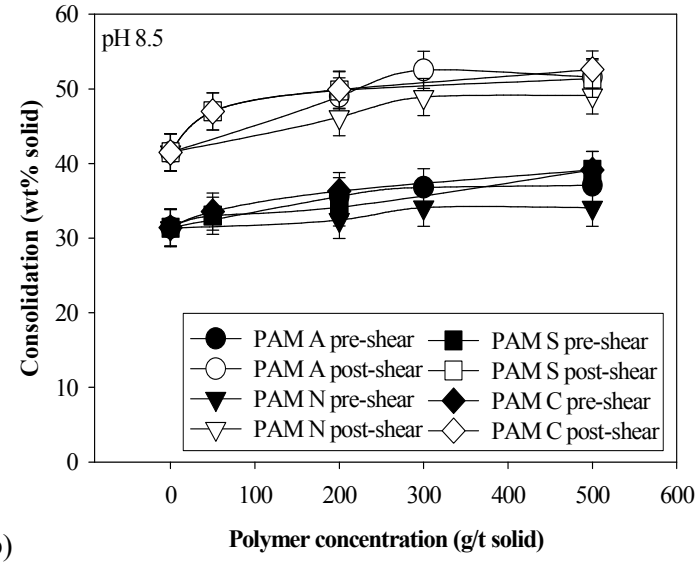


(c)

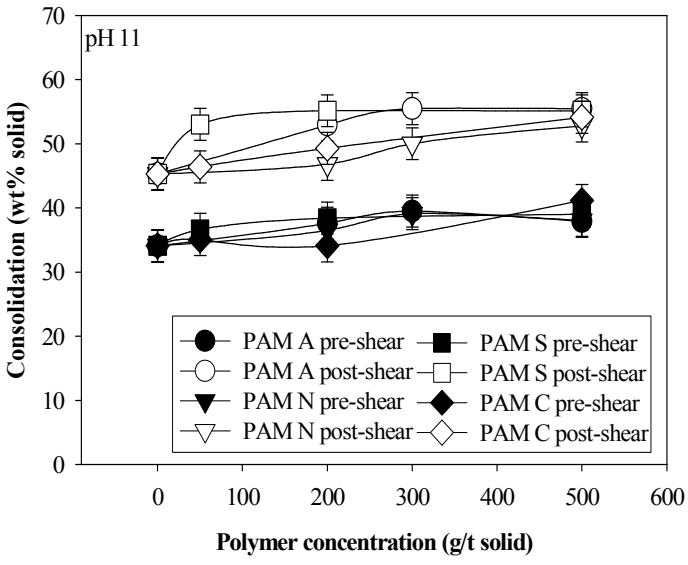
Figure 6.6: Summary of settling rates showing dewatering with all four polymers at (a) pH 6, (b) pH 8.5 and (c) pH 11



(a)



(b)



(c)

Figure 6.7: Summary of consolidation of iron oxide after dewatering with all four polymers at (a) pH 6, (b) pH 8.5 and (c) pH 11

6.3 CONCLUSION

The effect of anionic and cationic polyacrylamide flocculants, pH and shear on the interfacial chemistry, rheology and dewaterability of hematite dispersions has been studied. For enhanced settling behaviour, PAM C was the most effective flocculant at pH 6, where the polymer and the particles are both positively charged. Flocculation was, in general, more effective at and below the hematite particle iep. The addition of flocculants up to 500 g/t had either little effect or a small effect (7%) in improving the consolidation with the exception of PAM S at low pH, which increased consolidation by 10 wt%. Application of shear to the consolidated particle bed, in all cases, increased the consolidation dramatically by 10-20 wt%, with the best results occurring when the polymer and the particle have like charges.

For the selection of a flocculant, a polymer which will display a similar charge to that of the particles has been shown to provide an improved flocculation and dewatering performance. This indicates that the predominant flocculation mechanism for these polymers is bridging, facilitated through chemical and hydrogen bonding. Electrostatic or charge patch mechanisms are indicated where the polymers are of opposite charge to the particles.

Adsorption isotherms conformed to the Freundlich model indicating continued polymer adsorption with continued polymer addition, PAM C having the highest adsorbed amounts. PAM S had more of an effect on the zeta potential of iron oxide dispersions at and below the iep, as shown through their effects on the zeta potential. Shear yield stresses were greatest for iron oxide dispersions flocculated with PAM S and PAM C at all three pH values, with yield stress being higher at high pH.

CHAPTER 7 Synergistic effect of metal salt coagulants and polyacrylamide-acrylate flocculant on the dewaterability of hematite dispersions

7.1 SUMMARY

The effect of four metal salts ($Mn(NO_3)_2$, $MnSO_4$, $MnCl_2$, and K_2SO_4) as coagulants on enhancement of interfacial chemistry through zeta potential, flocculation performance and dewaterability of hematite (α-Fe_2O_3) dispersions was investigated at pH 6 and 11. PAM A flocculant was used in conjunction with the metal salts to improve the primary dewatering via coagulation-mediated fast settling floc formation and secondary dewatering through compact consolidation. The salt addition at ionic strength range $(1.0 – 4.0) \times 10^{-3}$ M enabled specific effects of the anions or cations to be probed at the two pH values studied. The sulphate ion had the greatest effect of dramatically reducing the magnitude of hematite particle zeta potential, especially at pH range 2 - 8. Mn (II)-based chloride and nitrate salts addition between pH 7 and 9 resulted in significant increase in zeta potential. Pre-addition of the salts had a dramatic impact on flocculated particle zeta potential where the zeta potential was greater in the presence of chloride and nitrate based-Mn (II) salts than Mn (II) and K^+-based sulphate salts. In contrast to results in previous chapters, pre-addition of the salt led to higher settling rates at high pH than at low pH.

Synergistic interactions between the sulphate ion and PAM A at high pH possibly led to higher ion-polymer complex charge, mitigating polyacrylamide adsorption. Mn (II) species, whilst having a subtle effect on the zeta potential at the lower pH, played a more influential part in the PAM A adsorption. The settling rate was significantly improved by the presence of the sulphate ion, however no noticeable effect on sediment consolidation was observed. The application of shear to sedimented pulps led to dramatically improved consolidation as observed in previous chapters.

7.2 INTRODUCTION

Iron oxide mineral is known to be present in many phases in mineral tailings, with anhydrous particles generally hydrolysing such that hydroxide groups (–OH) are present on the particle surface. These surface groups then either protonate (to $–OH_2^+$) or deprotonate (to $–O^-$) depending on the pH of the solution, and where the isoelectric point of the mineral lies [12]**.** In an aqueous environment, the iron oxide particles surface becomes hydrolysed to oxyhydroxide (FeOOH), and hydroxide ($Fe(OH)_3$) depending upon prevailing solution conditions [52, 53]. Single, double and triple coordination of Fe-OH groups at the particle surface may occur at various crystallographic faces. This may lead to different charging behaviour and reactivities at the various faces [52]. It has been established by several interfacial studies of iron oxide that isoelectric point (iep) values in the range of 5.5-9 are commonly observed [12, 50, 52-59].

Ionic species of soluble salts are commonly prevalent in plant process water and tailings at concentrations that can invariably impact on the pulp chemistry and dewatering behaviour. Hydrolysable metal ions and soluble salts have been previously shown to be influential in the manipulation of mineral particle surface chemistry and colloidal stability [31, 69, 70, 77, 79, 80, 90]. Dissolved salts (which act as coagulants) alter the interfacial chemistry of dispersions by reducing the zeta potential or surface charge on the particles, facilitating attractive interactions and improving aggregation. Multivalent metal ions such as Ca(II), Mn(II) and Fe (III) undergo hydrolysis and specific adsorption at certain solution pH values and may act to dramatically reduce the magnitude of the zeta potential of negatively charged mineral particles to zero [31, 50, 69, 74, 77, 79, 80]. They may even cause complete reversal of the original particle charge via hydrolysis, specific adsorption and surface nucleation. Both the hydrolysis and subsequent adsorption of hydrolysed metal ion complexes are pH and metal ion dependent. The nature of the mineral particle surface chemistry also plays an important role in the metal hydrolysis product adsorption process.

It is pertinent to note that whilst solution metal hydroxy complexes may specifically adsorb onto deprotonated iron oxide particles in aqueous suspensions and markedly impact on the electrokinetic zeta potential, simple ions such as NH_4^+ can also induce a similar effect [12]. Likewise, simple anionic species (e.g. $SO_4^=$) may also exert significant impact on the zeta potential of the positively charged oxide particles through specific adsorption, impacting upon colloidal stability and hence, mineral pulp dewaterability [74, 81].

In previous chapters (4-6), the mechanisms of high molecular weight homo- and co-polymer (both anionic and cationic) adsorption and bridging flocculation and concomitant dewatering behaviour of hematite dispersions were investigated at pH 6-11 in the presence of 10^{-3} M KNO_3 as an indifferent electrolyte. In the present work, the possible synergistic influence of aqueous anionic and cationic species from hydrolysing and non-hydrolysing metal salts as effective coagulants on the flocculation of hematite dispersions is investigated for dewatering improvement. The investigation was carried out at pH 6 and pH 11 which lie below and above the iep of hematite, respectively, enabling anionic or cationic species in solution to undergo electrostatic attraction with the iron oxide surfaces.

Four metal salts; $MnSO_4$, $MnCl_2$, $Mn(NO_3)_2$ and K_2SO_4 were used in conjunction with high molecular weight anionic polyacrylamide. Mn (II) has been shown to hydrolyse and specifically adsorb at $6 < pH < 8$ [31]. Anionic PAM A has proved to be an effective polymer for iron oxide flocculation and dewatering.

7.3 RESULTS AND DISCUSSION

7.3.1 Surface chemistry

Figure 7.1 displays the zeta potential of the hematite particles as a function of pH and in the absence and presence of coagulants: $MnSO_4$, $MnCl_2$, $Mn(NO_3)_2$ and K_2SO_4. All five of the conditions studied have 10^{-3} M KNO_3 background electrolyte and hence, the dispersion without any of the four coagulants added has been labelled as the "control." The iep of the control dispersion is ~ pH 8.5, and the zeta potential is high at pH 2 (~ +115 mV) and low at pH 12 (~ -70 mV). $Mn(NO_3)_2$ and $MnCl_2$ have the same effect on the zeta potential, where they both caused an overall increase in the magnitude of potential at between pH 6 and 8. This may be due to $Mn(OH)_2$ surface nucleation caused by Mn(II) hydrolysis, specific adsorption and precipitation which has been shown to occur at pH range 7 – 9 [11] (See Figure 7.2). Both $MnSO_4$ and K_2SO_4 also have similar effect, both significantly reducing the magnitude of the zeta potential through charge neutralisation by the $SO_4^{=}$ ion, particularly below the iep.

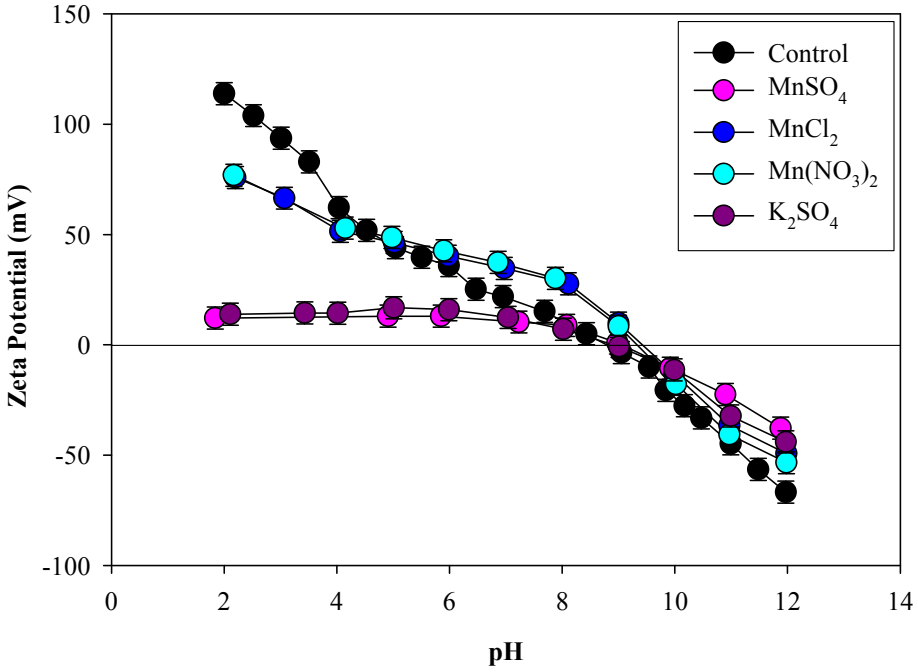


Figure 7.1: Zeta potential as a function of pH for iron oxide particles with 10^{-3} M $MnSO_4$, $MnCl_2$, $Mn(NO_3)_2$ and K_2SO_4. Note that 10^{-3} M KNO_3 is present in all samples, and is hence labelled the control group.

It may be expected that all three Mn(II) salts would have a similar effect on zeta potential if the anions behave as indifferent ions, as is the case with $Mn(NO_3)_2$ and $MnCl_2$. The decrease in zeta potential by $MnCl_2$ and $Mn(NO_3)_2$ may be attributed to the compression of the electrical double layer and charge shielding. The effect caused by $MnSO_4$, on the other hand, is consistent with specific adsorption of the $SO_4^{=}$ ion onto the surface of the positively charged hematite particles [90]. It is known that charge suppression at pH > iep and a shift of the iep to the right occurs as the result of specific adsorption of an electropositive ion, whilst a shift in iep to the left and suppression in charge at lower pH suggests specific adsorption of an anionic species [90].

****This drawing has been removed. Please see referenced source for drawing.****

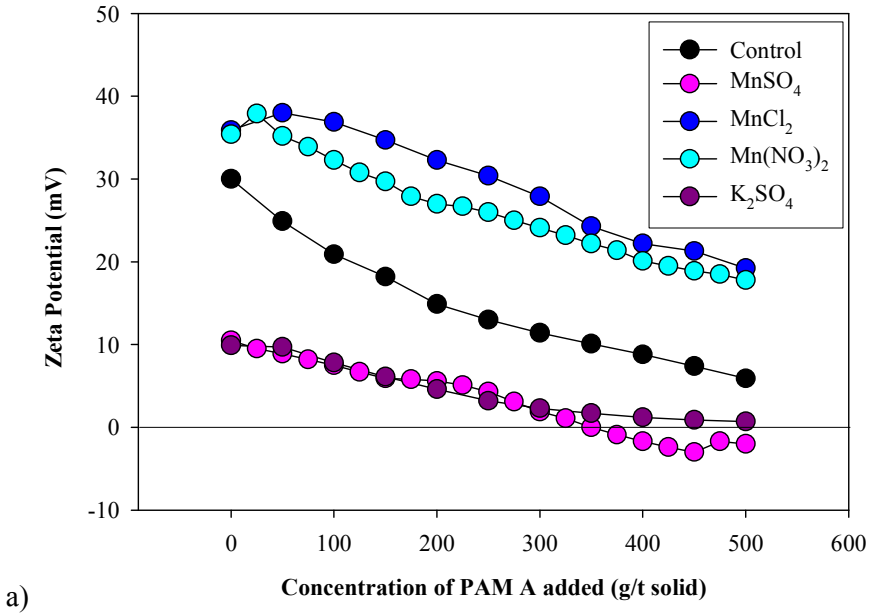
Figure 7.2: Calculated hydrolysis diagram (A) and fractional abundance (B) of Mn(II) with the distribution of various species: Mn^{2+} (open triangle), $Mn(OH)^{+}$ (open circle), $Mn(OH)_3^-$ and $Mn(OH)_4^{2-}$ taken from [31].

The striking impact of the $SO_4^{=}$ ion on the magnitude of the zeta potential of the positively charged particles was reproducibly shown when K_2SO_4 salt was added at the same ionic strength. It is evident that Mn (II), K^+, Cl^- and NO_3^- ions in solution exert an indifferent ion influence via electrical double layer compression with systematic zeta potential reduction. For the behaviour of $SO_4^{=}$ ions, Juang and Wu [74] observed a similar effect when Na_2SO_4 and $CuSO_4$ were added to a goethite (α-FeOOH) dispersion. In both cases, at pH values below the iep, the zeta potential was suppressed to < 20 mV, as was seen in this study. Above the iep, the zeta potential was similar to that of the control, as was also seen here. It was noted that whilst there was evidence to suggest specific inner-sphere adsorption of $SO_4^{=}$ ions, the constancy of the iep value suggests otherwise. It has been rationalised that

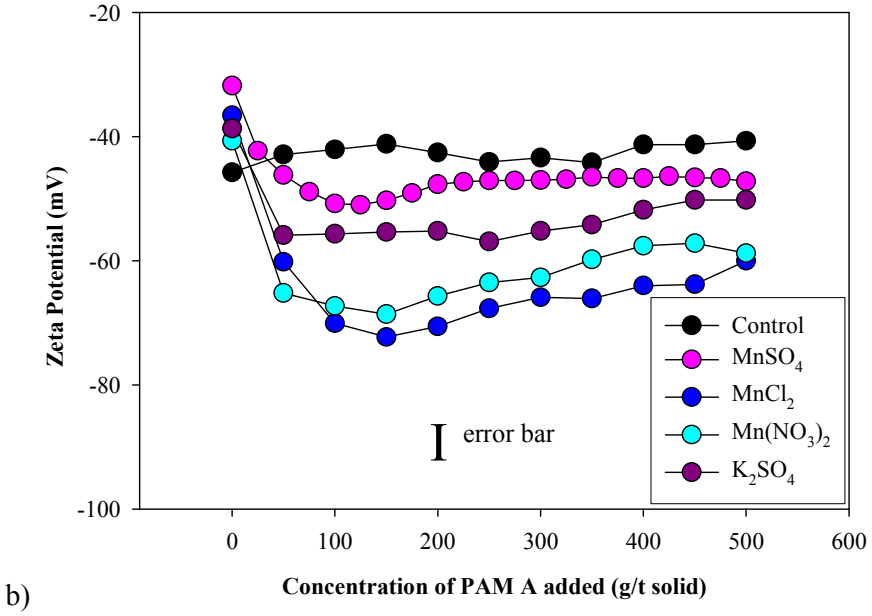
the $SO_4^{=}$ ion was electrostatically bound (physisorption), but that the outer-sphere binding complex was strong enough such that the $SO_4^{=}$ ion moved with the particle, reminiscent of a chemisorbed ion or inner sphere complex [29].

Figure 7.3a shows the zeta potential of hematite particles in the presence of 10^{-3} M $MnSO_4$, $MnCl_2$, $Mn(NO_3)_2$ and K_2SO_4 at pH 6, following the addition of up to 500 g PAM A/t solid, which is close to the maximum flocculant dosage for most industrial dewatering applications. In each case, the addition of the anionic polymer causes the positively charged particle zeta potential to become more negative as expected. It is also apparent that $Mn(NO_3)_2$ and $MnCl_2$ have a substantially similar effect on the electrokinetic zeta potential behaviour, as was the case for $MnSO_4$ and K_2SO_4. Increasing the anionic polymer dosage reduced the zeta potential of the particles from ~38 mV to ~20 mV, for the former. Polymer addition has the similar effect on each system here, suggesting that once the metal salt has adsorbed, there is no further synergistic effect with the polymer. Complete charge reversal occurred after the addition of 350 g/t PAM A for the dispersion with pre-adsorbed $MnSO_4$.

Figure 7.3b displays the zeta potential of iron oxide at pH 11, in the presence of salts and following the addition of 500 g PAM A/t solid. Addition of PAM A leads to a dramatic increase in the magnitude of the zeta potential for the dispersions containing $Mn(NO_3)_2$ and $MnCl_2$, which behave in a similar fashion. Upon addition of 100 g PAM A/t solid, it is apparent that the zeta potential has been shielded close to its full extent, and that further addition of anionic PAM A only serves to slightly decrease the negativity of the floc particle charge.



a)



b)

Figure 7.3: Zeta potential of iron oxide particles as a function of PAM A addition in the presence of 10^{-3} M $MnSO_4$, $MnCl_2$, $Mn(NO_3)_2$ and K_2SO_4 at (a) pH 6 and (b) pH 11. Note that 10^{-3} M KNO_3 is present in all samples, and is hence labelled the control group.

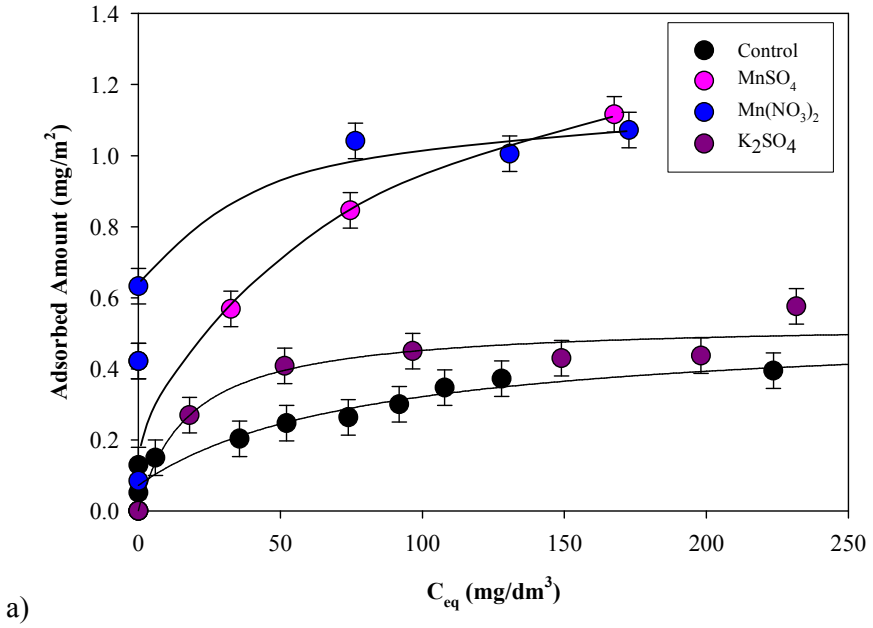
7.3.2 Adsorption isotherms

The isotherms for PAM A adsorption onto iron oxide at pH are shown in Figure 7.4a. The data for $MnCl_2$ are not included due to their close similarity to those for $Mn(NO_3)_2$. Thus, the data $Mn(NO_3)_2$ which contains the common NO_3^- ion with the control run are reported hereafter. The adsorbed amount of PAM A at pH 6 is greatly enhanced by prior addition of the Mn(II) salts, $Mn(NO_3)_2$ and $MnSO_4$ as opposed to the addition of the non Mn(II)-containing salts, K_2SO_4 and the control.

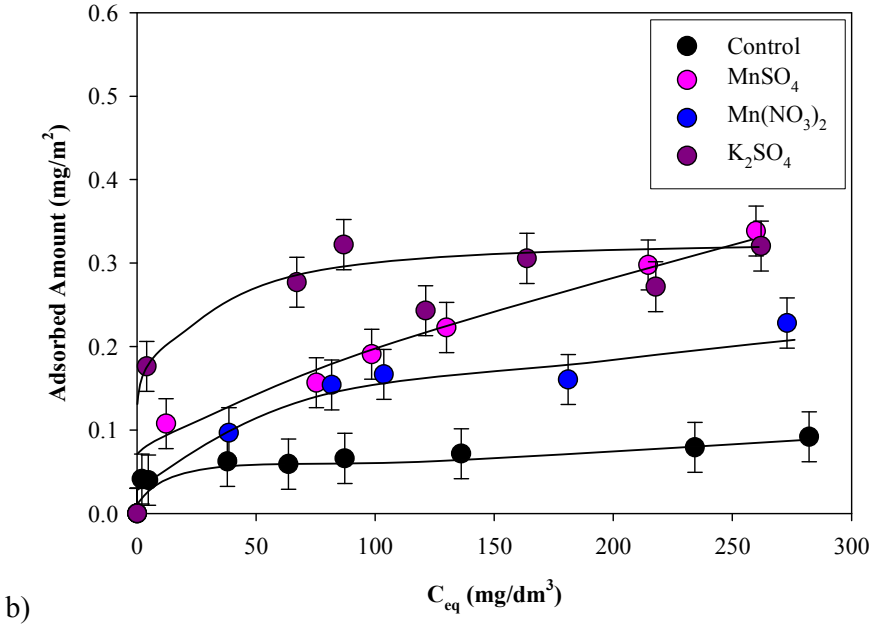
The adsorption isotherms were found to fit the Freundlich model for adsorption, and the adsorption affinities are displayed in Table 7.1. For pH 6, the adsorption affinities are ranked $Mn(NO_3)_2 > K_2SO_4 > KNO_3 > MnSO_4$, and the adsorption isotherms show the adsorbed amount to be much higher for those dispersions containing the Mn(II) species. The data in Figure 7.3 shows the effect of polymer adsorption on the zeta potential up to 500 g/t of PAM A addition, which represents approximately the second data point on each isotherm. At this point, the adsorption affinities show a trend similar to that of the zeta potential shown in Figure 7.3b at pH 11, at 500 g/t PAM A addition. The control and the K_2SO_4 containing dispersion have similar zeta potentials (at 500 g/t in Figure 7.3a), with the Mn(II)-containing dispersions showing opposite behaviour with one dispersion being positive and attractive to the negatively charged polymer ($Mn(NO_3)_2$), and the other being negative ($MnSO_4$), and hence repulsive. Despite this, it appears that the Mn(II) ion is dictating the adsorption behaviour.

Figure 7.4b, however, shows a different trend for the adsorption isotherms at pH 11. Whilst K_2SO_4 had little effect on the adsorption of PAM A at low pH, it has increased adsorption significantly at high pH. $MnSO_4$ has lead to higher PAM A adsorption again, whilst $Mn(NO_3)_2$ has had less of an effect, but still doubled the adsorbed amount compared to the control. This was also observed by Mpofu *et al*. [31] found that the $Mn(OH)^+$ ion greatly increased adsorption at pH 7.5, but had no significant effect at pH 10.5 where it precipitated as $Mn(OH)_2$ particles. This suggests that at high pH, it is the $SO_4^=$ ion facilitating strong anionic polymer adsorption, contrary to expectation. Chemical bonding through complexation was seen to occur at high pH between iron oxide particles and PAM A in Chapter 4, despite the anticipated electrostatically repulsive interactions. This has also been observed in other studies [35-37], and thus it is possible that the $SO_4^=$ ion somehow facilitates this complexation further to give higher adsorbed amount as observed here.

Higher adsorption is expected however, for the pulps with added ions, due to an increase in ionic strength and a reduction in the electrical double layer repulsion allowing greater adsorption.



a)



b)

Figure 7.4: Adsorption isotherms for PAM A adsorption onto iron oxide particles in the presence of 10^{-3} M $MnSO_4$, $Mn(NO_3)_2$ and K_2SO_4 at (a) pH 6 and (b) pH 11. Note that 10^{-3} M KNO_3 is present in all samples, and is hence labelled the control group.

Table 7.1: The Freundlich model adsorption affinities for pH 6 and 11 for iron oxide particle dispersions containing 10^{-3} M $MnSO_4$, $Mn(NO_3)_2$, K_2SO_4 and the control group

	$1/n_F$ adsorption affinity constant	
	pH 6	**pH 11**
Control	0.29	0.16
$MnSO_4$	0.41	0.61
$Mn(NO_3)_2$	0.14	0.38
K_2SO_4	0.23	0.13

Again, the Freundlich adsorption affinities from Table 7.1 reflect the zeta potential shown in Figure 2b. The adsorption affinities are ranked K_2SO_4 > KNO_3 > $Mn(NO_3)_2$ > $MnSO_4$, which reflects the zeta potential becoming less negative. The only discrepancy is that the trend for the potassium containing dispersions is reversed, which is expected due to the reduction in the double layer as a result of increased ionic strength for the K_2SO_4 system. The adsorption affinities again are not indicative of the adsorbed amount, which show the $SO_4^{=}$-containing pulps to have the highest adsorbed amounts with the highest and the lowest adsorption affinities. It is apparent that the addition of the metal salts at both pH values generally leads to a significant increase in polymer adsorption.

7.3.3 Dewatering behaviour

Figure 7.5 describes the settling rates of iron oxide particles in the presence of various metal salts, at two pH values (6 and 11). Flocculation with PAM A is either absent (0 g PAM A/t solid) or at 50 g PAM A/t solid, which is a standard industry flocculant dosage. In most cases, with the exception being dispersions containing Mn(II) at pH 6, flocculation with 50 g/t PAM A more than doubles the settling rate. It therefore appears that whilst Mn(II) addition more than doubles the adsorbed amount of PAM A at this pH, that this is detrimental to the settling rate. This suggests that the percentage of monolayer coverage has surpassed that required for optimal flocculation conditions.

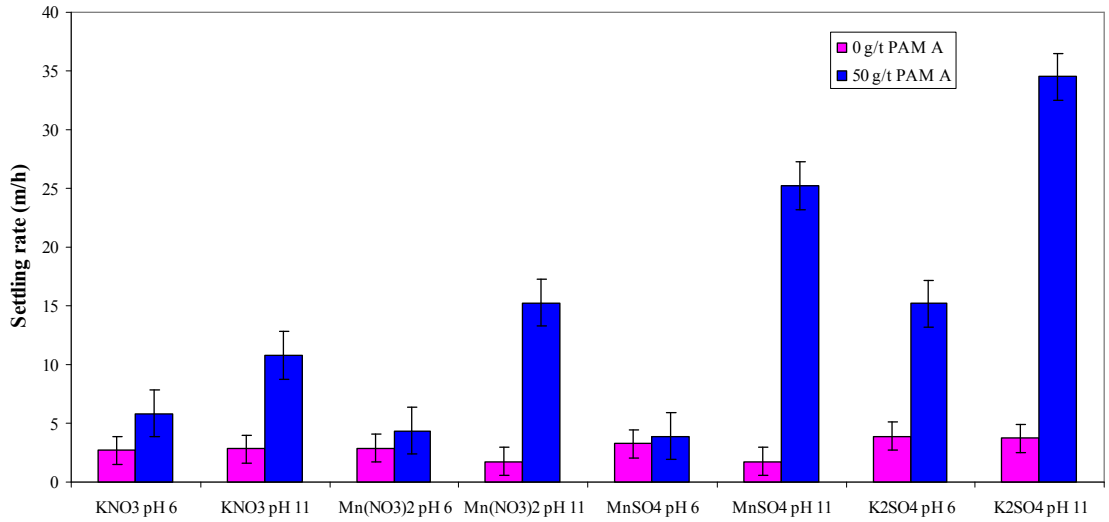


Figure 7.5: Settling rates of iron oxide particles as a function of pH in the presence of 10^{-3} M $MnSO_4$, $MnCl_2$, $Mn(NO_3)_2$ and K_2SO_4, both unflocculated and flocculated with 50 g/t PAM A. Note that 10^{-3} M KNO_3 is present in all samples, and is hence labelled the control group.

The settling rate at pH 11 increased significantly from ~13 m/h to ~33 m/h in the presence of K_2SO_4. This is similar to the large effect seen after the addition of $MnSO_4$ at pH 11, which increases the settling rate to ~25 m/h. There is higher adsorption of PAM A at the higher pH after addition of these ions, and the settling rates correlate with the adsorbed amounts shown in Figure 7.4b. Addai-Mensah and Ralston [46] reported improved settling rates of iron oxide dispersions (in the absence of polymer) from a base rate of 1.5 cm^3/min to 8 cm^3/min with the addition of 0.5 M NH_4Cl, but found that this addition had no significant effect on the consolidation. Bremmell and Addai-Mensah [77] found that the settling rates of talc suspensions improved in the presence of magnesium ions, which directly correlated to a reduced zeta potential allowing faster aggregation of particles.

Table 1 shows the overall total salt concentration and ionic strength for each dispersion. It is apparent that the ionic strength effect is not controlling the dewatering behaviour as when the concentration is low (e.g. for the control run), the settling rates are comparable with that for higher ionic strength $Mn(NO_3)_2$ – based dispersion. In general, the adsorbed amounts of PAM A at pH 11 due to coagulant action followed the sequence: K_2SO_4 > $MnSO_4$ > $Mn(NO_3)_2$ > KNO_3. This observation directly correlates with the settling rates,

suggesting that zeta potential, polymer adsorption, flocculation and dewatering behaviour (settling rate) are inter-linked.

Table 7.2: Salt concentration and ionic strengths of each dispersion condition

Metal salt	Salts present	Salt concentration (M)	Total salt concentration (M)	Ionic strength (M)	Total ionic strength (M)
KNO_3	KNO_3	1×10^{-3}	1×10^{-3}	1×10^{-3}	1×10^{-3}
$Mn(NO_3)_2$	$Mn(NO_3)_2$	1×10^{-3}	2×10^{-3}	3×10^{-3}	4×10^{-3}
	KNO_3	1×10^{-3}		1×10^{-3}	
$MnCl_2$	$MnCl_2$	1×10^{-3}	2×10^{-3}	3×10^{-3}	4×10^{-3}
	KNO_3	1×10^{-3}		1×10^{-3}	
$MnSO_4$	$MnSO_4$	1×10^{-3}	2×10^{-3}	4×10^{-3}	5×10^{-3}
	KNO_3	1×10^{-3}		1×10^{-3}	
K_2SO_4	K_2SO_4	1×10^{-3}	2×10^{-3}	3×10^{-3}	4×10^{-3}
	KNO_3	1×10^{-3}		1×10^{-3}	

Consolidation of the iron oxide dispersions with various metal salts adsorbed at two pH values, pre and post-shear, are shown in Figure 5. In all cases, the addition of 50 g PAM A/t solid has no effect on the consolidation of the system, as is consistent with previous chapters. It is also apparent that metal salt adsorption has no significant effect on the consolidation of iron oxide. Mpofu *et al*. [31] found Mn(II) effective in improving the dewaterability of kaolinite dispersions at its hydrolysis pH, but found that at higher pH, the precipitation of the Mn(II) hydrolysis product was detrimental to dewatering, which was not observed here. Application of shear after consolidation resulted in up to 15 wt% improvement in consolidation as has been observed in previous chapters. This is irrespective of pH, polymer and metal salt type addition.

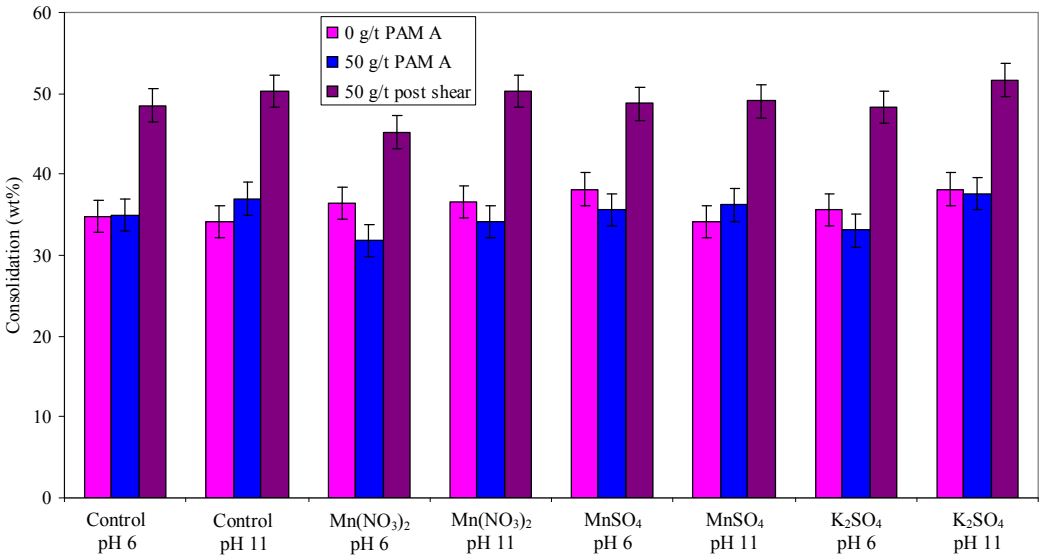


Figure 7.6: Consolidation of iron oxide particles as a function of pH in the presence of 10^{-3} M $MnSO_4$, $MnCl_2$, $Mn(NO_3)_2$ and K_2SO_4, both unflocculated and flocculated with 50 g/t PAM A. Note that 10^{-3} M KNO_3 is present in all samples, and is hence labelled the control group.

7.4 CONCLUSIONS

Metal salts have significant impact on zeta potential, anionic, polymeric flocculant adsorption and flocculation of iron oxide dispersions, impacting markedly on the pulp dewatering behaviour. The sulphate ion had the greatest effect on the interfacial chemistry, dramatically reducing the magnitude of the zeta potential, especially at pH range 2 - 8. Mn (II)-based chloride and nitrate salts addition between pH 7 and 9 resulted in significant increase in zeta potential. Synergistic interactions between the sulphate ion and anionic PAM at the higher pH possibly led to higher ion-polymer complex charge, mitigating polyacrylamide adsorption. Mn (II) species, whilst having subtle effect on the zeta potential at the lower pH, played a more influential role in the PAM A adsorption. The settling rate was most improved by the presence of the sulphate ion, however no noticeable effect on sediment consolidation was observed. However, application of modest shear to pre-sedimented pulps led to dramatically improved consolidation.

CHAPTER 8 Discussions and Applied Study*

SUMMARY

In this chapter, the key findings from the previous five experimental chapters (4-8), are summarised and discussed. A comparison is drawn between the four polyacrylamides used throughout this work, and their effects on the dewaterability of iron oxide. A case study was also conducted in conjunction with another author [148], on real plant tailings from Northparkes Mine, NSW.

* The applied study was prepared in conjunction with another author as part of an AMIRA project and the data is also published in that authors' thesis [148. McFarlane, A.J., *PhD Thesis*. 2006, Ian Wark Research Institute, University of South Australia.] and in a project report [94. Addai-Mensah, J. and J. Ralston, *Investigation of the role of interfacial chemistry on particle interactions, sedimentation and electroosmotic dewatering of model kaolinite dispersions.* Powder Technology, 2005. **160**: p. 35-39.]

8.1 DISCUSSION

8.1.1 Introduction

The aim of this study is to improve the settling behaviour and the consolidation of iron oxide dispersions through flocculation with polyacrylamides at different pH values and utilisation of the application of shear. Four high molecular weight polyacrylamides have been used in order to optimise the current dewatering practices. A non-ionic polymer, PAM N, two anionic polymers, PAM A and PAM S, and a cationic polymer, PAM C were investigated.

The work was carried out at pH 8.5, where the particles are at the iep, and at pH 6 and 11 where the particles are charged + 40 and – 40 mV, respectively. This allows the van der Waals and electrostatic interactions to be probed by observing the dewatering behaviour resulting from the interactions between positively, neutrally and negatively charged polymers and similarly charged mineral particle pulps.

The main aim of this investigation is to examine the effect of polymer structure type and adsorption behaviour on the zeta potential and rheology of iron oxide dispersions to enable their optimisation for primary dewatering and consolidation of sedimented pulps. Whilst this has been discussed previously to some extent (Chapters 5 and 6) regarding two pairs of polyacrylamide polymers, a comparison of all four polyacrylamides will be made here.

8.1.2 The mechanisms of polymer adsorption and their effect on dewatering

The adsorption mechanisms correlate well with the rheology data reported in Chapter 5. For PAM A flocculated pulps, the yield stresses are higher for systems at pH 6 and 11 than they are at pH 8.5, suggesting that the bidentate chelation mechanism of adsorption is stronger than the monodentate chelation, as would be expected through the extra chemical bond. The yield stress for pH 11 was lower than at pH 6 pre-shear, and it was suggested previously that this was due to an electrostatic barrier between the negative particle and the negative polymer needing to be overcome before extensive bonding could occur. After shear was applied to the flocculated particles, the yield stress was similar to that of pH 6

pre-shear, suggesting that this is indeed related to the adsorption mechanisms. The adsorbed amount for pH 11 is also lower than suggested by the flocculation and rheological data; this counterintuitive observation suggests that electrostatic repulsion played a large part in the adsorption process at high pH.

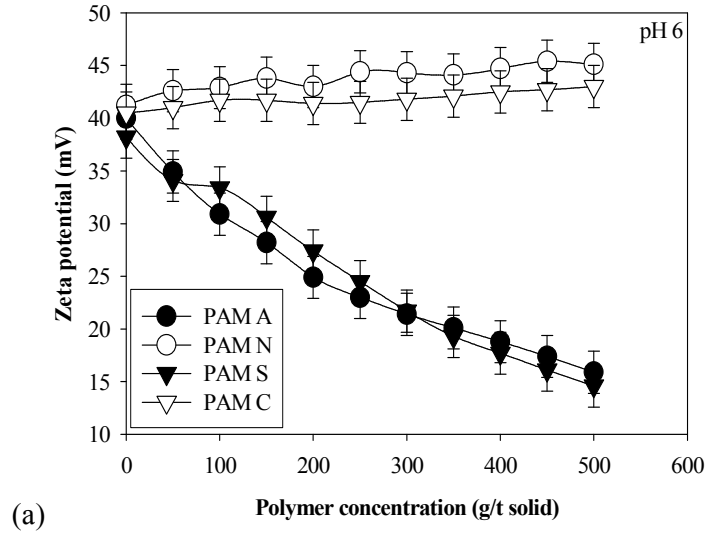
In correlation with the rheology data found in Chapter 5 for PAM N, the yield stress was higher where the hydrogen bonding is stronger for pH 11. At pH 6, the yield stress is slightly higher than for pH 8.5, again showing that the strength of the hydrogen bond influences the yield stress values.

Whilst the adsorption mechanisms do not appear to directly impact on the settling rates of the iron oxide dispersions, it does appear to underpin the rheology of the dispersion indicating that the secondary dewatering phase may be manipulated with more knowledge in this area.

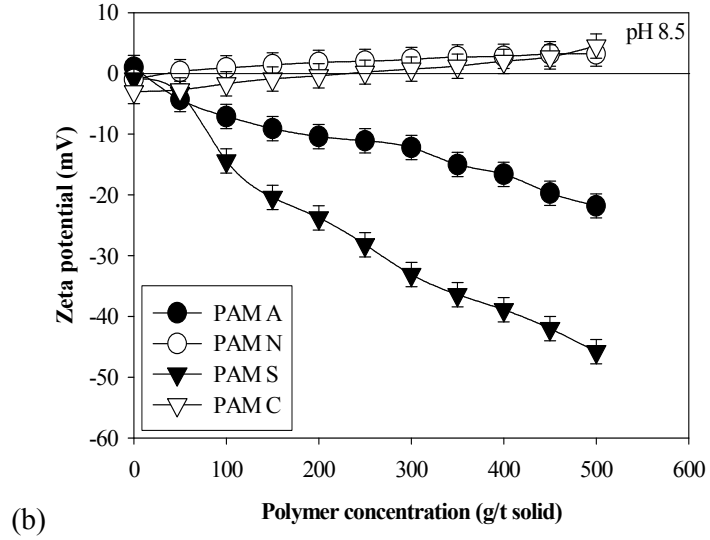
8.1.3 Influence of polymer structure type on interfacial chemistry

Figure 8.1 shows the zeta potential of iron oxide particles as a function of polymer concentration up to 500 grams polymer / ton solid. At pH 6 (Figure 8.1a), for zero polymer addition, the zeta potential was ~ 40 mV. PAM A and PAM S showed a similar trend of significantly lowering the zeta potential from ~ 40 mV to ~ 16 mV. Adsorption of polymers is known to shield the charge of particles however, as PAM A and PAM S are both anionically charged, their adsorption will also make the zeta potential more negative. Cationic PAM C had no marked effect on the zeta potential. PAM N, however, had a subtle effect which was ascribed in Chapter 5 to a thin patchy adsorbed polymer layer having a weak effect on the shear plane.

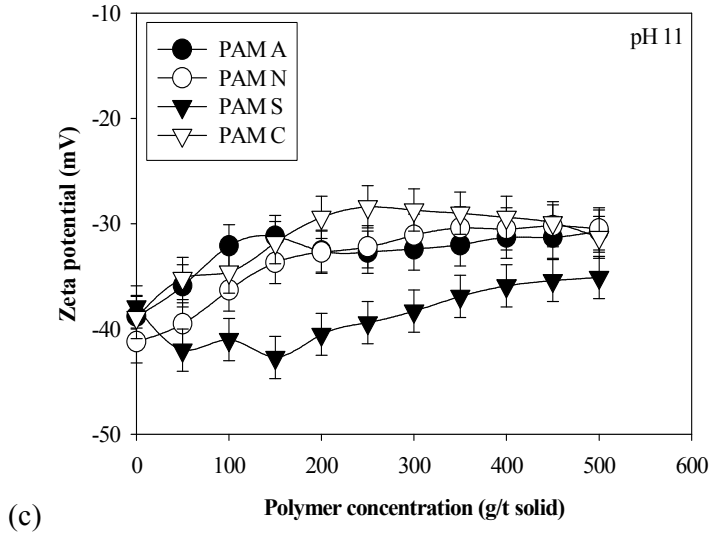
At pH 8.5 (Figure 8.1b), there is one major difference caused by the addition of polymer that is different to the effect caused at pH 6. PAM A decreased the zeta potential as previously by ~ 20 mV, whilst PAM S had a much greater effect, reducing the zeta potential of the particles by ~ 45 mV. The difference in charge could be attributed to PAM S having a lower pKa than PAM A (~1.5 vs 4.5), and therefore at pH 8.5, PAM S is more hydrolysed leading to a larger effect on the zeta potential.



(a)



(b)



(c)

Figure 8.1: The zeta potential of iron oxide particles in 10^{-3} M KNO_3 as a function of polymer addition at (a) pH 6, (b) pH 8.5 and (c) pH 11.

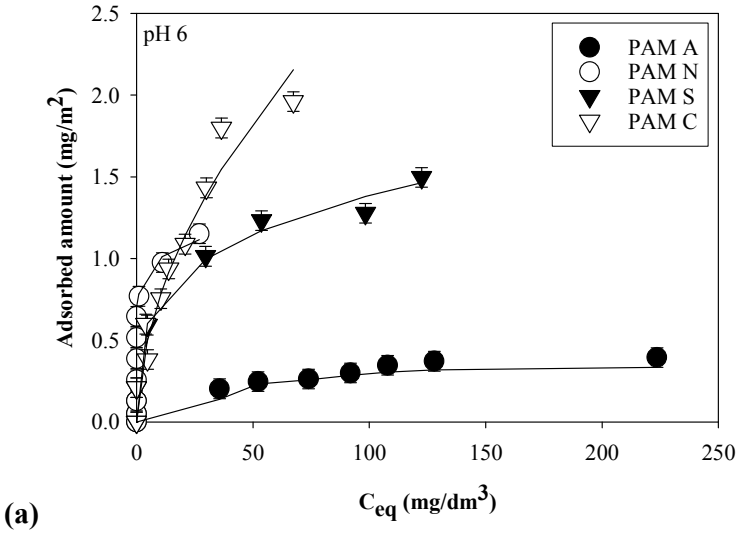
Figure 8.1c displays the zeta potential at pH 11 before and after polymer addition. PAM N, PAM C and PAM A all have a charge shielding effect on the zeta potential, due to the adsorption of polymer molecules onto particles causing a shift in the shear plane. PAM N has been noted to be partially hydrolysed at pH 11 (Chapter 4), which explains its similar behaviour to the other polymers. PAM S has more of a negative effect initially, with charge shielding behaviour beginning after 200 g/t polymer addition. The zeta potential appears to be relatively stable between 50-150 g/t.

8.1.4 Influence of polymer structure type on adsorption

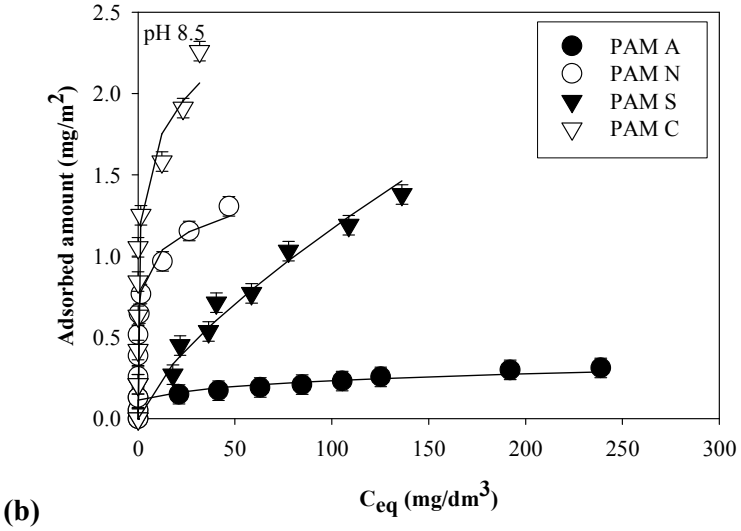
Figure 8.2 depicts the adsorption of the four polyacrylamide polymers onto iron oxide at three pH values. Regardless of pH, it can be seen that PAM S, PAM C and PAM N always have a higher adsorbed amount than PAM A.

The isotherms were fitted to both the Langmuir and Freundlich models as seen in Figure 8.3b. Through the analysis of minimum variances it was determined that the isotherms fitted the Freundlich model of adsorption, indicating that polymer continues to adsorb with increasing polymer concentration up to 7500 g/t solid, with no adsorption plateau being reached. The adsorption affinity constants were calculated using the Freundlich model [47, 90, 169] and are displayed in .

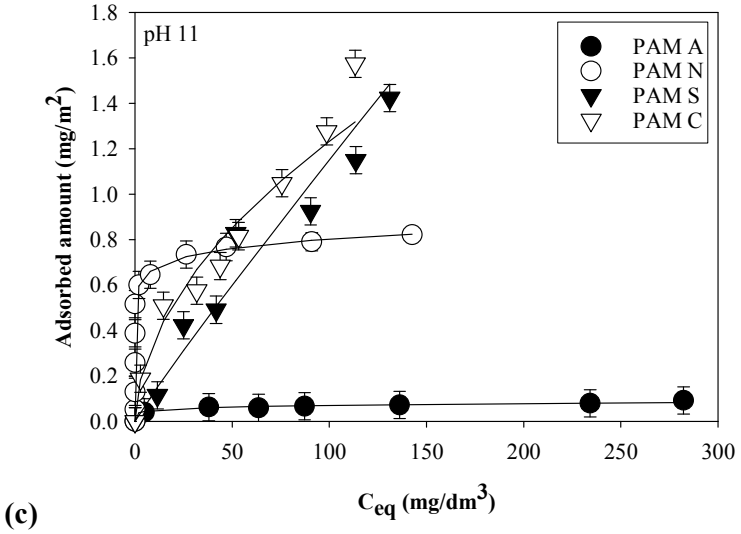
Figure 8.3a shows that PAM C has the highest adsorbed amount, followed closely by PAM N and PAM S, and then PAM A. This is contrary to expectation as anionic polymers, PAM A and PAM S, should be more attracted to the particles due to electrostatic attraction with the positively charged surface. However, this is reflected in the adsorption affinities. shows that PAM N had the highest adsorption affinity, followed by PAM S, PAM A and finally PAM C. Whilst PAM C did have a low adsorption affinity, it did have a higher adsorbent capacity than PAM A, indicating that electrostatics do play a role. Adsorption affinities will be discussed further in relation to dewatering in Section 8.1.5.



(a)



(b)



(c)

Figure 8.2: Adsorption of PAM onto iron oxide particles in 10^{-3} M KNO_3 at (a) pH 6, (b) pH 8.5 and (c) pH 11. Fits to the Freundlich model are included as solid lines.

Table 8.1: Freundlich model isotherm parameters summarised for PAM A, PAM N, PAM S and PAM C, at (a) pH 6, (b) pH 8.5 and (c) pH 11.

(a)

polymer	$1/n_F$ adsorption affinity constant	k_F (dm^3/g_{solid})
PAM A	0.29	0.40
PAM N	0.11	3.77
PAM S	0.27	1.91
PAM C	0.54	1.06

(b)

polymer	$1/n_F$ adsorption affinity constant	k_F (dm^3/g_{solid})
PAM A	0.24	0.38
PAM N	0.14	3.56
PAM S	0.73	0.20
PAM C	0.17	5.48

(c)

polymer	$1/n_F$ adsorption affinity constant	k_F (dm^3/g_{solid})
PAM A	0.16	0.16
PAM N	0.08	2.73
PAM S	0.94	0.07
PAM C	0.53	0.51

Figure 8.3b describes the adsorption isotherms for PAM A, PAM N, PAM S and PAM C onto iron oxide at pH 8.5, where the particles have no charge. PAM C had the highest adsorbed amount, followed by PAM N and PAM S, with PAM A again being the lowest. It has been established previously that higher adsorption is accompanied by faster adsorption kinetics for a polymer which has a smaller conformation at the interface. It was found with clays, that PAM A and PAM S adsorb slowly and have a more expanded conformation [148]. It has also been observed within this body of work and in the literature [8, 148], that PAM A has a more expanded interfacial conformation in solution than PAM N. With the adsorption affinities ranked PAM N > PAM S > PAM A > PAM C, it would appear that PAM C has the largest interfacial conformation. This follows logic due to intramolecular repulsion and a positively charged polymer adsorbed to a positively charged surface.

Figure 8.3c, where the particles are at pH 11 and are negatively charged, the adsorption isotherms for PAM A, PAM N, PAM S and PAM C are shown. At pH 11, we would

expect that the cationic polymer (PAM C) would have a higher adsorption due to electrostatic attraction to the surface, which is observed. PAM S also has high adsorption, indicating that electrostatic forces are not the dominant mechanism responsible for adsorption onto the oxide surface. It has been previously noted in Chapter 4 in spectroscopic studies that PAM A interacts with the negatively charged particles at high pH via a chemical bond to the iron oxide surface, and it appears that this may also be the case for PAM S and PAM C.

8.1.5 Adsorption and dewatering behaviour

The adsorption isotherms for all four polyacrylamides at all three pH values have been shown in Section 8.1.4. Adsorption affinities were ranked PAM N > PAM S > PAM A > PAM C for pH 6 (a), PAM N > PAM C > PAM A > PAM S for pH 8.5 (b), and PAM N > PAM A > PAM C > PAM S for pH 11 (c). It has been previously determined that faster adsorption kinetics (which can be applied to adsorption affinity) is concurrent with a small interfacial conformation [148]. Fast settling rates occur when particle bridging is maximised by a large interfacial polymer conformation [6, 148], and it is thus predicted that settling rates will have a negative correlation to the adsorption affinities.

Settling rates of the iron oxide dispersions flocculated with PAM A, PAM N, PAM S and PAM C can be seen in Chapter 6 in Figure 6.6. For all four flocculants and all three pH values, the settling rates of the dispersions increase with increasing polymer addition. PAM A, PAM S and PAM C are more effective flocculants than PAM N. This may be due to the non-ionic PAM N having a smaller interfacial conformation and therefore is less effective at bridging particles. The adsorption affinities were higher for PAM N in every case, predicting that it would have the poorest settling rates [148]. At pH 6, the adsorption affinities predict the settling behaviour, whereas for pH 8.5 and 11, the behaviour was not as predicted. At pH 6 (Figure 6.6a), where the particles are positively charged, it can be seen that the addition of >200 grams of polymer / ton solid yields settling rates of 100 m/h, except for PAM N. The highest settling rate of 45 m/h occurs with the addition of PAM C at 50 g/t.

Figure 6.6b shows the settling rates when the dispersion was comprised of neutrally charged particles. At pH 8.5, PAM N, after the addition of 500 g/t, only gives a settling

rate of ~20m/h. PAM A, PAM S and PAM C resulted in settling rates of 100 m/h upon the addition of 200 g/t. In this system, it is the PAM A flocculated system which has the highest settling rates at low polymer dosage, with 67 m/h obtainable upon flocculation with 50 g/t.

At pH 11, as seen in Figure 6.6c, it takes the addition of 500 g/t to achieve 100 m/h. The supernatant was also extraordinarily turbid, with the mud-line being indeterminable in many cases (hence the missing points on the graph). Flocculation with polymers at 200 g/t resulted in settling rates of 10-20 m/h, with PAM A being the best performer at 50 g/t with a settling rate of ~15 m/h.

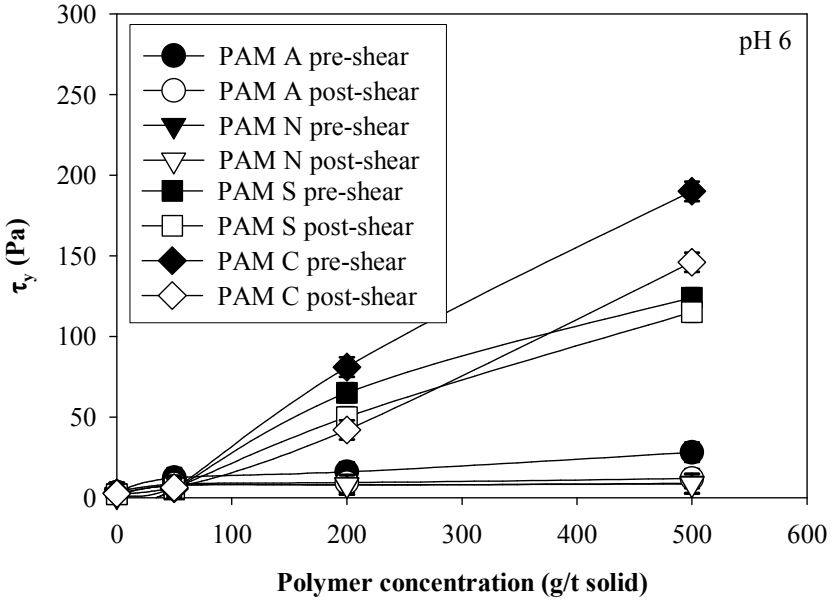
If electrostatic interactions were the driving force for flocculation, it would be expected that the two anionic polymers would flocculate best at pH 6 where their charge is opposite to that of the particles. This is not, however, the case. PAM C is a better flocculant at low dosages, which can be attributed to PAM C having a more expanded conformation at low pH due to intramolecular repulsion and being further from its pKb of 9.5. PAM A has a pKa of 4.5 and PAM S has a pKa of 1.5. This is similar to what is observed at pH 11, although to a lesser degree. PAM A has an expanded conformation at pH 11, and gives the highest settling rates before the mud-line becomes indeterminable. PAM S was difficult to observe due to turbidity also, but it was observed to have less of an effect than PAM A at 50 g/t.

As the particles are neutrally charged at pH 8.5, they will not facilitate strong electrostatic interactions during polymer adsorption and bridging flocculation. Anionic PAM A was the best flocculant, but the same behaviour was not observed for PAM S. This suggests that anionicity is not the dominant force here and that the specific functional groups on the polymer are impacting on flocculation. PAM S is a shorter polymer, as although the polymers share a similar molecular weight, the pendant group on the PAM S molecule contains four more carbons and a sulphonate group than does the PAM A molecule, making it smaller and less effective at bridging and hence a less effective flocculant. PAM A is known to specifically adsorb through the negatively charged carboxylate group, and has been observed (via infrared techniques) to do so at all three pH values [35-37].

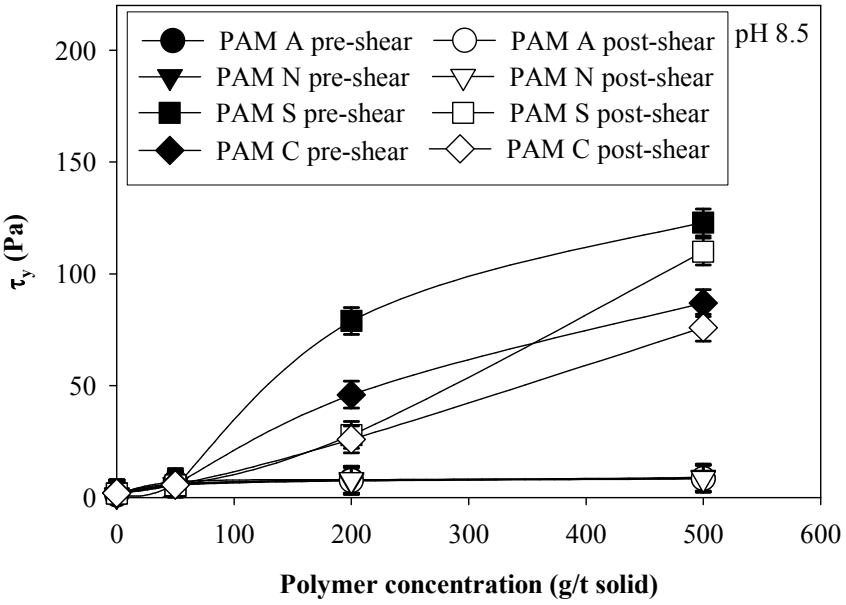
PAM N produces better settling rates at high pH compared to pH 8.5. This is due to partial hydrolysis which occurs at high pH (as discussed in Chapter 4), leading it to behave in the same manner as PAM A.

8.1.6 Influence of polymer structure type on pulp rheology

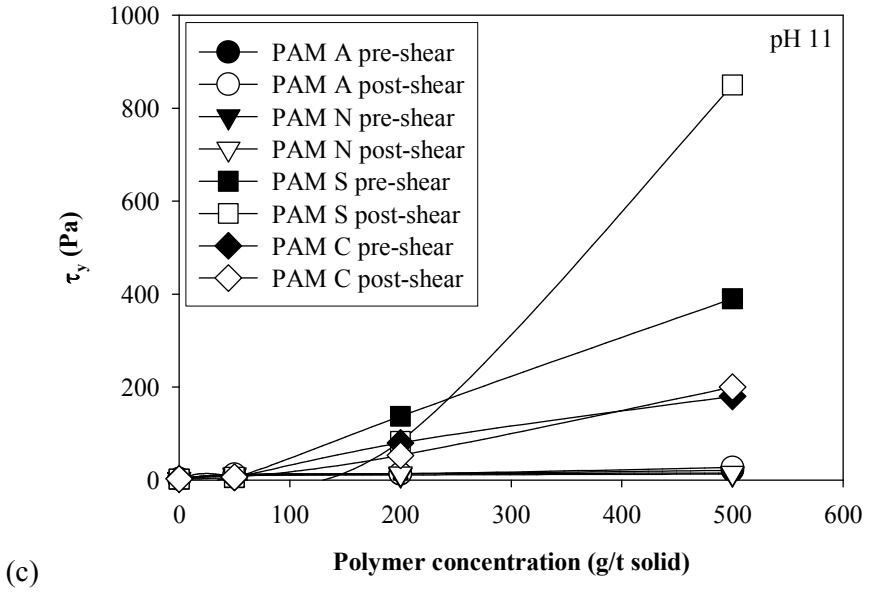
The shear yield stress as a function of polymer concentration is shown in Figure 8.3. In general, there is an increase in yield stress with an increase in polymer addition, which is due to the bridging and enhanced polymer particle interactions that form a stronger particle network and hence a higher yield stress. It is apparent that PAM S and PAM C, pre and post-shear, exert a much higher yield stress on each system than does PAM A and PAM N.



(a)



(b)



(c)

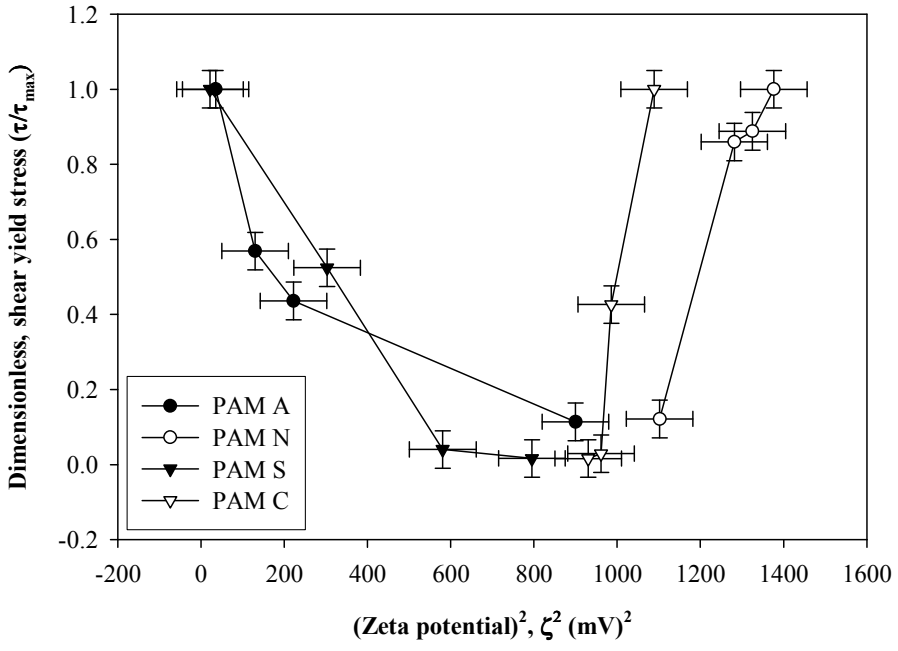
Figure 8.3: Shear yield stress as a function of PAM A concentration on iron oxide particles with 10^{-3} M KNO_3 at (a) pH 6, (b) pH 8.5 and (c) pH 11.

It is noted that the rheology of these pulps are independent of the zeta potential behaviour (PAM S and PAM A have similar trends, as does PAM C and PAM N), and of adsorption behaviour, indicating that the yield stress is influenced strongly by the polymer/particle interactions and bond strengths.

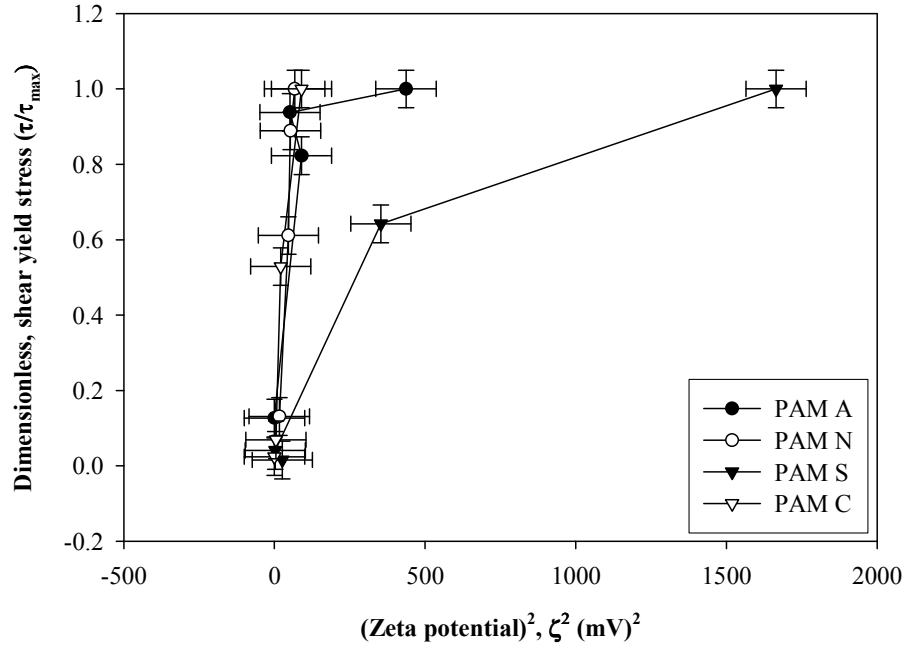
In Figure 8.3a, the rheology of pulps flocculated with PAM A, PAM N, PAM S, and PAM C at pH 6 is described pre and post-shear. With the exception of PAM N, the application of shear decreased the yield stress. As was observed in previous chapters (and is discussed below in the next section), the application of shear leads to a dramatic increase in consolidation. An increase in consolidation is expected to lead to an increase in yield stress which was not observed here. The decrease in yield stress indicates a dramatic change in the floc strength and polymer-particle interactions, indicating that the loosely formed large flocs broke down easily to enhance consolidation, but that this floc breakage lead to a lower observed yield stress. The same trend is displayed at pH 8.5 as shown in Figure 8.3b, where the PAM S and PAM C flocculated pulps exhibit much higher yield stresses than do the pulps flocculated with PAM A and PAM N. The fact that PAM S and PAM C flocculated pulps have higher yield stresses indicates that there are stronger, specific interactions between the polymers and the particles that give rise to a high yield stress.

At pH 11 in Figure 8.3c, flocculation of pulps with PAM A, PAM N, PAM S, and PAM C increased the yield stress as for pH 6 and 8.5, however a different effect is seen after the application of shear. For both pH 6 and 8.5, the application of shear in all cases lowers the yield stress. Here we see that for the PAM S and PAM A flocculated pulps (although it is difficult to see PAM A), that shear increases the yield stress. This may be attributed to elimination of longer range electrostatic repulsion by the input of greater energy into the dispersion, allowing the polymers to interact more closely and create stronger networks with the particles which facilitate a higher yield stress. This is also observed here anionic PAM S.

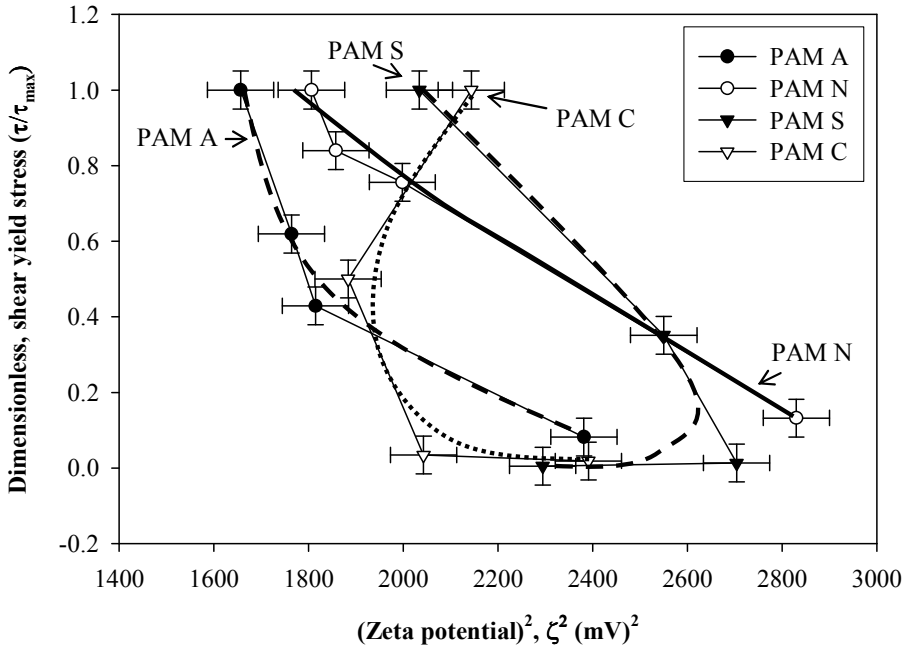
The shear yield stress as a function of the square of the zeta potential for iron oxide pulps flocculated with 0 – 500 g/t polymer is shown in Figure 8.4. The elastic floc model considers the contributions by van der Waals and electrical double layer interactions to the total particle interaction energy potential, as described by DLVO theory (see Equation 2.12). A linear relationship arising from the plot of the shear yield stress as a function of the square of the zeta potential for a given pulp chemistry indicates compliance with DLVO theory. A deviation from linearity indicates non-DLVO behaviour. In Figure 8.4a, PAM N and PAM C are observed to have a linear relationship, whereas PAM A and PAM S have a non-linear relationship. This indicates that PAM N and PAM C are compliant with DLVO theory at pH 6, whereas the trends observed with PAM A and PAM S addition deviate from linearity indicating non-DLVO forces are present. A similar affect is observed in Figure 8.4b.



(a)



(b)



(c)

Figure 8.4: The shear yield stress as a function of zeta potential squared, for iron oxide pulps flocculated with 0 – 500 g/t polymer in the presence of 10^{-3} M KNO_3 at (a) pH 6, (b) pH 8.5 and (c) pH 11.

In Figure 8.4c, a different effect is observed. All three of the ionic polymers exhibit non-DLVO behaviour. Bal [147] found gibbsite dispersions flocculated with PAM A and PAM N to be compliant with DLVO theory at and below the iep and non-compliant above it.

Whilst a definitive conclusion as to the reasons underpinning this behaviour was not reached, it was noted that enhanced settling rates at high pH confirmed the importance of bridging flocculation, which was deemed to be the predominant non-DLVO force present. Enhanced settling rates were not observed for this system. In the case of PAM N flocculated pulps there is no deviation from DLVO behaviour throughout the pH range studied, however there is little improvement in dewatering. For PAM C, settling rates are the lowest observed at pH 11 and the system does not conform to DLVO behaviour. At pH 6 and pH 8.5, where PAM C-induced settling rates are high, there is compliance with DLVO theory. This suggests that electrostatic mechanisms are dominant as observed in previous chapters. This is, however, not consistent with observations for the anionic polymers PAM A and PAM S, which displays non-DLVO forces at each pH. Given Bal's conclusion that bridging flocculation is the predominant non-DLVO force in a similar polymer-hydrophilic oxide system [147], it therefore follows logic that PAM A and PAM S are the most successful bridging flocculants due to their non-DLVO compliance at each pH.

8.1.7 Influence of polymer structure type, pH and shear on the consolidation of iron oxide dispersions

The influence of polymer structure type, pH and shear on the consolidation of iron oxide dispersions is depicted in Chapter 6, Figure 6.7. Polymer addition had a small effect on particle consolidation, but in all cases, shear can be seen to have a large effect. There are pH dependent trends observed, as discussed below.

For un-sheared and sheared dispersions at pH 6, Figure 6.7a shows that the addition of up to 500 g/t of PAM A, PAM N, and PAM C have no noticeable effect on the consolidation of sedimented pulps. PAM S, however, whilst not having much effect with the addition of up to 200 g/t, had a larger effect at 500 g/t by increasing the consolidation by ~10 wt%. The effect of shear is dramatic. In most cases, it increases the consolidation by 10-15 wt%, with the exception of PAM C, where the application of shear increases the consolidation by 15-20 wt%. This is due to the cationic polymer interactions with the positively charged dispersion. The input of energy into the dispersion by the application of shear allows the particles to pack closer together by overcoming the electrostatic barrier, allowing increased polymer/particle interactions and van der Waals forces to take effect. Also, due to the particles and the polymer both having a positive charge, this forms a lubricating layer

between the particles which allows them to slip past one another more easily to form a more compact, consolidated bed.

In Figure 6.7b, where the particles in the dispersion are neutral, all three of the charged polymers (PAM A, PAM S and PAM C) have an effect on the consolidation by raising it up to 7 wt%. PAM N, again, has a very subtle effect. At this pH, application of shear to the consolidated bed increased the sediments solid content by 10-15 wt%. A similar effect is observed for the pulps at pH 11 (Figure 6.7c), where we see a marked increase due to shear but insignificant polymer addition effect. It can be noted, however, that at pH 11, the pulps flocculated with anionic polymers PAM A and PAM S improved the most after the application of shear, in agreement with the pulp flocculated with cationic PAM C improving the most after shear at low pH, due to overcoming the electrostatic repulsion. It has been shown in previous work that despite electrostatic repulsion between the negatively charged polymer and particles, PAM A chemisorbs onto the iron oxide surface at pH 11. It has also been shown that the yield stress for PAM A-flocculated pulps increased after shear, indicating increased bonding and bridging between particles, allowing more compact consolidation.

8.1.8 The Atomic Force Microscope as a probe into the rheological properties of iron oxide dispersions

The AFM was, overall, a very useful tool for investigating the rheological properties of iron oxide dispersions. Force vs. distance curves provided a useful measure of the effective mobile layer thickness, which gave insight into the surface properties of the samples studied.

Particles in dispersions are affected not only by the polymer layer thickness, but the electrical double layer as well and it is useful to compare the thickness of the combined mobile layer for each system. AFM force vs. distance curves also allowed the formulation of a model for adsorbed polymer conformation, which is extremely useful in terms of flocculant selection for dewatering.

Lateral force measurements provided interesting results in the usual method of presentation; however, a new model was proposed to allow comparison directly between

rheological yield stress data measured in a bulk particle system, and lateral force measurements between a particle and a plate. This model provided further insight into the lateral forces experienced between the two surfaces, and allowed the interpretation of trends that were unseen in the previous format.

8.1.9 The influence of metal salt coagulants and PAM A on the dewaterability of hematite dispersions

PAM A was used in conjunction with four metal salts ($Mn(NO_3)_2$, $MnSO_4$, $MnCl_2$, and K_2SO_4) in an attempt to further enhance the dewatering of iron oxide. PAM A and PAM C were shown to be the most effective in terms of increasing settling rate in Section 8.1.5. At polymer dosages below 100 g/t, there was little difference between the polymers for enhancing consolidation. PAM A was chosen as it is preferable to use an anionic polymer than a cationic one for dewatering due to environmental disadvantages which occur with the use of cationic polymers. The work was carried out at 50 g/t which is an amount considered acceptable to industry.

In terms of improving the dewatering of iron oxide dispersions, it was the sulphate ion which best acted in synergy with the PAM A to increase the settling rates the most. The best combination was found to be at high pH where the particles are negatively charged.

8.2 CASE STUDY

8.2.1 Introduction

In order to assess the outcomes of the model systems investigated in previous chapters, thickener feed from Northparkes Cu deposit were kindly provided by Rio Tinto for testing. Details of the deposit geology including weathering products associated with the ore are found in Arundell [194]. The slurry was received as an aged (~ 6 months) coagulated suspension at 32.9 wt% solid, which was diluted to 18 wt% solid using supernatant electrolyte solution supplied separately in order to match regular thickener feed conditions at the mine. The tails are routinely concentrated to > 50 wt% solids prior to pumping to the tailings dam and the particular sample received achieved 58 wt% underflow solids. In order to reduce impoundment area and maximise water recovery, the operators desire an underflow which exceeds 60 wt% solids.

After characterisation of the surface, it was apparent that the surface had a low iep and thus PAM A, PAM S and PAM N were trialled as flocculants at the pristine pH (7.5), and at pH 6 and 9.

8.2.2 Characterisation

8.2.2.1 Solution speciation

Table 8.2: Solution speciation by ICP of the Northparkes tailing supernatant following 6 months aging with and without the presence of mineral particles.

Mineral phases	• Major: felspar, quartz, clay • Minor: mica, calcite, magnetite, gypsum, sulphides
Solution species	• Cations: Ca^{2+}, 580 ppm; Na^{+}, 475 ppm; K^{+}, 163 ppm; Mg^{2+}, 92 ppm. • Anions: SO_4^{2-}, 2250 ppm; Cl^{-} (735 ppm), [CO_3^{2-}, not measured] • Adsorbed species: Ca, Fe

Particle size	• -10 μm 25% • 10-100 μm 45% • +100 μm 30%
Zeta potential	• pH 7.5 (natural): -13 mV • pH 6: -10 mV, pH 9: -10 mV
Physical characteristics	• Colour – red brown coarse particles and grey-brown fines • Density: 2.67 g/cm^3 • black coloured magnetic phase present in coarse fraction
Sedimentation behaviour (unflocculated)	• Settling rate (bulk): 0.1 m/h • Consolidation (24 h): 55 wt% solid • Plant underflow: 58 wt% solid • (Coarse material sedimented rapidly and consolidated to 69 wt% solid)

8.2.2.2 Mineralogy

The XRD spectra shown in Figure 8.5 displays dominant quartz and albite (Na-feldspar) peaks in the 24-32 2θ range, with minor peaks in the 5-15 2θ range due to the presence of smectite, muscovite and kaolinite. The actual proportion of smectite and kaolinite clay will be higher than that indicated by the peak area/intensity due to the poorly crystalline nature of the clay matrix. The presence of albite in preference to orthoclase (K-feldspar) is unusual in that no Na was detected for any of the mineral phases probed by EDAX (see Table 8.2). The diffraction pattern obtained from fine and coarse particle fractions display similar peak distributions, with lower and higher intensities, respectively. This indicates that clays and other fine moieties may be attached to the coarse fraction, and that fine particles are not selectively clay, but comprise felspar and quartz, possibly in part due to attrition during beneficiation.

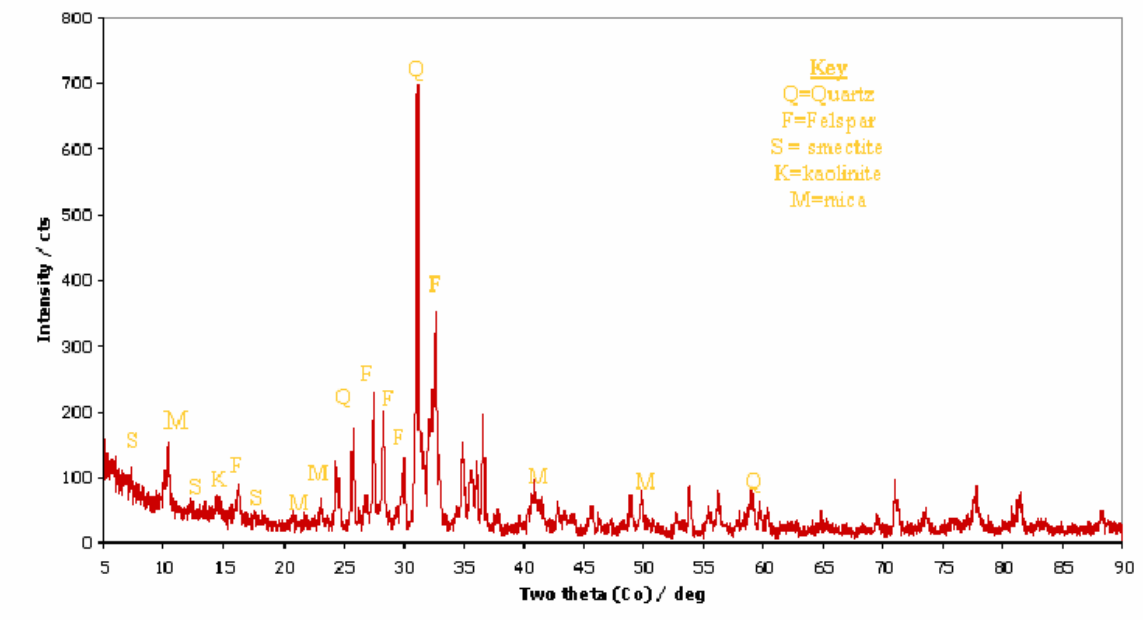


Figure 8.5: XRD diffraction pattern of the Northparkes tailings after washing to remove dissolved solids. Mineral identification shown in key

Table 8.3: Chemical, morphological and mineralogical assessment of coarse and fine particles in the Northparkes tailings via EDAX and SEM images.

	ID no.	Significant Elements	Shape characteristics	Possible mineral/s
Coarse ~ 100 µm	1	Al, Si, K, Fe		
	2	Si		Qz
	3	Al, Si, K		Fsp, Mi
	4	Al, Si, K		Fsp, Mi
	5	Al, Si, K		Fsp, Mi
	6	Al, Si, K		Fsp, Mi
	7	Ca, (Si), S	Angular shape, conchoidal fracture.	Gy
	8	Al, Si, K		
	9	Ca, (Fe), Al, Si, K		
	10	Si	Angular, conchoidal fracture.	Qz

Fine	21	Al, Si, K		Fsp, Mi
3-10 μm	22	Ca, Fe, Si,		
	23	Ca, (Fe, Al, Si, K)		Ca
	24	Ca, (Si, Mn)		Ca
	25	Si		Qz
	26	Al, Si		Ka
	27	Al, Si		Ka
	28	Al, Si, K		
	29	(Fe), Al, Si, S, K		Gy + Ka
	30	(Ca, K) Fe, Mg, Al, Si, Mn	Spherical agglomerate of platy particles	Sm

The fine EDAX sampling concentrated on relatively coarse particles (3-10 μm), which were surrounded by unanalysed ~1 μm particles (See Figure 8.6). Coarser particles comprised 80-300 μm sized, semi-spherical to angular shaped particles primarily comprised of felspar and quartz. Most of the particles probed by EDAX which gave Al, Si, K signatures gave no indication of the perfect cleavage characteristic of mica, suggesting most of these particles are felspar, possibly weathered to some extent. Backscattered electron images indicate the presence of sulphide minerals 20-30 μm in size.

8.2.2.3 Particle physical parameters (size, density and shape)

The density of the tailings particles was 2.67 g/cm^3 measured by pycnometry, which is typical for aluminosilicate minerals such as quartz, felspar, mica and clays. Measurement of both coarse and fine fractions gave similar values, suggesting that denser particles comprise only a minor proportion. The particles display a broad particle distribution from sub-micron to 0.3 mm size as is evident in the SEM images (Figure 8.6). Based on laser scattering data (Figure 8.7), coarse (+100 μm) particles comprised 30 % (by mass) of the tails, fines (-10 μm) about 25 %, with 45 % in the intermediate size range (10-100 μm). The particles appear to be angular to sub-rounded in shape, with little evidence of freshly cleaved or highly crystalline faces, possibly due to the action of natural weathering processes, plant processing and surface adhesion of sparingly soluble solution species. Most of the finest particles (-10 μm) were platy shaped, suggesting clays are the dominant colloidal sized mineral species.

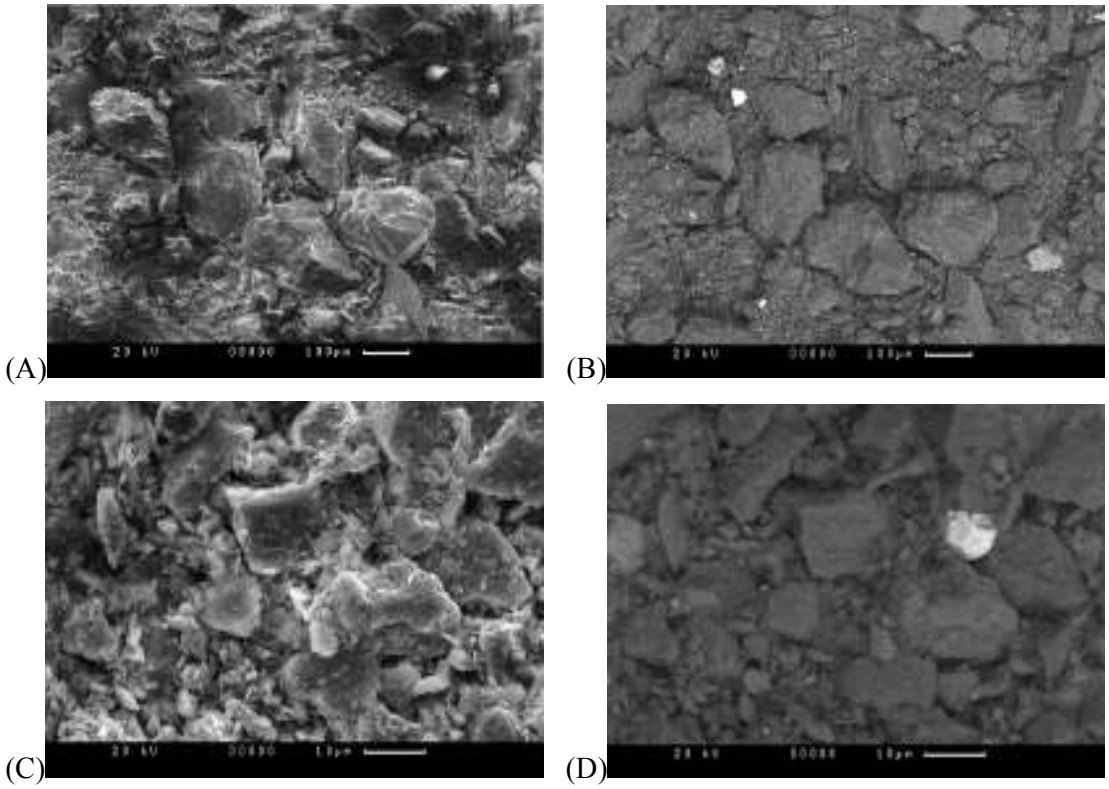


Figure 8.6: SEM images of the Northparkes tailings particles showing (A) coarse particles, secondary electron, (B) coarse particles, backscattered electron; (C) fine particle, secondary electron; (D) fine particles backscattered electron.

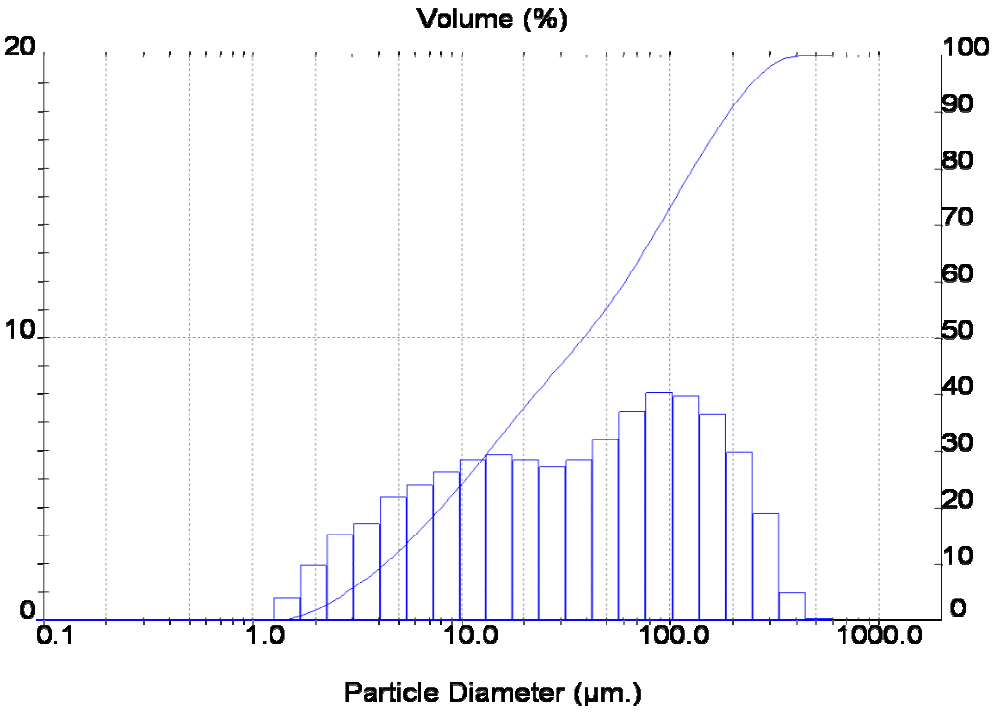


Figure 8.7: Particle size of the Northparkes tailings determined by laser diffraction

8.2.3 Interfacial Chemistry

The zeta potential of the fine particles at pH 7.5 is ~ -14 mV, which is close to the maximum zeta potential exhibited across the pH range measured. Figure 8.8 shows the zeta potential and attenuation particle size of the pulp particles as a function of pH after removal of the coarse particles by sedimentation. Large particles are largely invisible to the Acoustosizer since their large inertia limits the electroacoustic response of the particles. Sedimentation during measurement also causes mixing and pumping difficulties. The zeta potential became more negative in the pH range 11 to 7, possibly due to dissolution of Ca(II) hydrolysis products adsorbed to the particle surfaces as has been reported elsewhere [31, 195]. From pH 7 to 4, the magnitude of the zeta potential decreases due to particle dissolution and dehydroxylation of the particle surface. As a result, the background electrolyte content increased from 0.8 to 1.2 mS/m compared to 0.6 mS/m at pH 11, due to increased acid addition and solubilisation of the particle matrix. The particle dissolution is evident in the particle size plot which displays a decrease from 1.2 to 0.2 μm over the pH range 7 to 4, as a result of gas bubbles evolved from carbonate dissolution and/or precipitated solids (eg. $CaSO_4$). The zeta potential acid to base titration curve was steady between pH 4 and 10, after which the zeta potential became less negative, possibly due to reformation of Ca(II) hydrolysis products on the particle surfaces. The magnitude of zeta potential in this range is likely underestimated due to incorrect estimation of the background correction concentration, and the apparent positive values recorded may be an artefact of this. Although not indicated in Table 8.3 the EDAX probing reported Ca and Fe ubiquitously, although commonly in insufficient quantity to be regarded as primary components of the mineral phases present. Instead, these species may represent ion species concentrated at the particle surface which may influence zeta potential and adsorption site availability.

8.2.4 Optimisation procedure

The mineralogical assessment indicates that the dispersion is dominated by minerals of low iep, i.e., dominated by Lewis acid sites. In particular, the mineralogy of the colloidal size fraction is dominated by clays, which has been previously demonstrated to exhibit optimum consolidation after flocculation with PEO [148], followed by sedimentation and shear. The presence of Ca(II) ions in high concentration indicates that any smectite clay present is strongly coagulated and swelling impeded, although were this not the case

further Ca addition would have limited effect. Increasing the pH might facilitate optimisation via adsorption of hydrolysed $CaOH^+$ to the mineral surfaces and although this may be impractical on site, the role of pH effect may be useful in understanding the polymer-particle interfacial behaviour. The high electrolyte concentration provides adequate coagulation of the slurry, however, this would also be expected to inhibit the expansion of the anionic flocculants used previously, and may restrict the conformation of PEO also [196, 197], thus flocculation at reduced electrolyte concentration may be beneficial. Finally, the presence of a significant coarse fraction may allow examination of the role of co-flocculation and co-deposition in regards to particle size fraction.

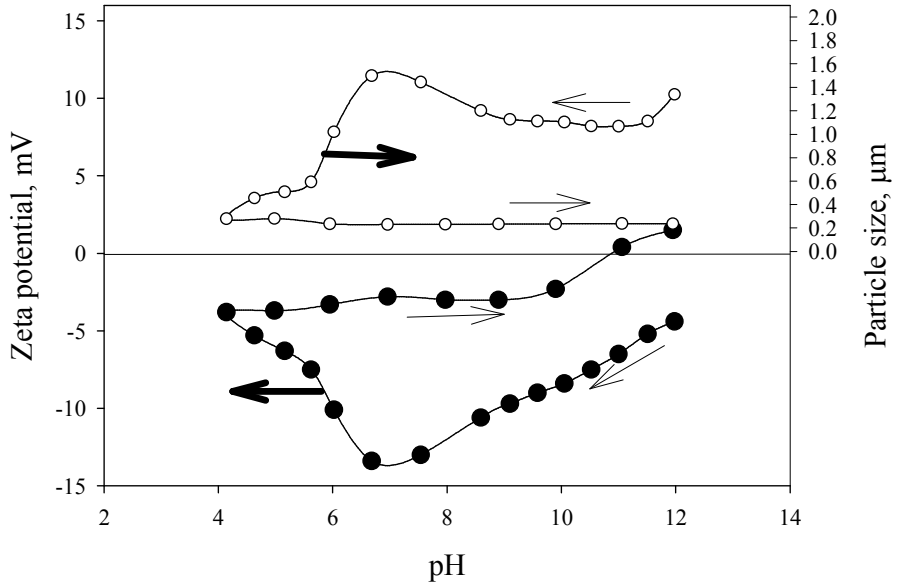


Figure 8.8: Zeta potential and attenuation particle size of the fine Northparkes tailings particles as a function of pH.

8.2.5 Settling behaviour

Initial flocculation with PEO, PAM A, PAM S and PAM N was carried out on ~23 wt% pulps (Figure 8.9). The polyacrylamide polymers induced large fast settling flocs > 30 m/h whereas PEO based flocs subsided at only 6 m/h. A significant amount of unadsorbed flocculant was present in the supernatant after settling, indicating that the dosage used was excessive. Of the minerals identified, clay, mica, felspar and quartz have low iep values which should enable PEO adsorption. The absence of significant turbidity after

flocculation suggests that adsorption to the fine fraction was successful, however the overall settling performance implies that adsorption onto some, if not many of the large particles was not possible, perhaps due to surface contamination by high iep species (such as $Ca(OH)_2$). In contrast to PEO, PAM A and PAM N, flocculation with PAM S resulted in a turbid reddish brown supernatant which clarified overnight by sedimentation. It appears that PAM S exhibits selective adsorption; however it is not clear from experiment or literature which mineral or surface species this occurs with.

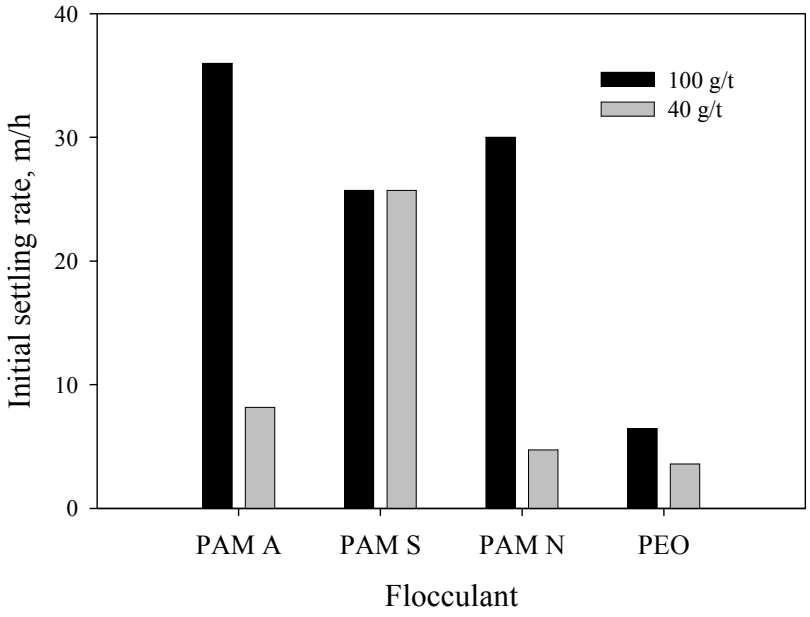


Figure 8.9: Settling rates of plant pulp as flocculated with different polymers at pH 7.5.

At lower polymer dosage, the settling rate of PAM A and PAM N based flocs were significantly diminished in comparison to high dosage. PAM S flocs exhibited rapid settling rates at both concentrations, and significantly exceeded the performance of PAM A and PAM N at 40 g/t. Therefore, the adsorption of PAM A and PAM N may be complete in 15 s (agitation time) at lower dosage, and higher concentrations allow extended periods of floc growth. Adsorption of PAM S is slower however, and at both concentrations a similar extent of floc growth occurred. A concentration effect is evident in the yield stress data (Figure 8.4), which implies that greater adsorption occurred at higher concentration enhancing floc strength, whilst the floc dimensions remained similar.

This is different to what was observed in the hematite system discussed in the previous chapters. PAM A and PAM S were superior to PAM N at 50 g/t when the system was

negatively charged, as the current system is at pH 7.5. This is due to the large influence of the clay content of the system, and these results are consistent with that observed previously for a predominantly clay system [148].

8.2.6 Influence of pH

Figure 8.10 shows the settling rates of the plant pulp at three pH values after flocculation with 40 g/t of PAM A, PAM N and PAM S. Further information on the mineral pulp flocculated with PEO is discussed further in another publication and will not be discussed further here [148]. PEO does not absorb to the iron oxide particles used throughout this study. The pH values are 6, 7.5 and 9, which are the pristine pH and ±2.5. The change in pH in all cases is detrimental to the settling rate of the pulp.

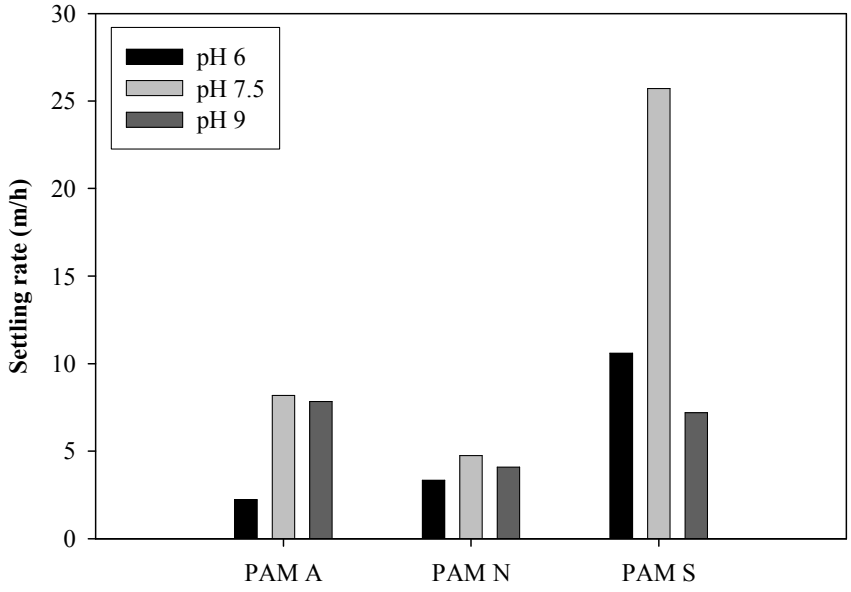


Figure 8.10: The settling rates of the plant samples flocculated with 40 g/t polymer at three pH values

Settling tests performed at pH 6 and 9 with polyacrylamide flocculants exhibited diminished settling performance at both pH values in comparison to pH 7.5 for all flocculants. Settling behaviour at pH 6 decreased according to flocculant type as PAM S> PAM N> PAM A, whereas at pH 9 the trend followed PAM S ≈ PAM A > PAM N. This is difficult to compare to the iron oxide samples considered in this thesis due to the fact that the zeta potential is negative throughout the range studied.

In Figure 8.11, the consolidation of the plant pulps at three pH values before and after shear is depicted. The effect caused by pH is, within experimental error, insignificant to the consolidation of the plant pulp. The effect of shear increases the consolidation of the pulp by up to 10 wt%. Figure 8.12, however, shows the effect of pH to be much more significant on the yield stress values. It is difficult to correctly estimate the zeta potential correctly at the 3 pH values, given that the effect is different when adding an acid or base (see Figure 8.8). If the zeta potential is taken from the lower of the two lines, it appears that that the zeta potential is approximately –14 mV for pH 7.5, and –10 mV for both pH 6 and 9. The different effects seen in the yield stress, however, suggest that they are more likely to be different. The yield stress gets consistently higher with pH for PAM A. For PAM N however, we see the same effect at both high and low pH, suggesting similar behaviour. For PAM S, the yield stress is higher for pH 6 and 9 than it is at pH 7.5, suggesting that the swing in pH has effected the formation of flocs in such a way as to make them stronger.

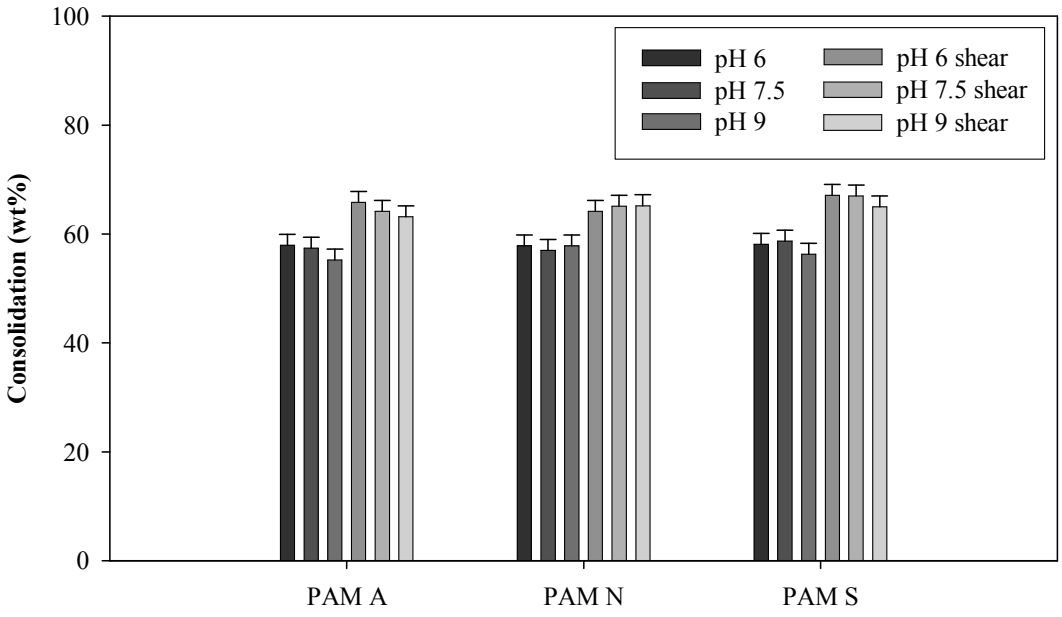


Figure 8.11: The consolidation of the plant samples flocculated with 40 g/t polymer at three pH values

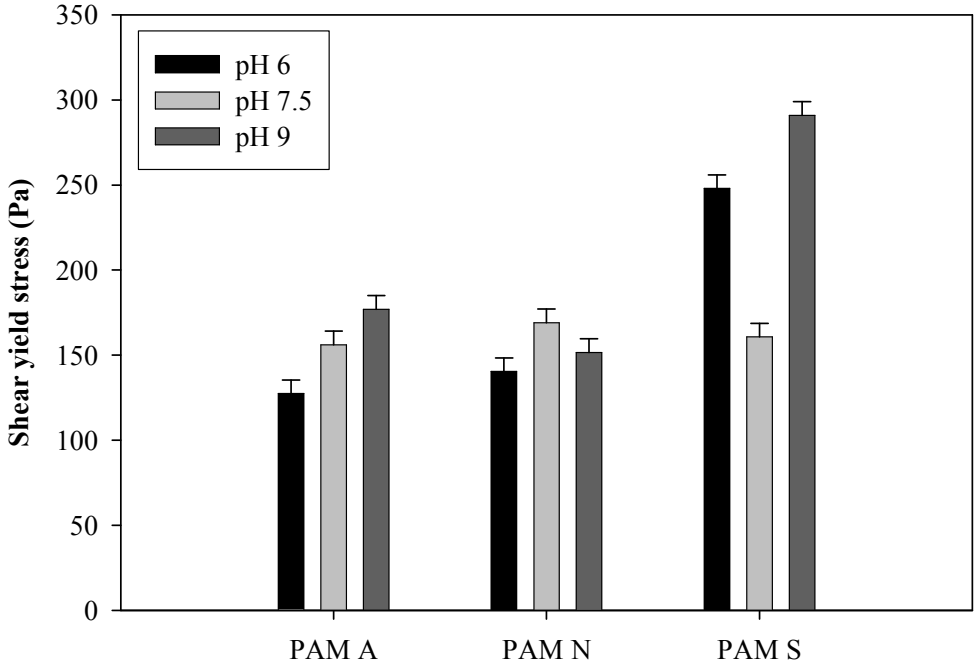


Figure 8.12: The shear yield stress of the plant samples flocculated with 40 g/t polymer at three pH values

8.3 SUMMARY

The effect of polymer structure type had a large effect on the surface chemistry and particle interactions of iron oxide dispersions. The adsorption mechanisms and isotherms, surface chemistry and rheology of flocculated iron oxide dispersions were measured. In general, it appears that a flocculant of the same charge as the dispersion is most effective for dewatering, and shear had a dramatic effect.

Polymer structure type also had a large impact on the dewaterability of real plant tailings. PAM A and PAM S were trialled with PAM N (as a baseline), and PAM S was found to more effective reiterating that polymer structure plays a large role in dewatering. There was general agreement with the fundamental studies of the model system, including the dramatic effect of shear on pulp consolidation.

CHAPTER 9 Conclusions and Future Recommendations

9.1 CONCLUSIONS

Adsorption isotherms and their impact on dewatering

Adsorption isotherms were determined for the adsorption of PAM A, PAM N, PAM S and PAM C onto iron oxide particles at dispersion pH values 6, 8.5 and 11. The Freundlich model for adsorption gave the best fit indicating that irreversible, multi-segment polymer adsorption increases with an increase in polymer concentration. This is in contrast to adsorption approaching monolayer coverage that would be the case if the isotherms were better fitted to the Langmuir model.

Adsorbed amount decreased with an increase in pH for each polymer except PAM C, which had its greatest adsorbed amount at pH 8.5.

Adsorption affinities were ranked PAM N > PAM S > PAM A > PAM C for pH 6, PAM N > PAM C > PAM A > PAM S for pH 8.5, and PAM N > PAM A > PAM C > PAM S for pH 11. PAM N had the highest adsorption affinity in each case, and produced the poorest settling rates. In general, the lower the adsorption affinity, the larger the expanded conformation of the polymer, and the greater the settling rate due to enhanced particle bridging by the expanded polymer,

Pre-treatment of the particles with metal salts led to greater adsorption of PAM A, with manganese ions facilitating adsorption at low pH and sulphate ions facilitating adsorption at high pH.

Adsorption mechanisms and their impact on rheology

Chemical adsorption was observed for PAM A adsorption onto hematite particles. Bidentate chelation occurred at pH 6 and 11 between the carboxyl group of the polymer and a hydroxyl group on the oxide particle surface. Monodentate chelation was observed at

the iep between the carboxyl group of the polymer and a hydroxyl group on the oxide particle surface. Hydrogen bonding through the carbonyl group on the polymer and the hydroxyl groups on the surface of the particles was also found to be present at all pH values, whilst the asymmetric COO^- was found to hydrogen bond with the iron oxide particle surface on either side of the iep only.

The polymer adsorption mechanisms showed some correlation with the dispersion rheology. For PAM A flocculated pulps, the yield stresses were higher for dispersions at pH 6 and 11 than they were at pH 8.5, suggesting that the bidentate chelation mechanism of adsorption is stronger than the monodentate chelation.

Whilst bidentate chelation occurred at pH 6 and pH 11, the shear yield stress for pre-shear PAM A flocculated pulps at pH 11 was lower than at pH 6 pre-shear due to the electrostatically repulsive barrier between the negatively charged hematite particles and the negatively charged polymer pendants hindering particle interactions and networking. After the repulsive barrier was overcome by shear at pH 11, the yield stress was similar to that of pH 6 pre-shear. This further concurs with the suggestion that the polymer adsorption mechanisms have an impact on the yield stress.

For non-ionic PAM N adsorption at all pH values, hydrogen bonding through the carbonyl group on the polymer with the mineral surface hydroxyls was indicated as the only adsorption mechanism present. Spectroscopic evidence was found to support a suggested hypothesis of hydrolysis of PAM N at high pH, consistent with its similar behaviour to poly acrylic acid flocculant (PAM A) at high pH.

The adsorption mechanisms do not appear to directly impact on the settling rates of the iron oxide dispersions, however, they appear to underpin the rheology of the dispersions suggesting that the secondary dewatering stage may be manipulated and optimised with more knowledge in this area.

<u>The effect of polymer structure type on zeta potential and rheology</u>

The polymer structure type greatly influenced the zeta potential of the dispersion particles. Flocculation with PAM A and PAM S caused a significant decrease of the magnitude of the zeta potential at all pH values, with PAM S having a greater effect at and above the iep

due to it being the salt of a strong acid and having a more expanded interfacial conformation. Flocculation with PAM N and PAM C did not have a significant impact on the zeta potential at and below the iep after the addition of up to 500 g polymer/t solid, however, at high pH they both shielded the zeta potential. Thus, the anionic polymers are more effective at manipulating the zeta potential of the particles. A polymer should be selected for enhanced dewatering based on its desirable physico-chemical characteristics, namely, an expanded interfacial conformation and the relative functional group charge type.

The effect of polymer structure type and shear on dispersion rheology

PAM S and PAM C flocculated sediment pulps exhibited the highest yield stresses at pH 6, 8.5 and 11. At pH 6, the yield stress for the flocculated sediment pulps was ranked PAM C > PAM S > PAM A > PAM N. At pH 8.5 it was ranked PAM S > PAM C > PAM A = PAM N, and PAM S > PAM C > PAM A > PAM N at pH 11. At each pH, the trends for highest and the lowest ranked flocculated pulp yield stresses are opposite to the highest and lowest ranked polymer adsorption affinities. At pH 11 the yield stresses are ranked completely in reverse to the adsorption affinities. This suggests that the faster the polymer adsorption, the lower the flocculated sediment pulp yield stress, and hence that fast flocculation leads to the formation of weaker bonds between the particles and the flocculant.

The yield stress post-shear for PAM A, PAM S and PAM C flocculated pulps at pH 6 showed a significant decrease when compared with the pre-shear measurement due to the break-up of large loose flocs resulting in weakening of the polymer-particle network bonds. Shear had little effect on PAM A flocculated pulps at pH 8.5, however, post-shear measurements for PAM S and PAM C flocculated pulps showed a significant decrease due to the break-up of flocs as shown at pH 6. For PAM N flocculated pulps at pH 6 and 8.5, shear had little to no effect on the rheology of the dispersion. This is consistent with the previous observation that high adsorption affinity leads to weak bonds formed and hence a low yield stress. There are no strongly bonded flocs to break up during the process of shear, and hence there is little to no effect on the yield stress. The post-shear yield stress for the anionic polymers (and PAM N which was shown to be partially hydrolysed at pH 11) at high pH showed a marked increase due to the input of shear energy overcoming the

electrostatic repulsion between the polymer molecules and the particles, thereby enhancing polymer-particle bridging interactions.

The effect of polymer structure type on dispersion settling and consolidation behaviour

The settling rates at pH 6 for the flocculated pulps were ranked PAM C > PAM S = PAM A > PAM N. At pH 8.5 they were ranked PAM A > PAM C > PAM S > PAM N, and at pH 11 they were ranked PAM A > PAM S > PAM C > PAM N. At pH 6, the polymer adsorption affinities correlated well with settling rates (where it was hypothesised that low adsorption affinities lead to faster settling rates), however they did not at pH 8.5 and 11.

A general observation that emerged for polymer structure type is that charged co-polymers out-perform uncharged homo-polymers in settling rate amplification at all pH values and in all combinations (positively/negatively/neutrally charged polymer with positively/negatively/neutrally charged particle combinations).

The sediment consolidation behaviour was not significantly impacted upon by polymeric flocculant structure type or metal salt addition. The addition of up to 500 g/t polymer in general produced an increase in consolidation of approximately 5-7 wt% solid.

The effect of pH on the dewatering behaviour of iron oxide dispersions

Both the settling rates and consolidation were improved to a greater extent by polymers of similar charge to the particles in the dispersion. Settling rates were the highest at and below the iep for the charged polymers due to their charge-mediated expanded conformation and enhanced flocculation performance. Lower settling rates were displayed by the practically non-ionic PAM N-based dispersions and this is believed to be due to its more contracted interfacial conformation limiting its bridging capabilities.

At pH 6, PAM C flocculated pulps settled fastest, where both the polymer and the particle are positively charged. Likewise, at pH 11, PAM A and PAM S flocculated pulps settled fastest, where both the polymer and the particle are negatively charged. This is due to the expanded interfacial conformation of the polymer facilitating particle bridging. Hydrogen bonding is the main adsorption mechanism known to occur under such conditions,

fostering polymer bridging mechanisms for the flocculation of the similarly charged mineral particles and polymer chains to provide the superior dewatering results.

At pH 6, PAM A and PAM S flocculated pulps settle faster than PAM N flocculated pulps. This is due to the electrostatic attraction that occurs between the polymer and the particles resulting in fast dewatering logically through the charge patch and charge neutralisation mechanisms. The electrostatic attraction also facilitates hydrogen bonding of other parts of the polymer with particles, and hence enhances polymer bridging mechanisms as well.

At pH 8.5 where the particles are not charged, flocculation with the charged polymers still produced high settling rates. This is due to their large interfacial conformation facilitating polymer bridging mechanisms following adsorption of the charged polymers via hydrogen bonding.

At pH 11, whilst PAM A and PAM S produced the best settling rates (as stated above), PAM C and PAM N were relatively neutral and produced settling rates similar to neutral PAM N at pH 6, where the particle charge is of roughly equal magnitude (but opposite charge). This is due to the neutral polymers having a smaller interfacial conformation.

The effect of shear on sediment pulp consolidation

The application of shear had a pronounced effect on the consolidation of the model dispersion, improving sediment consolidation by 10-20 wt%. This is a significant improvement and was independent of both pH and flocculant/salt addition.

Shear-induced consolidation enhancement of iron oxide particles was greater when a given flocculant had the same charge as the iron oxide particles.

Case study of tailings from Northparkes mine

An applied case study on the dewatering of real plant tailings containing felspar, quartz, clay, mica, calcite, magnetite, gypsum, and sulphides mineral particles has been successfully performed in the manner of the fundamental studies of model iron oxide dispersions. Good agreement between the flocculation and concomitant dewatering

behaviour of the model and real mineral pulps was achieved. Polymeric flocculants of similar charge to the dispersion particles were most effective for enhanced dewatering rates, as found in the model system studies. Furthermore, PAM S exhibited superior flocculation / dewatering performance in comparison with PAM A and PAM N at all three corresponding pH values (6, 7.5 and 9).

Shear was found to increase the consolidation of pre-sedimented plant pulp by up to 10 wt% under all test conditions, in agreement model iron oxide dispersion studies. The results of the applied studies confirm that the observations made from fundamental studies of a pure single mineral in this work may be judiciously applied to real mineral dispersions of complex mineralogy, enabling useful appropriation of the important research outcomes.

9.2 FUTURE RECOMMENDATIONS

1. Work done by McFarlane [148] indicated that enhancement in orthokinetic flocculation and settling rate can be made by optimising the agitation speed and time utilised in settling tests. This should be investigated for this system considering the positive pulp consolidation effect due to shear. Further optimisation for the shear speed and time should also be investigated further.

2. Infrared investigations into the adsorption mechanisms of PAM A with adsorbed metal salt coagulants could be investigated to determine the adsorption characteristics of this system.

3. There is no literature in the area of PAM S and PAM C adsorption mechanisms as studied via infrared. Such spectroscopic studies should be made in this area in the manner of those done in Chapter 4. This should also provide further insight into the influences of polymer structure type on flocculation.

4. The spherical iron oxide particles used as colloid probes should be ground (or partially dissolved) in order to be suitable for use in the Acoustosizer (or Rank Brother II) to determine their zeta potential for comparison with the calculations made through AFM measurements.

5. Determination of the desirable rheological parameters for a flocculated dispersion could be determined and a polymer with bonding mechanisms of suitable strength (as determined via infrared techniques) may be selected to facilitate enhanced dewatering.

6. AFM imaging work could be conducted in order to observe adsorbed polymer structure and hence conformation/morphology.

7. Investigations into the effect of stimulus sensitive polymers on the dewaterability of iron oxide may be of interest. Focus should be on polymers that can adapt a more contracted interfacial conformation after stimulus as to draw the particles closer together to enhance consolidation.

8. In terms of the physical properties of dewatering (settling and consolidation), it has been made clear throughout this work that it is desirable to choose a flocculant of similar charge to the particles to enhance dewatering. It is also clear that polymer structure type dramatically impacts on settling rates and thus further investigations into other flocculants with the correct charge (i.e. the same as the particles in the chosen dispersion) for the desired system should be undertaken.

CHAPTER 10 References

1. Farinato, R.S., S.-Y. Huang, and P. Hawkins, *Colloid-Polymer Interactions: from fundamentals to practice*, ed. R.S. Farinato, Dublin, P.L. 1999: John Wiley and Sons Inc. N.Y.

2. Dickinson, E. and L. Eriksson, *Particle Flocculation by Adsorbing Polymers.* Advances in Colloid and Interface Science, 1991. **34**: p. 1-29.

3. Bajpai, A.K. and S.K. Bajpai, *Kinetics of polyacrylamide adsorption at the iron oxide - solution interface.* Colloids and Surfaces A: Physicochemical and Engineering Aspects, 1995. **101**: p. 21-28.

4. Biggs, S., *Steric and Bridging Forces between Surfaces Bearing Adsorbed Polymer: An Atomic Force Microscope Study.* Langmuir, 1995. **11**: p. 156-162.

5. Bremmell, K.E., S.R. Biggs, and G.J. Jameson, *Polyelectrolyte adsorption at the solid/liquid interface - Interaction forces and stability.* Colloids and Surfaces A: Physicochemical and Engineering Aspects, 1998. **139**: p. 199-211.

6. Mpofu, P., J. Addai-Mensah, and J. Ralston, *Investigtion of the effect of polymer structure type on flocculation, rheology and dewatering behaviour of kaolinite dispersions.* International Journal of Mineral Processing, 2003. **71**: p. 247-268.

7. Zhang, J., C. Huguenard, C. Scarnecchia, R. Menghetti, and J. Buffle, *Stabilisation and destabilisation of hematite suspensions by neutral and anionic polyacrylamide.* Colloids and Surfaces A: Physicochemical and Engineering Aspects, 1999. **151**: p. 49-63.

8. Mpofu, P., J. Addai-Mensah, and J. Ralston, *Flocculation and dewatering behaviour of smectite dispersions: effect of polymer structure type.* Minerals Engineering, 2004. **17**: p. 411-423.

9. Das, K.K. and P. Somasundaran, *A kinetic investigation of the flocculation of alumina with polyacrylic acid.* Journal of Colloid and Interface Science, 2004. **271**(102-109).

10. Radeva, T. and I. Petkanchin, *Electric properties and conformation of polyethylenimine at the hematite-aqueous solution interface.* Journal of Colloid and Interface Science, 1997. **196**: p. 87-91.

11. Besra, L., B.P. Singh, P.S.R. Reddy, and D.K. Sengupta, *Influence of surfactants on filter cake parameters during vacuum filtration of flocculated iron ore sludge.* Powder Technology, 1998. **96**: p. 240-247.

12. Addai-Mensah, J. and J. Ralston, *Interfacial Chemistry and Particle Interactions and their Impact Upon the Dewatering Behaviour of Iron Oxide Dispersions.* Hydrometallurgy, 2004. **74**: p. 221-231.

13. Ferretti, R., S. Stoll, J. Zhang, and J. Buffle, *Flocculation of hematite particles by a comparitively large rigid polysaccharide: schizophyllan.* Journal of Colloid and Interface Science, 2003. **266**: p. 328-338.

14. Addai-Mensah, J., I. Larson, and J. Ralston, *Interfacial Chemistry and Water Minimisation in Tailings Treatment.* AMIRA International, Project Report., 1999.

15. Senden, T.J., J.M. Di Meglio, and I. Silberzan, *The conformation of adsorbed polyacrylamide and derived polymers.* Polymers at interfaces, 2000. **4**: p. 1143-1152.

16. Karmakar, G.P. and R.P. Singh, *Flocculation studies using amylose-grafted polyacrylamide.* Colloids and Surfaces A: Physicochemical and Engineering Aspects, 1998. **133**: p. 119-124.

17. Mpofu, P., J. Addai-Mensah, and J. Ralston, *Interfacial chemistry, particle interactions and improved dewatering behaviour of smectite clay dispersions.* International Journal of Mineral Processing, 2005. **75**: p. 155-171.

18. Hulston, J., R.G. de Kretser, and P.J. Scales, *Effect of temperature on the dewaterability of hematite suspensions.* International Journal of Mineral Processing, 2004. **73**: p. 269-279.

19. Gebhardt, J.E. and D.W. Fuerstenau, *Flotation behaviour of hematite fines flocculated with polyacrylic acid.* Minerals & Metallurgical Processing, 1986(August): p. 164-170.

20. Kaggwa, G.B., S. Froebe, L. Huynh, J. Ralston, and K.E. Bremmell, *Morphology of adsorbed polymers and solid surface wettability.* Langmuir, 2005. **21**: p. 4695-4704.

21. Morris, G.E., D. Fornasiero, and J. Ralston, *Polymer depressants at the talc-water interface: adsorption isotherm, microflotation and electrokinetic studies.* International Journal of Mineral Processing, 2002. **67**: p. 211-227.

22. Addai-Mensah, J., J. Dawe, R.A. Hayes, C.A. Prestidge, and J. Ralston, *The unusual colloid stability of gibbsite at high pH.* Journal of Colloid and Interface Science, 1998. **203**: p. 115-121.

23. Asmatulu, R., *Enhancement of the Dewaterability Characteristics of Fine Silica Particles.* Turkish Journal of Engineering and Environmental Sciences, 2002. **26**: p. 513-519.

24. Besra, L., D.K. Sengupta, and S.K. Roy, *Influence of surfactants on flocculation and dewatering of kaolin suspensions by cationic polyacrylamide (PAM C) flocculant.* Separation and Purification Technology, 2003. **30**: p. 251-264.

25. Besra, L., D.K. Sengupta, S.K. Roy, and P. Ay, *Polymer adsorption: its correlation with flocculation and dewatering of kaolin suspensions in the presence and absense of surfactants.* International Journal of Mineral Processing, 2002. **66**: p. 183-202.

26. Besra, L., D.K. Sengupta, S.K. Roy, and P. Ay, *Influence of polymer adsorption and conformation on flocculation and dewatering of kaolin suspension.* Separation and Purification Technology, 2004. **37**: p. 231-246.

27. Glover, S.M., Y.D. Yan, G.J. Jameson, and S. Biggs, *Dewatering properties of dual-polymer-flocculated systems.* International Journal of Mineral Processing, 2004. **73**: p. 145-160.

28. Krentz, D.-O., G. Oelmeyer, J. Laudan, and W.-M. Kulicke, *Influence of flocculant charge on the dewaterability of flocculated clay suspensions.* Colloid and Polymer Science, 2003. **281**: p. 423-430.

29. McFarlane, A.J., K.E. Bremmell, and J. Addai-Mensah, *Optimising the dewatering behaviour of clay tailings through interfacial chemistry, orthokinetic flocculation and controlled shear.* Powder Technology, 2005. **160**: p. 27-34.

30. McFarlane, A.J., K.E. Bremmell, and J. Addai-Mensah, *Improved dewatering behaviour of clay minerals dispersions via interfacial chemistry and particle interactions optimization.* Journal of Colloid and Interface Science, 2006. **293**: p. 116-127.

31. Mpofu, P., J. Addai-Mensah, and J. Ralston, *Influence of hydrolysable metal ions on the interfacial chemistry, particle interactions, and dewatering behaviour of kaolinite dipersions.* Journal of Colloid and Interface Science, 2003. **261**: p. 349-359.

32. Mpofu, P., J. Addai-Mensah, and J. Ralston, *Temperature influence of nonionic polyethylene oxide and anionic polyacrylamide on flocculation and dewatering behaviour of kalonite dispersions.* Journal of Colloid and Interface Science, 2004. **271**: p. 145-156.

33. Sabah, E., H. Yuzer, and M.S. Celik, *Characterization and dewatering of fine coal tailings by dual-flocculant systems.* International Journal of Mineral Processing, 2004. **74**: p. 303-315.

34. Chibowski, S. and M. Wisniewska, *Study of electrokinetic properties and structure of adsorbed layers of polyacrylic acid and polyacrylamide at the Fe_2O_3-polymer solution interface.* Colloids and Surfaces A: Physicochemical and Engineering Aspects, 2002. **208**: p. 131-145.

35. Jones, F., J.B. Farrow, and W. van Bronswijk, *An infrared study of a polyacrylate flocculant adsorbed on hematite.* Langmuir, 1998. **14**(6512-6517).

36. Kirwan, L.J., P.D. Fawell, and W. van Bronswijk, *In Situ FTIR-ATR Examination of Poly(acrylic acid) Adsorbed onto Hematite at Low pH.* Langmuir, 2003. **19**: p. 5802-5807.

37. Kirwan, L.J., P.D. Fawell, and W. van Bronswijk, *An in situ FTIR-ATR study of polyacrylate adsorbed onto hematite at high pH and high ionic strength.* Langmuir, 2004. **20**: p. 4093-4100.

38. McFarlane, A.J., K.E. Bremmell, and J. Addai-Mensah, *Microstructure, rheology and dewatering behaviour of smectite dispersions during orthokinetic flocculation.* Minerals Engineering, 2005. **18**: p. 1173-1182.

39. Jones, F., J.B. Farrow, and W. van Bronswijk, *Flocculation of haematite in synthetic Bayer liquors.* Colloids and Surfaces A: Physicochemical and Engineering Aspects, 1998. **135**: p. 183-192.

40. Yan, Y.D., S.M. Glover, G.J. Jameson, and S. Biggs, *The flocculation efficiency of polydisperse polymer flocculants.* International Journal of Mineral Processing, 2004. **73**: p. 161-175.

41. Besra, L., D.K. Sengupta, S.K. Roy, and P. Ay, *Studies on flocculation and dewatering of kaolin suspensions by anionic polyacrylamide flocculant in the presence of some surfactants.* International Journal of Mineral Processing, 2002. **66**: p. 1-28.

42. Besra, L., D.K. Sengupta, and S.K. Roy, *Influence of unasdorbed and weakly adsorbed flocculants on separation properties of kaolin suspensions.* International Journal of Mineral Processing, 2006. **78**: p. 101-109.

43. Franks, G.V. *Solid/liquid separation using temperature sensitive flocculation*. in *Chemeca*. 2006. Auckland, New Zealand.

44. Chin, B.D., J.H. Park, M.H. Kwon, and O.O. Park, *Rheological properties and dispersion stability of magnetorheological (MR) suspensions.* Rheol Acta, 2001. **40**: p. 211-219.

45. Heller, H. and R. Keren, *Anionic Polyacrylamide Polymers Effect on Rheological Behaviour of Sodium-Montmorillonite Suspensions.* Soil Science Society of America Journal, 2002. **66**: p. 19-25.

46. Addai-Mensah, J., K.E. Bremmell, G. Levay, and J. Ralston, *Project P523A Optimising Dewatering Through Interfacial Chemistry.* 5th Progress Report, AMIRA International, 2004.

47. Shaw, D.J., *Introduction to Colloid and Surface Chemistry*. 4 ed. 1991: Butterworth-Heinemann.

48. Healy, T.W., D.V. Boger, L.R. White, Y.K. Leong, and P.J. Scales. *Thickening and clarification; How much do we really know about dewatering?* in *6th AusIMM Extractive Metallurgy Conference*. 1994. Brisbane.

49. Bajpai, A.K. and S.K. Bajpai, *Kinetics of flocculation of iron oxide particles by hydrolyzed polyacrylamide.* Indian Journal of Chemistry Section A - Inorganic Bio-inorganic Physical Theoretical & Analytical Chemistry, 1997. **36**: p. 867-873.

50. Hunter, R.J., *Zeta Potential in Colloid Science: Principles and Applications*. Colloid Science: A Series of Monographs, ed. R.H. Ottewill, Rowell, R.L. 1981: Academic Press.

51. Lee, L.T. and P. Somasundaran, *Adsorption of polyacrylamide on oxide minerals.* Langmuir, 1989. **5**: p. 854-860.

52. Hiemstra, T., J.C.M. De Witt, and W.H. Van Reimsdijk, *Multisite proton adsorption modelling at the solid/solution interface of (hydr)oxides.* Journal of Colloid and Interface Science, 1989. **133**: p. 105-118.

53. Hingston, F.J., P. A.M., and J.P. Quirk, *Ion adsoprtion by goethite and gibbsite: I. The role of the proton in determining adsorption envelopes.* Journal of Soil Science, 1972. **23**: p. 177-192.

54. Cromieres, L., V. Moulin, B. Fourest, and E. Giffaut, *Physico-chemical characterisation of the colloidal hematite/water interface: experimentation and modelling.* Colloids and Surfaces A: Physicochemical and Engineering Aspects, 2002. **202**: p. 101-115.

55. Hirosue, H., N. Yamada, E. Abe, and H. Tateyama, *Coagulation of red mud suspensions with an organic coagulant.* Powder Technology, 1988. **54**: p. 27-30.

56. Matijevic, E., R.J. Kuo, and H.P. Kolny, *Stability and deposition phenomena of monodispersed hematite sols.* Journal of Colloid and Interface Science, 1981. **80**: p. 509-523.

57. Matijevic, E. and P.J. Scheiner, *Ferric hydrous oxide sols.* Journal of Colloid and Interface Science, 1978. **63**: p. 509-523.

58. Parks, G.A., *The isoelectric points of solid oxides, solid hydroxides, and aqueous hydro complex systems.* Chemical Reviews, 1965. **65**(2): p. 177-198.

59. Toikka, G., R.A. Hayes, and J. Ralston, *Adhesion of iron oxide to silica studied by atomic force microscopy.* Journal of Colloid and Interface Science, 1996. **180**: p. 329-338.

60. Fleer, G.J., L.K. Koopal, and J. Lykelema, *Polymer adsorption and its effect on the stability of hydrophobic colloids: I. Characterisation of pol(vinyl alcohol) adsorption on silver iodide.* Kolloid-Zeitschrift & Zeitschrift fur Polymer, 1972. **250**: p. 689.

61. Loewenberg, M. and R.W. O'Brien, *The dynamic mobility of nonspherical particles.* Journal of Colloid and Interface Science, 1992. **150**: p. 158-168.

62. O'Brien, R.W., *Electroacoustic effects in a dilute suspension of spherical particles.* Journal of Fluid Mechanics, 1988. **190**: p. 71-86.

63. O'Brien, R.W., *The dynamic mobility of a porous particle.* Journal of Colloid and Interface Science, 1995. **171**: p. 495-504.

64. O'Brien, R.W., *The dielectric response of a dilute supension of semiconducting particles.* Journal of Colloid and Interface Science, 1996. **177**(280-281).

65. O'Brien, R.W., D.W. Cannon, and W.N. Rowlands, *Electroacoustic determination of particle size and zeta potential.* Journal of Colloid and Interface Science, 1995. **173**: p. 406-418.

66. Hunter, R.J., *Introduction to modern colloid science*. 1993, New York: Oxford University Press, Inc.

67. Csoban, K., M. Parkanyi-Berka, P. Joo, and P. Behra, *Sorption experiments of Cr(III) onto silica.* Colloids and Surfaces A: Physicochemical and Engineering Aspects, 1998. **141**: p. 347-364.

68. Healy, T.W., *Research in colloid and surface chemistry*. 1969, Melbourne: University of Melbourne.

69. Huang, P. and D.W. Fuerstenau, *The effect of the adsorption of lead and cadmium ions on the interfacial behaviour of quartz and talc.* Colloids and Surfaces A: Physicochemical and Engineering Aspects, 2001. **177**: p. 147-156.

70. James, R.O. and T.W. Healy, *Adsorption of hydrolysable metal ions at the oxide-water interface I. Co(II) adsorption on SiO_2 and TiO_2 as model systems.* Journal of Colloid and Interface Science, 1972. **40**(1): p. 42-52.

71. James, R.O. and T.W. Healy, *Adsorption of hydrolysable metal ions at the oxide-water interface III. A thermodynamic model of adsorption.* Journal of Colloid and Interface Science, 1972. **40**(1): p. 65-80.

72. James, R.O. and T.W. Healy, *Adsorption of hydrolysable metal ions at the oxide-water interface II. Charge reversal of SiO_2 and TiO_2 colloids by adsorbed Co(II), La(III), and Th(IV) as model systems.* Journal of Colloid and Interface Science, 1972. **40**: p. 53-64.

73. James, R.O., P.J. Stiglich, and T.W. Healy, *Analysis of models of adsorption of metal ions at oxide/water interfaces.* Journal of Colloid and Interface Science, 1975. **59**: p. 142-156.

74. Juang, R.-S. and W.-L. Wu, *Adsorption of sulfate and copper(II) on Geothite in relation to the changes of zeta potentials.* Journal of Colloid and Interface Science, 2002. **249**: p. 22-29.

75. Larson, I. and R.J. Pugh, *Qualitative adsorption measurements with an atomic force microscope.* Langmuir, 1998. **14**: p. 5676-5679.

76. Wiese, G.R. and T.W. Healy, *Adsorption of Al (III) at the TiO_2-H_2O Interface.* Journal of Colloid and Interface Science, 1975. **51**: p. 434-442.

77. Bremmell, K.E. and J. Addai-Mensah, *Interfacial-chemistry mediated behaviour of colloidal talc dispersions.* Journal of Colloid and Interface Science, 2005. **283**: p. 385-391.

78. Hunter, R., *Foundations of Colloid Science*. 2nd ed. 2001, Oxford: OUP.

79. Nystrom, R., M. Linden, and J.B. Rosenholm, *The influence of Na^+, Ca^{2+}, Ba^{2+}, and La^{3+} on the ζ potential and the yield stress of calcite dispersions.* Journal of Colloid and Interface Science, 2001. **242**: p. 259-263.

80. Johnson, S.B., D.R. Dixon, and P.J. Scales, *The electrokinetic and shear yield stress properties of kaolinite in the presence of aluminium ions.* Colloids and Surfaces A: Physicochemical and Engineering Aspects, 1999. **146**: p. 281-291.

81. Nowostawska, U., S.G. Sander, K.M. McGrath, and K.A. Hunter, *Effects of coagulants on the surface forces of colloidal alumina under water treatment conditions.* Colloids and Surfaces A: Physicochemical and Engineering Aspects, 2005. **266**(214-222).

82. Brooks, D.E., *Effect of neutral polymers on the electrokinetic potential of cells and other charged particles.* Journal of Colloid and Interface Science, 1973. **43**: p. 670.

83. de Kretser, R.G., P.J. Scales, and D.V. Boger, *Surface Chemistry-rheology inter-relationships in clay suspensions.* Colloids and Surfaces A: Physicochemical and Engineering Aspects, 1998. **137**: p. 307-318.

84. Johnson, S.B., G.V. Franks, P.J. Scales, D.V. Boger, and T.W. Healy, *Surface chemistry-rheology relationships in concentrated mineral suspensions.* International Journal of Mineral Processing, 2000. **58**: p. 267-304.

85. Butt, H.-J., *Force measurements with the atomic force microscope: Technique, interpretation and application.* Surface Science Reports, 2005. **59**: p. 1-152.

86. Dzaloshinskii, I.E., E.M. Lifshitz, and L.P. Pitaerskii, *The General Theory of van der Waals Forces.* Advances in Physics, 1961. **10**: p. 165-209.

87. Lifshitz, E.M., *The Theory of Molecular Attractive Forces Between Solid Bodies.* Journal of Experimental Theory of Physics (*USSR*), 1955. **29**(83-94).

88. Hamaker, H.C., *London-van der Waals Attraction Between Spherical Particles.* Physica, 1937. **4**(1058-1072).

89. Adamson, A.W. and A.P. Gast, *Physical Chemistry of Surfaces. 6th ed. 1997, Canada: John Wiley & Sons.* 6th ed. 1997, Canada: John Wiley & Sons.

90. Hunter, R.J., *Foundations of Colloid Science*. 2nd ed. 2001: Oxford University Press.

91. Israelachavili, J.N., *Intermolecular and surface forces*. 2nd ed. 1992: Academic Press, London, UK.

92. Hermansson, M., *The DLVO theory in microbial adhesion.* Colloids and Surfaces B: Biointerfaces, 1999. **14**: p. 105-119.

93. Moudgil, B.M., P. Singh, and J.J. Adler, in *Applied surface and colloid chemistry*, K. Holmberg, Editor. 2002.

94. Addai-Mensah, J. and J. Ralston, *Investigation of the role of interfacial chemistry on particle interactions, sedimentation and electroosmotic dewatering of model kaolinite dispersions.* Powder Technology, 2005. **160**: p. 35-39.

95. de Kretser, R.G., P.J. Scales, and D.V. Boger, *Improving clay-based tailings disposal: Case study on coal tailings.* AIChE Journal, 1997. **43**: p. 1894-1903.

96. Tombacz, E. and M. Szekeres, *Colloidal behaviour of aqueous montmorillonite suspensions: The specific role of pH in the presence of indifferent electrolytes.* Applied Clay Science, 2004. **27**: p. 74-94.

97. Zbik, M. and R.G. Horn, *Hydrophobic attraction may contribute to aqueous flocculation of clays.* Colloids and Surfaces A: Physicochemical and Engineering Aspects, 2003. **222**: p. 323-328.

98. Leong, Y.K., D.V. Boger, P.J. Scales, and T.W. Healy, *Interparticle forces arising from adsorbed surfactants in colloidal suspensions: An additional attractive force.* Journal of Colloid and Interface Science, 1996. **181**: p. 605-612.

99. Israelachavili, J.N., R.K. Tandon, and L.R. White, *Measurement of forces between mica surfaces in aqueous polethylene oxide solution.* Journal of Colloid and Interface Science, 1980. **78**: p. 430-443.

100. Bremmell, K.E. and P.J. Scales, *Adhesive Forces between Adsorbed Anionic Polyelectrolyte Layers in High Ionic Strength Solutions.* Colloids and Surfaces A: Physicochemical and Engineering Aspects, 2004. **247**: p. 19-25.

101. Chibowski, S., M. Wisniewska, A.W. Marczewski, and S. Pikus, *Application of the SAXS method and viscometry for determination of the thickness of adsorbed polymer layers at the ZrO_2 - polymer solution interface.* Journal of Colloid and Interface Science, 2003. **267**: p. 1-8.

102. Zaman, A.A., *Effect of polyethylene oxide on the viscosity of dispersions of charged silica particles: interplay between rheology, adsorption and surface charge.* Colloid and Polymer Science, 2000. **278**: p. 1187-1197.

103. Farrokhpay, S., G.E. Morris, D. Fornasiero, and P. Self, *Effects of chemical functional groups on the polymer adsorption behaviour onto titania pigment particles.* 2004, 2004. **274**: p. 33-40.

104. Zaman, A.A., R. Tsuchiya, and B.M. Moudgil, *Adsorption of Low-Molecular-Weight Polyacrylic Acid on Silica, Alumina, and Kaolin.* Journal of Colloid and Interface Science, 2002. **256**: p. 73-78.

105. Sato, T. and R. Ruch, *Stabilisation of Colloidal Dispersions by Polymer Adsorption*. 1980, New York: Marcel Dekker.

106. Solberg, D. and L. Wagberg, *Adsorption and flocculation behavior of cationic polyacrylamide and colloidal silica.* Colloids and Surfaces a-Physicochemical and Engineering Aspects, 2003. **219**(1-3): p. 161-172.

107. Nguyen, Q.D. and D.V. Boger, *Yield stress measurement of concentrated suspensions.* Journal of Rheology, 1983. **27**(4): p. 321-349.

108. Nguyen, Q.D. and D.V. Boger, *Direct yield stress measurement for concentrated suspensions.* Journal of Rheology, 1985. **29**: p. 335-347.

109. Ametov, I. and C.A. Prestidge, *Hydrophobic interactions in concentrated colloidal suspensions: A rheological investigation.* Journal of Physical Chemistry B, 2004. **108**: p. 12116-12122.

110. McFarlane, A.J., K.E. Bremmell, and J. Addai-Mensah, *Rheology of flocculated kaolinite dispersions.* Korea-Australia Rheology Journal, 2005. **17**(4): p. 181-190.

111. Scales, P.J., S.B. Johnson, T.W. Healy, and P.C. Kapur, *Shear yield stress of partially flocculated colloidal suspensions.* AIChE Journal, 1998. **44**: p. 538-544.

112. Firth, B.A. and R.J. Hunter, *Flow properties of coagulated colloidal suspensions: The elastic floc model.* Journal of Colloid and Interface Science, 1976. **57**: p. 266-275.

113. Johnson, S.B., *The relationship between the surface chemistry and shear yield stress of mineral suspensions*. 1998, PhD thesis, University of Melbourne.

114. Kapur, P.C., P.J. Scales, D.V. Boger, and T.W. Healy, *Yield stress of suspensions loaded with size distributed particles.* AIChE Journal, 1997. **43**: p. 1171-1179

115. Prestidge, C.A., *Rheological investigations of DLVO and non-DLVO particle interactions in concentrated mineral suspensions*. Mineral Processing and Extractive Metallurgy Review, 1999. **20**: p. 57-74.

116. Abu-Orf, M.M. and B. Ormeci, *Measuring sludge network strength using rheology and relation to dewaterability, filtration, and thickening - Laboratory and full-scale experiments* Journal of Environmental Engineering - ASCE, 2005. **131**: p. 1139-1146.

117. Abu-Orf, M.M. and S.K. Dentel, *Rheology as tool for polymer dose assessment and control* Journal of Environmental Engineering - ASCE, 1999. **125**: p. 1133-1141.

118. Binning, G., C.F. Quate, and C. Gerber, *Atomic Force Microscope.* Physical Review Letters, 1986. **56**: p. 930.

119. Chan, D.Y.C., R.R. Dagastine, and L.R. White, *Forces between a rigid probe and a liquid interface I. The repulsive case.* Journal of Colloid and Interface Science, 2001. **236**: p. 141-154.

120. Pochard, I., J. Boisvert, J. Persello, and A. Foissy, *Surface charge, effective charge and dispersion/aggregation properties of nanoparticles.* Polymer International, 2003. **52**(619-624).

121. Such, M.W., D.E. Kramer, and M.C. Hersam, *Reproducible lateral force microscopy measurements for quantitative comparisons of the frictional and chemical properties of nanostructures.* Ultramicroscopy, 2004. **99**: p. 189-196.

122. Yuan, Y. and A.M. Lenhoff, *Measurement of mobility of adsorbed colloids by lateral force microscopy.* Journal of Colloid and Interface Science, 2003. **267**: p. 352-359.

123. Feiler, A., I. Larson, P. Jenkins, and P. Attard, *A Quantitative Study of Interaction Forces and Friction in Aqueous Colloidal Systems*. Langmuir, 2000. **16**(26): p. 10269-10277.

124. Zhao, F., Y.-K. Du, J. Tang, X.-C. Li, and P. Yang, *Morphology of adsorption of anionic polyelectrolytes to mica substrate in different environment visualised by atomic force microscopy.* Colloids and Surfaces A: Physicochemical and Engineering Aspects, 2005. **252**: p. 153-156.

125. Hamly, I.W., S.D. Connell, and S. Collins, *In situ atomic force microscopy imaging of adsorbed block copolymer micelles.* Macromolecules, 2004. **37**(14): p. 5337-5351.

126. Li, S.L. and A.F. Palmer, *Structure and mechanical response of self-assembled poly(butadiene)-b-poly(ethylene oxide) colloids probed by Atomic Force Microscopy.* Macromolecules, 2005. **38**(13): p. 5686-5698.

127. Wang, J. and P. Somasundaran, *Adsorption and conformation of carboxymethyl cellulose at solid-liquid interfaces using spectroscopic, AFM and allied techniques.* Journal of Colloid and Interface Science, 2005. **291**: p. 75-83.

128. Biggs, S. and T.W. Healy, *Electrosteric Stabilisation of Colloidal Zirconia with Low-molecular-weight Polyacrylic Acid: An Atomic Force Microscope Study.* Journal of The Chemical Society, 1994. **90**(22): p. 3415-3421.

129. Woodward, N.C., M.J. Snowden, and B.Z. Chowdhry, *Measurement of the Interaction Forces between Poly(N-isopropylacrylamide-acrylic acid) Microgel and Silica Surfaces by Colloid Probe Microscopy.* Langmuir, 2002. **18**: p. 2089-2095.

130. Filip, D., V.I. Uricanu, M.H.G. Duits, D. van den Ende, J. Mellema, W.G.M. Agterof, and F. Mugele, *Microrheology of aggregated emulsion droplet networks, studied with AFM-CSLM.* Langmuir, 2006. **22**(2): p. 560-574.

131. Gillies, G. and C.A. Prestidge, *Interaction forces, deformation and nano-rheology of emulsion droplets as determined by colloid probe AFM.* Advances in Colloid and Interface Science, 2004. **108-09**: p. 197-205.

132. Gillies, G. and C.A. Prestidge, *Colloid probe AFM investigation of the influence of cross-linking on the interaction behavior and nano-rheology of colloidal droplets.* Langmuir, 2005. **21**(26): p. 12342-12347.

133. Gunning, A.P., A.R. Mackie, P.J. Wilde, and V.J. Morris, *Atomic force microscopy of emulsion droplets: Probing droplet-droplet interactions.* Langmuir, 2004. **20**(1): p. 116-122.

134. Saiki, Y., *PhD Thesis*. 2006, Ian Wark Research Institute, University of South Australia.

135. Pietrement, O. and M. Troyon, *Quantitative study of shear modulus and interfacial shear strength by combining modulated lateral force and magnetic force modulation spectroscopies.* Surface and Interface Analysis, 2001. **31**: p. 1060-1067.

136. Pederson, H.G. and L. Bergstrom, *Forces Measured between Zirconia Surfaces in Poly(acrylic acid) Solutions.* Journal of the American Ceramic Society, 1999. **82**(5): p. 1137-45.

137. Greenwood, R. and L. Bergstrom, *Electroacoustic and rheological properties of aqueous Ce-ZrO_2 (Ce-TZP) suspensions.* Journal of European Ceramic Society, 1997. **17**: p. 537-548.

138. Alfano, J.C., P.W. Carter, A.J. Dunham, M.J. Nowak, and K.R. Tubergen, *Polyelectrolyte-induced aggregation of microcrystalline cellulose: reversibility and shear effects.* Journal of Colloid and Interface Science, 2000. **223**: p. 244-254.

139. Chen, H.T., S.A. Ravishankar, and R.S. Farinato, *Rational polymer design for solid-liquid separations in mineral processing applications.* International Journal of Mineral Processing, 2003. **72**: p. 75-86.

140. Gregory, J., ed. *The action of polymeric flocculants*. American Institute of Chemical Engineers, ed. B.M. Moudgil and P. Somasundaran. 1985: New York.

141. Gregory, J., *Polymer Adsorption and Flocculation in Sheared Suspensions.* Colloids and Surfaces, 1988. **31**: p. 231-253.

142. Kitchener, J.A., *Principles of action of polymeric flocculants.* Journal of Colloid and Interface Science, 1972. **4**: p. 217-229.

143. Rubio, J. and J.A. Kitchener, *The flocculation properties of polyethylene oxide.* Journal of Colloid and Interface Science, 1981. **2**: p. 79-95.

144. Runkana, V., P. Somasundaran, and P.C. Kapur, *Mathematical modelling of polymer-induced flocculation by charge neutralisation.* Journal of Colloid and Interface Science, 2004. **270**: p. 347-358.

145. Hogg, R., *The role of polymer adsorption kinetics in flocculation.* Colloids and Surfaces, 1999. **146**: p. 253-263.

146. Nabzar, L., E. Pefferkorn, and R. Varoqui, *Stability of polymer-clay suspensions, The polyacrylamide-sodium kaolinite system.* Colloids and Surfaces, 1988. **30**: p. 345-353.

147. Bal, H., *Masters Thesis*. 2006, Ian Wark Research Institute, University of South Australia.

148. McFarlane, A.J., *PhD Thesis*. 2006, Ian Wark Research Institute, University of South Australia.

149. Petzold, G., M. Mende, K. Lunkwitz, S. Schwarz, and H.M. Buchhammer, *Higher efficiency in the flocculation of clay suspensions by using combinations of oppositely charged polyelectrolytes.* Colloids and Surfaces a-Physicochemical and Engineering Aspects, 2003. **218**(1-3): p. 47-57.

150. Yu, J.F., D.S. Wang, X.P. Ge, M.Q. Yan, and M. Yang, *Flocculation of kaolin particles by two typical polyelectrolytes: A comparative study on the kinetics and floc structures.* Colloids and Surfaces a-Physicochemical and Engineering Aspects, 2006. **290**(1-3): p. 288-294.

151. McCarron, A.M., S. Crispo, and T. Smith-Palmer, *The Flocculation of kaolin by cationic polyacrylamides and the effect of cationic surfactant on this process.* Journal of Applied Polymer Science, 2002. **83**(11): p. 2382-2389.

152. Kozlov, M. and T.J. McCarthy, *Adsorption of Poly(Vinyl Alcohol) from Water to a Hydrophobic Surface: Effects of Molecular Weight, Degree of Hydrolysis, Salt and Temperature.* Langmuir, 2004. **20**(21): p. 9170-9176.

153. Xiao, L., G.-Y. Xu, A.-M. Chen, and S.-L. Yuan, *The Adsorption of Hydrophobically Modified Polyacrylates at Interfaces of Quartz/Liquid and Gas/Liquid.* Colloids and Surfaces A: Physicochemical and Engineering Aspects, 2003. **219**(1): p. 233-242.

154. Kaggwa, G., S. Froebe, L. Huynh, J. Ralston, and K. Bremmell, *The Morphology of Adsorbing Polymers and Solid Surface Wettability.* Langmuir, 2004. **21**(10): p. 4695-4704.

155. McFarlane, A.J., K.E. Bremmell, and J. Addai-Mensah, *The influence of flocculant adsorption kinetics on the dewaterability of kaolinite and smectite clay mineral dispersions.* Colloids and Surfaces A, submitted, 2007.

156. Hogg, R., P. Bunnaul, and H. Suharyono, *Chemical and physical variables in polymer-induced flocculation.* Minerals & Metallurgical Processing, 1993. **May**: p. 81-85.

157. Paeng, K., J. Choi, Y. Park, and D. Sohn, *Temperature effect of hydrophobically modified polyethylene oxide at the air-water interface.* Colloids and Surfaces A: Physiochemical and Engineering Aspects, 2003. **220**: p. 1-7.

158. Jenckel, E. and B. Rumbach, *Adsorption of High Polymers from Solution.* Z. Elektrochem, 1951. **55**: p. 612-18.

159. Rossi, S., P.F. Luckham, and T.F. Tadros, *Influence of non-ionic polymers on the rheological behaviour of Na+ -montmorillonite clay suspensions. Part II. Homopolymer ethyleneoxide and polypropylene oxide-polyethylene oxide ABA copolymers.* Colloids and Surfaces A: Physiochemical and Engineering Aspects, 2003. **215**: p. 1-10.

160. Somasundaran, P. and V. Runkana, *Investigation of the flocculation of colloidal suspensions by controlling adsorbed layer microstructure and population balance modelling.* Chemical Engineering Research & Design, 2005. **83**(A7): p. 905-914.

161. Liufu, S.C., H.N. Xiao, and Y.P. Li, *Adsorption of cationic polyelectrolyte at the solid/liquid interface and dispersion of nanosized silica in water.* Journal of Colloid and Interface Science, 2005. **285**(1): p. 33-40.

162. Giles, C.H., D. Smith, and A. Huitson, *A General Treatment of Classification of the Solute Adsorption Isotherm. I - Theoretical.* Journal of Colloid and Interface Science, 1974. **47**(3): p. 755-765.

163. Theng, B.K.J., *Formation and Properties of Clay-Polymer Complexes*. 1979, Amsterdam, The Netherlands: Elsevier Scientific Publishing Co.

164. Morris, G.E., *Adsorption characteristics of polyacrlamide at the water-talc interface*. 1996, PhD thesis, Ian Wark Research Institute, University of South Australia.

165. Morris, G., *The Adsorption Characteristics of Polymeric Depressants at the Talc-Water Interface*, in *Ian Wark Research Institute*. 1996, University of South Australia: Adelaide.

166. Huang, H.-H., J.V. Calara, J.D. Bauer, and J.D. Miller. *Adsorption Reactions in the Depression of Coal by Organic Colloids*. in *Recent Developments in Separation Science*. 1978. West Palm Beach, Florida: CRC.

167. Langmuir, I., *Adsorption of gases on plane surfaces of glass, mica and platinum.* Journal of American Chemical Society, 1918. **40**: p. 1361-1403.

168. Freundlich, H.M.F., *Over the adsorption in solution.* Journal of Physical Chemistry, 1906. **57**: p. 385-471.

169. Hiemenz, P.C., *Principles of colloid and surface chemistry*. 2nd, revised and expanded ed. 1986, New York: Marcel Dekker.

170. Rossi, S., P.F. Luckham, and T.F. Tadros, *Influence of non-ionic polymers on the rheological behaviour of Na^+ -montmorillonite clay suspensions - I Nonylphenol-polypropylene oxide-polyethylene oxide copolymers.* Colloids and Surfaces A: Physiochemical and Engineering Aspects, 2002. **201**: p. 85-100.

171. Vermohlen, K., H. Lewandowski, H.-D. Narres, and E. Koglin, *Adsorption of polyacrylic acid on aluminium oxide: DRIFT spectroscopy and ab initio calculations.* Colloids and Surfaces A: Physicochemical and Engineering Aspects, 2000. **170**: p. 181-189.

172. Lu, X. and M. Yongli, *Characterisation of the Interfacial Interaction between Polyacrylamide and Silicon Substrate by Fourier Transform Infrared Spectroscopy.* Macromolecules, 2005. **38**: p. 839-843.

173. Scoggins, M.W. and J.W. Miller, *Spectrophotometric Determination of Water Soluble Organic Amides.* Analytical Chemistry, 1975. **47**(1): p. 152-154.

174. Nguyen, T.T., L.J. Janik, and M. Raupach, *Diffuse relectance infrared Fourier transform (DRIFT) spectroscopy in soil science.* Australian Journal of Soil Research, 1991. **29**: p. 49-67.

175. Ducker, W.A., T.J. Senden, and R.M. Pashley, *Measurement of forces in liquid using a force microscope.* Langmuir, 1992. **8**: p. 1831-1836.

176. *Asylum MFP-3D Cantilever calibration.* www.asylumresearch.com.

177. Green, C.P., H. Lioe, J.P. Cleveland, R. Proksch, and J.E. Sader, *Normal and torsional spring constants of Atomic Force Microscope cantilevers.* Review of Scientific Instruments, 2004. **75**: p. 1988-96.

178. Green, C.P. and J.E. Sader, *Torsional frequency response of cantilever beams immersed in viscous fluids with applications to the atomic force microscope.* Journal of Applied Physics, 2002. **92**: p. 6262-74.

179. Cain, R.G., S. Biggs, and N.W. Page, *Force Calibration in Lateral Force Microscopy.* Journal of Colloid and Interface Science, 2000. **227**: p. 55-65.

180. Walpole, R.E. and R.H. Myers, *Probability and Statistics for Engineers and Scientists*. 4th ed. 1989, New York: Macmillan Publishing Co.

181. Hollander, A.F., P. Somasundaran, and C.C. Gryte, *Adsorption characteristics of polyacrylamide and sulfonate-containing polyacrylamide copolymers on sodium kaolinite.* Journal of Applied Polymer Science, 1981. **26**: p. 2123-2138.

182. Kharlampieva, E. and S.A. Sukhishvili, *Polyelectrolyte Multilayers of Weak Polyacid and Cationic Copolymer: Competition of Hydrogen-Bonding and Electrostatic Interactions.* Macromolecules, 2003. **36**: p. 9950-9956.

183. Beta, I.A., H. Bohlig, and B. Hunger, *Structure of adsorption complexes of water in zeolites of different types studied by infrared spectroscopy and inelastic neutron scattering.* Physical Chemistry Chemical Physics, 2004. **6**(8): p. 1975-1981.

184. Asselman, T. and G. Garnier, *The role of anionic microparticles in a poly(acrylamide)-montmorillonite flocculation aid system.* Colloids and Surfaces a-Physicochemical and Engineering Aspects, 2000. **170**(1): p. 79-90.

185. Ayol, A., S.K. Dentel, and A. Filibeli, *Dual polymer conditioning of water treatment residuals.* Journal of Environmental Engineering - ASCE, 2005. **131**: p. 1132-1138.

186. Bal, H., K.E. Bremmell, and J. Addai-Mensah. *Single and dual polymer flocculation and dewatering behaviour of gibbsite dispersions*. in *Chemeca*. 2006. Auckland, New Zealand.

187. Bal, H., K.E. Bremmell, and J. Addai-Mensah. *Polyelectrolyte enhanced particle interactions and dewaterability of gibbsite dispersions*. in *Chemeca*. 2006. Auckland, New Zealand.

188. Nasser, M.S. and A.E. James, *The effect of polyacrylamide charge density and molecular weight on the flocculation and sedimentation behaviour of kaolinite suspensions.* Separation and Purification Technology, 2006. **52**(2): p. 241-252.

189. Nuysink, J. and L.K. Koopal, *The effect of polyethylene oxide molecular weight on determination of its concentration in aqueous solutions.* Talanta, 1982. **29**: p. 495-501.

190. Pattanaik, M. and S.K. Bhaumik, *Adsorption behaviour of polyvinyl pyrrolidone on oxide surfaces.* Materials Letters, 2000. **44**: p. 352-360.

191. Hollander, A.F., *Master's Thesis*. Columbia University. 1979, New York.

192. Tekin, N., A. Dincer, O. Demirbas, and M. Alkan, *Adsorption of cationic polyacrylamide onto sepiolite.* Journal of Hazardous Materials, 2006. **134**(1-3): p. 211-219.

193. Middleton, J.C., D.F. Cummind, and C.L. McCormick, *Rheological properties of hydrophobically modified acrylamide-based polyelectrolytes*. Water Soluable Polymers, ed. S.W. Shalaby, C.L. McCormick, and G.B. Butler. 1990: American Chemical Society.

194. Arundell, M.C., *Northparkes Cu-Au Mines, Central N.S.W.* Regolith Expression of Australian Ore Systems., ed. C.R.M. Butt, et al. 2005.

195. Malysiak, V., C.T. O'Connor, J. Ralston, A.R. Gerson, L.P. Coetzer, and D.J. Bradshaw, *Pentlandite-feldspar interaction and its effect on separation by flotation.* International Journal of Mineral Processing, 2002. **66**(1-4): p. 89-106.

196. Adachi, Y., *Dynamic aspects of coagulation and flocculation.* Advances in Colloid and Interface Science, 1995. **56**: p. 1-31.

197. Pang, P. and P. Englezos, *Phase separation polyethylene oxide (PEO)-water solution and its relationship to the flocculating capability of PEO.* Fluid Phase Equilibria, 2002. **194-197**: p. 1059-1066.

198. Bremmell, K.E., A. Evans, and C.A. Prestidge, *Deformation and nano-rheology of red blood cells: An AFM investigation.* Colloids and Surfaces B-Biointerfaces, 2006. **50**(1): p. 43-48.

199. Toikka, G. and R.A. Hayes, *Direct measurement of colloidal forces between mica and silica in aqueous electrolyte.* Journal of Colloid and Interface Science, 1997. **191**: p. 102-109.

200. Toikka, G., R.A. Hayes, and J. Ralston, *The application of lateral force microspcopy to particle removal in aqueous polymer solutions.* Journal of Adhesion Science and Technology, 1997. **11**(12): p. 1479-1489.

201. Coffinier, Y., S. Janel, A. Addad, R. Blossey, L. Gengembre, E. Payen, and R. Boukherroub, *Preparation of superhydrophobic silicon oxide nanowire surfaces.* Langmuir, 2007. **23**(4): p. 1608-1611.

202. Kumpika, T., W. Thongsuwan, and P. Singjai, *Atomic force microscopy imaging of ZnO nanodots deposited on quartz by sparking off different tip shapes.* Surface and Interface Analysis, 2007. **39**(1): p. 58-63.

203. Gliemann, H., Y. Mei, M. Ballauff, and T. Schimmel, *Adhesion of spherical polyelectrolyte brushes on mica: An in situ AFM investigation.* Langmuir, 2006. **22**(17): p. 7254-7259.

204. Kuhner, F., M. Erdmann, L. Sonnenberg, A. Serr, J. Morfill, and H.E. Gaub, *Friction of single polymers at surfaces.* Langmuir, 2006. **22**(26): p. 11180-11186.

205. Uner, B., M.K. Ramasubramanian, S. Zauscher, and J.F. Kadla, *Adhesion interactions between poly(vinyl alcohol) and iron-oxide surfaces: The effect of acetylation.* Journal of Applied Polymer Science, 2006. **99**(6): p. 3528-3534.

206. Long, J., H. Li, Z. Xu, and J.H. Masliyah, *Role of colloidal interactions in oil sand tailings treatment.* American Institute of Chemical Engineers Journal, 2006. **52**: p. 371-383.

207. Gregory, J., ed. *Stability and flocculation of suspensions*. Processing of solid-liquid Suspensions, ed. P.A. Shamlou. 59-92.

208. Yilmaz, H., K. Sato, and K. Watari, *AFM interaction study of α-alumina particle and c-sapphire surfaces at high ionic strength electrolye solutions.* Journal of Colloid and Interface Science, 2007. **307**: p. 116-123.

209. Azizi, M., W. Schneider, and W. Plieth, *Electrolytic co-deposition of silicate and mica particles with zinc.* Journal of Solid State Electrochemistry, 2005. **9**(6): p. 429-437.

210. Eisele, T.C., S.K. Kawatra, and S.J. Ripke, *Water chemistry effects in iron ore concentrate agglomeration feed.* Mineral Processing and Extractive Metallurgy Review, 2005. **26**(3-4): p. 295-305.

211. Zhou, S.Q., *An approximate analytic expression for the surface charge density surface potential relationship for a spherical colloidal particle.* Journal of Colloid and Interface Science, 1998. **208**(1): p. 347-350.

212. Neumeister, J.M. and W.A. Ducker, *Lateral, normal, and longitudinal spring constants of atomic force microscopy cantilevers.* Review of Scientific Instruments, 1994. **65**: p. 2527-2531.

213. Enachescu, M., R.J.A. van den Oetelaar, R.W. Carpick, D.F. Ogletree, C.F.J. Flipse, and M. Salmeron, *Observation of proportionality between friction and contact area at the nanometer scale.* Tribology Letters, 1999. **7**: p. 73-78.

214. Chaudhury, M.K., T. Weaver, C.Y. Hui, and E.J. Kramer, *Adhesive contact of a cylindrical lens and a flat sheet.* Journal of Applied Physics, 1996. **80**: p. 30-37.

APPENDIX Atomic Force Microscopy measurement of forces between two iron oxide surfaces

A.1 SUMMARY

Interaction force measurements (both normal and lateral) were taken between two iron oxide surfaces in the presence and absence of polymer over a range of concentrations at high pH. Force vs. distance curves mostly showed repulsion on approach and retraction of the colloidal probe, except in cases where adhesion occurred due to polymer entanglement and polymer bridging. Observed adhesion was consistent with forces observed in the literature. Zeta potentials were calculated for each experimental condition via fits of the data to the linear Poisson-Boltzmann equation, and the results were consistent with that observed in Chapter 5.

Lateral force measurements revealed PAM A addition to have a greater effect on the lateral force, due to an expanded interfacial conformation causing polymer entanglement and polymer bridging. PAM N addition had little effect on the lateral force due to its small surface coverage as a result of its small interfacial conformation.

This chapter was ultimately left out of the thesis as the work was unable to produce the kind of results that were useful to this body of work as a whole.

A.2 INTRODUCTION

The Atomic Force Microscope (AFM) has been well utilised for the determination of surface properties of oxides [4, 20, 59, 75, 124, 126-128, 131, 132, 135, 136, 198-200]. AFM imaging of surfaces can be useful in the determination of the surface morphology of adsorbed species [20, 201, 202], whilst colloidal probe measurements can reveal information about the interparticle force characteristics between two surfaces with and without adsorbed species present [4, 5, 59, 100, 129, 199, 203, 204].

Full comprehension of the flocculation mechanisms of polyacrylamides and their influence on the dewaterability of iron oxide requires an understanding of the prevailing forces between the particles in solution, both in the presence and absence of any polymer. Colloidal probe measurements will allow determination of specific forces operating between two particles as a result of flocculation.

Whilst rheological measurements made in Chapter 5 indicate the bulk particle interactions between flocculated iron oxide dispersions, AFM force measurements are required to provide a more direct picture of the forces present between particles. Lateral forces are measured between the colloid probe and the surface whilst the probe is being drawn with force across it in a lateral motion. This is comparable to the shear yield stress measurements shown in Chapter 5, which measured the amount of force required for flow to occur in the same lateral motion.

A.3 AFM INTERPARTICLE FORCE MEASUREMENTS

A.3.1 The effect of polymer addition at high pH on interparticle normal forces

Figure 0.1 shows the repulsive force on approach of two iron oxide surfaces in the absence of polymer, and after addition of 20 ppm PAM A and PAM N at pH 11. After the addition of both polymers, the repulsion experienced between the two surfaces decreases. It is known from Chapter 4 and other examples in the literature [7, 10, 54] that the addition of polymer to iron oxide surface shields the zeta potential, and reduces the negative charge

and hence we see, predictably, a decrease in the repulsion experienced between these two surfaces on approach. It is also known from Chapter 5 that the rheological properties of iron oxide pulps flocculated with both polymers are similar, despite differences in structure, as PAM N was shown to hydrolyse at high pH in Chapter 4. It therefore follows logic that the addition of both polymers at high pH would have similar effects on the forces between these surfaces, as was observed to be the case here. It is apparent, however, that PAM N has more of a shielding effect than PAM A, which will be investigated further throughout this chapter.

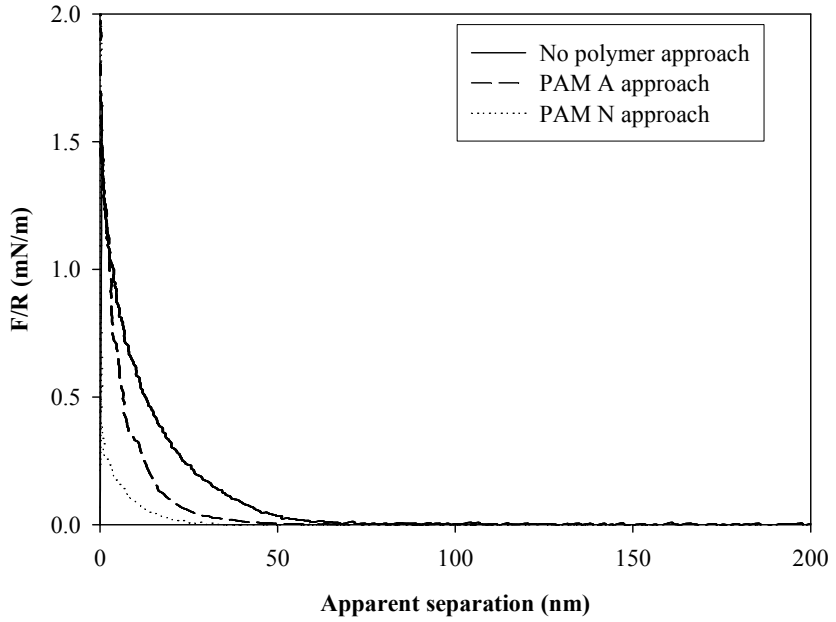
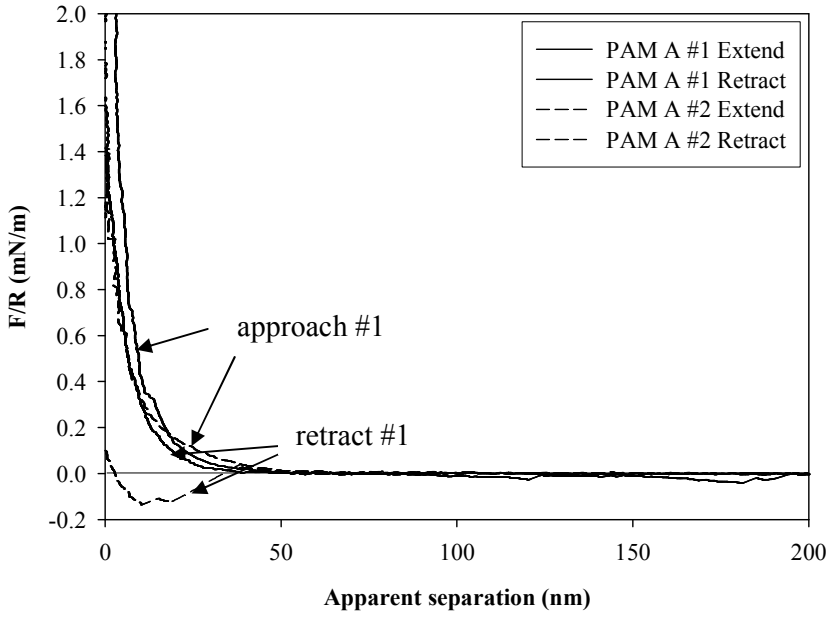


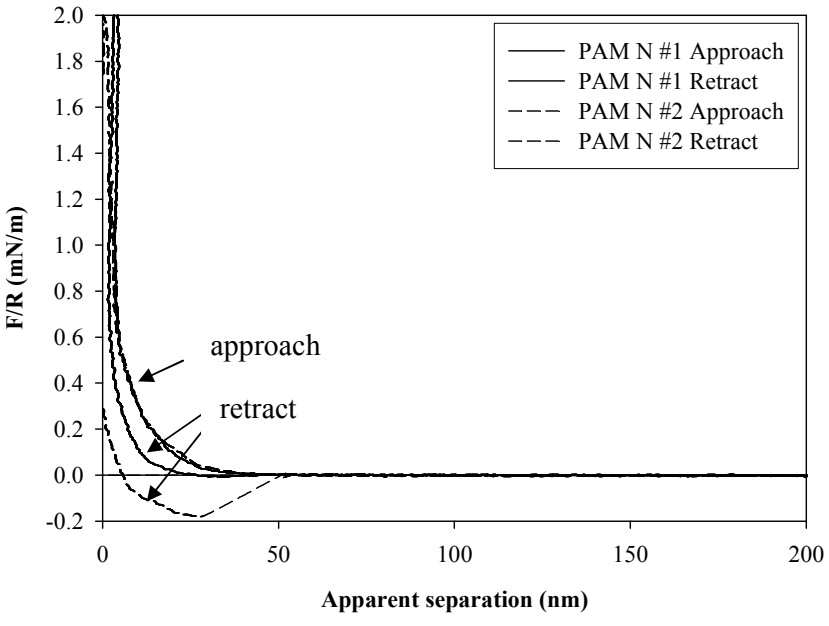
Figure 0.1: Force vs Separation for two iron oxide surfaces at pH 11 with and without the presence of polymer at 20 ppm.

Figure 0.2 shows the variability observed in the same system as in Figure 0.1. Figure 0.2(a) shows examples of two force curves (approach and retract) for the same iron oxide surfaces in the presence of PAM A at 20 ppm, whilst Figure 0.2(b) shows the same for PAM N. In Figure 0.2(a) and (b) it is apparent that there is some variability in the behaviour upon retraction of the iron oxide probe. Both graphs show an example of a force curve taken where the retraction curve is repulsive, and one where the retraction curve shows adhesion. This is due to entanglement of the high molecular weight polymer strands causing adhesion on retraction, and the bridging action of the polymer patches on the two surfaces as observed in previous studies in the presence of polymer [100, 200, 205]. It

should be noted that in all AFM experiments conducted in this chapter, that this same variability was present.



(a)



(b)

Figure 0.2: Force vs Separation for two iron oxide surfaces at pH 11 after the addition of (a) 20 ppm PAM A and (b) 20 ppm PAM N.

The observed adhesion force (approximately 0.12 mN/m) is comparable to that found by Bremmell and Scales [100], who found the adhesion between an iron oxide plate and a

silica probe in the presence of polyacrylate (similar to PAM A but 73 mol % substituted with COO^- groups instead of 25 mol %) to be 0.2 mN/m after addition of 10 ppm polymer at pH 10.4. This was however, in the presence of a 1 M salt solution, whereas all experiments in this body of work were carried out at 10^{-3} M salt solution. In accordance with observations made by Bremmell and Scales [100] and Biggs [4], Long *et al*. [206] found no adhesive forces at higher concentrations of polymer.

Previous discussions in Chapters 4 and 5 have shown PAM N to have a more contracted interfacial conformation than PAM A, and thus we would expect the surface coverage to be lower at 20 ppm than it is for PAM A (as seen in Table 0.1). The amount of polymer present in each scenario here is known from the concentration and was calculated as a percentage of the adsorbent capacity determined via the Freundlich isotherm fits (determined in Chapter 4) to give a percentage of surface coverage. It should be noted that 5% of adsorbent capacity does not necessarily equate to 5% of surface coverage, as the polymer may take a flat interfacial conformation at the surface and form trains that cover more of the surface than if the interfacial conformation was expanded with mainly loops and tails. This value will, however, be expressed as a percentage of surface coverage for convenience. A measurement was included beyond 100% surface coverage in order to determine if the expected electrosteric stabilisation causes particles to flocculate or stabilise as shown through both the force vs. distance measurements and lateral force measurements.

Table 0.1: Percentage of adsorbent capacity for each polymer and each concentration.

	PAM A	**PAM N**
0 ppm	0.0 %	0.0 %
2 ppm	12.8 %	1.7 %
10 ppm	64.1 %	8.3 %
20 ppm	128.2 %	16.7 %

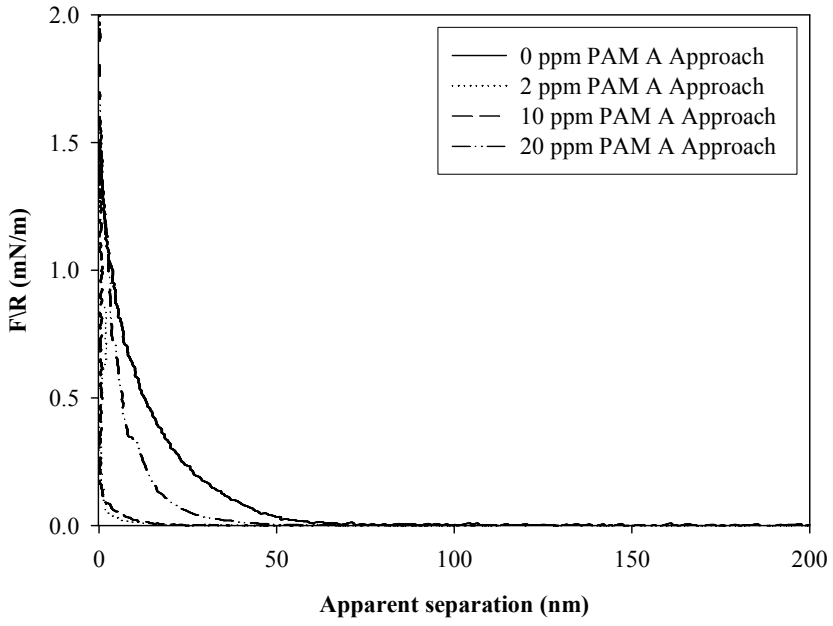
In Figure 0.3(a), the effect of PAM A concentration on the forces present between two iron oxide surfaces is described at pH 11. All measurements were taken during the same

experiment, beginning with the 0 ppm measurement. After this measurement was completed, the electrolyte was exchanged for a solution of 2 ppm PAM A and allowed to equilibrate. After completion of this measurement, the solution was exchanged for a 10 ppm PAM A solution and so on. Refer to Chapter 3 for more details. Addition of 2 ppm PAM A and PAM N (see Figure 0.3 (b)) causes dramatically different effects.

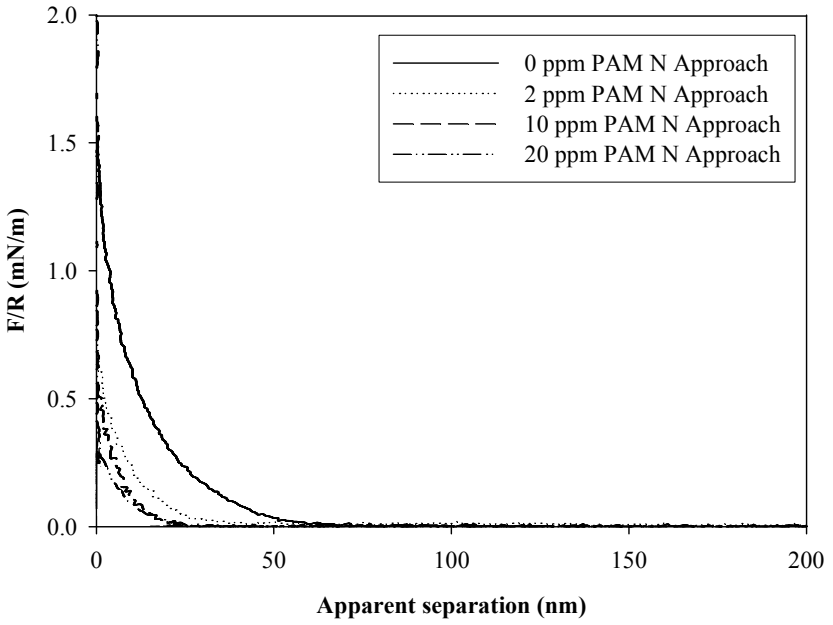
Repulsion is greatest in the absence of polymer where electrostatic repulsion is experienced between the two highly charged surfaces. The addition of 2 and 10 ppm PAM A effectively shields the surface charge of the iron oxide. As the polymer dosage increases to over 100% surface coverage, an increase in electrosteric repulsion is observed. This is consistent with the literature in which it is known that over-flocculation of a dispersion can lead to stabilisation rather than flocculation in the manner in which dispersants are used [7, 128, 207].

Similarly to Figure 0.3 (a), the effect of PAM N concentration is described on the same surface at pH 11 in Figure 0.3 (b). Whilst the concentration of the polymer added remains the same as for PAM A, there is a difference in the adsorption behaviour of these two polymers at this pH. In Figure 0.3 (b) it is apparent that increased polymer addition decreases the repulsion experienced between the two surfaces. This is similar to what would be expected by an increase in salt concentration due to a reduction in long range repulsion experienced by the two surfaces on approach, as observed by Yilmaz *et al*. [208] in their study on a mineral system at pH 11 with increasing KCl concentration. With increased PAM N addition, the surface coverage increases whilst remaining below 100% of adsorbent capacity. As more polymer covers the surface the repulsion decreases, similar to the behaviour observed below adsorbent capacity for PAM A (2 and 10 ppm).

PAM A has a more expanded interfacial conformation and therefore shifts the plane of shear further away from the particle than the more contracted non-ionic PAM N molecules. This effectively shields the zeta potential. PAM N molecules, whilst being present in approximately the same numbers as PAM A, have a smaller hydrodynamic radius and are not electrostatically repelled by the surface as the PAM A molecules are. This allows the PAM N molecules to uncoil across the surface, and adsorb in trains rather than in loops and tails. Whilst this is also effective at shielding the zeta potential, it has been shown in Chapter 5 to be detrimental to dewatering as it is the loops and tails that lead to successful flocculation.



(a)

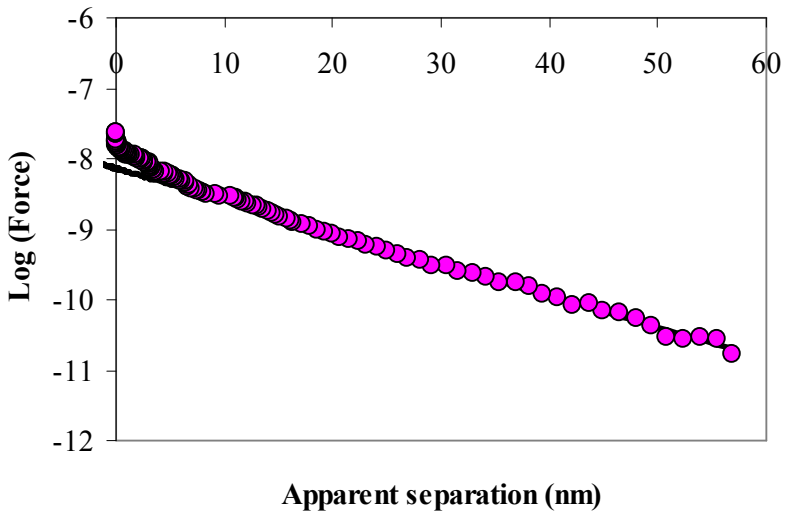


(b)

Figure 0.3: Force vs Separation for two iron oxide surfaces at pH 11 with increasing concentration of (a) PAM A and (b) PAM N.

Assuming electrostatic forces are predominant at large distances, it is possible to estimate the surface potential, i.e. the zeta potential, by fitting the experimental data to the

renormalized linear Poisson-Boltzmann equation (Equation 2.8). An example of the fitting procedure is shown in **Figure 0.4**. The example shows the approach curve for two iron oxide surfaces in the presence of 20 ppm PAM A. In this case, the zeta potential of the surfaces was determined to be ~ -48 mV which corresponds to that measured of the dispersion under similar conditions (Figure 5.1).



(a)

Figure 0.4: Log(Force) vs. separation for the approach of two iron oxide surfaces in the presence of 20 ppm PAM A at pH 11, with the fit to the Poisson-Boltzmann equation symbolised as a line.

For surfaces in the absence of polymer, the zeta potential of the magnetite was estimated from the force curves between a magnetite particle and a mica sheet. Estimation of the zeta potential of the hematite plate was then calculated using the estimation of the zeta potential of the magnetite particle. After polymer addition, the zeta potential of the overall system is calculated as an average of the two. The difference in surface potential will become less relevant as the polymer molecules coat the surface, and for this analysis individual surface potential of the particle and the plate are not required and the system is treated as symmetrical.

Force vs. distance measurements were taken between the magnetite probe and a freshly cleaved mica surface over a range of pH values. As the zeta potential of mica is well characterised in the literature [209], the zeta potentials of the magnetite probe could be

approximated via fitting of the data to the Poisson-Boltzmann equation. The results of these calculations are displayed in Figure 0.5 along with the literature values for mica. The magnetite has an iep in the range of 3-4 consistent with a magnetite sample reported by Eisele *et al*. [210], indicating the wide applicability of the Poisson-Boltzmann equation to various systems. Despite having a much lower iep than the hematite used throughout the experiments in Chapters 4-6, the approximate zeta potential at pH 11 is similar, being ~ -50 mV.

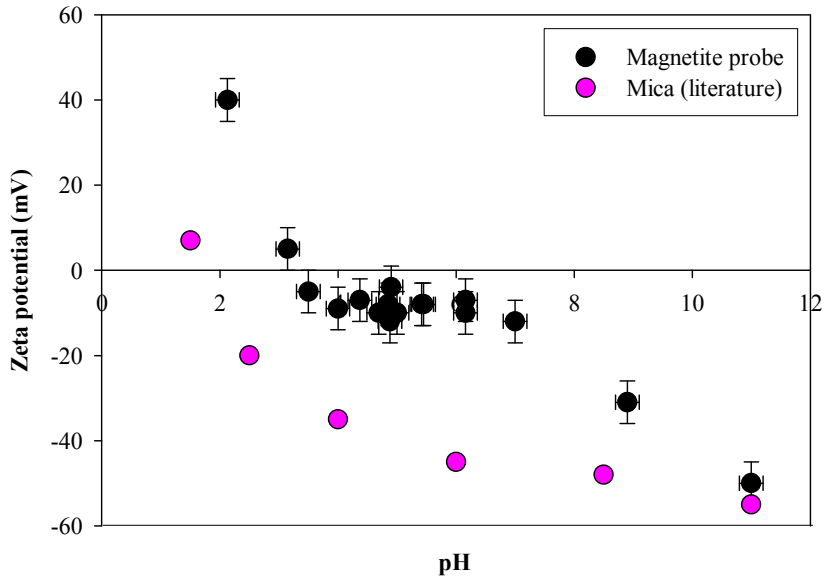


Figure 0.5: The approximate zeta potential of the magnetite probe as calculated via the Poisson-Boltzmann equation using mica values from the literature [209].

The calculated surface potential for each experiment shown previously and to follow is described below in Table 0.2 and represented schematically in Figure 2.1. The zeta potential of the iron oxide surface is high and negative without polymer (shown in Figure 0.5 examples (a) and (e)). This is higher than expected in this system (due to the magnetite probe having an approximate zeta potential of -50 ± 5 mV), and higher than reported in other studies. Addai-Mensah and Ralston reported hematite to have a zeta potential of ~ -60 mV at pH 11, whilst it was found to be approximately -40 mV in Chapter 4. Whilst Cromiéres *et al*. have pointed to the variability in the zeta potential of iron oxide dispersions, it still appears that -86 mV is of a higher magnitude than that generally reported for iron oxide systems. This may be due to the fact that the Poisson-Boltzmann equation models the zeta potential approximately [211], and also as the zeta potential of

the magnetite probe was an approximation of surface potential via the same method taking the zeta potential for mica from the literature.

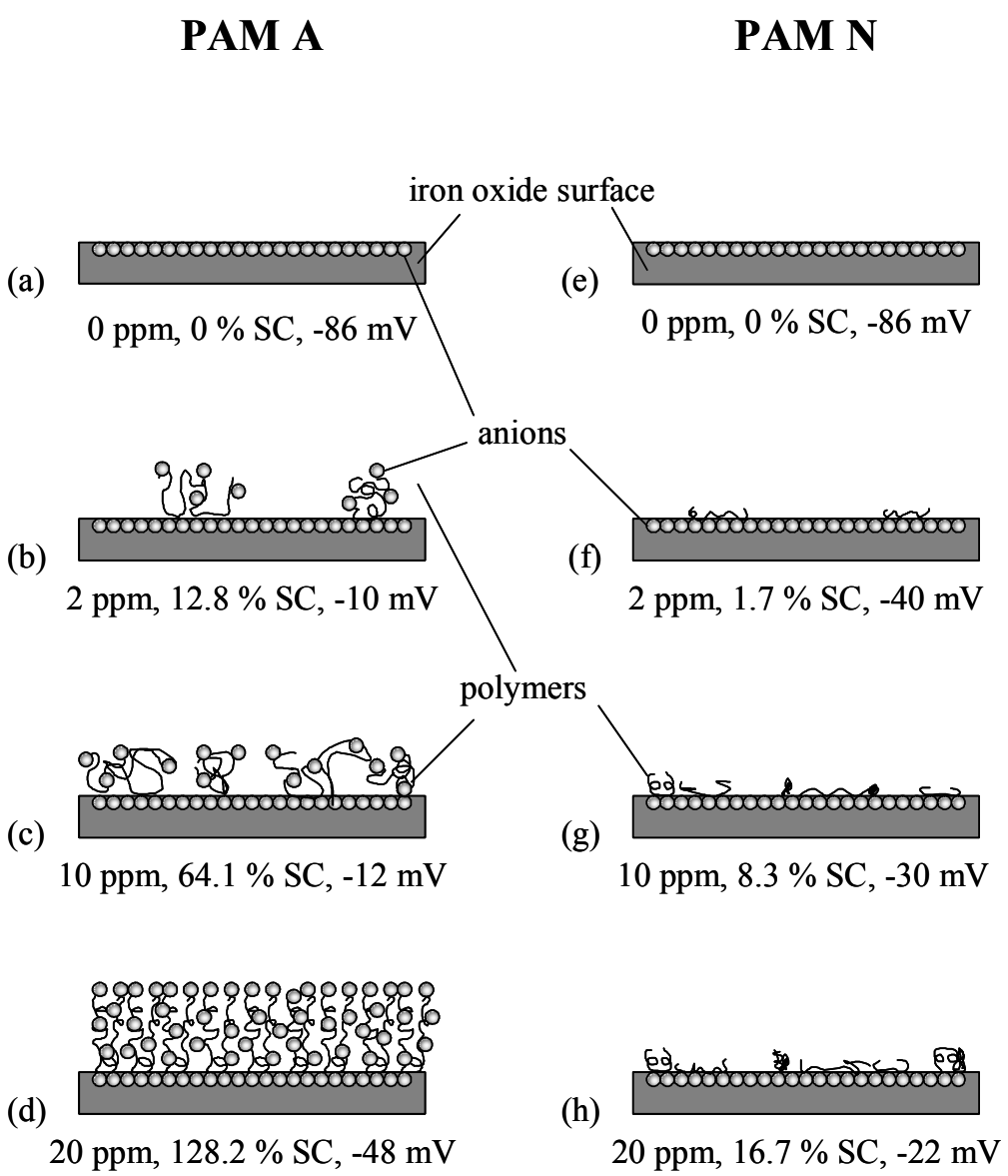


Figure 0.6: Schematic representation of polymer addition to iron oxide (SC = surface coverage).

After the addition of 2 ppm polymer shown in examples (b) and (f), addition of each polymer has drastically different effects. PAM A addition is equivalent to 12.8 % surface coverage, while PAM N addition is only 1.7 %. As PAM A is charged and highly expanded, it shifts the plain of shear further from the surface than PAM N does. This is the

cause for the large shielding effect of PAM A, observed through the reduction in zeta potential. The presence of the highly expanded PAM A would generally be expected to cause a greater amount of steric repulsion than observed at 2 ppm and 10 ppm. It therefore appears that the highly expanded polymer provides little resistance to the cantilever at surface coverage values 12.8 and 64.1%. In addition, the polymer is only 25 mole% substituted with anionic groups and thus may not provide much steric repulsion between the surfaces at these surface coverages. PAM N adsorbs onto the iron oxide in a flatter conformation that does not shift the plane of shear as much, however, the flat conformation of PAM N on the surface ensures the shielding of the charge as it adsorbs.

Table 0.2: Calculated effective surface potential of each polymer system at each concentration.

	PAM A	PAM N
0 ppm	-86 mV	-86 mV
2 ppm	-10 mV	-40 mV
10 ppm	-12 mV	-30 mV
20 ppm	-48 mV	-22 mV

After 10 ppm addition, PAM A has fully covered the surface and is rearranging to allow more polymer to adsorb (now 64.1 % surface coverage). This is simultaneously shielding the charge of the surface and increasing the charge via the addition of more anions. PAM N, however, is still continuing to adsorb with trains along the surface, continuing through to 20 ppm addition in example (h). The continued addition of PAM N at low surface coverage shields the surface charge with continued polymer addition. These results are consistent with those observed in Chapter 5, where the addition of polymer below 50% surface coverage at high pH shields the charge of the iron oxide surfaces.

After over flocculation with 20 ppm PAM A, steric repulsion occurs due to the saturation of charged electrolyte on the iron oxide surfaces. The extra addition of anions only serves to further increase the negativity at the plane of shear, and combined with the steric effect, gives rise to a more negative effective zeta potential.

The thickness of the effective mobile layer between the particles (which consists of the electrical double layer, the adsorbed polymer layer thickness or a combination of both) can be estimated as half of the deflection commencement distance of a force curve (see point A in Figure 0.7). At point C, the force-distance curve reaches the linear compliance region where the surfaces of the hard core components are in contact with the maximum effective contact radius at infinite force. At the distances between points A and C, the effective mobile layers are penetrating each other with the effective contact radius of R(F) for the relevant force of F (point B). This will be discussed further in Section A.4.

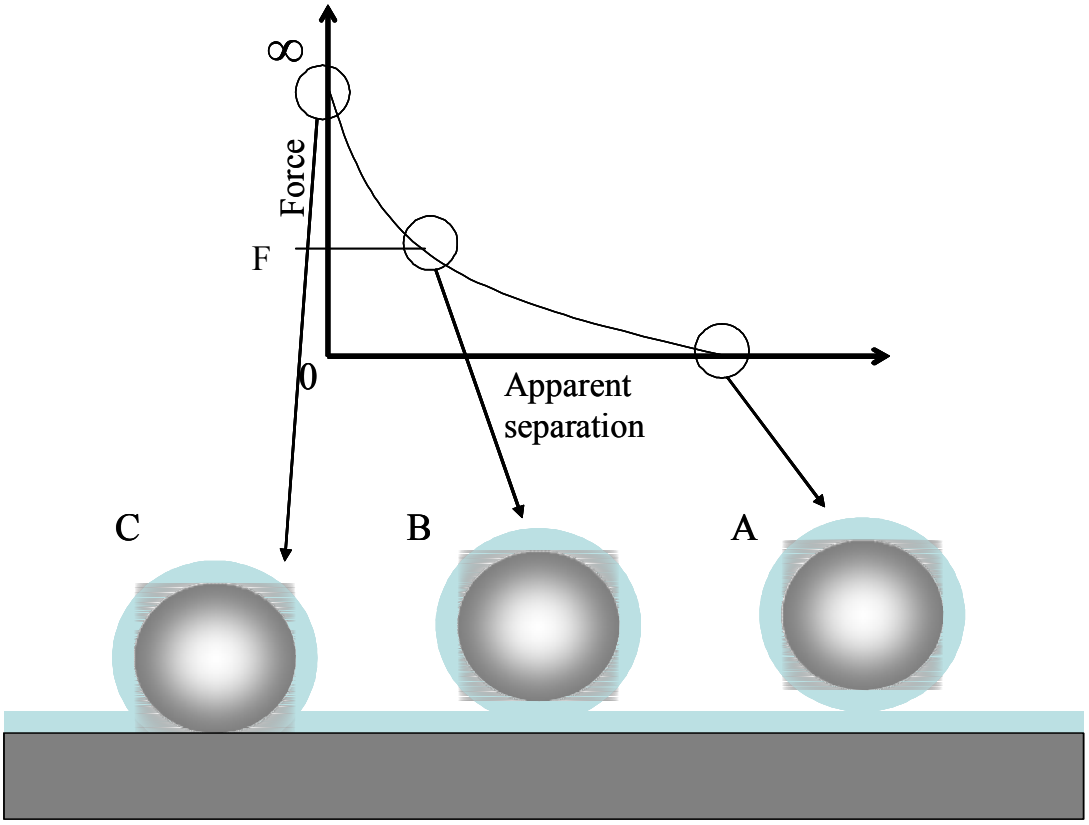


Figure 0.7: Schematic representation of a force curve and particle position upon approach, where the apparent separation at (A) is twice the effective mobile layer, (B) is the thickness to which the (layer-covered) probe will penetrate the mobile layer under the applied force, and (C) is at infinite force where the surfaces are considered to be in contact. The layer on the particle and the plate can be considered the effective mobile layer.

The estimation of the adsorbed layer thickness from point A (see Figure 0.7) is given below in **Error! Reference source not found.**. This is another reflection of the combined zeta potential and polymer conformation schematically represented in Figure 0.6. In the case of PAM A addition, it is expected that the polymer layer would be thicker at 20 ppm where there is effective saturation of the iron oxide surface with the polymer, and thus the effective mobile layer grows at this point. For PAM N, however, it is not expected that at concentrations below 20% surface coverage that the adsorbed polymer layer would increase in thickness and thus the reduction seen in the effective mobile layer thickness is a direct representation of the reduction of surface charge by the shielding of the polymer.

Table 0.3: Estimated effective mobile layer thickness from the interaction force measurements in Figure 0.2.

	0 ppm (nm)	**2 ppm (nm)**	**10 ppm (nm)**	**20 ppm (nm)**
PAM A	32.5	7.5	8.75	22.5
PAM N	32.5	20	12.5	10

A more direct comparison between the effects of PAM A and PAM N on the surface forces between two iron oxide surfaces is made in Figure 0.8, where the repulsive forces on approach are observed. With PAM A concentration at 2 ppm and PAM N concentration at 20 ppm, there is approximately 12.8 and 16.7% surface coverage, respectively. It is noted that whilst PAM N has a slightly higher coverage, PAM A still shields more of the repulsion of the surfaces, which would be expected due to PAM A shifting the plane of shear out further than PAM N, due to it's larger hydrodynamic radius. This would give rise to a smaller zeta potential and hence less repulsion should be experienced between the two surfaces. Steric repulsion is not experienced between the two surfaces after PAM A addition as the surface coverage is too low.

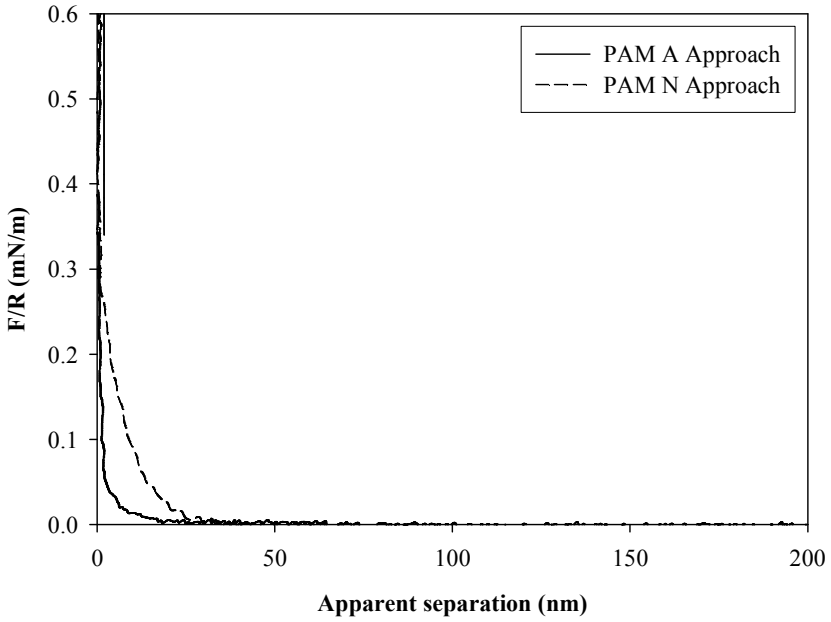


Figure 0.8: Force vs Separation for two iron oxide surfaces at pH 11 with PAM A and PAM N addition with similar % surface coverage.

A.4 AFM LATERAL FORCE MEASUREMENTS

All AFM lateral force measurements described hereafter are an average of at least 6 measurements taken at different places on the iron oxide surface for each set of experimental conditions. The measurements were taken as a friction loop, and the voltage measured as shown in Figure 3.10. An example of this is shown in a measurement taken between the two surfaces at pH 11 (in the absence of polymer), as depicted in Figure 0.10. This measurement allows calculation of the lateral force via Equation 3.5 as discussed in Section 3.7.2.

In Figure 0.10 the effect on the lateral force after the addition of up to 20 ppm of both PAM A and PAM N is observed. PAM A follows similar trends with the force vs. distance measurements, in that by reducing the repulsion experienced between the surface and the probe on approach, the friction between the two surfaces would increase due to the decrease in their mutual repulsion. Also, after the initial dosage of PAM A addition, there is no significant change in lateral force. This is consistent with the surface coverage being

large in each case. Even though there is only just over 10 % surface coverage after the addition of 2 ppm, the expanded interfacial conformation nearly ensures that the particle and the plate do not come into contact. The interaction at this point (and after further PAM A addition) upon approach of the two surfaces is between the polymer molecules rather than the surface. It follows logic that they are no more or less attracted to each other no matter the number, and they will still be expected to give rise to a higher lateral force than PAM N due to entanglement of the expanded polymer molecules and bridging flocculation that is known to occur at high pH (Chapter 6).

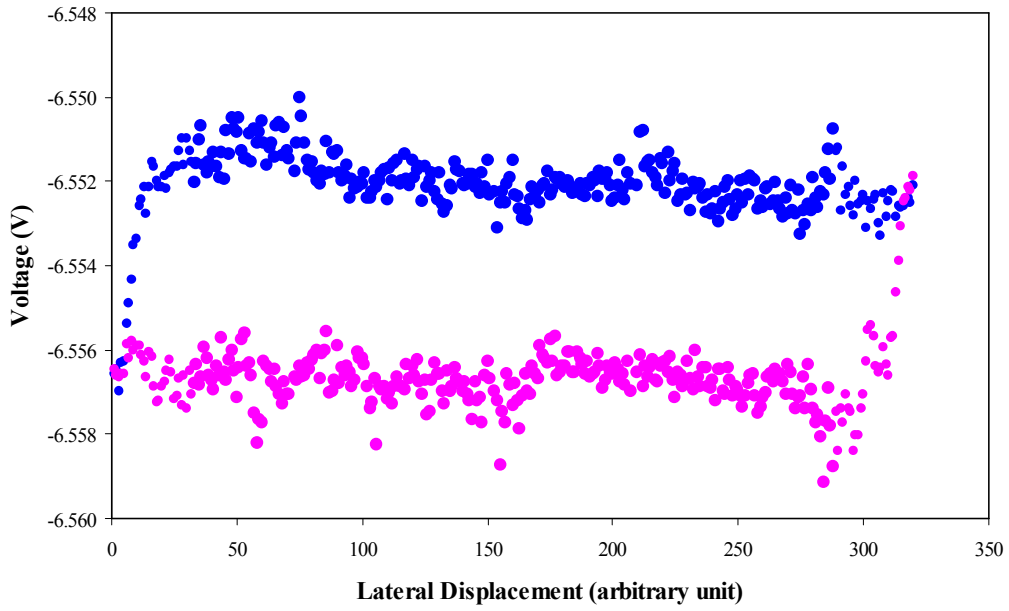


Figure 0.9: The lateral displacement (the 256 points in each trace are over a total distance of 25.6 μm), where ● are the trace points and ● are the retrace points.

PAM N, however, seems to have little effect on the lateral force experienced between the two iron oxide surfaces. This is due to the neutral polymer having low surface coverage. It does appear (although technically within experimental error) that after the addition of 20 ppm PAM N (where the surface coverage is approximately 17%), there is an increase in lateral force due to an increase in polymer bridging. This supports the conclusion that the polymer is in contracted conformation, or that it is adsorbed in a flat conformation at the surface. If there are less loops and tails, then there is less chance of entanglement, and therefore not likely to be a large impact on the lateral force.

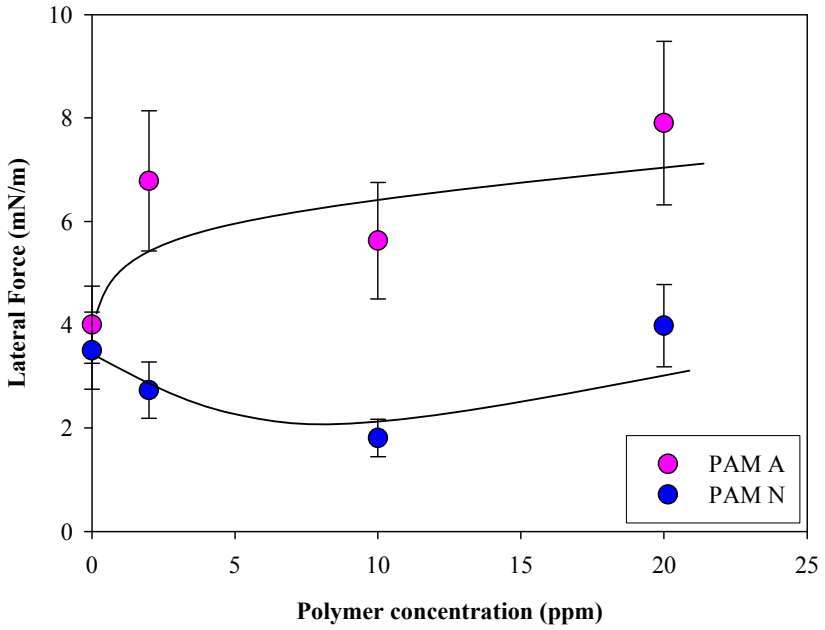


Figure 0.10: Lateral force measurements between two iron oxide surfaces after addition of PAM A and PAM N up to 20 ppm at pH 11 in 10^{-3} M KNO_3.

In Chapter 5, Figure 5.1, the zeta potential is shielded by polymer addition quite quickly up to 200 g/t polymer addition. At this point, the zeta potential seems to form more of a plateau (although the zeta potential is still approaching zero), with the bulk of the shielding occurring in the first 200 g/t of polymer addition. For pH 11, 200 g/t polymer represents approximately 40 % surface coverage for PAM A addition, and approximately 7 % surface coverage for PAM N addition. This illustrates PAM Ns effectiveness at shielding the charge despite a small amount of polymer being absorbed to the surface, further illustrating that PAM N adsorbs in a flat conformation and forms trains along the surface.

Yilmaz *et al*. [208] reported the lateral force between α-alumina and c-sapphire to be approximately 440 nN at pH 11 in similar salt conditions. That is approximately 20 times the lateral force found in our system at that pH. Bal [147] found significantly higher yield stress values after the addition of PAM A and PAM N to gibbsite and thus it is expected that the lateral forces would be higher than that observed here.

Toikka *et al*. [200] measured the lateral force between an iron oxide probe and a silicon wafer in the presence of 10^{-5} M (10 ppm) of a tri-block polyethylene oxide – polypropylene oxide co-polymer, and found that the measured lateral force for a system

was five times smaller than the pull-off force measured under identical conditions. Toikka *et al*. observed the lateral force of the iron oxide – silica system to be approximately 0.18 mN/m at pH 5.8, which is approximately 20 times less than the force observed in our system. At 10 ppm polymer addition with 5nN loading force (as was used in these experiments), Toikka *et al*. found the lateral force to be 0.20 mN/m, which is approximately ten times smaller than the force observed in this system after the addition of another non-ionic polymer, PAM N. It is however, pertinent to note that Toikka *et al*. used a different type of cantilever with a torsional spring constant approximately 1000 times smaller than the one used in this study. This seems to be very small and on comparison with another study, they found that their spring constant were approximately 200 times smaller than that observed by Neumeister and Ducker [212] and thus it may be possible that the lateral forces in their system may have been underestimated.

A.5 COMPARISON BETWEEN RHEOLOGICAL DATA AND LATERAL FORCE MEASUREMENTS

The lateral force F(L) shown in Figure 0.10 can be converted to shear strength (τ) via the following equation [179]:

$$\tau = \frac{F(L)}{A} \qquad \textbf{Equation 0.1}$$

where A is the real area of contact. There are multiple ways in which A can be calculated [213], all requiring pre-calculation of the elastic modulus which may be difficult to obtain for the present system due to the highly mobile environment of the polymers adsorbed at the iron oxide surfaces. In the case observed here where there is no adhesion observed between the surfaces, the models reduce to the Hertz equation where the equilibrium contact radius (R_c) is given by [214]:

$$R_c^3 = \frac{R_{eff} P}{E} \qquad \textbf{Equation 0.2}$$

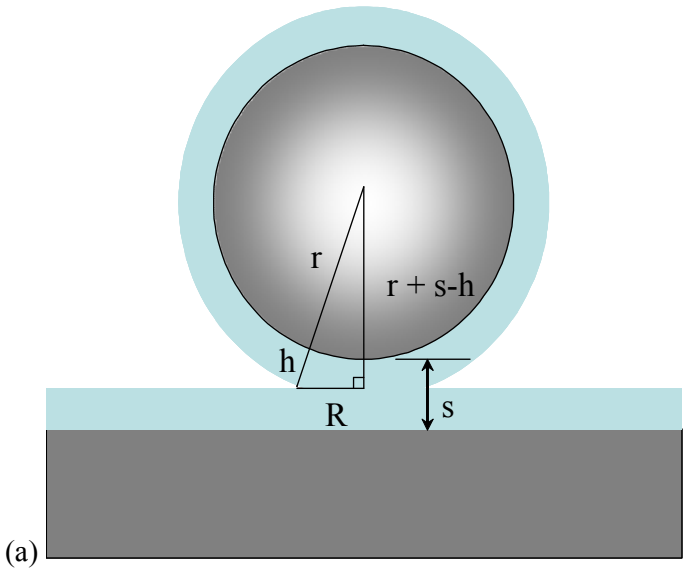
where R_{eff} is the effective radius (= $R_1R_2/(R_1 + R_2)$), P is the applied load and E is the total elastic modulus given by:

$$E = \frac{4(E_1 + E_2)}{3\pi}$$ **Equation 0.3**

where R_1 and R_2 and E_1 and E_2 are the radii and elastic modulus of the two contact surfaces, respectively. Given the complexity of this method and that regardless of the approach, this comparison (between the shear yield stress of hematite particles in a bulk, three dimensional system and the lateral force measured between iron oxide surfaces in a two dimensional system) is qualitative, it seems more appropriate to estimate the contact area, A, than the elastic modulus.

When estimating the real area of contact between a surface and a spherical probe, several factors must be considered. A schematic representation of the contact area is shown in Figure 0.7. At point B shown in **Error! Reference source not found.**, the distance, s, is given at the applied force value of 5 nN. The effective mobile layer (as determined in Table 0.3) is given by h, and r is the radius of the probe. The radius of the contact area is given by R, and can be calculated using the Pythagoras theorem. In either case presented below (example (a) is where the effective mobile layers are touching and example (b) shows the probe pressing into the layer), s-h can be positive or negative. R is given by:

$$R = \sqrt{(r+h)^2 - (r+s-h)^2}$$ **Equation 0.4**



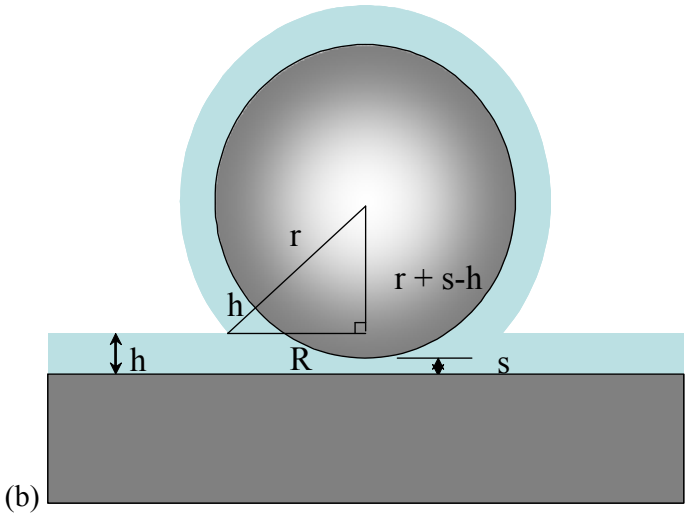


Figure 0.11: Schematic representation of the radius of the area of contact (R), where h is the effective mobile layer, r is the radius of the probe and s is the distance between the solid surfaces at an applied force of 1 nN. (a) where the effective mobile layers are in contact and (b) where the probe has pressed through the effective mobile layer.

Given R, the area of contact (assumed as a circle with area πR^2) can be calculated. This allows conversion of the lateral force (in N) to lateral force (in Pa) such that it can be compared with the yield stress data in Chapter 5. This comparison is shown in Table 0.4, and graphically in Figure 0.12. Whilst both yield stress and lateral force have been normalised for a surface area of 1 m^2, there is a significant difference in the actual area of each due to the individual experimental differences and the method of calculation. Yield stress measures the lateral force of randomly positioned dispersed particles in contact with the shear plane within a planar area of 1 m^2, whilst lateral force measures the friction between a 1 m^2 plate sliding over another wall. In other words, over the 1 m^2 surface area, the actual contact surface area is very small for yield stress and is exactly 1 m^2 for lateral force. However, it is sufficient for this exercise to compare the observed trends. PAM A in each case has both a higher surface coverage (due to its more expanded conformation) than PAM N, and also higher yield stresses/lateral forces due to the expanded polymer conformation causing entanglement and bridging of the surfaces.

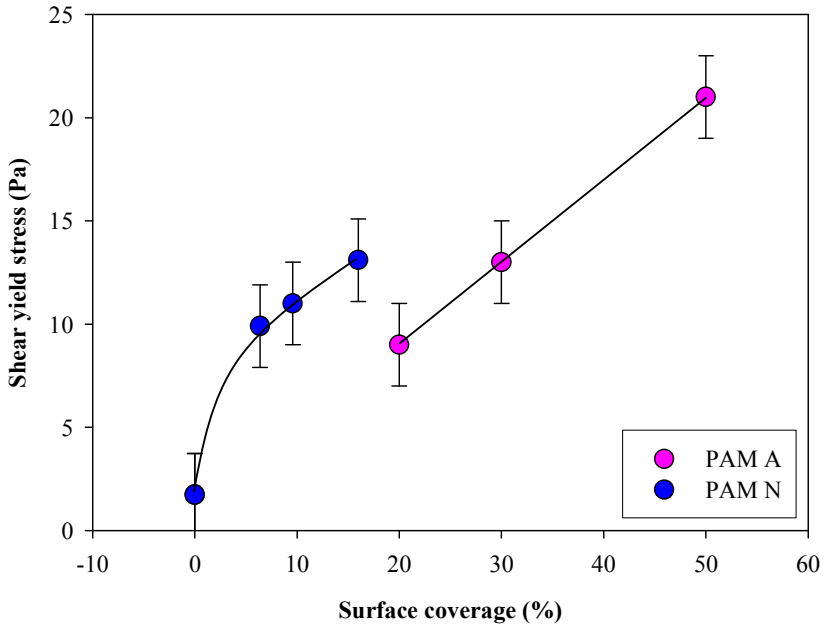
Table 0.4: A comparison between the bulk rheology of flocculated iron oxide dispersions and the lateral forces observed in similar systems under similar conditions (SC = surface coverage).

Yield Stress (Pa)

SC %	PAM A	SC %	PAM N
0.0	1.7	**0.0**	1.7
20.0	9.0	**6.4**	9.9
30.0	13.0	**9.6**	11.0
50.0	21.0	**16.0**	13.1

Lateral Force (Pa)

SC %	PAM A	SC %	PAM N
0.0	15764.6	**0.0**	15764.6
30.9	129339.7	**3.4**	32463.9
154.6	108484.6	**17.1**	24368.6
309.3	94084.0	**34.1**	102078.7



a)

b)

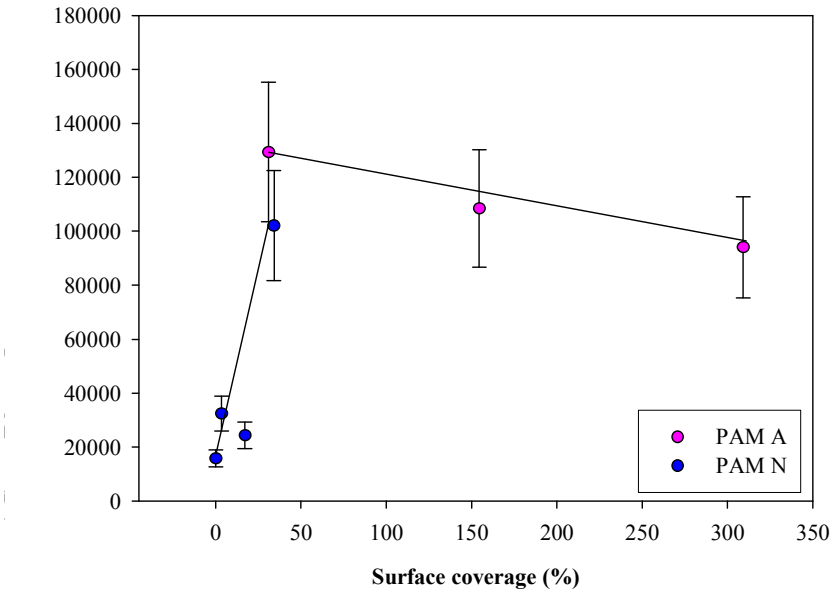


Figure 0.12: Rheology/Lateral Force comparison for PAM A and PAM N at different surface coverage for (a) Yield Stress and (b) Lateral Force.

It is observed that the lateral force increases with increased surface coverage for PAM N, which is expected due entanglement of the polymer layers and the reduction in surface charge. This was unclear in the previous presentation of this data in Figure 0.2, and thus this model allows a more in depth analysis of the data. The force vs. distance measurements for the effect of PAM N concentration (Figure 0.2b) showed a decrease in repulsion between the surfaces upon PAM N addition. This is consistent with the above observation of the lateral forces that show that as the repulsion decreases, the friction experienced between the two surfaces increase. In the case of PAM A addition, it is apparent that once the full surface coverage occurs (100%) that the polymer layers experience less friction due to increased electrosteric repulsion observed in the force vs. distance curves in Figure 0.2a.

A.6 CONCLUSION

Normal and lateral force measurements were taken between two iron oxide surfaces in the presence and absence of PAM A and PAM N at pH 11. Force curves generally showed repulsion between the surfaces over a range of polymer concentrations, except in cases where adhesion occurred on retraction of the probe due to the polymer molecules bridging the two surfaces (as observed as bridging flocculation in previous chapters) or through entanglement of polymer molecules.

Zeta potentials of the surfaces were calculated using the Poisson-Boltzmann equation, and were observed to be shielded by the polymer molecules as shown in previous chapters. A proposed model of the interfacial polymer adsorption was given as a result of these calculations, where PAM A was again observed to have a more expanded conformation than PAM N.

Lateral forces were observed between the two surfaces, where it was found that PAM A had a larger effect than PAM N, giving higher yield stress values. A model was proposed for the comparison of the shear yield stress observed via bulk rheology measurements and the lateral forces observed via AFM measurements. The lateral force data showed that the lateral forces between the surfaces are heavily dependent on the zeta potential observed in each case. PAM A and PAM N were shown to have similar behaviour at high pH, consistent with observations in previous chapters.